Searching for the Top

observation of the heaviest elementary particle at the LHC

Alexander Dimos Doxiadis

Dutch title:	*Zoeken naar de top* *waarneming van het zwaarste elementaire deeltje bij de LHC*
Cover:	Marc Faasse - www.marcfaasse.com
Cover Typography:	Maarten van Maanen
Print:	GVO drukkers & vormgevers B.V. - Ponsen & Looijen
ISBN:	978-90-6464-474-0

Netherlands Organisation for Scientific Research

This work is part of the research programme of the Foundation for Fundamental Research on Matter (FOM), which is part of the Netherlands Organisation for Scientific Research (NWO). The research has been supported by VIDI grant 680-47-219 of Dr. I.B. van Vulpen.

Searching for the Top

observation of the heaviest elementary particle at the LHC

ACADEMISCH PROEFSCHRIFT

ter verkrijging van de graad van doctor
aan de Universiteit van Amsterdam
op gezag van de Rector Magnificus
prof. dr. D.C. van den Boom
ten overstaan van een door het college van promoties ingestelde
commissie, in het openbaar te verdedigen in de Agnietenkapel
op donderdag 7 juli 2011, te 12:00 uur

door

Alexander Dimos Doxiadis

geboren te München, Duitsland

Promotor: Prof. dr. S.C.M. Bentvelsen
Copromotor: Dr. I.B. van Vulpen

Overige Leden: Dr. J.F. Arguin
Prof. dr. N. de Groot
Prof. dr. ir. P.J. de Jong
Prof. dr. P.M. Kooijman
Prof. dr. E.L.M.P. Laenen
Prof. dr. M.H.M. Merk
Dr. M. Vreeswijk

Faculteit der Natuurwetenschappen, Wiskunde en Informatica

CONTENTS

INTRODUCTION

> In the beginning there was nothing, which exploded.
> *Terry Pratchett*

To understand the universe, means understanding its smallest constituents. Although the visible matter particles and the forces that bind them only account for about 17% of the matter that we can deduce from gravitational considerations [1], they play in integral part in shaping the universe. From the quark-gluon plasma of the very early universe, to the understanding of neutrinos coming from violent explosions in far away galaxies, the driving forces behind these processes is governed by the Standard Model of particle physics [2]. This model is one of the great achievements of physics over the last one hundred years and governs three out of the four known fundamental forces of nature. While gravity is not incorporated, the Standard Model is one of the most precisely tested theories ever invented. The model is however not complete and extensions or new models are needed to explain things like dark matter or the (very small) neutrino masses.

Particle physics knows a long history of theoretical and experimental successes. One cannot proceed without the other. Every new discovery on either side brings answers as well as questions. The latest big experiment in this long line is the Large Hadron Collider (`LHC`) at `CERN`. Built in the old tunnel of its predecessor, the `LEP` collider, it collides protons at an energy higher than ever achieved before. This, in combination with unprecedented high luminosity, makes the `LHC` the perfect place for discoveries.

Of all the Standard Model particles that have been experimentally measured, the top-quark is by far the heaviest. With a mass that is comparable to that of a gold atom, it was also one of the last particles to be discovered. The top-quark plays a special role in high energy physics. Its mass is close to the scale of the electroweak symmetry breaking and its coupling to the Higgs-field is almost unity. Through precision measurements in the electroweak sector, information can be gathered about the Higgs-boson mass in relation to the top-quark mass. The top-quark mass is an important parameter of the Standard Model.

A measurement of the top-quark pair production cross section is an analysis that involves precise knowledge of the entire detector. In the decay channel with one lepton (the semi-leptonic decay channel) it means identifying the lepton, measuring many high momentum jets and large missing transverse energy. Since the theoretical value of the top-quark pair production cross section is well predicted, its measurement can be considered a ‘standard candle’.

The cross section determination is however not just a test of the detector performance and understanding. Above all, measuring the top-quark pair production cross section is a test of the Standard Model and quantum chromodynamics in particular and it will be the main objective of this thesis. In addition, the top-quark signature resembles the event topology of many new physics models (beyond the Standard Model). Extensions of the Standard Model like supersymmetry or resonances that would involve extra dimensions would show up in the top-quark measurement.

In order to select a clean sample of top-quark candidate events, the possible backgrounds have to be understood. From earlier measurements at the `Tevatron` collider it is expected that almost all backgrounds are reasonably well modeled and can be controlled. There is however one background that cannot be easily simulated or theoretically predicted: QCD multi-jet events. We will show that this is indeed a potentially large background and that Monte Carlo simulation can only be used a guideline. The main focus of this thesis will be: the possibility of QCD events to pass the isolated high-$\mathrm{p_T}$ lepton requirement that is used to select semi-leptonic $t\bar{t}$ events. We will show that data-driven methods are needed to obtain an accurate estimate of this background.

Due to the incident that occurred on the 10th of September 2008 and the delay that followed, the center of mass energy planned to achieve at the `LHC` was lowered from 14 TeV first to 10 TeV and later to 7 TeV. This explains the use of two different sets of Monte Carlo samples in this thesis, since some work dates back to the time of the 10 TeV simulated samples. Finally on the 30th of March 2010 the first high-energy proton-proton collisions at $\sqrt{s} = 7$ TeV were measured by `ATLAS` and the analysis of data started. Even with just 2.89 pb^{-1} the first top-quark pair production cross section measurement was published [3] which uses the data-driven method for the estimation of the QCD background that is the subject of this thesis.

Outline

In Chapter 1 we will describe the Standard Model briefly and focus on the production and decay of the top-quark in more detail. We will also present some details behind the Monte Carlo simulation and the samples that we used for this thesis. The `LHC` and the `ATLAS` detector will be presented in Chapter 2. We will briefly discuss some of the detector performance issues important to our measurement. The reconstruction of objects and the selection of top-quark candidate events will be presented in Chapter 3. We will see in this chapter clearly which background samples are dominant for the analysis.

Chapters 4 and 5 are studies performed on 10 TeV simulation that serve as background information to the final analysis. We will first study extra leptons in multi-jet events and then present two existing data-driven methods to gain some experience with the methodology. Finally in Chapter 6 we will have a first look at the data. We will show distributions that are important to the top-quark pair production measurement and the estimation of the QCD background. In Chapter 7 we will develop and study a method to perform a data-driven estimation of the QCD background called the ‘matrix-method’. The results from this method will be used in Chapter 8 to finally extract the top-quark production cross section.

Amsterdam, March 2011

CHAPTER 1

STANDARD MODEL AND LHC PHYSICS

1.1 The Standard Model

The Standard Model of particle physics describes the fundamental building blocks of nature. It started getting shape in the sixties and seventies and is the most accurate theory ever produced. It describes all known matter particles in the universe and (besides gravity) their interactions. The Standard Model is a relativistic quantum field theory [4] based on symmetries found in nature. 'Symmetries' in this case means that certain transformations can be made to the particles or fields of the theory, that leave the physics unchanged. These global symmetries are important since they lead to conserved quantities or charges. Local transformations, i.e. transformations that vary depending on their position, generally spoil the symmetry property, but the symmetry can be restored by the introduction of gauge fields. The full Standard Model is described by such local symmetries where the corresponding gauge fields describe the various interactions.

The symmetry transformations of the Standard Model are the $SU(3)_C \times SU(2)_L \times U(1)_Y$ groups. The associated charges of the global symmetry are the colour charge (C), the weak isospin (I) and the hypercharge (Y). The local variant of the symmetry transformations introduces a number of gauge fields that describe the interactions. The $SU(2)_L \times U(1)_Y$ sub-group is associated with the electroweak part of the theory. Its gauge fields correspond to the $W^{\pm}$ and the Z-bosons as force carriers of the weak force and the γ as carrier of the electromagnetic force. The gauge fields of the local $SU(3)_C$ group are the eight different gluons, the carriers of the strong force.

The elementary particles of the Standard Model are the fermions (spin $\frac{1}{2}$, where we have set $c = \hbar = 1$): quarks and leptons. The left-handed quarks and leptons are grouped together in isospin doublets and the right-handed quarks and leptons are isospin singlets under $SU(2)$. The $W^{\pm}$-boson only couples to the left-handed fermions. The right-handed quarks and the right-handed leptons[1] only couple to the weak force through the Z-boson. In contrast to leptons, quarks carry colour charge and thus couple also to the strong force. Colour comes in three variants, called red, green and blue. The particles that can be found on our planet abundantly are the up (u) and down (d) quark and the electron (plus its neutrino). These particles form a family in the sense that they form a complete normalizable set. However, copies of this first family particles were discovered that revealed the existence of the second and third family, consisting of particles that are ordered in the same structure as the first family, but with higher mass. It is not known if even more families of particles exist. All particles also have a counterpart called 'anti-particle' with the same mass and quantum numbers, but opposite charge. In Table 1.1 the force carriers and all elementary particles are presented with their spin and electric charge.

	particles			spin	electric charge
Quarks	$(u,d)_L$	$(c,s)_L$	$(t,b)_L$	$(\frac{1}{2},\frac{1}{2})$	$(+\frac{2}{3},-\frac{1}{3})$
	u_R	c_R	t_R	$\frac{1}{2}$	$+\frac{2}{3}$
	d_R	s_R	b_R	$\frac{1}{2}$	$-\frac{1}{3}$
Leptons	$(\nu_e,e^-)_L$	$(\nu_\mu,\mu^-)_L$	$(\nu_\tau,\tau^-)_L$	$(\frac{1}{2},\frac{1}{2})$	(0,-1)
	e^-_R	μ^-_R	τ^-_R	$\frac{1}{2}$	-1
Gauge bosons	g			1	0
	$W^\pm$ and Z			1	±1 and 0
	γ			1	0
Scalar boson	H			0	0

Table 1.1: *The Standard Model particles listed with the spin and electric charge. The subscripts L and R denote the helicity.*

The last particle yet to be experimentally observed in this overview of the Standard Model is the Higgs-boson (H). This boson has spin zero and is special in many ways. It has been given multiple well sounding names like the *holy grail of particle physics* and the *God particle*. These names (however badly chosen) reflect the importance of the Higgs-boson [7–10]. Its existence is linked to the fact that the $W^\pm$ and Z-boson masses are zero in a local gauge invariant theory. To introduce non-zero masses in a renormalizable and regularizable manner, spontaneous breaking of the electroweak symmetry is invoked by the Higgs-potential. The broken symmetry leads to masses of the well know electroweak gauge bosons, but leaves the photon massless (as expected). The Higgs-potential describes a non-zero Higgs-field in the vacuum with a vacuum expectation value (vev) of about 246 GeV. Also the existence of a Higgs-boson is predicted, with unknown mass. Through the introduction of the Higgs-field it is now also possible to give the fermions mass through coupling to the Higgs-field with the Yukawa coupling. As will be shown later, the top-quark mass is close to the vev which renders the Yukawa coupling almost unity for the top-quark. Observation of the Higgs-boson would indicate

---

[1] There is no right-handed neutrino in the Standard Model [5, 6].

that this mechanism of symmetry breaking is indeed realized in nature. It is this elusive particle that is one of the main physics goals at the `LHC`.

The Standard Model is however not complete and we mention some of the indications of this. From gravitational considerations the amount of matter in the universe can be determined and only about $\frac{1}{6}$th is described by the Standard Model and the rest is called 'dark matter' [1]. Possible dark matter candidates are given by 'Supersymmetry', an extension of the model [11]. Other indications are for example the massless neutrino, which has been found to be in fact massive (albeit with very small mass) [6] and the fact that gravity is not yet included in the model. Apart from the observation of the Higgs-boson, the search for new physics beyond the Standard Model was a big motivation for the construction of the `LHC`.

1.2 Hadron collider environment

Although the Large Hadron Collider (`LHC`) is designed to collide protons at a center of mass energy ($\sqrt{s}$) of 14 TeV, the first high energy collisions at the `LHC` occurred at $\sqrt{s} = 7$ TeV, in the spring of 2010. The operation of the `LHC` was forced to a lower energy [12] due to a malfunction of an electrical connection that had occurred a year earlier and caused massive mechanical damage. Compared to the `Tevatron` however, which is operated at a center of mass energy of 1.96 TeV, the `LHC` produces collisions at more than a factor three higher center of mass energy.

It is expected that the `LHC` will have delivered about 1 fb^{-1} of data to both the large multi-purpose experiments `ATLAS` and `CMS` [13] by the end of 2011. An intervention is scheduled for the year 2013 following the first long run-period to upgrade and make the machine ready to collide at design energy. This can be compared to the `Tevatron` which has provided the two experiments `DØ` and `CDF` with about 8 fb^{-1} of data [14].

As we show shortly, the higher center of mass energies will probe the colliding protons deeper and result in more available phase space for the production of particles. This in turn will lead to larger cross sections for particle production at the `LHC` compared to the `Tevatron`. In Figure 1.1 the cross sections for various processes are shown for $p\bar{p}$ collisions and for pp collisions as a function of $\sqrt{s}$.

Between the `Tevatron` and `LHC` energies, around a center of mass energy of 4 TeV, a number of discontinuities in the extrapolations of Figure 1.1 can be seen. The discontinuities can be understood by realizing that in fact two curves are drawn: the $p\bar{p}$ cross section for the `Tevatron` and the pp cross section for the `LHC`. Since the production of some particles depends on quark and anti-quark annihilation (like the production of $W^{\pm}$-bosons) and hence depends on the amount of anti-quarks, these two curves are not necessarily identical.

The proton is built up out of partons: the valence quarks (uud), sea quarks and gluons. To understand the behaviour of the cross section curves in Figure 1.1 it is important to take the momentum fraction x that a parton carries of the total momentum of the colliding proton into account. The probability to find a parton with momentum fraction

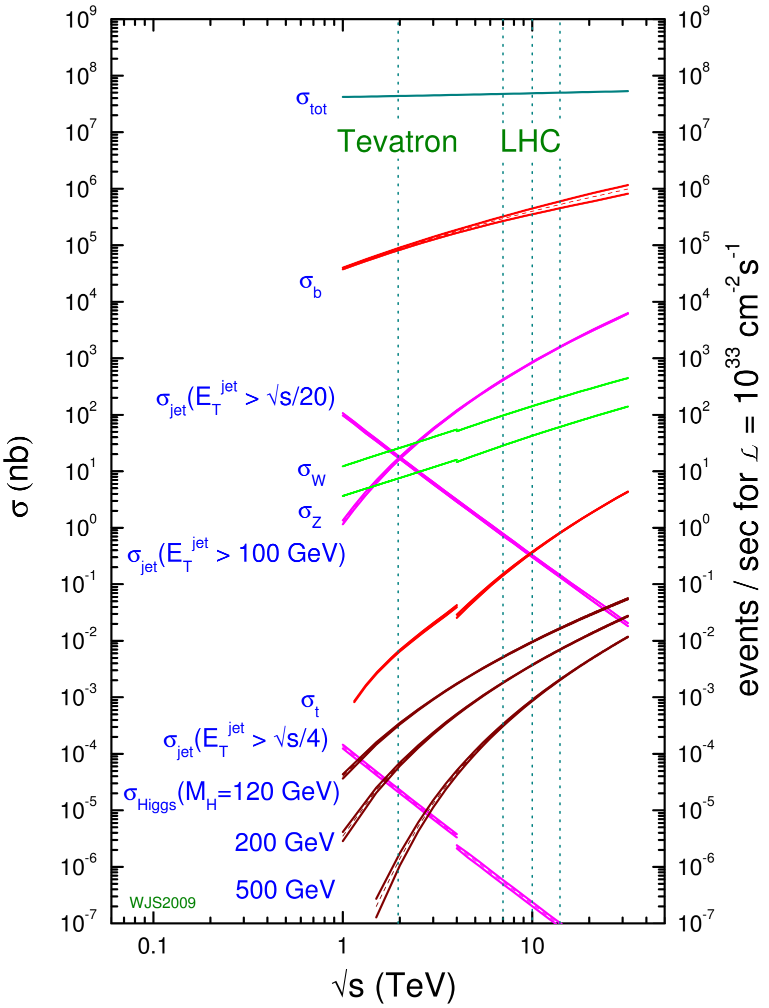

Figure 1.1: *Predicted cross sections of various processes at the* `Tevatron` *and* `LHC`*. Figure taken from [15].*

x in the proton is given by the parton density function, PDF. In Figure 1.2 the parton density functions `MSTW2008NLO` [16] are shown as a function of the momentum fraction x for two different values of Q^2 [17], which is the scale or resolution at which the proton is probed. Probing the proton deeper, that is at higher energy transfer Q^2, more details will be resolved leading to higher sea quark and gluon densities. The energy transfer in the hard scatter is also referred to as $\hat{s}$.

If a massive object with invariant mass M is formed in the hard scatter of two partons, the rapidity y in the lab frame is given by the energy (E) and the momentum along the

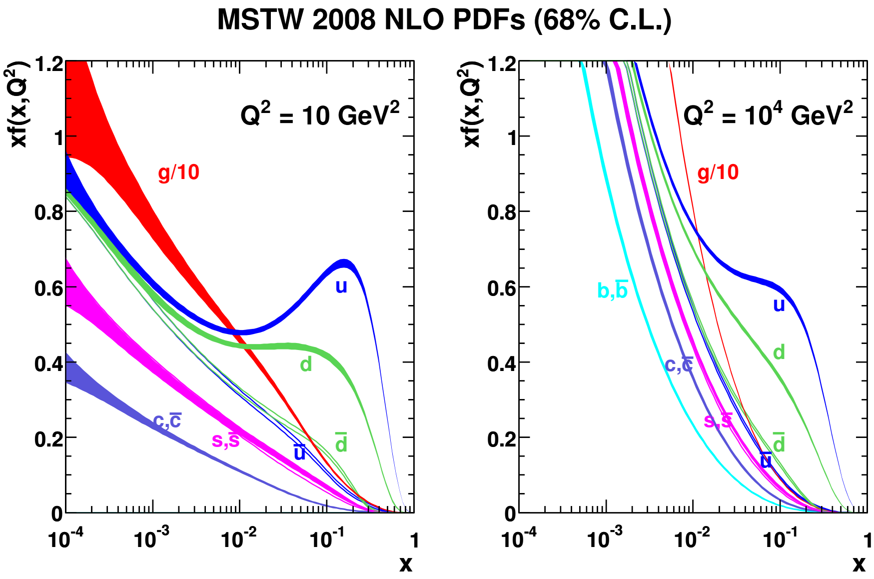

Figure 1.2: *The PDF (parton distribution function)* `MSTW2008NLO` *for different values of* Q^2 *as a function of the parton momentum fraction* x *of the proton. Figure taken from [17].*

beam-line ($\mathrm{p_z}$) of M [18]:

$$y = \frac{1}{2}\ln\frac{E+\mathrm{p_z}}{E-\mathrm{p_z}}.$$

Using this definition, the momentum fractions x_1 and x_2 of the partons in the proton-proton interaction can be derived as:

$$\begin{aligned} x_1 &= \frac{M}{\sqrt{s}}e^{+y}, \\ x_2 &= \frac{M}{\sqrt{s}}e^{-y}. \end{aligned} \tag{1.1}$$

By writing the effective center of mass energy squared for the partonic process as $\hat{s} = x_1 x_2 s$ the minimum momentum fraction needed for the production of a heavy object can be computed given the center of mass energy of the colliding particles. Since at least enough energy has to be present to produce the heavy object with rest-mass M_{rest}, $\hat{s} = M^2 \geq M^2_{\mathrm{rest}}$. Using Equation 1.1 for the production of a top-quark pair with rest-mass $M_{t\bar{t}} \sim 350$ GeV and no momentum along the beam-line ($y = 0$) and setting $x_1 \approx x_2 = \langle x \rangle$, the values obtained for the `Tevatron` are $\langle x \rangle \sim 0.2$ and for the `LHC` $\langle x \rangle \sim 0.025/0.035/0.05$ at $\sqrt{s} = 14/10/7$ TeV. This means that at the `LHC` partons with lower momentum fraction compared to the `Tevatron` can produce top-quark pairs.

Since the parton densities increase when going to lower values of x, see Figure 1.2, especially for gluons, the cross sections also increase, see Figure 1.1. Apart from higher cross section there is another difference between the `LHC` and the `Tevatron` that can be derived using Equation 1.1: produced particles will have on average a higher boost at the `LHC`. This can be seen by comparing again a top-quark pair produced at threshold at the `Tevatron` ($\langle x \rangle = x_1 = x_2 = 0.2$) with the `LHC`. At the same value of $x_1 = 0.2$ already a value of $x_2 \geq 0.003$ is enough to produce the top-quark pair at the `LHC`. Assuming massless partons with no transverse momentum, this leads to a produced mass state with $x = x_1 - x_2$, i.e. large momentum along the beam-line. The top and antitop-quark will thus have larger boosts at the `LHC` with respect to the `Tevatron`.

1.3 Top-quark physics

The top-quark is special in the Standard Model for different reasons. It was the last quark to be experimentally observed and this happened only in 1995 at the `Tevatron` by the `D0` and `CDF` experiments [19,20]. The existence of the top-quark was no surprise however: it was postulated as the weak isospin partner of the bottom-quark after its discovery in 1977 [21,22]. The idea of a third family of elementary particles was brought forward by Kobayashi and Maskawa already in 1973 to explain CP-violation in the Standard Model [23]. The large mass of the top-quark was not anticipated however. Apart from the large mass of the top-quark (comparable to that of a gold atom), it is also the only quark that decays before it hadronizes which means it passes its quantum numbers unambiguously to its decay products. We will look into some of the areas of top-quark physics in the following sections.

In the previous section it was shown that cross sections are higher at the `LHC` than at the `Tevatron` for many processes. This means that also the production of the heaviest quark, the top-quark, will be abundant. The `LHC` has been called a *top factory* since based on $\sqrt{s} = 14$ TeV and instantaneous luminosity of $10^{33}\text{cm}^{-2}\text{s}^{-1}$ the production rate could be as high as nine million $t\bar{t}$ pairs per year [24], see right-hand side of Figure 1.1. Using the more recent numbers for the 2011 period at $\sqrt{s} = 7$ TeV [13] an expected 165 $\cdot 10^3$ $t\bar{t}$ pairs will be produced, which is of the same order of magnitude as produced at the `Tevatron` in its entire lifetime. The production rates will rise quickly with higher center of mass energy and increasing instantaneous luminosity, making the `LHC` the perfect place to perform precision studies on top-quarks. Note also that the production cross section of the top-quark rises steeper with $\sqrt{s}$ than of most backgrounds, resulting in a cleaner top-quark environment at the `LHC` than at the `Tevatron`.

The world average of the top-quark mass from direct measurements is 173.3 ± 1.1 GeV [25,26]. This mass is usually taken to represent the *pole mass*, which is the real part of the perturbative top-quark propagator. This mass has, like all quark masses, an intrinsic uncertainty of the order of $\Lambda_{\text{QCD}} \sim 200$ MeV [27]. The precise definition of the top-quark mass depends directly on the experimental techniques used to determine it. In this thesis m_t will represent the MC mass which is usually taken to represent the pole mass[2] (up to ~ 1 GeV inherent theoretical uncertainty).

1.3.1 Top-quark pair production

Whereas in the previous section we gave heuristic arguments for the production of heavy mass objects, like a $t\bar{t}$ pair, here we follow a more formal approach. The production of top-quark pairs at a hadron collider is described by perturbative QCD. The hard scattering process is then given by the interaction between two partons (constituents of the colliding hadrons) with a given momentum fraction x of the hadron, see Section 1.2. The parton model description of the collision of two protons leading to the production of a top-quark pair is shown graphically in Figure 1.3.

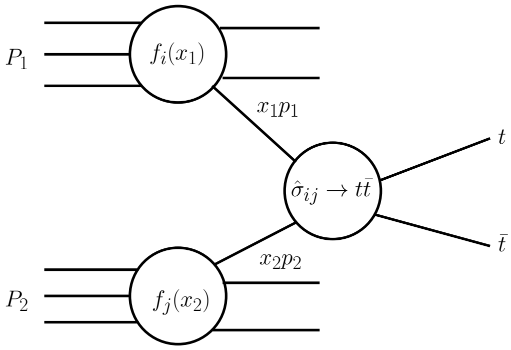

Figure 1.3: *Parton model description of a hard scattering using the factorization model: partons i and j with momentum fractions x_1 and x_2 coming from the colliding protons P_1 and P_2 creating a top-quark pair.*

In this figure the $P_1(p_1)$ and $P_2(p_2)$ are the incoming protons with momentum p_1 and p_2 respectively and the hard scatter is given by the interaction of parton i and j with momentum x_1p_1 and x_2p_2 respectively. The probability to find parton i in the proton with momentum fraction x_1 is given by the function $f_i(x_1, \mu_f^2)$ which is the PDF as shown already in Figure 1.2. The parton-parton cross section for the $t\bar{t}$ production is written here as $\hat{\sigma}_{ij\to t\bar{t}}$. The separation of PDF's on the one side and the hard scatter on the other is called factorization [29, 30] and is possible since both describe different energy scales. The factorized proton-proton cross section for the production of top-quark pairs is then given by [31]:

$$\begin{aligned}\sigma_{P_1P_2\to t\bar{t}} = \sum_{i,j} \int_0^1 dx_1 \int_0^1 dx_2 f_i\left(x_1, \mu_f^2\right) f_j\left(x_2, \mu_f^2\right) \\ \times\, \hat{\sigma}_{ij\to t\bar{t}} \left(m_t, x_1p_1, x_2p_2, \alpha_s(\mu_r^2), \frac{Q^2}{\mu_r^2}, \frac{Q^2}{\mu_f^2} \right),\end{aligned} \tag{1.2}$$

---

[2] Other mass definitions give rise to difference in the top-quark mass up to 10 GeV [28].

with μ_f^2 the factorization scale, the scale at which the PDF's are evaluated and μ_r^2 the renormalization scale, the scale at which α_s is evaluated. A commonly used convention is to set $\mu_f^2 = \mu_r^2 = m_t^2$ and since a $t\bar{t}$ pair is produced also $Q^2 = M_{t\bar{t}}^2 \approx m_t^2$. Since $\alpha_s(m_t^2) < 1$, the partonic cross section can be computed using perturbation theory:

$$\hat{\sigma}_{ij\to t\bar{t}} = \alpha_s^2 \sum_{m=0}^{n} c_m \alpha_s^m, \tag{1.3}$$

with c_m governing all the kinematical variables and α_s the expansion parameter [32]. The lowest order in QCD is $\mathcal{O}(\alpha_s^2)$ and called leading order (LO). In the ideal case one would expand the series up to $n = \infty$, this is however impossible due to an exponentially increasing amount of diagrams that need to be included. The choice of the scale of the PDF and α_s ensures the absorption of all non-perturbative effects at scales below μ_r^2 and μ_f^2. The PDF's and the $\hat{\sigma}_{ij\to t\bar{t}}$ still have a residual dependence on the factorization and renormalization scale due to uncomputed higher orders. The overall cross section $\sigma_{P_1P_2\to t\bar{t}}$ (a physical quantity) should not depend on these scales, since they are not physical. By the inclusion of higher orders (more powers in the expansion parameter α_s) the dependence on the scales becomes smaller. The theoretical uncertainty due to the finite order of computation (scale uncertainty) is quoted by computing the changes in σ when varying the scale from $\mu = m_t/2$ to $\mu = 2m_t$. The PDF's and α_s are experimentally determined and can be extrapolated to any scale μ with the use of the DGLAP evolution equations [29, 33–36] and the renormalization equations [37] respectively.
The Feynman diagrams corresponding to $\hat{\sigma}_{ij\to t\bar{t}}$ at LO are shown in Figure 1.4 for $q\bar{q} \to t\bar{t}$ and $gg \to t\bar{t}$.

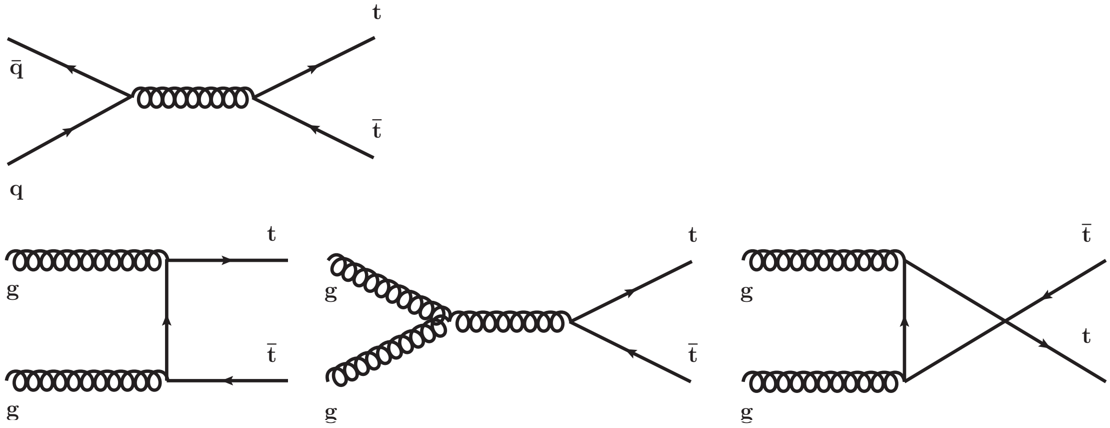

Figure 1.4: *Leading order Feynman diagrams contributing to $t\bar{t}$ production. Top: quark annihilation. Bottom: gluon fusion.*

There is no LO contribution from $gq \to t\bar{t}$ since the first Feynman diagram of this production channel (actually this is then $qg \to t\bar{t}q$) is at order $\alpha_s^3(m_t^2)$ which is NLO. The relative contribution per production channel to the total partonic cross section changes as a function of $\sqrt{s}$. As was already shown in Section 1.2 the minimal x values for the production of a top-quark pair at the `LHC` are low (varying from 0.025 to 0.05 depending on the center of mass energy). Since the gluon density at these values of x is high, as seen in Figure 1.2, the dominant production channel will be $gg \to t\bar{t}$ at the `LHC`. In Table 1.2 the theoretical cross section predictions are shown for various center of mass energies and the production channel [24, 32, 38]. The negative contribution in the $qg \to t\bar{t}$ channel can be understood by considering the $q\bar{q} \to t\bar{t}$ channel where one gluon is coming from gluon splitting: these processes are already included in the PDF. The negative contributions are then a consequence of the somewhat artificial classification of production channels. Note that at the `LHC` with $\sqrt{s} = 7$ TeV the production cross section without gg production would be of the order of 30 pb.

			$\sigma_{t\bar{t}}$(pb)	$gg \to t\bar{t}$	$q\bar{q} \to t\bar{t}$	$qg \to t\bar{t}$
`Tevatron`	$\sqrt{s} = 1.96$ TeV	LO	6.78	8.4%	91.6%	-
		NLO	6.85	13.8%	87.3%	-1.1%
`LHC`	$\sqrt{s} = 7$ TeV	LO	124	75.5%	24.5%	-
		NLO	162	82.8%	17.7%	-0.5%
`LHC`	$\sqrt{s} = 14$ TeV	LO	692	86.6%	13.4%	-
		NLO	903	89.2%	9.7%	1.1%

Table 1.2: *Theoretical $t\bar{t}$ production cross section at LO and NLO for both the `Tevatron` and the `LHC`. Numbers have been calculated with `MCFM` [38] using the `MSTW2008(N)LO` PDF and setting the top-quark mass to $m_t = 172.5$ GeV.*

There is no full next-to-next-to leading order (NNLO) computation for the production cross section of top-quark pairs available, but the approximate NNLO results has already considerably lower scale uncertainties than the lower order calculation [39]. In fact the scale uncertainty is now of the same order as the uncertainty originating from the PDF's. At $\sqrt{s} = 7$ TeV the latest approximate `NNLO` calculation for a top-mass of 172.5 GeV results in a cross section of [40]:

$$\sqrt{s} = 7 \text{ TeV}: \quad \sigma(t\bar{t}) = 164.57\,^{+4.30}_{-9.27}\,(\text{scale})\,^{+7.15}_{-6.51}\,(\text{PDF}). \tag{1.4}$$

For this cross section calculation[3] the `CTEQ6.6` NLO PDF [42] was used and it will be the default value for the top-quark production cross section analysis of this thesis. The difference between LO and NLO cross section is often quoted in the form of the K-factor, which is defined by: K = σ(NLO)/σ(LO). For the $t\bar{t}$ production cross section K $\simeq$ 1.3 at the `LHC`[4], which shows that including higher order corrections can have large effects.

---

[3] The actual calculation was performed following the recipe by Moch et al. [40] by using the `HATHOR` tool [41] in order to extract the cross section for $m_t = 172.5$ GeV and $\sqrt{s} = 7$ TeV.

[4] The K-factor can even be higher when comparing the NLO and LO cross section computed with the same order PDF. Using the NLO PDF K $\simeq$ 1.5 [24].

Measurement at the `Tevatron`

The production cross section of top-quarks pairs has of course already been measured at the `Tevatron`. The latest combination of results of both `CDF` and `DØ` at $\sqrt{s} = 1.96$ TeV and $m_t = 172.5$ GeV are given by [43–46]:

$$\begin{aligned} \texttt{CDF}: \ \sigma_{t\bar{t}}(p\bar{p}) &= 7.50^{+0.48}_{-0.48}\ \text{pb} \qquad \int \mathcal{L}\text{dt} = 4.6\ \text{fb}^{-1} \\ \texttt{DØ}: \ \sigma_{t\bar{t}}(p\bar{p}) &= 7.70^{+0.79}_{-0.70}\ \text{pb} \qquad \int \mathcal{L}\text{dt} = 4.3\ \text{fb}^{-1}. \end{aligned} \tag{1.5}$$

Since the `CDF` measurement is based on the analysis of a slightly larger data-set and includes the fully hadronic $t\bar{t}$ channel (see next section), the uncertainties cannot easily be compared. The latest approximate NNLO result for the `Tevatron` center of mass energy $\sqrt{s} = 1.96$ TeV is $\sigma(t\bar{t}) = 7.04\ ^{+0.24}_{-0.36}$ (scale) $^{+0.14}_{-0.14}$ (PDF) [28] (`MSTW2008`, $m_t = 173$ GeV). The results agree well with each other and also with the theoretical predictions. For both experiments the statistical and systematic uncertainties are of equal size.

Cross section dependence on the top-quark mass

The production cross section of the top-quark pair depends on the mass m_t. In Figure 1.5 the dependence of the production cross section on the top-quark mass is shown for NLO and (approximate) NNLO [28]. Since the dependence of $\sigma(t\bar{t}\,)$ on m_t is theoretically well known, a measurement of the top-quark pair production cross section is an alternative measurement of the top-quark mass. Note however that the theoretical uncertainties would still lead to an uncertainty in the mass measurement of a few GeV which is not competitive to the direct measurements yet.

The measurement of the top-quark pair production cross section is an important measurement for many reasons. Not only because it utilizes all different aspects of particle detection (see Section 1.3.2) and not only because it offers an independent top-quark mass measurement, it is also on itself an important test of the Standard Model. Beyond the Standard Model $t\bar{t}$ production, for example through heavy resonances [47,48] or the coupling of the top-quark to a charged Higgs-boson [49], would alter the measured cross section compared to the theoretical Standard Model (SM) prediction. On top of this, the top-quark pair production cross section is a measurement that can be performed with only a small amount of data [50]. This is why the determination of the $t\bar{t}$ production cross section will be the focus of this thesis.

1.3.2 Top-quark decay

Due to the large mass of the top-quark it can decay into an on-shell W-boson and a b-quark: $t \to Wb$. The decay-width of the top-quark is given in the Born approximation by [24]:

$$\Gamma_{t\to Wb} = \frac{G_F m_t^3}{8\pi\sqrt{2}}|V_{tb}|^2 \left(1 - \frac{M_W^2}{m_t^2}\right)^2 \left(1 + 2\frac{M_W^2}{m_t^2}\right), \tag{1.6}$$

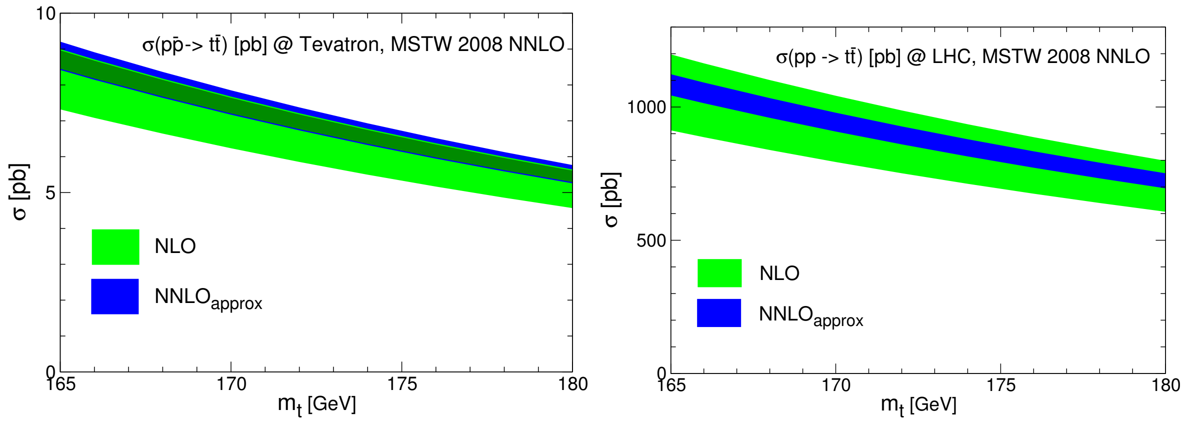

Figure 1.5: *The dependence of the total production cross section of $t\bar{t}$ on the top-quark mass for NLO and (approximate) NNLO using the `MSTW2008NLO` PDF. The band denotes the theoretical uncertainty due to scale variations and PDF uncertainty. Left: at the `Tevatron` with $\sqrt{s} = 1.96$ TeV. Right: at the `LHC` with $\sqrt{s} = 14$ TeV. Figures taken from [28].*

where G_F is the Fermi constant and $|V_{tb}|$ the CKM matrix element. $|V_{tb}|$ has been determined from the weak decay of heavy hadrons using the unitarity of the CKM matrix to be ~ 0.999 [25], meaning that $\Gamma_{t \to Wb} \approx \Gamma_t$. By using $G_F = 1.16637 \cdot 10^{-5}$ GeV^{-2}, $M_W = 80.40$ GeV and $m_t = 171$ GeV Equation 1.6 yields $\Gamma_t = 1.44$ GeV. A detailed evaluation including QCD corrections to order α_s and weak corrections to order α as well as the width of the W-boson and $m_b \neq 0$ [24] yield a final prediction of $\Gamma_t = 1.28$ GeV. The proper life-time of the top-quark can then be computed to be $\tau_t = 1/\Gamma_t \approx 5 \cdot 10^{-25}$ s. This is an order of magnitude shorter than the time-scale of hadronization: $1/\Lambda_{\rm QCD} \approx 3 \cdot 10^{-24}$ s. This means that the top-quark will decay before it hadronizes, making it the only quark that passes on its quantum numbers like spin and helicity to its decay products in a direct manner.

Event topology of top-quark pair events

Top-quark pair events can be characterized by the way the W-bosons subsequently decay. The W-boson can decay into a pair of light quarks $(q\overline{q'})$ or leptonically into $l\overline{\nu_l}$. If both W-bosons from the top-quark pair decay leptonically the channel is called 'dileptonic', only one W-boson decaying into a lepton 'semi-leptonic' and both W-bosons hadronically yields the name 'fully hadronic'. This results in the decay channels as shown in Figure 1.6 [32, 51], where the area of the figure is proportional to the branching ratio into a certain channel.

This thesis will focus on the semi-leptonic decay channel. The fraction of $t\bar{t}$ events that decay semi-leptonically can be computed from the branching ratio of $W \to q\overline{q'} = 67.6\%$ [25] to be 43.8 % (dileptonic 10.5 % and fully hadronic 45.7 %). The semi-leptonic decay

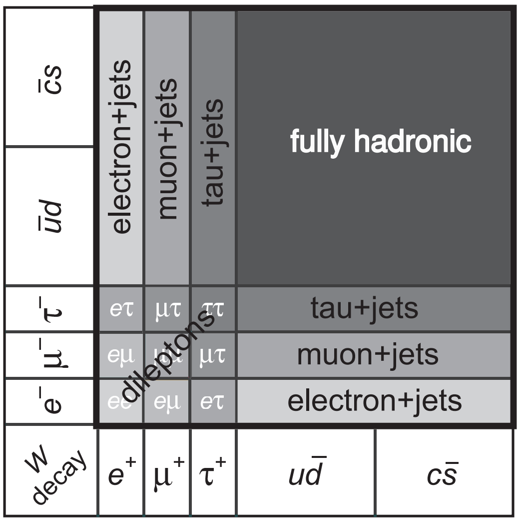

Figure 1.6: *The decay channels of the top-quark pair. Figure taken from [32, 51].*

channel is characterized by two b-quarks and two light quarks, a lepton and a neutrino that will escape the detector without detection. The quarks will form jets, see Section 1.4.1, making the $t\bar{t}$ decay a multi-jet event with a lepton and missing energy due to the neutrino. We will investigate this event topology in more detail in Section 3.3. The decay channel can further be specified by the lepton-flavour: $t\bar{t}(e)$ for an electron and $t\bar{t}(\mu)$ for a muon. In Figure 1.7 an illustration is shown of the semi-leptonic (left) and the fully hadronic (right) $t\bar{t}$ decay channel.

Since the lepton produced in the $t\bar{t}$ decay originates from the heavy W-boson, which will have quite a large boost at the `LHC`, it will have high-$\mathrm{p_T}$ and will appear isolated. The average $\mathrm{p_T}$ of the lepton is however not higher than at the `Tevatron`, about 40 GeV, since the W-boson only couples to left-handed fermions[5]. Assuming no right-handed W-bosons (W_R) in top-quark decay, the fraction of longitudinally polarized W-bosons (W_0) can be written as [52, 53]:

$$F_0 \equiv \frac{\Gamma(t \to W_0)}{\Gamma(t \to W_0) + \Gamma(t \to W_L)} = \frac{\frac{1}{2}(m_t/M_W)^2}{1 + \frac{1}{2}(m_t/M_W)^2},$$

which is $\sim 70\%$ due to the large mass of the top-quark. This then in turn leads to the lepton being emitted on average in the opposite direction of the boost of the W-boson, due to the absence of a right-handed neutrino. The lepton therefore will only have about half the W-boson mass as momentum [31] and the neutrino will on average have a higher momentum. This feature offers an interesting way of investigating the Standard Model couplings since top-quark decay is the only real source of longitudinally polarized W-bosons at a hadron collider.

---

[5] Left-handed in the sense of the projection operator $P_L = \frac{1}{2}(1 - \gamma^5)$ [31]. This is only the same as helicity, $\epsilon = \frac{\vec{s} \cdot \vec{p}}{|\vec{s}||\vec{p}|}$, in the limit of massless particles.

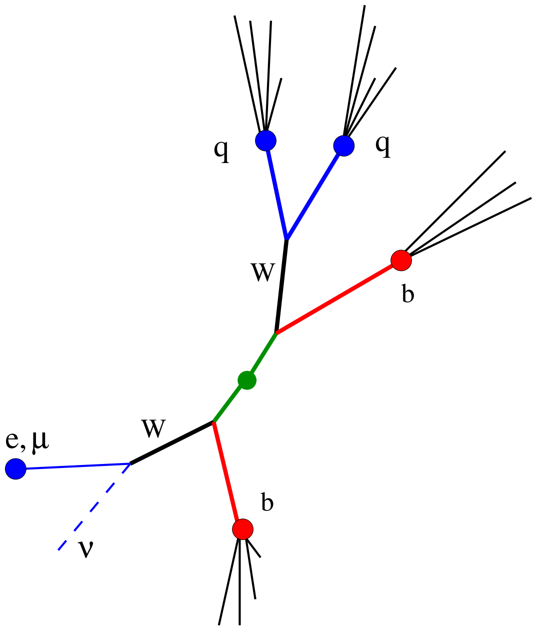

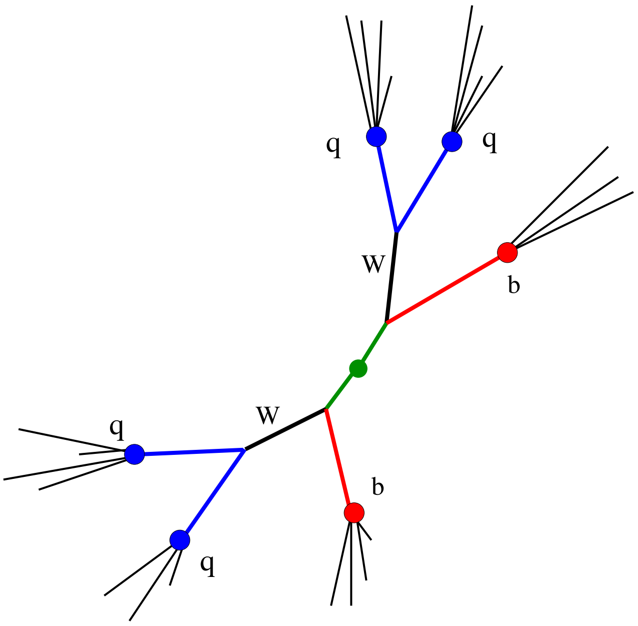

Figure 1.7: *Left: Illustration of the semi-leptonic $t\bar{t}$ channel where one W-boson decays leptonically and the other hadronically. Right: The fully hadronic channel, i.e. both W-bosons decay hadronically.*

1.3.3 Top-quark in relation to the Higgs-boson

Thanks to the precise measurements performed in the electroweak sector, information about the Standard Model parameters can be inferred and sensitivity to the top-quark mass and the Higgs-boson mass is gained through radiative corrections. The electroweak quantities (mass, width and couplings of the $W^\pm$ and Z-boson) depend in the SM on only five parameters (at leading order only three). The parameters can be determined using the best electroweak measurements. These measurements include the electromagnetic coupling constant α [54], the Fermi constant G_F determined from the muon lifetime [55] and the Z-boson mass measured at `LEP` and `SLC` [56]. The masses of the $W^\pm$ and Z-bosons can be expressed in terms of the top-quark mass as a function of the radiative corrections Δr as [57]:

$$M_W^2 = \frac{\pi\alpha}{\sqrt{2}G_F} \cdot \frac{(1+\Delta r/2)}{\sin^2\theta_W}, \tag{1.7}$$

with $\sin^2\theta_W \equiv 1 - M_W^2/M_Z^2$. Contributions to Δr come from the top-quark and the Higgs-boson by one-loop diagrams. The dependence on the Higgs-boson mass, m_H, is only logarithmic whereas there is a quadratic dependence on m_t [31]:

$$\begin{aligned}\Delta r_{top} &\simeq -\frac{3G_F}{8\sqrt{2}\pi^2\tan^2\theta_W}m_t^2,\\ \Delta r_H &\simeq \frac{3G_F M_W^2}{8\sqrt{2}\pi^2}\left(\ln\frac{m_H^2}{M_Z^2}-\frac{5}{6}\right).\end{aligned} \tag{1.8}$$

This means that the constraints on m_H are much weaker from the electroweak sector than on m_t. This was used to predict the top-quark mass already before its direct measurement in 1995 [19, 20]. This predictive success provides confidence in the SM and the possibility to use the precision measurements and direct measurements of the top-quark and the W-boson mass to infer on the mass of the SM Higgs-boson. Figure 1.8 shows the direct and indirect measurements of m_t and M_W and the latest fits to electroweak precision data of the mass of the Higgs-boson [58].

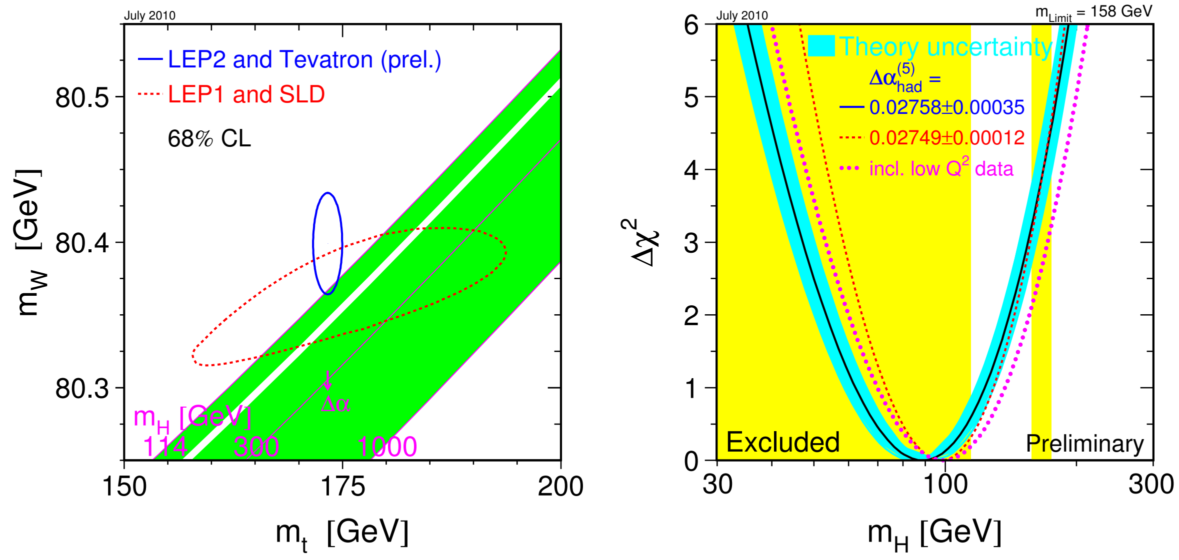

Figure 1.8: *Left: the direct (solid) and indirect (dotted) measurements of M_W and m_t at a 68% confidence level. Shown are also lines of constant Higgs-boson mass. Right: the 'blueband' plot of the $\Delta\chi^2$ distribution as a function of the Higgs-boson mass obtained by indirect measurement by LEP, SLD, CDF and D0. The blue line is the theoretical uncertainty. Also included are the exclusion limits at 95% confidence level from direct searches by LEP (lower limit) and the exclusion from 158 GeV to 175 GeV by CDF and D0. Figures taken from [58].*

From the $\Delta\chi^2$ distribution it can be concluded that a light Higgs-boson is preferred by the SM electroweak fit. Figure 1.8 indicates that there is some tension in the Standard Model. The electroweak precision measurements seem to favour a low Higgs-boson mass, but this is excluded below 114.4 GeV from direct searches by `LEP` [59]. The `LHC` will hopefully solve this tension in the coming years.

1.3.4 Top-quarks beyond the Standard Model

The top-quarks plays an important role in most searches for physics beyond the Standard Model. The first reason for this is that the top-quark pair decay is a multi-jet event. Together with the presence of a high momentum lepton and large missing energy, the decay resembles many super symmetric decays or other new physics models. Another reason for its importance is the direct role it plays in many models due to its large mass. It was mentioned already in Section 1.3.1 that new physics models like top-quark decay to charged Higgs-bosons or heavy resonances might influence the measured $t\bar{t}$ production cross section and hence might be discovered there. There is however another top-quark measurement that is even more sensitive to physics beyond the Standard Model: the invariant mass of the top-quark pair ($M_{t\bar{t}}$). It has been shown that the $M_{t\bar{t}}$ distribution functions almost as a model independent way of finding new physics phenomena [60].

Many extensions of the Standard Model predict new particles that could decay into top-quark pairs and hence would show up in the $M_{t\bar{t}}$ distribution as (narrow) peaks. These particles usually have masses in the TeV region. The models include 'Little Higgs' models [61] and models that predict extra dimensions that have 'Kaluza-Klein' excitations of the graviton [62]. Some of these models could be discovered within the first year of data taking and `ATLAS` will concentrate on these model independent searches in the coming period [48, 63, 64].

For the early analysis in this thesis there is however not enough data to perform the $M_{t\bar{t}}$ studies. We will concentrate on the inclusive production cross section measurement. Typical cross sections for $pp \to X \to t\bar{t}$ are of the order of 3 pb (1 pb) for a mass of the heavy resonance of $m_X = 500$ GeV (1 TeV) [48]. Given the uncertainties, these cannot be measured in an inclusive cross section measurement.

1.4 Event generation and detector simulation

A key aspect of high energy physics is Monte Carlo event generation (MC) and the simulation of the detectors. From designing new experiments to the optimization of analyses, MC is a vital tool when it comes to understanding the collision between protons with the production of new heavy particles and their decays. MC programs use random numbers to perform integration over available phase space. They are able to handle the decay of top-quark pairs, but also the generation of particles predicted in theoretical extensions of the Standard Model. In Section 1.4.1 some MC generator techniques will be discussed, we will briefly mention the detector simulation in Section 1.4.2 and the MC samples used in the rest of this thesis will be presented in Section 1.4.3.

1.4.1 Monte Carlo generator techniques

In order to simulate events and their decay, the generation chain is split into smaller pieces. As an example, the production of $t\bar{t}H + X$ is shown schematically in Figure 1.9 [32,65]. The various stages that have to be handled by event generators are the hard scatter (HS) which depends on the parton density function (PDF), parton showering divided into the initial and final state radiation (ISR, FSR), hadronization, decay and the underlying event (UE).

Figure 1.9: *Schematic view of the production of $t\bar{t}H + X$ in a pp collision. Shown in the ellipses are the various stages that need to be handled by simulation programs: the hard scatter (HS) which depends on the parton density function (PDF), initial and final state radiation (ISR and FSR), the hadronization and decay of particles and the underlying event (UE). Figure taken from [32,65].*

The reason that this separation into different stages can be made is that they occur at different energy scales and can therefore be seen as independent (as was discussed before under the name of factorization). In this section we will discuss these stages and the programs used to simulate them. Some generators can generate the full event chain up to the detector level. These general purpose generators include `HERWIG` [66] and `PYTHIA` [67], both used in this thesis. It is however more common to use specialized generators to replace part of this simulation chain in order to improve accuracy for certain processes and interface them with the general purpose generators.

The hard scatter

The hard scatter describes the main interaction in particle collisions. This interaction at parton level occurs at the highest Q^2 scale and is the place where heavy (new) objects are formed. It is described by the matrix elements of the interaction (integrated over the phase space). The matrix elements are governed and computed by Feynman rules and a number of programs are dedicated to the computation of matrix elements. `Alpgen` [68] is a sum of LO matrix element generators for various processes with up to six additional jets. There are also programs that compute the matrix element up to the one-loop level (NLO) including `MC@NLO` [69] and `POWHEG` [70].

Parton showering

Parton showering is the process describing the evolution to low values of Q^2 by subsequent radiation of partons. It is this feature of QCD that generates events with extra jets. Parton showering happens in an energy regime below that of the hard scatter down to the energy scale where perturbation theory breaks down and hadronization starts. The hard scatter is described by an energy scale Q^2, usually taken to be m^2 of the produced particles, whereas the hadronization scale is around Λ^2_{QCD}. Matrix element calculation diverge when the emitted gluons become collinear ($\theta_{qg} \downarrow 0$) or have low energy ($E_g \downarrow 0$). Parton showering is treated by generators with DGLAP functions [29, 33–36] and Sudakov form factors [71]. The DGLAP equations are essentially the same as used for the evolution of the PDF's and represent the probability of a parton a to split into partons b and c with momentum fraction z and $1 - z$ respectively. The Sudakov form factors describe the probability of parton a not to split between energy scale Q^2 and Q^2_{cut}, where Q^2_{cut} is the scale at which hadronization starts. Parton shower algorithms know the distinction between initial state radiation (ISR) and final state radiation (FSR), i.e. showering before or after the hard scatter. This distinction is however somewhat artificial since it does not have a gauge invariant meaning.

Matching matrix element to parton showers

When combining higher order matrix elements and parton showers ('matching') there is the problem of double counting. One could imagine introducing an extra order in the matrix element by attaching a gluon to an outgoing quark or vice versa. The same Feynman graph could however also be realized by the parton shower algorithm where the quark radiates a gluon. The main idea behind all schemes to avoid double counting is that the high-p_T and wide-angle emissions of partons are described by the matrix elements [32]. This region of phase space is then handled by the matrix elements and the rest by the parton shower algorithm. Separation of the phase space into two regions is the solution to avoid double counting.

For the `Alpgen` generated events a technique called `MLM` matching [72] is used to match the parton shower to the LO matrix elements. A cone around the emitting parton defines the border region between matrix element regime and parton showers. A veto is placed on parton showering in the region already covered by the matrix elements and it has been shown that the resulting physics does not strongly depend on the exact choice of the cone size [73].

The `MC@NLO` generator, based on the full NLO calculation of the matrix element, makes use of negative event weights ($\sim 13\%$) to compensate for the possible double counting when matching NLO diagrams to parton showering. `POWHEG` [70], a relatively recent addition to NLO generators, uses a scheme that is very similar to matrix element corrections, as explained in more detail by [32], that results in all positive event weights. Both `MC@NLO` and `POWHEG` can be interfaced with `HERWIG` for the hadronization (see next section) and UE stages (the `POWHEG` generated samples can also be hadronized by `PYTHIA`).

Hadronization and decay

When the energy of partons is down to about the hadronization energy ($Q^2 \sim \Lambda^2_{\mathrm{QCD}}$), thus entering the non-perturbative regime, the forming of colourless hadrons begins. In the Monte Carlo generators this is achieved by fragmentation. The two main fragmentation models used are *string fragmentation* and *cluster fragmentation*. The first is used by `PYTHIA` [67] and the latter by `HERWIG` [66]. String fragmentation uses strings between quark and anti-quark pairs to represent the colour field and in this representation gluons cause kinks in the strings. When the distance between the two partons grows, so does the potential energy until the string breaks to create new $q\bar{q}$ pairs. Hadrons are formed from the partons and newly created quarks. In cluster fragmentation all gluons are split into $q\bar{q}$ pairs after the parton showering. Colour singlet clusters are then formed from the available quarks and anti-quarks which decay into lighter clusters or hadrons. Clusters that are too light to decay are interpreted as the lightest hadrons of their flavour. In the fragmentation process typically a number of parameters appear that need to be tuned to the data. Both `HERWIG` and `PYTHIA` are tuned with pre-`LHC` data to describe the hadronization process. After the formation of hadrons the decay of unstable into stable particles is performed according to experimental values. This means for example that mesons like kaons or pions are made to decay according to the branching ratios as they have been measured.

Underlying event

Apart from the two partons that constitute the hard scatter, the other partons of the incoming protons also have to be described. Their interaction is collectively called the underlying event and is generally believed to generate particles at much lower transverse energies than the hard scatter. The underlying event may create extra jets and will contribute to multiple jet events. In `ATLAS` either `PYTHIA` is used to model the underlying event or a dedicated program like `JIMMY` [74, 75], where usually `JIMMY` is interfaced with `HERWIG`. The basic principle when modeling the underlying event is that the 2→2 is the dominant process in all the interactions since it occurs at LO in α_s. Both [76] `PYTHIA` and `JIMMY` have been tuned to the `Tevatron` data. They do however differ in their extrapolation the `LHC`, so this will be an interesting area of research in the first period of data taking. The first results from data show higher charged particle multiplicities (mainly at low momenta) than expected from both the `HERWIG` and the `PYTHIA` Monte Carlo simulation [77]. This difference is not expected to have an impact on the top-quark pair production cross section measurement.

1.4.2 Detector simulation

The generated events are universal for hadron collider experiments. The detector simulation is responsible for the `ATLAS` detector specific evolution of a generated event. All particles with lifetimes above 30 picoseconds are taken to be stable and will be handled by the `GEANT4` program [78], which takes care of the propagation through the detector. The material and the geometry of the `ATLAS` detector are described by more than 25 million volumes. Particles that traverse these volumes loose energy according to interaction models. In a second step these energies are converted to detector response signals. The detector responses have been calibrated in test-beams and are incorporated in the physics models [79]. These detector responses will then have to be translated back into physical objects that can be used for analysis. This very last step is performed by the `ATLAS` simulation and reconstruction algorithm within the `Athena` framework [80] that handles the Monte Carlo events in the same manner as data events to reconstruct the full events. The reconstructed events then consist of higher level analysis objects like electrons, muons and jets with their properties like momentum, energy and electric charge.

1.4.3 Description of signal and background samples

In this section the Monte Carlo samples are discussed that are used in this thesis [73, 81, 82]. Details about all samples can be found in Appendix B.

Top-quark pair signal samples

The details of the decay channels of $t\bar{t}$ events have already been discussed in Section 1.3.2. The event topology of a typical semi-leptonic $t\bar{t}$ decay consists of multiple high-$\mathrm{p_T}$ jets, an isolated high-$\mathrm{p_T}$ lepton and missing transverse energy. The $t\bar{t}$ MC samples that are used in this thesis are divided into semi-leptonic and dileptonic in one sample and fully hadronic in another sample. For the main analysis the full NLO `POWHEG` generated samples[6] have been used interfaced with `PYTHIA` and only the non-fully hadronic sample has been taken into account. Since we concentrate on the semi-leptonic muon channel, the fully hadronic sample is not expected to contribute to the background. The sample is generated with a top-quark mass of $m_t = 172.5$ GeV. More samples have been generated for systematic studies with `MC@NLO` with different top-quark masses. Also samples interfaced with `HERWIG` and samples with different parameter settings for ISR and FSR have been produced. Table 1.3 lists the inclusive cross section for the signal sample and for the background samples that were used in the main analysis [81].

process	matrix element	parton shower	σ [pb]	K-factor
non fully hadronic $t\bar{t}$	`POWHEG`	`PYTHIA`	79.1	1.13
W+jets	`ALPGEN`	`HERWIG`	17866.4	1.22
Z+jets	`ALPGEN`	`HERWIG`	2540.4	1.22
single top	`MC@NLO`	`HERWIG`	37.4	-
di-boson	`HERWIG`	`HERWIG`	16.2	-
QCD light	`ALPGEN`	`HERWIG`	144269.0	-
QCD $b\bar{b}$	`ALPGEN`	`HERWIG`	29299.0	-

Table 1.3: *Inclusive cross sections for signal and various background samples for the $\sqrt{s} = 7$ TeV analysis and their generators [81]. The K-factor for $t\bar{t}$ denotes the scaling to the NNLO cross section as given by Equation 1.4. The QCD cross section is after applying a muon-filter, see in QCD multi-jet Section.*

W and Z-bosons plus extra jets

The $W^{\pm}$ and the Z-boson have already been discovered in 1983 by the `UA1` and `UA2` experiments [83, 84]. The best estimates of their masses are currently given by $M_W = 80.399 \pm 0.023$ GeV and $M_Z = 91.188 \pm 0.002$ GeV [25]. Both bosons can be directly produced at the `LHC` and both decay into leptons or quarks. The decay modes and their branching ratios are given by [25]:

$$\begin{array}{rclrcl} W & \to & l\overline{\nu_l} & 32.40 & \pm & 0.27\% \\ W & \to & q\overline{q'} & 67.60 & \pm & 0.27\% \\ Z & \to & l^+l^- & 10.10 & \pm & 0.01\% \\ Z & \to & \nu\bar{\nu} & 20.00 & \pm & 0.06\% \\ Z & \to & q\bar{q} & 69.91 & \pm & 0.06\%. \end{array}$$

The Z-boson events will not constitute an important background to top-quark analyses since they are easily removed by rejecting dilepton events with $M_{l^+l^-} \sim M_Z$. Since it is however exactly the $W^{\pm}$-boson decay into leptons that characterizes the $t\bar{t}$ decays

---

[6] For the analysis in Chapters 4 and 5 the $t\bar{t}$ sample generated by `MC@NLO` was used. Note that this analysis was performed at $\sqrt{s} = 10$ TeV.

we are interested in, $W^{\pm}$-boson events are a major background to our analysis. The main difference between $W^{\pm}$-boson decay and $t\bar{t}$ decay will be the number of jets in the event. It is therefore important to model this background well and especially understand the amount of additional jets. The $W^{\pm}$ events are generated with `ALPGEN` that handles the generation at LO of zero up to five additional partons. The samples are generated exclusively for a number of partons at matrix element level (except the five or more partons which form an inclusive sample). Hard jets from the matrix element arising from gluons, u, d, s and c quarks (all taken massless) are included. In combination with parton showering the events will be very similar to $t\bar{t}$ decays. Heavy quarks (b-quarks) are only produced in the parton shower and will have predominantly low $\mathrm{p_T}$. There are however separate samples that contain W+$b\bar{b}$+jets where the b-quark comes from the matrix element. A heavy flavour overlap removal is performed to ensure that there is no double counting of the heavy flavour final states [81].

Adding extra partons to the final state adds also extra uncertainty to the final state, since every added parton adds a factor α_s which adds to the scale uncertainty. The cross section of $W^{\pm}$ plus extra jets is therefore not well predicted and the MC can only be used as a rough indication of the background. The size of this contribution to the measurement of the top-quark pair production will be determined from data. The added samples used in the main analysis in this thesis have an inclusive cross section which is a factor hundred larger than the $t\bar{t}$ cross section (about a factor twenty for Z+jets), see Table 1.3.

QCD multi-jet

A priori one would expect QCD multi-jet events not to form an important background to our lepton driven analysis since they do not produce prompt leptons. It is however possible for jets to fake leptons in the detector or for leptons to be produced in semi-leptonic decay of heavy quarks. These processes, especially the faking of leptons, adds extra uncertainty to the simulation, since they depend strongly on the detector description and the specifics of the reconstruction algorithms used. This uncertainty is added to the already large uncertainty in the normalization of the QCD multi-jet samples, as explained below. The exact amount of background in events selected on leptons and multiple jets due to QCD events is therefore uncertain. We will see that only data-driven methods give reliable results as background estimations and the MC should only be used to study the properties of these events, but not the normalization. It is this QCD multi-jet background that will be the main focus of this thesis.

The cross section for 2→2 QCD events, i.e. events with two high energetic jets called di-jet events, is enormous at the `LHC`. The cross section has been estimated to be around $1 \cdot 10^8$ pb for jets with $\mathrm{p_T}$ over 10 GeV [73, 81]. The di-jet events themselves are not a large background to semi-leptonic top-quark analyses, but due to parton showering and higher order interactions, many more jets might be found in the events. Already for these di-jet events there are ten Feynman diagrams that contribute at LO [29], which makes higher order computations very complex. The highest accuracy available at the moment for the production of QCD events with extra partons is at LO. The problem with only using LO generators is the scale uncertainty. Since the scale $\mu^2 = \mu_r^2 = \mu_f^2$ is usually taken equal to the mass squared of the produced particle or the sum of the jet momenta, the scale is much lower than for example in top-quark pair production. This means also that perturbation theory does not work as well since α_s is not a small number. This implies that generating events with multiple jets has large scale uncertainties due to high orders in α_s. It has been shown for example that even at NLO the uncertainties are still large for the normalization of the production of $b\bar{b}$ by comparing predictions from `POWHEG` with `MC@NLO` [85]. It will turn out that the predicted QCD multi-jet background in events with a topology similar to top-quark decay is about a factor three smaller than seen in data, see Chapter 6.

The QCD multi-jet MC events are produced with `ALPGEN` interfaced with `HERWIG` and `JIMMY`. As for the W+jets samples, the QCD light jets and the QCD+$b\bar{b}$+jets are produced separately. An overlap removal procedure is used also here to avoid double counting of events. Especially the QCD+$b\bar{b}$+jets events are a potentially large background to top-quark searches since they contain multiple jets, two of which originate from b-quark fragmentation. These events might also produce isolated high-p_T leptons in semi-leptonic heavy meson decays making the event topology of these events almost the same as for $t\bar{t}$ events.

A problem occurs when generating QCD events due to their large cross section: the generation of QCD events with many jets and a high-p_T lepton is highly inefficient. Since most of the events do not contain more than two high-p_T jets and do not contain a lepton, they are no potential background in an event selection aimed at $t\bar{t}$ events. Especially the lepton requirement renders less than 1% of the generated events useful. A procedure called filtering solves this problem. Events are selected if they contain a true muon with p_T of at least 10 GeV. By only processing these events, a sample can be produced that contains at least a few thousand events after the full requirement of an isolated high-p_T lepton. Since the cross section for the production of jets with an energy E_T falls as $\sim 1/E_T^2$, the samples are further divided into different jet-slices. These jet-slices are labeled `J0 - J5`, representing the p_T of the highest-p_T jet of the event at generator level. In Table 1.4 the definition of the p_T slices is shown [81] and the cross section (before filtering) is presented for the ones used in this thesis.

Adding all sub-samples gives a sample of multi-jet QCD events with muons equivalent to a luminosity of the order of 10 pb^{-1}. The inclusive QCD cross section after filtering is shown in Table 1.3 for the QCD+light jet sample and the QCD+$b\bar{b}$ sample. The cross section is large even after filtering and even for the heavy flavour sample. We will see however that the number of simulated events with four of more high-p_T jets and an isolated high-p_T lepton will be small. Given also the large uncertainty in the normalization of the MC samples, the QCD multi-jet background will have to be determined from data.

name	p_T^{min} [GeV]	p_T^{max} [GeV]	σ [pb]
J0	8	17	-
J1	17	35	$87.8 \cdot 10^6$
J2	35	70	$23.2 \cdot 10^6$
J3	70	140	$1.6 \cdot 10^6$
J4	140	280	$64.3 \cdot 10^3$
J5	280	∞	$2.1 \cdot 10^3$

Table 1.4: *The p_T slices used in QCD production. The highest-p_T jet determines the slice. For the samples that were used in this thesis the approximate pre-filter cross section is given.*

Other background samples

After having discussed the two main backgrounds to our top-quark analysis, we list here for completeness the details of the remaining, less important samples.

- single top: single top-quark production is quite different from the production of $t\bar{t}$ pairs since it occurs through electroweak interactions. Samples are generated with `MC@NLO` together with `HERWIG`. The cross section for single top production is fairly small compared to $t\bar{t}$ production (see Table 1.3) and due to the small number of high-p_T jets in the event after requiring the top-quark to decay leptonically, this will not be a large background.

- di-boson: the production of di-boson events (WW, WZ, ZZ) is simulated with `HERWIG`. The production cross section of di-boson events is small and requiring events to contain multiple jets and an isolated high-p_T lepton will reject most of these events.

Sample mixture

All the background samples discussed in this chapter, except the QCD multi-jet samples, produce ‘prompt’ leptons. Here ‘prompt’ means a lepton that originates from the hard scatter. We will call all background samples that contain prompt leptons the ‘prompt background’. The prompt background samples have been mixed according to their cross sections with the signal sample for convenience [81,86]. This mixed sample represents a luminosity of 163 pb^{-1} and is used throughout this thesis. The QCD samples were also added in a separate sample. Since the statistics of the lower jet slices is much higher then of the higher ones, the events are given weights, ranging from 0.3 to 2. Adding the weights of the mixed QCD sample represents an integrated luminosity of 9.84 pb^{-1}.

1.5 Summary

The top-quark is a special particle in the Standard Model. Due to its large mass it is not only an interesting particle to analyze and probe, but it also plays an important role in the electroweak fits and helps to constraint the Higgs-boson mass. At the `LHC` top-quark pairs will be produced predominantly through gluon fusion and decay into W-bosons and b-quarks, which results in multi jet events with high-$\mathrm{p_T}$ leptons and missing transverse energy. At a center of mass energy of 7 TeV (the `LHC` center of mass energy during the first data-taking period) the production cross section is 165 pb which translates into the production of about 450 $t\bar{t}$ pairs in the first 3 pb^{-1} of data.

Monte Carlo simulation is an invaluable tool in particle physics and the basic techniques have been discussed. The major backgrounds to the semi-leptonic top-quark pair production measurement are expected to be W+jets and QCD multi jet events. Since the latter can only be modeled with large uncertainties, obtaining a reliable estimate of the QCD background will be the main objective of this thesis.

CHAPTER 2

LHC AND THE ATLAS DETECTOR

Top-quark physics would not be possible without an accelerator that provides the high energetic particle collisions that lead to the production of top-quark pairs and a detector to analyze them. We will present the Large Hadron Collider (`LHC`) in Section 2.1. In Section 2.2 we will discuss the `ATLAS` detector that enables us to measure and reconstruct the top-quark pair candidates. The chapter will finish with a short summary in Section 2.3.

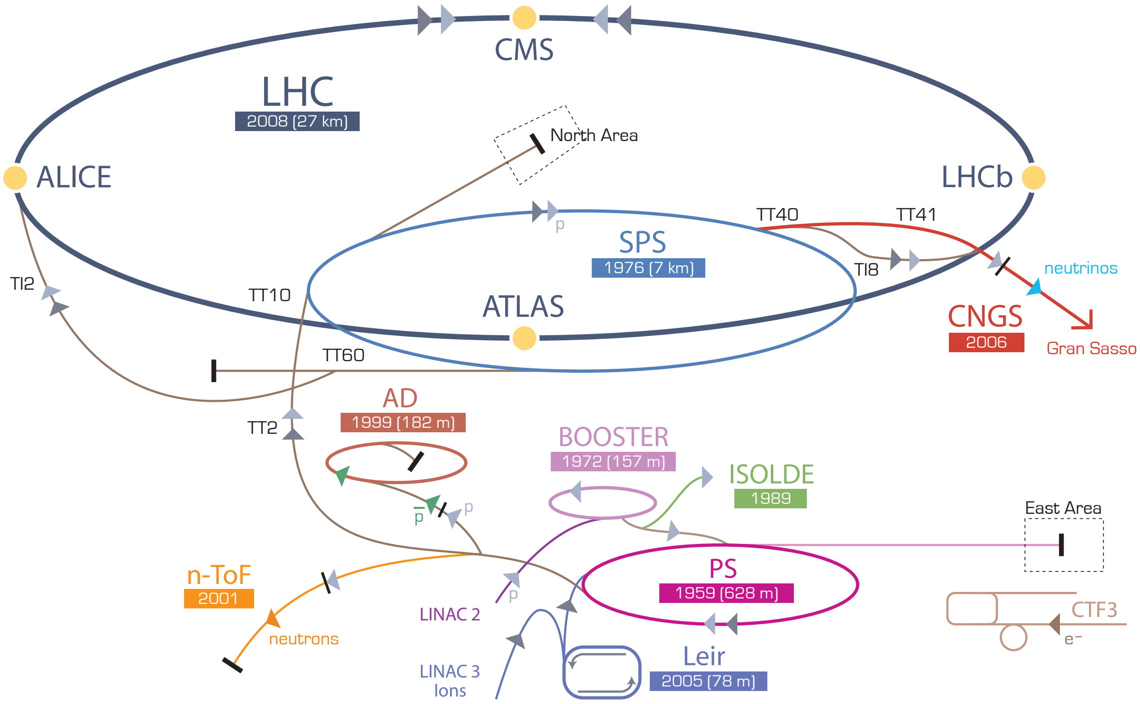

Figure 2.1: *The `CERN` accelerator complex with the `LHC` the largest ring in a chain of accelerators. Figure taken from [87].*

2.1 The Large Hadron Collider

The Large Hadron Collider (`LHC`) is situated about 100 m underground near the border between France and Switzerland and the city of Geneva. It is built in the 27 km long tunnel of a former accelerator called the Large Electron Positron collider (`LEP`) located at the `CERN` laboratory [88]. In Figure 2.1 the overview of the `CERN` accelerator complex is shown with the pre-accelerators and the `LHC`-ring [87].
Before the protons reach their final velocity of 99.9999991% of the speed of light corresponding to a center of mass energy of 14 TeV in the `LHC`, they are first accelerated to an energy of 50 MeV and then injected into the `BOOSTER` which ramps up their energy to 1.14 GeV. The protons are then further accelerated by the Proton Synchroton (`PS`) to 26 GeV before the Super Proton Synchroton (`SPS`) increases the beam energy to 450 GeV. This is the injection energy of the `LHC`, where they will be accelerated to a design energy of 7 TeV, which takes around 20 minutes. The `LHC` will reach the highest center of mass energy ever achieved of 14 TeV and about 600 million collision will occur every second [89]. It was mentioned however already in Section 1.2 that this energy will not be reached until the year 2013. The `LHC` was taken into operation (after the delay of more than one year in 2008) in December 2009 and collided protons at injection energy ($\sqrt{s}$ = 900 GeV). On the 30th of March 2010 the first collision at center of mass energy of 7 TeV occurred. It has recently been decided to continue operations at this energy until 2012 and then schedule a long shut down to prepare the machine for design energy [13].

The `LHC` consist of two beams of protons rotating in opposite directions which cross at four interaction points in the ring. Over 1200 dipole magnets operated at up to 9 T are needed to control the beam consisting of, at design value, 2808 bunches of protons. Each bunch is made up out of 10^{11} protons and has a spacing of about 25 ns to the next bunch. This yields roughly 40 million bunch crossings (with an average of 23 interactions per bunch crossing) per second. Table 2.1 shows the values of the parameters during the data-taking period in 2010 used in this thesis (until the end of August, see Section 6.1) and the design parameters [13, 88].

parameter	2010	design
beam energy	3.5 TeV	7 TeV
instantaneous luminosity	$\leq 10^{31}$ cm^{-2}s^{-1}	10^{34} cm^{-2}s^{-1}
bunch spacing	$\geq$ 50 ns	25 ns
particles per bunch	$\sim 0.9 \cdot 10^{11}$	10^{11}
bunches per beam	$\leq$ 50	2808

Table 2.1: *The `LHC` parameters for the 2010 operation and their design values [13, 88]. The quoted value for the instantaneous luminosity is the peak value.*

At each interaction point a detector is located to study the interactions, see Figure 2.1. Two of the four large experiments are designed to study specific phenomena in great detail: the `LHCb` detector [90] is specialized to measure B-mesons in order to study CP-

violation and `ALICE` [91] has been built to study the quark-gluon plasma (in heavy ion collisions, but they will also analyze pp collisions). Both `CMS` [92] and `ATLAS` [79] are so called general purpose detectors. This means that they both cover almost full solid angle and are designed to study a large range in particle types and momenta. Both experiments will make precision studies of the SM. They will also try to find the SM Higgs-boson and simultaneously look for signs of physics phenomena that cannot be explained by the SM.

2.2 The ATLAS detector

The `ATLAS` detector, see Figure 2.2 for a cut-away view [79], weighs over 7000 tonnes and is designed to cover a wide range of physics goals. Its right-handed Cartesian coordinate system has the origin in the interaction point at the center of the detector. The x-axis points from the origin to the center of the `LHC` ring and the y-axis upwards.

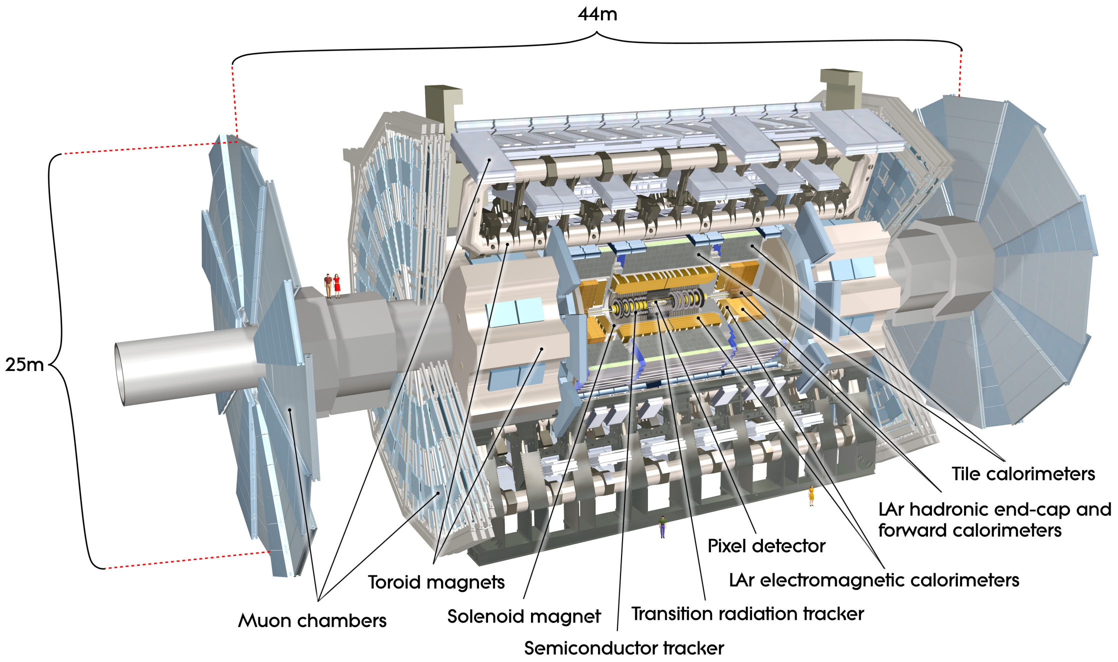

Figure 2.2: *Cut-away view of the* `ATLAS` *detector. Figure taken from [79].*

One of the benchmark processes the `ATLAS` detector was built to detect is the decay of the Higgs-boson. Since the dominant decay channel of the Higgs-boson is unknown, due to its unknown mass, the detector has to be able to cope with all possible decay scenarios. A light Higgs-boson decays predominantly into hadrons, which is hard to distinguish from the large QCD multi-jet background. This would make the $H \to \gamma\gamma$ the most important decay channel and requires excellent photon identification. For the heavier Higgs-boson ($m_H > 130$ GeV) the most promising decay channels are $H \to$

$ZZ \to l^+l^-l^+l^-$ and $H \to W^+W^- \to l^+\nu l^-\nu$ which require outstanding identification of leptons and reconstruction of missing transverse energy. Another benchmark process is the detection of SUSY with high-$\mathrm{p_T}$ jets, requiring an outstanding jet reconstruction. These benchmark requirements, combined with the high-luminosity environment at the `LHC` and the large center of mass energy, have been translated into the following design requirements [79, 93, 94]:

- Electronics that are fast and radiation hard to withstand the high luminosity environment.
- Ensuring no high momentum particle can escape detection by large acceptance in pseudorapidity and full coverage in azimuthal angle.
- Charged particle momentum resolution and reconstruction efficiency are required to be good in the inner tracker. For the reconstruction of secondary vertices, vertex detectors close to the interaction region are needed.
- Very good and hermetic electromagnetic calorimetry is needed for electron and photon identification and measurement as well as (almost) full coverage hadronic calorimetry to reconstruct jets and missing transverse energy.
- Good muon reconstruction efficiency and resolution over a large range of muon momenta as well as the ability to reconstruct the muon charge is required.
- In order to achieve an acceptable trigger rate for most interesting physics processes an efficient trigger system is needed for low transverse momentum objects with high background rejection.

These requirements meet the needs for the reconstruction of a top-quark pair decay, see Section 1.3.2, making `ATLAS` the perfect instrument to study top-quarks. Construction of the detector, which is located at point 1 in the `LHC` ring in a cavern 92 m under the ground, started in 2003 and was fully completed in 2008. The detector is 44 m long and 25 m high and has an almost perfect cylindrical shape. Its name comes from one of its most characteristic features, the toroid magnets: A Toroidal LHC ApparatuS. The detector consists of four large super conducting magnets: a solenoid, a barrel toroid and two end-cap toroids, see Section 2.2.1. Its main detector components are the inner detector (identification and momentum measurement of charged particles), the calorimeters (energy measurement of particles) and the muon spectrometer (muon identification and momentum measurement). We will describe the detector hardware in this chapter and discuss the reconstruction details in Chapter 3.

2.2.1 The magnet system

Since the `ATLAS` detector got its name from the magnet system and because it plays an integral part of particle (momentum) reconstruction, we discuss it in some more detail. The magnet system consists of a super-conducting solenoid magnet and a super-conducting toroid magnet, built up out of a barrel part and two end-caps. In Figure 2.3 (left) the schematic set-up of the entire magnet system is shown [79].

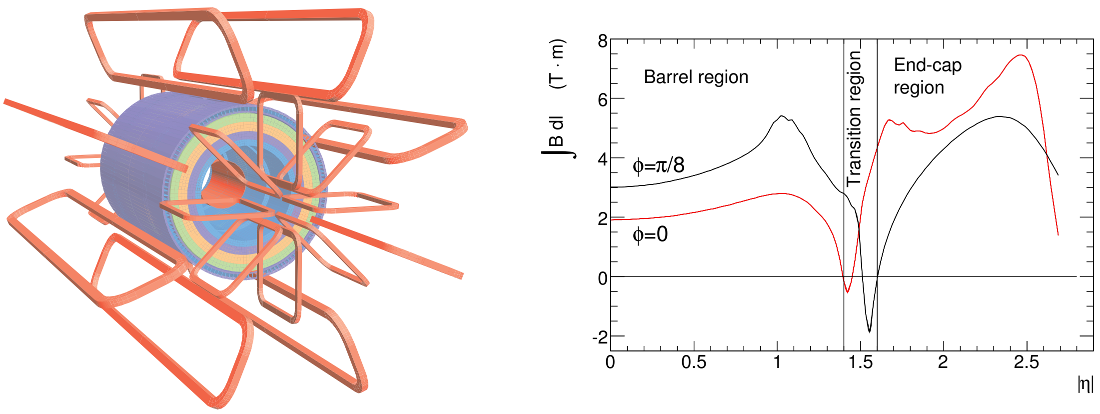

Figure 2.3: *Left: geometry of magnet windings and tile calorimeter steel. The eight barrel toroid coils, with the end-cap coils interleaved are visible. The solenoid winding lies inside the calorimeter volume. The outer diameter is 20 m and the length is 25 m. Right: Predicted field integral as a function of* $|\eta|$ *from the innermost to the outermost MDT layer in one toroid octant, for infinite-momentum muons. The curves correspond to the azimuthal angles* ϕ*=0 (red) and* ϕ*=*$\pi/8$ *(black). Figures taken from [79].*

Solenoid magnet

The central solenoid, which is embedded in the electromagnetic calorimeter (Section 2.2.3), produces a magnetic field along the beam axis inside the inner detector that has a strength of up to 2 T. It is operated at a current of 7730 A and the magnetic field it produces bends the trajectory of charged particles inside the inner detector.

Toroidal magnet system

The toroid magnet is one of the most distinctive features when the `ATLAS` detector is depicted. The eight super-conducting rectangular coils of the barrel toroid are clearly visible and define (together with the muon system) the dimensions of the detector. The system is operated at a temperature of 4.6 K and an operational current of 20.5 kA. The field strength, which is cylindrical around the beam axis, varies from 0.15 T to 2.5 T. The end-cap toroids consist of also eight coils with the same nominal current and operation temperature as the barrel coils. Their field strength varies from 0.2 to 3.5 T.

B-field sensors

Although the strength of the magnetic field (B-field) is well modeled in the barrel region and in the end-caps, there are a few regions where it is only known with a large uncertainty caused by the interplay of the barrel and end-cap toroid magnet fields (especially in the transition region with $1.4 < |\eta| < 1.6$) and material effects. Since the magnetic field gradient can reach up to 1 mT/mm, the local bending power uncertainties will add to the overall muon momentum resolution. Also temperature fluctuations during operation might change the B-field. To illustrate the change in the B-field in the transition region see Figure 2.3 (right) where the predicted field integral is shown for infinite momentum muons. This can be interpreted as the bending power. Note that the transition region is marked by large changes of the field integral and the muon momentum resolution will suffer most in this region due to uncertainty in the bending power.

In order to precisely reconstruct the momentum of muons in all regions of $|\eta|$, B-field sensors have been installed in `ATLAS`. Over 1800 sensors have been placed on the chambers of the muon spectrometer (see Section 2.2.4) that are equipped with temperature sensors and with Hall probes to measure the field strength from the induced voltage due to the Hall effect in three dimensions. The sensors are calibrated so that the absolute value of the B-field can be measured [95]. From the read-out of these sensors a precise magnetic field map can be constructed with a precision of 0.2 mT up to $|B| = 1.4$ T and about 1 mT up to $|B| = 2.5$ T. The design muon momentum resolution is 10% for a muon with p_T of 1 TeV, which translates into a predicted sagitta of about 0.5 mm. To achieve the required muon momentum resolution a relative precision of the magnetic field measurement of 1 mT/2.5 T $= 4 \cdot 10^{-4}$ for the sensors is sufficient [96]. This then translates into a requirement on the root mean square (RMS) relative to the mean of the B-field measurement. In Figure 2.4 (left) the position of the sensors is shown and the RMS of all sensors is presented (right) during nominal operation [97].

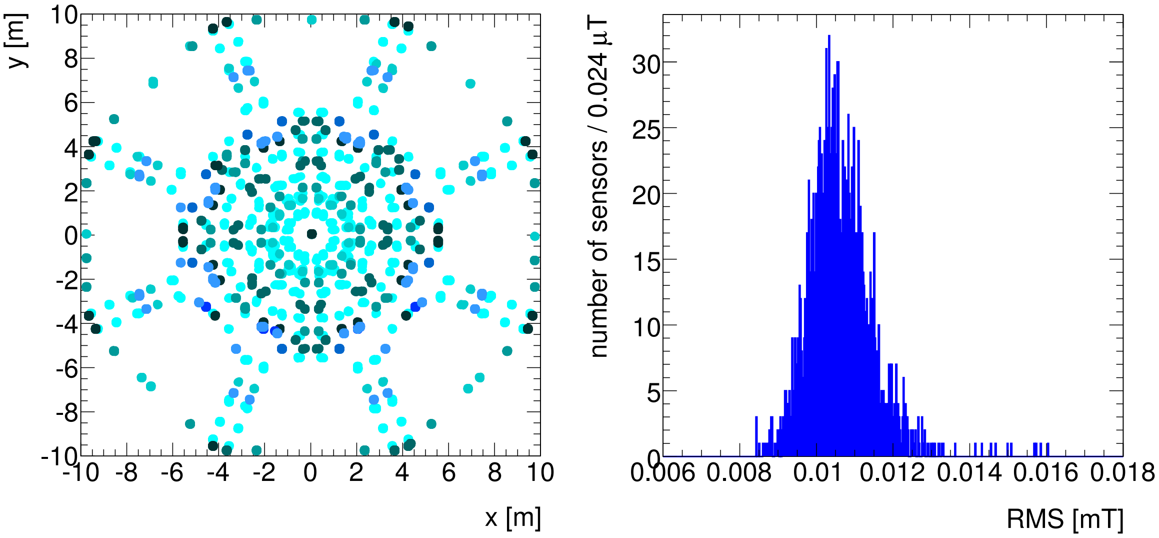

Figure 2.4: *Left: the location of the B field sensors installed on the chambers of the muon system in the xy plane. Right: the root mean square of the measured B-field for all sensors during nominal operation.*

Both the RMS and the width of the RMS distribution are of $\mathcal{O}(10^{-5})$, which is an order of magnitude better than the required resolution of the sensors and thus satisfies the requirements of the muon reconstruction.

2.2.2 Inner detector

The inner detector is the heart of the `ATLAS` detector with a length of 6.2 m and a diameter of 2.1 m. It is responsible for identifying and reconstructing the trajectories of the charged particles (tracks) from the interaction with a typical required resolution of $\sigma_{\mathrm{p_T}}/\mathrm{p_T} = 0.05\% \times \mathrm{p_T} \oplus 1\%$. It is also important for the reconstruction of vertices. Since it is immersed inside the solenoidal field of 2 T, the charge and momentum of the particles can be measured by the bending of the tracks. In Figure 2.5 a cut-away view is shown of the `ATLAS` inner detector [79].

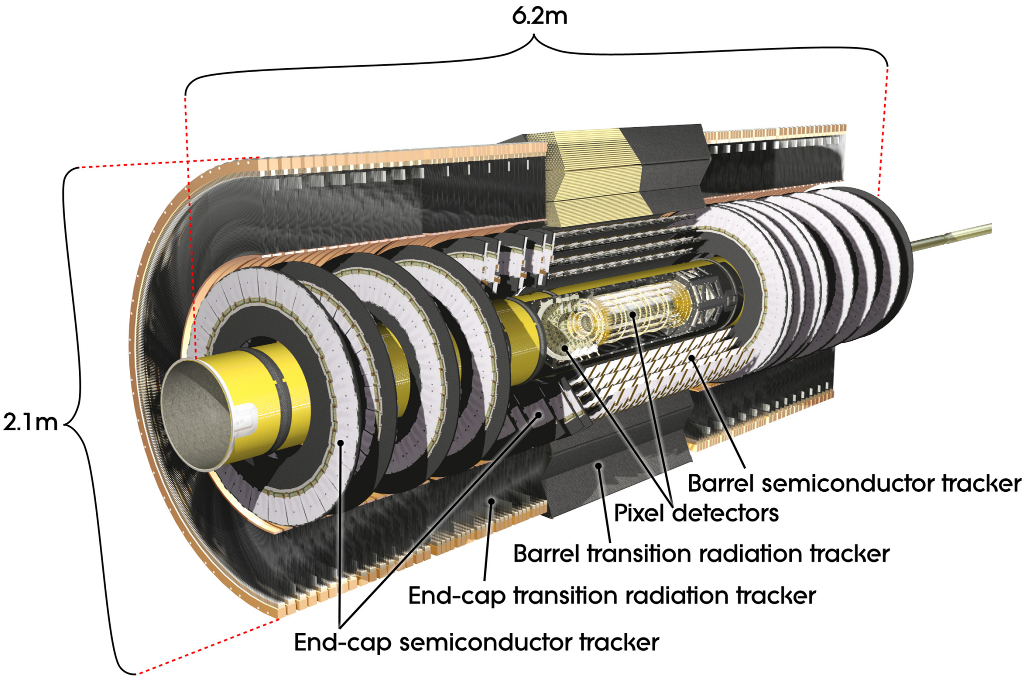

Figure 2.5: *Cut-away view of the* `ATLAS` *inner detector. Figure taken from [79].*

The inner detector can reconstruct tracks above ~ 0.1 GeV up to $|\eta| = 2.5$. The vertex-layer of the pixel detector is important for the reconstruction of primary and secondary vertices needed to separate jets coming from b and c-quarks and τ's from jets coming from light flavour quarks. As has been shown in the previous chapter, b-jets are an important part of identifying $t\bar{t}$ events. The inner detector is built up out of three parts, which will be described below. The tracking performance will also be shown.

The pixel detector

The pixel detector is made of high-granularity semiconducting silicon detectors used for pattern recognition and vertex finding. The tracking layer located closest to the interaction point, the vertexing layer, is used for the reconstruction and measurement of the position of vertices. It has three layers in the barrel region (at radii of 5.05, 8.85 and 12.25 cm away from the beam-line) and consists of three discs in the end-cap. Traversing charged particles generate free electron and hole pairs. The electronics of the pixel detector is sensitive to the strength of the collected electron signal through the measurement of the time over a threshold. Each charged particle will hit a cluster of sensors and the amount of charge is used to determine the center of the cluster. The pixels have a size of 50×400 μm^2 in $R - \phi \times z$ and a resolution of 12 μm in $R - \phi$ and 110 μm in z. The full detector consists of 80.4 million read-out channels.

The SCT detector

The silicon microstrip tracker, SCT, consists of eight layers in the barrel region that are mounted in sets of two modules with a small stereo angle (40 mrad) to yield four space points for each traversing track (at radii of 29.9, 37.1, 44.3 and 51.4 cm from the beam-line). There are nine end-cap disks where the modules are mounted in concentric circles. The intrinsic resolution of the modules is ~ 17 μm in $R - \phi$ and 580 μm in z (barrel) or R (end-cap). In total the SCT has more than 6 million read-out channels.

The TRT detector

The transition radiation tracker, TRT, provides a large number of hits per track by the use of 4 mm straw tubes, enabling tracking up to $|\eta| = 2$ (ranging from radii of 55.4 to 108.2 cm from the beam-line). It is an important part in the identification of electrons due to the measurement of photons from transition-radiation. The TRT only measures in $R - \phi$ with an accuracy of 130 μm per straw tube. When charged particles cross a straw tube they ionize the drift gas in the tubes. The time until the ions reach the wire in the straw is measured to compute the distance the particles traversed the tube from the wire. The TRT is mounted on 73 concentric layers in the barrel region and on 18 disks per end-cap adding to over 350 thousand read-out channels.

Tracking

The efficiency to reconstruct charged particle trajectories is important when performing precision measurements since it is the basis of particle identification and momentum measurements. Extensive studies have been performed to measure and simulate the tracking efficiency with the latest detector description. The track reconstruction efficiency is defined as:

$$\epsilon_{\mathrm{trk}}(\mathrm{p_T}, \eta) = \frac{\mathrm{N_{rec}^{matched}}(\mathrm{p_T}, \eta)}{\mathrm{N_{gen}}(\mathrm{p_T}, \eta)},$$

where $\mathrm{N}_{\mathrm{rec}}^{\mathrm{matched}}(\mathrm{p_T}, \eta)$ is the number of reconstructed tracks matched to a generated charged particle and $\mathrm{N}_{\mathrm{gen}}(\mathrm{p_T}, \eta)$ is the number of generated particles in that bin. The matching is performed with a cone matching algorithm. The track reconstruction efficiency from non-diffractive Monte Carlo in events with more than two charged particles (hadrons) is shown in Figure 2.6 for the η of the tracks (left) and the $\mathrm{p_T}$ of the tracks (right) [77].

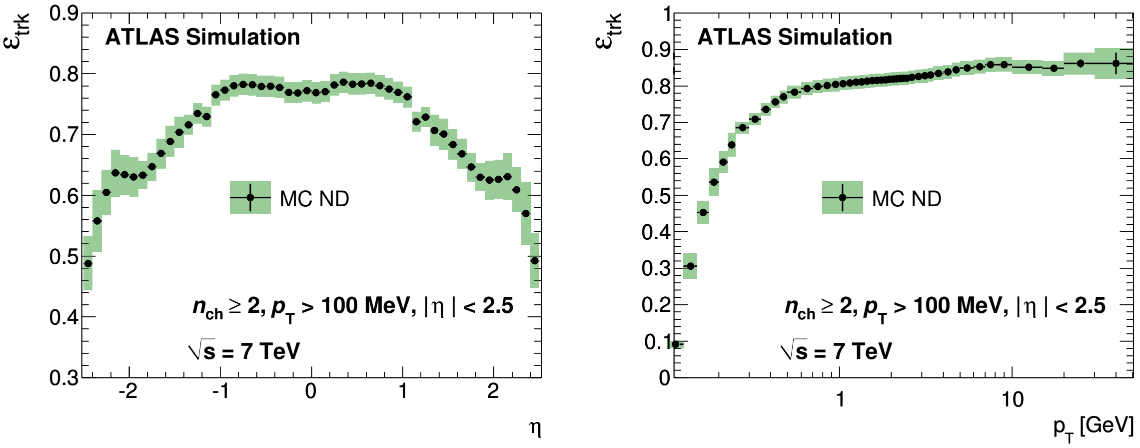

Figure 2.6: *The tracking efficiency in simulation as derived from non-diffractive (ND) MC. Left: as a function of η of the tracks. Right: as a function of p_T of the tracks. The statistical errors are shown as black lines, the total errors as green shaded areas. All distributions are shown at $\sqrt{s} = 7$ TeV for the number of charged particles (n_{ch}) in the event ≥ 2, $p_T > 100$ MeV, $|\eta| < 2.5$. Figures taken from [77].*

The tracking efficiency is higher in the barrel than in the end-caps because particles pass through more dead material in the end-cap region. In Figure 2.6 (right) we see that as a function of $\mathrm{p_T}$ of the tracks the efficiency reaches a plateau above ~ 1 GeV. The difference between Monte Carlo and data has been studied recently. Figure 2.7 shows the comparison between data and simulation for tracks with $\mathrm{p_T}$ between 100 and 500 MeV. Shown are the average number of silicon hits in the Pixel detector (left) and the transverse impact parameter (right) [77]. The latter is the distance of closest approach in the transverse plane of a track to the interaction point.

The agreement is remarkable. It not only means that the behaviour of the inner detector is well understood and modeled, but also that the detector is well commissioned. This high degree of agreement is due to extensive studies with cosmic particles even before the first collisions were ever produced. The transverse impact parameter plays an important role in the identification of particles that do not originate from the primary vertex, but from the decay of long-living particles. It will also be in important parameter in identifying muons from semi-leptonic b-quark decays later in this thesis.

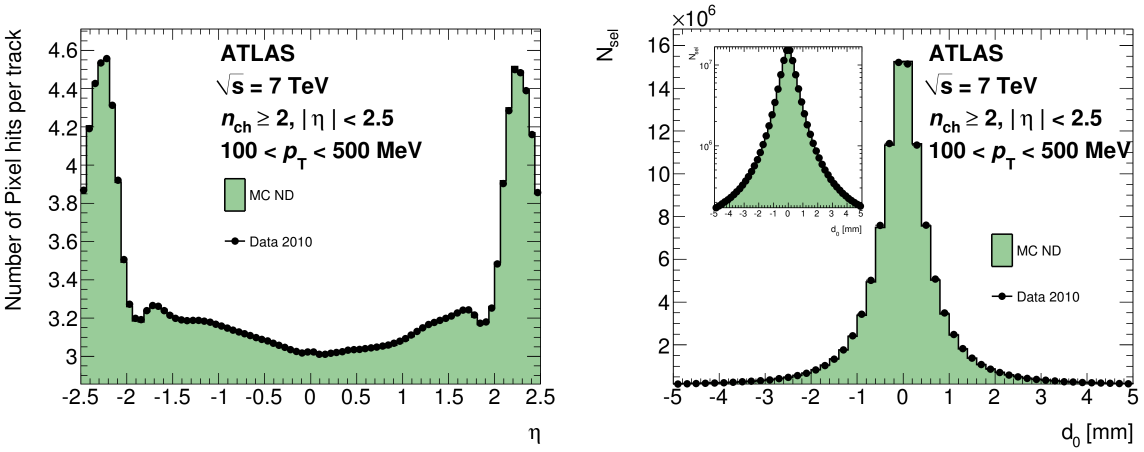

Figure 2.7: *Comparison between data and simulation at $\sqrt{s} = 7$ TeV for tracks with transverse momentum between 100 and 500 MeV. Left: the average number of silicon hits on reconstructed track as a function of η in the Pixel detectors. Right: the transverse impact parameter d_0. The p_T distribution of the tracks in non-diffractive (ND) MC is re-weighted to match the data and the number of events is scaled to the data. Figures taken from [77].*

2.2.3 Calorimeters

The calorimeters are sub-detectors used to measure the energy of particles. They are usually divided into an electromagnetic and a hadronic part, since different materials are needed for the measurement of electrons and photons on one side and hadrons on the other. In Figure 2.8 (left) a cut-away view is shown of the `ATLAS` calorimeters [79]. The calorimeters cover the region up to $|\eta| \leq 4.9$ with different techniques used for the requirements in the various ranges in pseudorapidity. The fine granularity of the electromagnetic calorimeter, ECAL, in the region of the inner detector is perfectly suited for precision measurements of electrons and photons. The more coarse granularity of the hadronic calorimeter, HCAL, is on the other hand sufficient for the requirements on jet reconstruction and missing energy measurements. The required resolution for the calorimeters is $10\%/\sqrt{\mathrm{E}} \oplus 0.7\%$ for the ECAL and $50\%/\sqrt{\mathrm{E}} \oplus 3\%$ for the HCAL (less in the forward region).

The calorimeters consist of alternate layers of an absorbing material where the particles produce showers, loose their energy and are finally stopped and an active material where the particle showers are measured. By this ‘sampling’ procedure the energy of the traversing particles can be determined. We will describe the ECAL and the HCAL below, as well as the jet and $\not{E}_{\mathrm{T}}$ reconstruction performance.

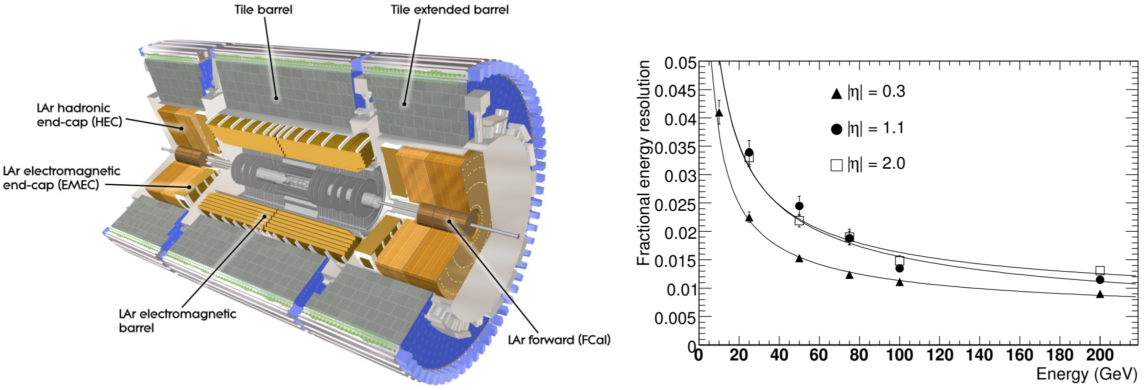

Figure 2.8: *Left: cut-away view of the* ATLAS *calorimeters. Right: expected relative energy resolution as a function of energy for electrons at* $|\eta|$*=0.3, 1.1 and 2.0. The curves represent fits to the points at the same* $|\eta|$ *by a function containing a stochastic term, a constant term and a noise term. Figures taken from [79].*

Electromagnetic calorimeter

The ECAL is responsible for the measurement of the energy of electrons and photons. It is divided into a barrel ($|\eta| < 1.5$) and two end-caps ($1.4 < |\eta| < 3.2$) and has a typical granularity of $\Delta\eta \times \Delta\phi = 0.025 \times 0.025$. The active medium used is liquid argon and lead is present as the absorber. An accordion shape ensures no cracks in $R - \phi$. The ECAL covers over 24 radiation lengths, a radiation length being the typical lengths over which the energy of an electron is reduced by a factor e. This ensures that the showers are contained within the volume of the ECAL. The expected resolution for electrons at different values of $|\eta|$ as a function of their energy is shown in Figure 2.8 (right) [79]. The resolution is worse in the end-caps than in the barrel region due to the presence of more material. Note also that the 'crack-region', i.e. the region between the barrel and the end-caps between $|\eta|$ of 1.37 and 1.52 is usually not used for precision measurements since the energy resolution is degraded.

Hadronic calorimeter

The HCAL performs the energy measurements of all particles that interact strongly. The typical granularity is $\Delta\eta \times \Delta\phi = 0.1 \times 0.1$. It uses scintillating tiles as active material in the barrel region. This tile calorimeter extends up to $|\eta| = 1.0$ with two extended tile barrels that cover $0.8 < |\eta| < 1.7$. The end-cap region is covered by a liquid argon detector in the region $1.5 < |\eta| < 3.2$. In order to obtain a reliable estimate for the missing transverse energy, it is important to measure the energy of all particles in an event. For this purpose there is also a forward calorimeter, FCAL, to ensure the measurement of very forward particles. The FCAL is also a liquid argon detector and covers $3.1 < |\eta| < 4.9$ and consists of three modules. The first is optimized for electromagnetic measurements (using copper as absorber) and two others are hadronic calorimeters (using tungsten). The HCAL has a minimum depth of ten interaction lengths to minimize possible punch-through to the muon system of unstopped hadronic particles.

Calorimeter performance

We will focus in this section on the detector response. The details of jet reconstruction and calibration will be discussed in Section 3.2.3. To study whether the measured energy in the calorimeter is well modeled, the energy balance in di-jet events has been exploited. In these events the ratio is taken of a jet ('reference' jet) to the jet in the opposite direction ('probe' jet). The ratio is not expected to be exactly unity, but should be well described by MC if the calorimeter is well simulated and understood. In Figure 2.9 (left) the ratio of the calorimeter response of a 'reference' jet to a 'probed' jet as a function of η for data and MC is shown [98].

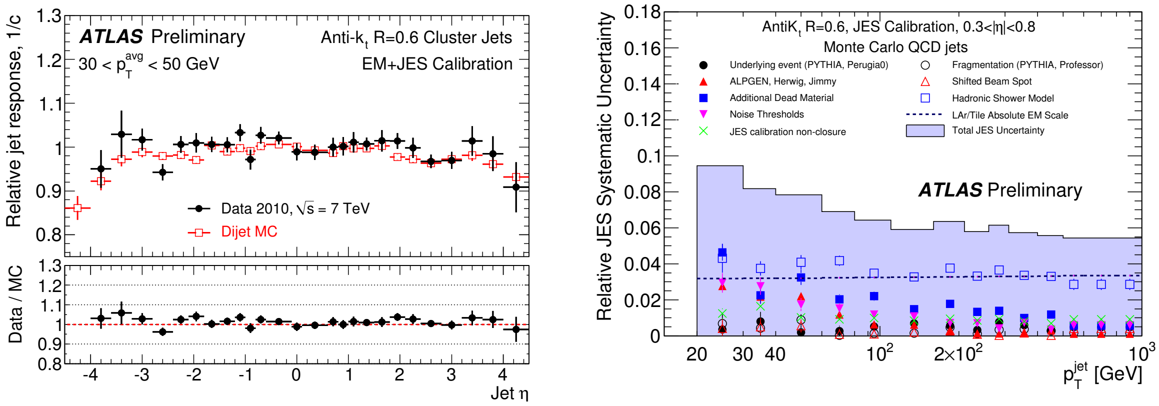

Figure 2.9: *Left: ratio of calorimeter response between the reference and the probe jet as a function of probe jet pseudorapidity for 30 GeV < p_T^{jet} <50 GeV. Figure taken from [98]. Right: relative jet energy scale systematic uncertainty as a function of p_T^{jet} for different η regions in the calorimeter barrel. The total uncertainty is shown as the solid blue area. The individual sources are also shown, with statistical errors if applicable. Figure taken from [99].*

The agreement between data and Monte Carlo is reasonable, within 5% and 10% for the barrel and the end-caps respectively. The agreement is a measure of the uncertainty of the MC based jet energy scale corrections. The energy resolution of jets is better in the barrel than in the end-cap region [98]. The reason for this is the increasing noise contribution when moving from the low noise tile calorimeter to the higher noise liquid argon detector. The noise term has been shown to vary from 0.5 GeV to 1.5 GeV.
We can conclude that the calorimeter response is well modeled. Although jet reconstruction is already well understood, it will turn out that jet energy scale calibration, the translation of the reconstructed energy to the absolute true jet energy scale, will be the

leading source of systematic uncertainty in our final measurement of the top-quark pair production cross section. In Figure 2.9 (right) we show the jet energy scale systematic uncertainty as a function of the jet-p_T for jets in the barrel region. The total uncertainty adds up to about 10% in the worst case and this will directly influence our measurement.

For the measurement of the top-quark pair production cross section as well as most new physics models the missing transverse energy ($\not\!\!E_T$) is an important quantity, as was already mentioned in Section 1.3.2. It is however also a difficult quantity to measure and reconstruct, since it involves good understanding of all detector components. The details of the $\not\!\!E_T$ reconstruction are given in Section 3.2.4. Figure 2.10 shows the distribution of $\not\!\!E_T$ as it was measured in minimum bias events (i.e. not triggered on high-p_T objects) [100].

Also here the agreement is good and gives confidence that the missing transverse energy is well understood. For our analysis the high-end of the tail of the distribution is not a big concern since we will typically select events with $\not\!\!E_T$ above 20 GeV, i.e. in the well modeled region. On average the $\not\!\!E_T$ distribution in minimum bias events is expected to be compatible with zero, which is indeed the case. The events with high $\not\!\!E_T$ are found to be events with high-p_T jets which enter the transition region between the calorimeters and have mis-measured energy.

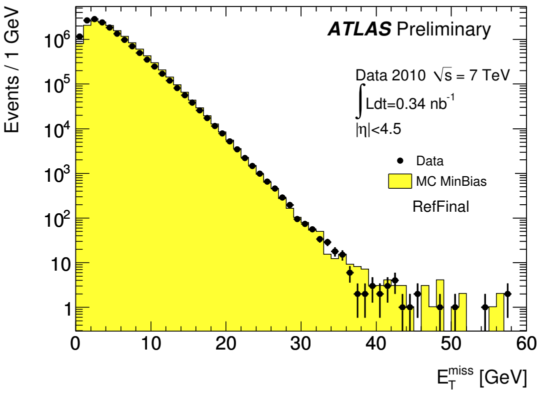

Figure 2.10: *Distribution of $\not\!\!E_T$ as measured in a data sample of 15.2 million selected minimum bias events (dots) at 7 TeV center-of-mass energy, recorded in April 2010. The expectation from Monte Carlo simulation is superimposed (histogram) and normalized to the number of events in data. Figure taken from [100].*

2.2.4 Muon spectrometer

The muon system is by far the largest sub-detector of `ATLAS`. It is responsible for the identification and momentum measurement of muons. Its design performance is 10% momentum resolution for muons with p_T of 1 TeV. Note that only at high momenta the muon spectrometer performance is independent on the inner detector. The muon spectrometer is built outside of the inner detector, the calorimeters and the solenoid magnet such that the only charged particles that reach it are high-p_T muons. In Figure 2.11 (left) a cut-away view of the `ATLAS` muon spectrometer is shown [79].

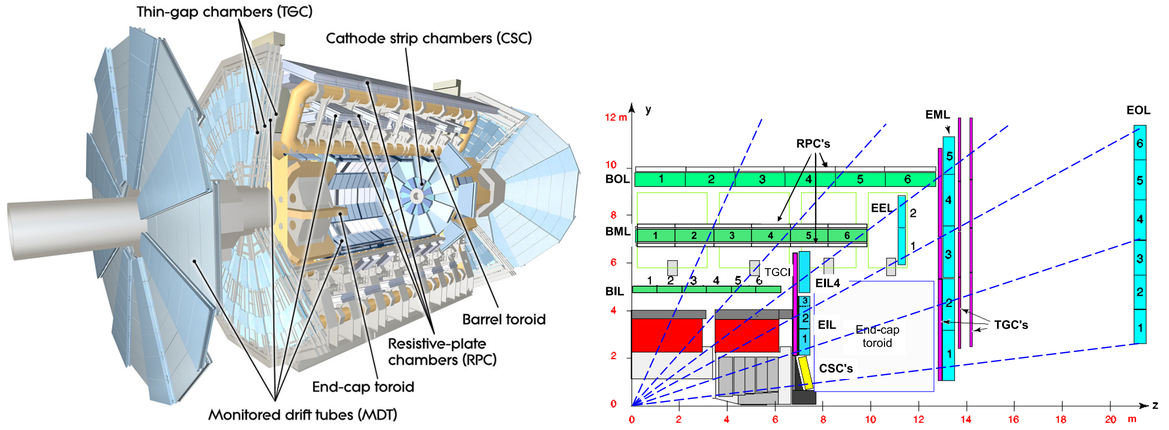

Figure 2.11: *Left: cut-away view of the* `ATLAS` *muon spectrometer. Right: cross section of the muon system in a plane containing the beam axis (bending plane). Infinite-momentum muons would propagate along straight trajectories which are illustrated by the dashed lines and typically traverse three muon stations. Figures taken from [79].*

In the muon spectrometer muons with momenta ranging from 3 GeV up to about 3 TeV can be reconstructed. Their momenta can be measured due to the bending in the toroidal magnetic field. Muon measurement in `ATLAS` is a combination of inner detector tracks and the muon spectrometer tracks. For low momenta, the resolution is dominated by the inner detector performance, whereas the high-p_T muon momentum resolution is given by the muon spectrometer. Note however that also for the low momentum muons the identification in the muon spectrometer is important. Muons only reconstructed by using the muon spectrometer tracks are called stand alone muons.

Muon spectrometer design

The muon spectrometer consist of a barrel and two end-caps. The barrel is built out of three layers of muon drift tube (MDT) chambers arranged cylindrically around the beam line [101]. The stations are called barrel inner (BIL), barrel middle (BML) and barrel outer layers (BOL). The end-caps also consist of three layers. In Figure 2.11 (right) a cross section is shown of the `ATLAS` muon spectrometer in the yz-plane, the bending plane of charged particles in the toroid field [79].
The MDT chambers measure muons up to $|\eta| = 2.7$. Cathode strip chambers (CSC) are installed close to the beam line in the end-caps because of their fine granularity and fast operation and they cover the region $2 < |\eta| < 2.7$. An MDT is an aluminum tube of 30 mm radius that is filled with a drift gas and equipped with a gold plated anode wire in the middle. When charged particles traverse the MDT the ionized particles in the tube will drift to the wire and the measured drift time can be converted to a drift circle.

Note that the MDT chambers provide high precision measurement in a plane parallel to the tubes, but usually not along the tubes. This information comes either from the trigger chambers (mentioned hereafter) or the inner detector. The intrinsic resolution is about 30 μm per MDT chamber. The muon trigger system is formed by resistive plate chambers (RPC) in the barrel region ($|\eta| < 1.05$) and thin gap chambers (TGC) in the end-cap region. The trigger covers the region $|\eta| < 2.4$.

Muon spectrometer performance

In Figure 2.12 the expected fractional momentum resolution in simulation for muons with $p_T = 100$ GeV as a function of η (left) is shown.

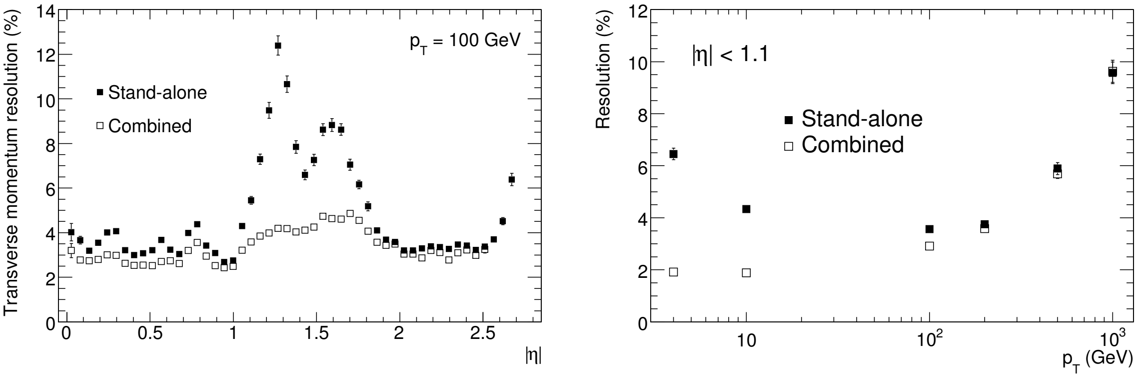

Figure 2.12: *Expected stand-alone and combined fractional momentum resolution in simulation. Left: for muons with $p_T = 100$ GeV as a function of $|\eta|$. Right: as a function of p_T with $|\eta| <1.1$. Figures taken from [79].*

The degradation in Figure 2.12 (left) in the region with $1.1< |\eta| <1.7$ is due to the absence of the middle muon stations in the barrel/end-cap transition region for the initial data-taking (which is modeled in MC), the low bending power of the magnetic field in the transition region between the barrel and end-cap toroids and the material of the coils of the end-cap toroids. The expected fractional momentum resolution for muons as a function of p_T is presented in Figure 2.12 (right). Note that the best resolution is expected in the p_T region from 10 to 100 GeV, which is the p_T range where muons from $t\bar{t}$ decay are expected to be found. The resolutions have also been measured in data. Figure 2.13 shows the distributions of the resolution as measured in data as a function of η (left) and as a function of p_T (right). The measurement is performed using a pure sample of $W \to \mu\nu_\mu$ events and the resolution is determined from the difference in measurement between the inner detector and the muon spectrometer. The muons have p_T above 10 GeV [102].

The plots show worse resolution in data than in MC. This is however studied and well understood [102]. In the barrel region ($|\eta| < 1.1$) the worsening comes from the additional material that the muons have to traverse which is not yet accounted for in

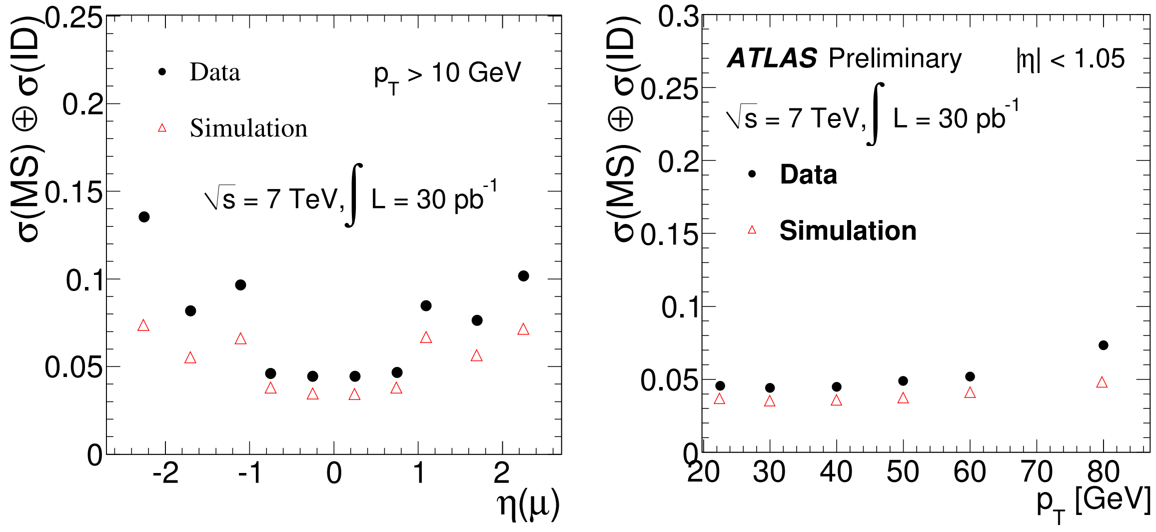

Figure 2.13: *Sum in quadrature of the MS and ID resolutions. Data (dark dots) are compared with signal* $W \to \mu\nu$ `PYTHIA` *Monte Carlo simulation (light triangles) [67]. Left: as a function of the muon* η *Right: as a function of the muon* p_T ($|\eta| < 1.05$)*. Figures taken from [102].*

the simulation, this adds to about 15 % extra material. The alignment of the barrel part of the muon spectrometer is almost at design level thanks to alignment with muons from cosmic showers. In the end-cap region the alignment did not have the benefit of the cosmic muon radiation. The use of preliminary calibration and alignment constants causes the worsening of the resolution. For the measurement that we will perform in this thesis the muon momentum resolution is not of great importance, the identification of muons however is. We will show that identifying prompt muons is crucial when selecting top-quark candidate events.

2.2.5 Trigger and data flow

At design conditions bunch-crossings will occur in the `ATLAS` detector at 40 MHz with on average 23 collisions per crossing resulting in an enormous event rate. Each event in raw data format is approximately 1.5 MB which would lead to an unmanageable amount of data to be reconstructed and written to storage. To deal with these rates `ATLAS` utilizes a staged trigger approach to reduce the rate to 200 Hz which will then be stored and reconstructed. The exact choice of the mixture of triggers used (the 'trigger menu') depends on the event rate and the physics goals [103]. The first period of data taking was characterized by much lower event rates (< 500 kHz) and during the first days of operation events were accepted and recorded at each bunch crossing. The higher the rates the more events will have to be rejected and the more difficult it becomes to distribute the trigger budgets amongst the various physics analyses. Some trigger items (examples are single electron or muon triggers with a low p_T cut) will get saturated with the higher rates and will need prescaling. Prescaling is a way of only accepting a fraction of the events that pass a certain trigger.

Level 1 (`L1`)

The very first stage in the trigger chain is the `L1` trigger system. It is fast (decisions are taken in less than 2.5 μs) and it reduces the rates to about 75 kHz. The `L1` trigger defines regions of interest (RoI) in the detector where interesting features have been found. Trigger items are high-p_T photons, electrons or muons, jets and large missing transverse energy by using the muon trigger chambers and the (not fully detailed) calorimeter information.

Level 2 (`L2`)

The second trigger system in line is the `L2` trigger which is slower than the `L1` stage, on average 40 ms per event. It reduces the rate to 3.5 kHz. The `L2` trigger uses the RoI information provided by the `L1` trigger, but with the full detector granularity and available information.

Event filter (`EF`)

The `EF` uses the full offline object reconstruction algorithms and is therefore the slowest stage in the trigger chain, typically around 4 seconds per event. It brings the rate down to the required 200 Hz.

Data flow

If an event has passed a certain trigger chain the event is fully reconstructed and written out into the appropriate stream. This means that all events passing muon (electron) triggers end up in the muon (egamma) stream. There are various different streams including a minimum bias stream that consists of events that are randomly triggered and the debug stream that includes all events that took longer than expected to reconstruct. For the top-quark analysis with leptons the important streams are the egamma stream and the muon stream that contain all events triggered on a lepton. The reconstructed streams are stored in an event data format called `RDO`'s, raw data objects [80]. These `RDO`'s are then trimmed of some of the more basic event information that is not needed by most analyses, like all the hits of all tracks, to the format used by the physics analyzers: the `AOD`'s, analysis data objects. The `AOD`'s are distributed from the `CERN` computing facility to all `Tier1` centers in the world (large computing facilities that are the center of a web of smaller centers called `Tier2`'s). The analyses are then typically run over the `GRID` [104] on those `AOD`'s. The total amount of data recorded by `ATLAS` in 2010 in the form of `AOD`'s was around 108 TB.

2.3 Summary

We have presented in this chapter the features of the `LHC` that will provide the `ATLAS` experiment with *pp* collisions at high center of mass energies and luminosity. The `ATLAS` detector and the various detector parts that are important to the analysis of the top-quark have been discussed. It was also shown that the detector is in excellent shape to perform the first measurement of the top-quark pair production cross section. In the following chapter the reconstruction and selection of objects for the analysis will be described as well as the event selection. From Chapter 6 onwards we will analyze the data that has been recorded by `ATLAS` in the first half of 2010.

CHAPTER **3**

OBJECT AND EVENT SELECTION

In this chapter we will focus on the selection of objects and on the selection of events for our top-quark pair production cross section analysis. All decay products of the top-quark pairs will play a role in identifying top-quark candidate events and selecting them from the large background of W+jets and QCD multi-jet events. The selection that will be presented in this chapter is based on Monte Carlo simulation and is optimized for data analysis at a center of mass energy of 7 TeV (Chapters 6, 7 and 8). Chapters 4 and 5 are based on 10 TeV Monte Carlo with slightly different selections and are a thorough investigation into the origin of QCD background where the precise selections do not change the overall conclusions.

In Section 3.1 we present the trigger used for the selection of the interesting events. Section 3.2 will focus on the object selection and Section 3.3 will cover the event selection adopted to select top-quark pair candidates and an indication of the remaining type and level of backgrounds. The chapter concludes with a summary in Section 3.4.

3.1 Lepton trigger

Since the rate of interactions occurring inside the `ATLAS` detector is higher than the data acquisition system can process and than can be reconstructed, the very first step in any physics analysis is the trigger system, see Section 2.2.5. In this thesis we will focus on the semi-leptonic muon $t\bar{t}$ decay channel, where one of the W-bosons decays into a muon and a neutrino and the other one decays hadronically, see Figure 1.7 (left). The muon is expected to have high transverse momentum and to be isolated as was shown in Section 1.3.2. In pp collisions the muon will be our handle to trigger the top-quark pair events (this section), but also to reject major backgrounds (following sections and chapters).

The trigger that was used for the first data analysis from Chapter 6 onwards is a 10 GeV muon trigger. For the Monte Carlo samples this is the `EF_mu10_MSonly` trigger which is seeded by the `L1_MU10` trigger. In Figure 3.1 the trigger efficiency is shown for the `L1_MU10` trigger relative to offline reconstruction of muons as a function of their transverse momentum [105] for Monte Carlo and also for early data ($\sim 94\ \mathrm{nb}^{-1}$).

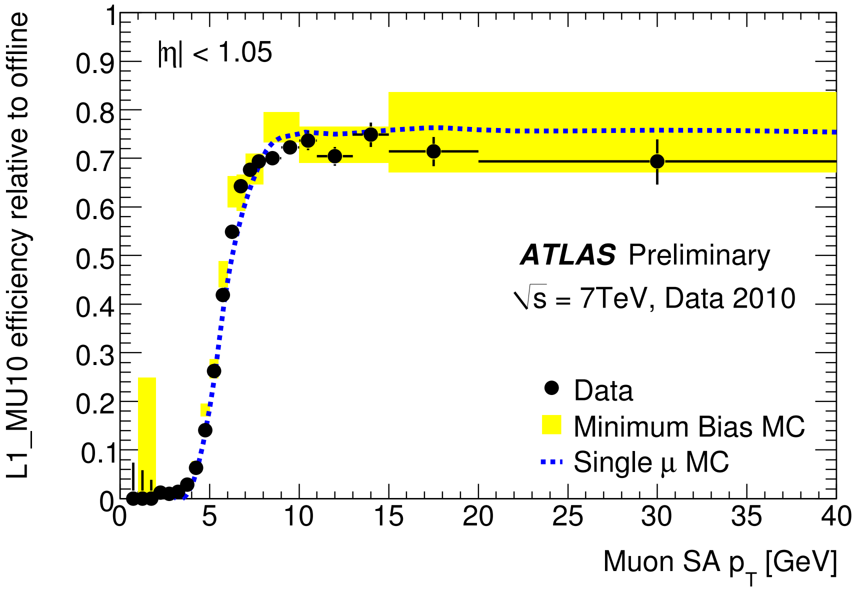

Figure 3.1: *Efficiency of the* `L1_10_MSonly` *trigger relative to offline reconstruction for muons as function of the muon* p_T *in the barrel region* ($|\eta| < 1.05$)*. Figure taken from [105].*

The efficiency of `L2_MU10` relative to `L1_MU10` and that of `EF_mu10_MSonly` relative to `L2_MU10` is close to 100 %. The offline selection requirement on the muon $\mathrm{p_T}$ (Section 3.2) will be higher than 10 GeV ensuring that the selection is not influenced by the turn-on of the trigger. This is important since the efficiency is not well described in the turn-on region. From Figure 3.1 it is clear that by selecting muons in the offline selection with $\mathrm{p_T}$ above 15 GeV only the plateau efficiency is important for the measurement. Using a *tag-and-probe* method in a sample of $Z \to \mu^+\mu^-$ events the efficiency in the plateau region for Monte Carlo is computed to be 84% [106] (higher in the endcaps and lower in the barrel region) for the full trigger chain of `EF_mu10_MSonly`. Note that the efficiency in Figure 3.1 is for the barrel region. We will see in Chapter 6 that for data analysis the difference in trigger efficiency between data and Monte Carlo will be corrected for by the use of scale factors.

3.2 Offline object selection

In this section we will present all the selections applied to define the objects that will be used in this thesis for analysis: electrons, muons, jets and missing transverse energy. Note that these are the definitions used for all the numbers and plots in this chapter (Monte Carlo) and also the ones used for data analysis from Chapter 6 onwards.

3.2.1 Electrons

Electron candidates are reconstructed in the inner detector and the electromagnetic (EM) calorimeter, see Section 2.2.2 and 2.2.3. The reconstruction of electrons is seeded by clusters in the EM calorimeter with $\mathrm{E_T}$ over 2.5 GeV that are matched with a track with $\mathrm{p_T}$ over 0.5 GeV [107–110]. Electrons selected for analysis (analysis electrons) are required to have $\mathrm{p_T}$ over 20 GeV and $|\eta_{cluster}|$ within 2.5. Electron candidates in the transition region ($|\eta| \in [1.37, 1.52]$) are excluded. Also the ratio of E/p where E is the energy measured in the EM calorimeter and p the momentum of the track has to be consistent with the electron hypothesis. To suppress background from photon conversion a hit in the first layer of the pixel detector is required. A requirement on the energy in a cone around the electron direction is imposed to reject non-isolated electrons from heavy flavour decays or jets faking electrons.

3.2.2 Muons

Muons in `ATLAS` are identified in the muon spectrometer (Section 2.2.4) and in the inner detector (Section 2.2.2). Muons reconstructed by only using the muon spectrometer information are called ‘stand alone’ muons. For most analyses ‘combined’ muons are used which are reconstructed by two different algorithms [111]. Both combine an inner detector track with a muon spectrometer track. The $\chi^2_{matched}$ of the track-matching then decides whether the match is successful. These algorithms are:

`Staco`:

this algorithm statistically combines the information of the inner detector track with the muon spectrometer track at the interaction point. This combination is performed by merging the two sets of track parameters to have the benefit of two independent measurements.

`MuId`:

unlike `Staco` which combines the tracks from the inner detector and the muon spectrometer, this algorithm performs a global refit of all the hits associated to these tracks to compute the combined track parameters.

Both muon algorithms perform well and the differences between them are small. For the first top-quark data analyses the `MuId` muons are used due to slightly lower fake rates. Since we will concentrate on the muon as a handle to reject backgrounds in this thesis, we mention the cuts that define an isolated high-$\mathrm{p_T}$ muon in detail:

- muon candidate from the `MuId combined` algorithm
- $|\eta| < 2.5$
- $\mathrm{p_T} > 20$ GeV
- $\mathrm{E_T^{dR=0.30}} < 4$ GeV[1]

---

[1] $\mathrm{E_T^{dR=0.30}}$ is the transverse energy in a cone of $\mathrm{dR} = \sqrt{(\Delta\phi)^2 + (\Delta\eta)^2} = 0.30$ around the muon.

- $\mathrm{p_T^{dR=0.30}} < 4$ GeV[2]
- no jet with $\mathrm{p_T} > 20$ GeV closer than $\mathrm{dR} = 0.40$ to the muon.

The last three requirements can be seen as quality cuts and they will be the subject of a large part of the following chapters. It turns out that the isolation of the muon is an important tool to reject events that contain muons from QCD multi-jet events.

3.2.3 Jets

Jets are reconstructed in `ATLAS` in the calorimeters (Section 2.2.3). In this thesis two jet algorithms were used that differ in both their input collection (*calorimeter towers* or *topological clusters*) and also in their clustering procedure (*cone jets* or *anti-kt jets*) [109,112]. The *cone jets* were the main jet algorithm in `ATLAS` for a long time not in the last place because of the high computational speed. Since they are however not collinear and infrared safe [113,114], the *anti-kt* is the default algorithm used for data analysis.

`Cone4H1TowerJets`

This algorithm uses *towers* formed by calorimeter cells that are collected into bins in a grid of $\Delta\eta \times \Delta\phi = 0.1 \times 0.1$ by summing up their signal. All cells are taken into account and towers with negative signal (due to noise) are recombined with nearby towers to make for positive signal towers. These towers are then used as the seeds for the 'Cone4' jet finding algorithm, where all objects within a cone of $\mathrm{dR} = 0.40$ are combined with the seed. Of this newly created object the energy and momentum are calculated and a new direction and cone are defined and the combination procedure is repeated. This is done iteratively until stable jets are found.

`AntiKtH1TopoJets`

These jets are reconstructed from *topological clusters* which are formed from cells that seed the clustering by using thresholds of $|\mathrm{E_{cell}}|/\sigma_{\mathrm{cell}} > 4$, 2 or 0 for the signal above the total noise of a cell. In the case of multiple maxima in one cluster, the cluster is split into smaller ones. Contrary to the tower algorithm the clusters do include noise suppression which makes them less noisy than the above described towers. The 'AntiKt' algorithm [114] then uses the topological clusters to form jets. A distance measure between two objects i, j is defined:

$$d_{ij} = \min\{\mathrm{p_{T,i}^{-2}}, \mathrm{p_{T,j}^{-2}}\}\frac{\Delta \mathrm{R_{ij}^2}}{\mathrm{R}} = \min\{\mathrm{p_{T,i}^{-2}}, \mathrm{p_{T,j}^{-2}}\}\frac{\Delta\eta_{\mathrm{ij}}^2 + \Delta\phi_{\mathrm{ij}}^2}{\mathrm{R}}, \tag{3.1}$$

where R is a measure for the size of the jet (0.4 in this case). Also the distance to the beam of each object is computed by $d_{iB} = \mathrm{p_{T,i}^{-2}}$. If the minimum of this list of measures is d_{ij}, then the objects i, j are removed from the list, combined into a new object k, which is then added to the list. If the minimum however is d_{iB}, then the object i is

---

[2] $\mathrm{p_T^{dR=0.30}}$ is the transverse momentum of all tracks in a cone of $\mathrm{dR} = 0.30$ around the muon.

labeled a jet and removed from the list. By this iterative procedure objects then either become part of a jet or jets themselves. Since the measure is proportional to $\frac{1}{\mathrm{p}_\mathrm{T}^2}$, the 'hardest' objects are clustered first. This procedure is collinear and infrared safe because no seeds are used, which is not the case for the 'Cone4' algorithm [113,114]. This feature is important especially when studying final states with three or more jets [115].

Jet calibration

One of the most important and at the same time non-trivial quantities of any jet is the jet energy scale. To translate detector responses into partonic energies, the energy scale is of great importance. When the jet energy scale has large uncertainties, this will translate directly into any top-quark measurement since we will select events by the number of their high-p_T jets, see Section 3.3. To account for lost energy in material and the fact that the response to hadronic energy is smaller than to electromagnetic energy, jet calibration is performed. Both the above algorithms use the long-standing `H1` calibration which is based on cell weighting in the calorimeters [109, 112]. All cells are weighted according to their energy density. For the analysis of the first data however a newer calibration scheme was used: the `EMJES` calibration (which stands for 'at the electromagnetic scale with jet energy scale calibration') [116,117]. The `EMJES` calibration is more simple and therefore more robust for early analyses. The energies of the cells are taken at the electromagnetic level meaning no hadronic corrections are made. The jets are calibrated as a whole (the jet four vector) by a Monte Carlo based factor that depends only on the jet p_T and $|\eta|$. In this manner material effects and the difference for hadronic responses are corrected. For this chapter and for the data analysis from Chapter 6 onwards, we will select `AntiKtH1TopoJets` with p_T over 20 GeV and within $|\eta| < 2.5$, calibrated with the `EMJES` scheme.

Identifying jets from *b*-quarks

Since two of the jets from the decay of a top-quark pair originate from b-quark fragmentation, the identification of jets originating from b-quarks, *b-tagging*, is a strong tool to select top-quark pair candidate events. The b-tagging of jets can be achieved in various ways, but the most straightforward option is looking for jets originating from secondary vertices. Due to the longer lifetime of B-mesons, they can travel distances of up to a few millimeters from the interaction point before decaying and forming jets. For the top-quark analyses in `ATLAS` we use the `SV0` algorithm [109,118–120]. The `SV0` secondary vertex tagging-algorithm returns a weight for each jet, according to the probability that the jet originated from a B-meson. In Figure 3.2 the efficiencies and rejections are presented for $t\bar{t}$ events for jets originating from b-quarks and from light quarks as a function of the `SV0` weight [120].

Light jets are in this case jets that are not close ($\Delta R > 0.3$) to a b-quark, c-quark or τ particle. By choosing a given weight to define b-jets, both the b-tag efficiency and the

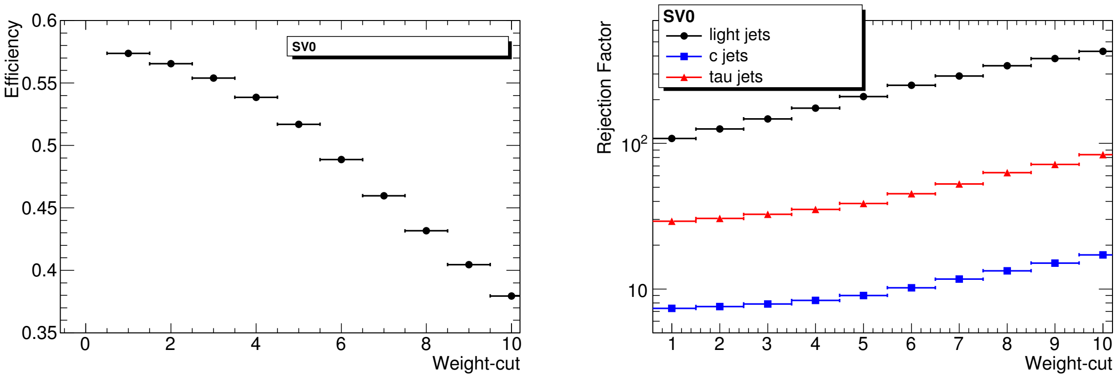

Figure 3.2: *Efficiencies and rejections for SV0 b-tagger in $t\bar{t}$ events, for jets with $p_T > 15$ GeV and $|\eta| < 2.5$. Left: efficiency for b-jets. Right: rejection for light jets, c-jets and τ-jets. Figures taken from [120].*

mistag rate are given. We use a working point where the b-tagging efficiency of b-jets in $t\bar{t}$ events is 50 %, which corresponds to a `SV0` weight of 5.72. The mistag rate at this point is $\sim 1\%$ for a weighted sample of light jets, c-jets and τ-jets.

3.2.4 Missing transverse energy

The missing transverse energy ($\not{E}_{\mathrm{T}}$) is an important variable to select top-quark events as was shown in Section 1.3.2 due to the escaping high-$\mathrm{p_T}$ neutrino. It will be this variable that provides the first handle on the large QCD multi-jet background as we will see in Section 3.3.1. The $\not{E}_{\mathrm{T}}$ is built from two terms: the transverse energy of all the cells in the calorimeter and the muon energy. Since the variable involves all the different detector components and expectations for loss terms due to material, it is a difficult variable to measure at the beginning of data-taking. For our analysis we use the `MET_RefFinal_MUID_EMJES` [121]. This $\not{E}_{\mathrm{T}}$ definition uses the same calibration scheme for jets as the jets we select, ensuring a consistent treatment of $\not{E}_{\mathrm{T}}$. The $\not{E}_{\mathrm{T}}$ is computed by first associating all measured energies to particles (electrons, photons, taus, jets and muons) and then summing up their more refined transverse energy terms. Calorimeter cells that are not associated to a physics object are summed in a term called *Cellout* and added to the $\not{E}_{\mathrm{T}}$.

3.3 Top event selection

Section 1.3.2 describes how a top-quark pair decays and in this section we will translate this into an event selection to select top-quark pairs above the large background. Throughout this chapter we will consider Monte Carlo simulation for two kinds of background events to $t\bar{t}$ analysis: *QCD multi-jet* events and *prompt backgrounds*. The latter is labeled *prompt* since these background events consist of all the different types of events that produce prompt leptons like $t\bar{t}$ events. They are a mixture of W+jets, Z+jets, single top and di-boson events, see Section 1.4.3. QCD events do not produce prompt leptons and will therefore be quoted separately.

3.3.1 Base selection

Top-quark pair decays are characterized, in the semi-leptonic decay channel, by the presence of a high-p_T isolated lepton, the neutrino which escapes detection and will cause missing transverse energy ($\not\!\!E_T$) and at least four jets (two of which originate from a b-quark). Before we present the cut-flow numbers for different samples at the end of this section, we will look at the distributions of the variables to justify qualitatively the imposed selection criteria. The 'base' event selection that will be used to select top-quark pair candidates for the semi-leptonic muon channel will reflect these properties and is given by:

Base selection:

1. `EF_mu10_MSonly` muon trigger
2. one (and only one) isolated muon with $p_T > 20$ GeV
3. no isolated electron with $p_T > 20$ GeV
4. $\not\!\!E_T > 20$ GeV
5. at least four selected jets with $p_T > 25$ GeV

Requirements 1, 2 & 3 are the lepton requirements and reject the enormous background of events without an isolated high-p_T muon like fully hadronic $t\bar{t}$ events and QCD multi-jet events. Also the rejection of dileptonic $t\bar{t}$ events with where one lepton is an electron and one lepton is a muon is part of these requirements.

Requirement 4 is the main selection to reject QCD multi-jet events (after the trigger and lepton requirement). QCD events are not expected to have large $\not\!\!E_T$ with respect to $t\bar{t}$ events or the prompt backgrounds because there is in principle no escaping high-p_T neutrino. This can be seen in Figure 3.3 where the $\not\!\!E_T$ is shown for $t\bar{t}$ events, QCD multi-jet events and also 'prompt backgrounds' after the trigger and lepton requirement. The cut at 20 GeV rejects a large part of the QCD background, but does hardly influence the $t\bar{t}$ signal and the prompt backgrounds.

Requirement 5 rejects a large fraction of the W+jets background. In Figure 3.4 (left) the number of selected jets is shown after trigger and lepton requirement for $t\bar{t}$, QCD and prompt backgrounds. In Figure 3.4 (right) the p_T of the jet with the fourth highest p_T is shown for $t\bar{t}$ and prompt backgrounds (the QCD has been omitted here since the Monte Carlo statistics are low after requiring four high-p_T jets).

The left plot of Figure 3.4 shows why the selection of events with at least four selected jets is in place: this requirement rejects a large part of the prompt background sample (mainly W+jets). The right plot justifies the p_T requirement of 25 GeV for all four

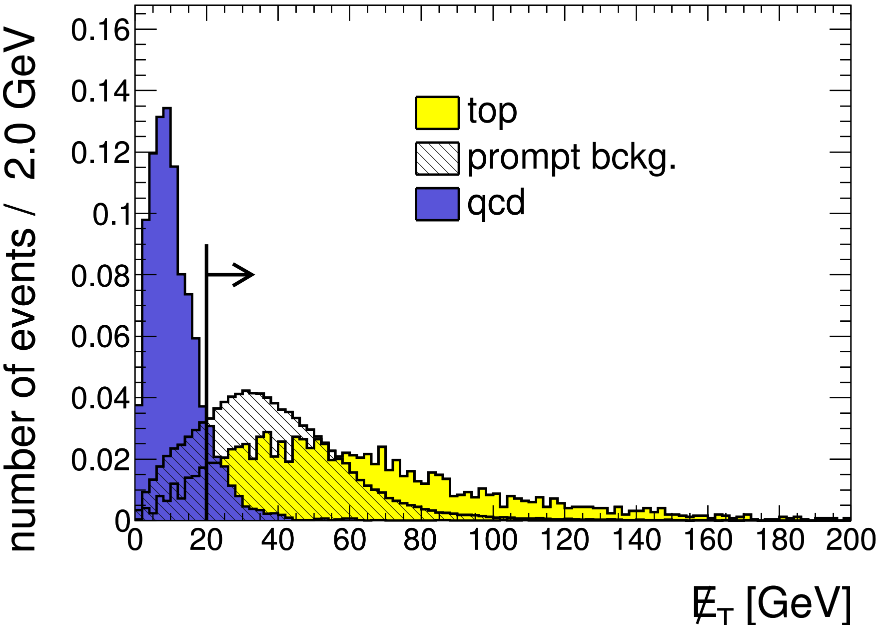

Figure 3.3: *The normalized (to unity) missing energy distribution after the trigger and lepton requirement for $t\bar{t}$, QCD and prompt backgrounds. The arrow indicates the selected region.*

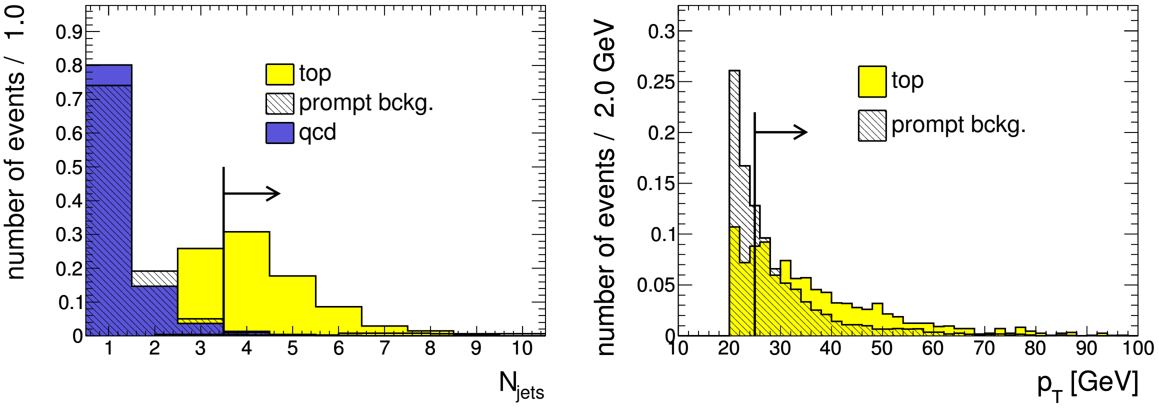

Figure 3.4: *Left: the number of selected jets after the trigger and lepton requirement for $t\bar{t}$, QCD and prompt backgrounds. Right: the p_T of the selected jet with the fourth highest p_T after the trigger and lepton requirement for $t\bar{t}$ and prompt backgrounds. Both plots are normalized to unity. The arrow indicates the selected region.*

selected jets, since only a small fraction of $t\bar{t}$ events is rejected, while a larger fraction of the prompt backgrounds is rejected.

Cut flow

To quantify the qualitative discussion about the various event selection requirements Table 3.1 presents the number of events that pass a given requirement (the lepton requirement includes the trigger and the rejection of events with electrons) for various samples normalized to 2.89 pb^{-1} (this with future knowledge of the integrated luminosity of our data analysis). The selection requirements are cumulative.

	base selection				additional	
	no cut	lepton cut 1-3	$\not\!\!E_{\mathrm{T}} > 20$ cut 4	$\geq$4 jets cut 5	b-tag	trian.
QCD	$1.3 \cdot 10^7$	1833.0	171.9	2.3	1.5	0.3
W+jets	$1.1 \cdot 10^5$	15031.6	13929.0	22.1	1.9	1.8
Z+jets	$1.1 \cdot 10^4$	1044.7	545.6	1.9	0.2	0.1
di-boson	46.6	14.3	11.8	0.3	0.1	0.1
single top	108.0	14.9	13.4	0.9	0.6	0.5
total bck	$1.3 \cdot 10^7$	17938.5	14671.7	27.6	4.2	2.8
top	251.0	44.2	40.4	19.2	14.4	13.7
total	$1.3 \cdot 10^7$	17982.8	14712.1	46.7	18.6	16.4

Table 3.1: *Number of events passing a given cut for various Monte Carlo samples. All samples are normalized to 2.89* pb^{-1} *and the cuts are cumulative.*

The table shows that the number of QCD events is a factor hundred larger than the second largest background before all cuts[3]. The trigger and lepton requirement already decreases this numbers to the same order of magnitude as W+jets events. After the $\not\!\!E_{\mathrm{T}}$ requirement QCD can no longer be considered a large background. The QCD production cross section has however large uncertainties, see Chapter 1. It is clear that this background needs to be studied in more detail to gain confidence that it is understood and can be handled sufficiently. The W+jets background is rejected mainly through the requirement on the number of high-$\mathrm{p_T}$ jets.

The signal to background ratio after base selection $S/B = 0.7$. Especially the W+jets background is still sizable at this stage. There are still differences between signal and the two main backgrounds to be exploited that result in additional requirements to obtain a much larger signal over background ratio for $t\bar{t}$ analysis in the next section: one to lower the W+jets background contribution and one to have an extra handle on QCD background.

3.3.2 Additional requirement 1: at least one *b*-tagged jet

As was shown in Section 1.3.2, two of the jets in the semi-leptonic decay channel of $t\bar{t}$ events originate from a b-quark. This feature can be used to suppress the still large

---

[3] Some of the QCD samples used in the mix are already pre-selected to contain true muons with $\mathrm{p_T}$ over 10 GeV, see Section 1.4.3

W+jets background after base selection since almost no b-jets are expected in those events.

There is a small contribution to this background from $W+bb$+jets events which will pass the b-tag requirement, but the majority of events with W-bosons is characterized by light jets.

In Figure 3.5 the number of b-tagged jets (`SVO` > 5.72) is shown for $t\bar{t}$, QCD and prompt backgrounds after the trigger and lepton requirement. The requirement of at least one jet with a b-tag rejects a large fraction (more than 90%) of the W+jets events. This is also shown by the numbers after b-tag requirement in Table 3.1 where the numbers are presented after the base selection.

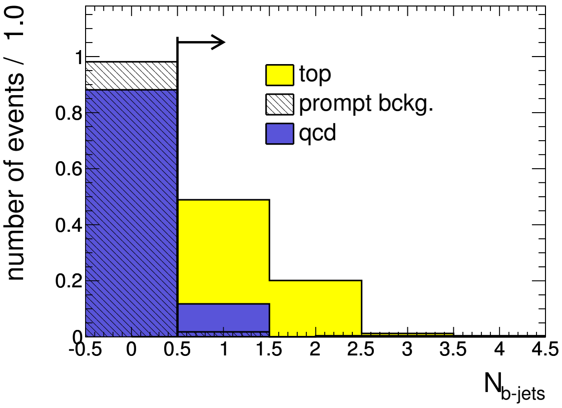

Figure 3.5: *The normalized number of b-tagged jets after the trigger and lepton requirement for $t\bar{t}$, QCD and prompt backgrounds. The arrow indicates the selected region.*

3.3.3 Additional requirement 2: triangular cut

When considering the numbers of Table 3.1 it seems that the QCD background is well under control. As was mentioned before however, the production cross section of QCD multi-jet events has large uncertainties. To control a possibly higher QCD contribution there is one extra requirement that rejects QCD events: the triangular cut. The cut is defined as:

$$(\not{E}_{\mathrm{T}} + \mathrm{M}_W^{\mathrm{trans}}) > 60 \text{ GeV},$$

where $\mathrm{M}_W^{\mathrm{trans}}$ is the transverse W-mass computed from the lepton and the $\not{E}_{\mathrm{T}}$, given by

$$\mathrm{M}_W^{\mathrm{trans}} = \sqrt{(\mathrm{p_T} + \not{E}_{\mathrm{T}})^2 - (\mathrm{p_x} + \not{E}_{\mathrm{x}})^2 - (\mathrm{p_y} + \not{E}_{\mathrm{y}})^2}.$$

The cut is based on differences between QCD events on the one hand and $t\bar{t}$ and prompt background events on the other. As was shown in Section 3.3.1, QCD events do in general not have large missing energy. The other difference that is exploited in the triangular cut is the absence of W-bosons in QCD events, which is reflected in low transverse W-mass ($\mathrm{M}_W^{\mathrm{trans}}$). In Figure 3.6 the $\mathrm{M}_W^{\mathrm{trans}}$ is presented as a function of the $\not{E}_{\mathrm{T}}$ for $t\bar{t}$ and QCD events. The black line indicates the triangular cut.

From the figure it is clear that the triangular cut is powerful in reducing the QCD background. In Table 3.1 this is reflected by the reduction of QCD with a factor five while the $t\bar{t}$ content is virtually unaffected.

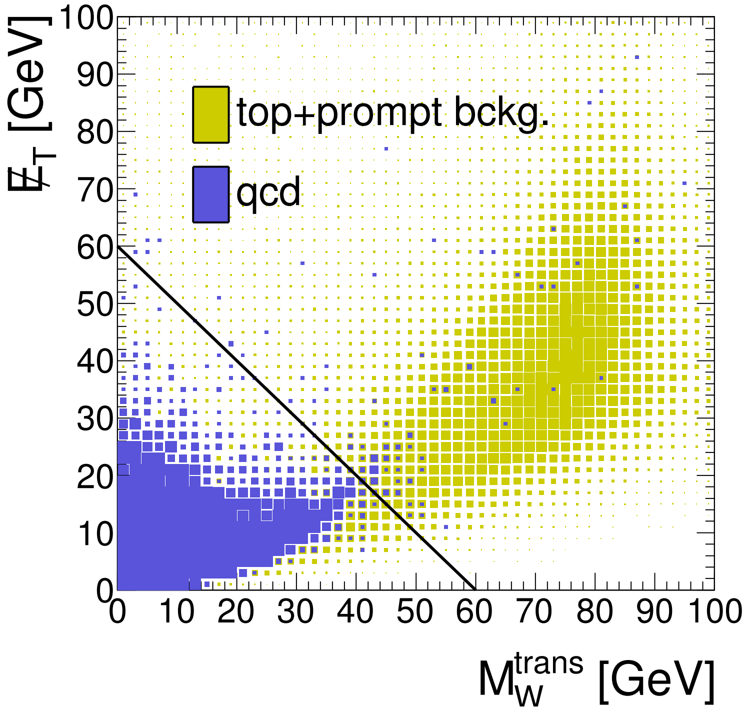

Figure 3.6: *The missing energy versus the transverse W-mass after the trigger and lepton requirement for QCD and $t\bar{t}$ plus prompt backgrounds. The line that represents the triangular cut is also drawn and the arrow indicates the selected region.*

Applying both the additional requirements yields a signal to background ratio of $S/B = 4.9$, which is a great improvement from $S/B = 0.7$ after the base selection.

3.4 Summary

In this chapter we have investigated the object selection and event selection for our top-quark pair production cross section analysis. The Monte Carlo simulation after the base selection shows that the W+jets contribution is larger than the $t\bar{t}$ content. The number of QCD events is also not negligible, especially when considering the large uncertainty on the production rate of this background. We have shown two additional requirements that each reject one of these backgrounds. Requiring at least one b-tagged jet purifies the $t\bar{t}$ candidate events with respect to the W+jets events. The triangular cut on the other hand rejects almost purely QCD events. With those two additional requirements a highly pure $t\bar{t}$ selection is possible. Although the remaining QCD content seems negligible, with the large uncertainties it is exactly this background that is the most worrisome and that will be studied in the rest of this thesis.

In the following two chapters we will focus in detail on the origin of leptons in QCD events to understand the class of events that survive the lepton requirement.

CHAPTER 4

STUDY OF EXTRA LEPTONS IN MULTI-JET EVENTS

When selecting a sample of $t\bar{t}$-candidates, the main potential background, aside from W+jets events, are QCD multi-jet events. These events are produced solely by QCD interactions and their production rate has a large uncertainty, see Section 1.4.3. The cross section for QCD multi-jet events (even with four or more reconstructed jets) is orders of magnitude larger than the production of top-quark pairs [73, 81]. Rejection for the base selection relies mainly on the requirement of an isolated lepton and large missing energy in the event, which are in principle absent for QCD multi-jet events. Although the missing energy requirement also removes a large fraction of the QCD events, see Table 3.1, the biggest rejection comes from the requirement of an isolated high-$\mathrm{p_T}$ lepton in the event. QCD events could pass the isolated lepton cut either by jets faking a lepton or by decaying heavy flavours like B-mesons that do actually produce a genuine lepton in the detector. We will focus only on muons in this thesis. The muons created by jets or decaying mesons are called *extra* muons to distinguish them from the prompt muons that come from hard interactions, which in our case originate from the decay of the W-boson that is produced by a decaying top-quark.

In this chapter the origin and properties of leptons in multi-jet events will be investigated in detail. This study is based on $\sqrt{s} = 10$ TeV Monte Carlo simulations with slightly different selection requirements than discussed in the previous chapter. However, our ambition is to minimize the dependence of the analysis on the simulation, and we therefore propose a strategy to determine the yield of the extra leptons from data alone. In order to develop this 'data driven' method for the main analysis in Chapter 7, we first study the main characteristics of the extra leptons in this chapter and two existing data-driven methods in Chapter 5. The next two chapter can therefore be regarded as background studies for the main analysis described in Chapter 7.

The strategy to understand the rates in which these QCD events pass the isolated lepton criterion will be outlined in Section 4.1. Heavy flavour decay to muons is discussed in Section 4.2 and the classification of the extra muons and their dependency on various observables and parameters is presented in Section 4.3. In Section 4.4 the results are tested to make extrapolations from $t\bar{t}$ to different event topologies. Also in that section the origin of muons in a large QCD multi-jet sample are investigated.

4.1 Strategy

At the time of this study, no large fully simulated QCD multi-jet sample was available. Since the goal of this chapter is to understand the production of non-prompt muons in $t\bar{t}$-like topologies, where events have multiple high-$\mathrm{p_T}$ jets and hard b-partons, this study is performed on the large sample of $t\bar{t}$ MC events, see Section 1.4.3 [122,123]. Due to their richness in high energy jets and their high b-quark content they are extremely suitable to be used in a study on extra muons. To study the rate and origin of extra muons the goal is to find muons that pass all muon selection criteria, see Section 3.2, in the $t\bar{t}(e)$ channel, that is the $t\bar{t}$ decay channel where one of the W-bosons decays leptonically into an electron and no high-$\mathrm{p_T}$ isolated prompt muons from the hard interaction are present. By studying these muons and investigating their origin a set of characteristic parameters can be derived. We will then show that we can extrapolate the yield of extra muons to different event topologies. Once this has been shown, we are confident that the production mechanism of extra muons is understood and we can then develop a data-driven method independent on the absolute rate predictions from Monte Carlo to relate the yield of extra leptons from one topology to another. This procedure will be further discussed in Chapter 5. In order to study this we will first concentrate on the physics background of extra muons, that is real muons that are produced, but do not originate from the decay of a W-boson in $t\bar{t}$ events.

4.2 Heavy flavour decay to muons

One of the sources of extra muons from multi-jet events is expected to be the decay of heavy flavours in jets. More specifically, the largest contribution is expected to come from the decay of B-mesons. As they will form an important part in the study of extra muons, in this section the branching ratio of $b \to \mu + X$ and the $\mathrm{P_T^{Rel}}$ variable will be investigated.

Inclusive branching ratio

Both the b-parton and the c-parton that produce heavy mesons can decay weakly to a muon, a neutrino and a hadronic remainder (X). In Figure 4.1 this is shown as an example for the decay of a B^+ ($u\bar{b}$) into a $\bar{D}^0$ ($u\bar{c}$) and a muon plus neutrino. The $\bar{D}^0$ can then form a jet with the remaining particles that originate from the shower.

The branching fraction of B-mesons to muons is ~11% [124]. This number however only incorporates direct decay of a b-quark to muons. There are also indirect decay channels that include the hadronic decay to a D-meson that can subsequently decay semi-leptonically to a kaon, muon and a neutrino. There are numerous ways to produce

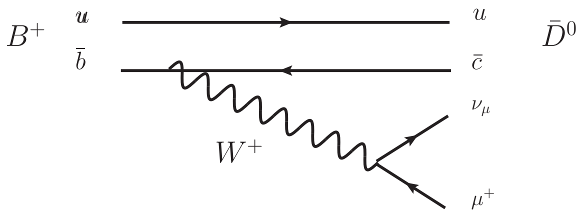

Figure 4.1: *Leptonic decay of B^+ into a $\bar{D}^0$ and a muon plus neutrino.*

a muon from a high-p_T b-quark and it is difficult to compute the full inclusive branching fraction of $b \to \mu + X$, but using the Monte Carlo truth information each generated muon (true muon) can be traced back to its originating parton. In Figure 4.2 (left) the p_T of all b-partons from top-quark decay that produced a true muon is shown divided by the p_T spectrum of all b-partons from top-quark decay. This can be interpreted as the inclusive fraction of b-partons that produce a muon as a function of b-parton p_T. As expected, it is almost independent of the b-parton p_T and is roughly 30% which is almost three times larger than would have been expected directly from the branching ratio of B-mesons to muons. Note that no reconstruction effects have been taken into account here and most of the muons will have relatively low p_T, so the rate of reconstructed isolated high-p_T muons from b-partons will be much lower. In Figure 4.2 (right) the probability of a true b-parton to produce a true muon with $p_T > 20$ GeV as a function of the b-parton p_T is shown.

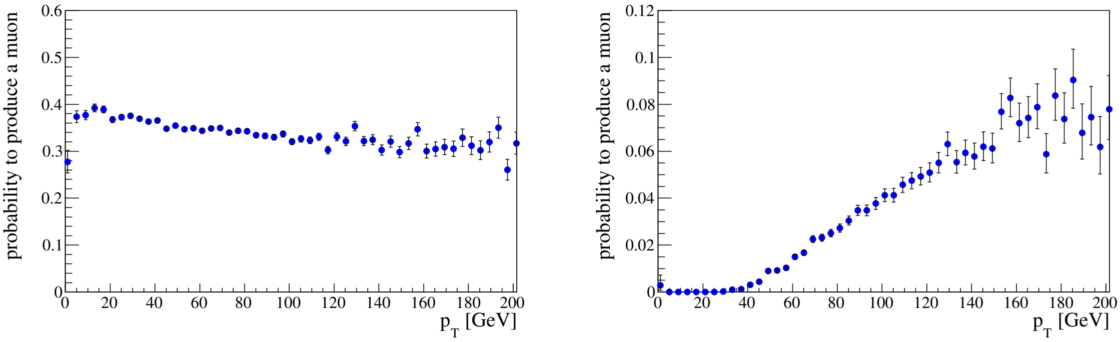

Figure 4.2: *Probability of a true b-parton to produce a true muon as a function of the b-parton p_T. Left: for all muons. Right: for muons with $p_T > 20$ GeV.*

In the right plot of Figure 4.2 one can see that the probability to produce a muon with $p_T > 20$ GeV increases with increasing b-parton p_T after starting around 30 GeV. Note that for a b-parton with $p_T = 200$ GeV the probability to produce a high-p_T muon ($p_T > 20$ GeV) is around 10%. In the next sections we will investigate how these numbers change when taking reconstruction effects and selection cuts on the muon into account.

The $\mathrm{P_T^{Rel}}$ variable

It has been noted that b-partons have a high inclusive branching ratio to muons. There is however another reason why b-partons will be the dominant source of extra muons: in general the $\mathrm{p_T}$ of the muon relative to the remaining jet will be larger for muons from b-quarks with respect to muons from lighter quarks. The muon gets a significant momentum due to the mass difference of the B-meson and its decay products in the rest frame of the meson. This momentum is much lower when the muon is produced from a lighter quark, like the c-quark. This can be best seen by introducing the variable $\mathrm{P_T^{Rel}}$ [125]. The $\mathrm{P_T^{Rel}}$ variable is defined as the transverse momentum of the muon with respect to the meson momentum axis, which is the combined momentum axis of muon, jet and neutrino, see Figure 4.3 (left). If the decaying meson is boosted, then the $\mathrm{P_T^{Rel}}$ variable is a measure for the transverse boost of the muon with respect to the remaining meson axis. In Figure 4.3 (right) the normalized $\mathrm{P_T^{Rel}}$ distribution is shown for true muons from B-mesons (dark) and D-mesons (light) in $t\bar{t}(e)$ events.

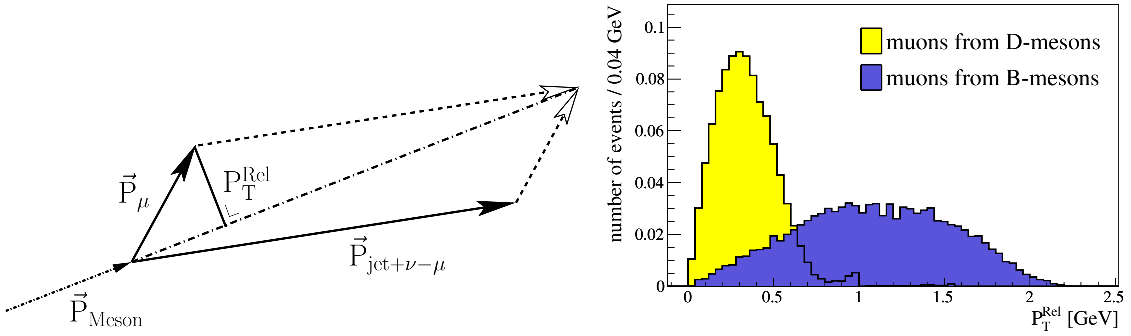

Figure 4.3: *Left: the definition of P_T^{Rel}: the transverse momentum of the muon with respect to the momentum of the originating meson, $\vec{P}_{Meson}$. Right: Normalized P_T^{Rel} distribution for true muons from B-mesons (dark) and D-mesons (light) in $t\bar{t}(e)$ events.*

As expected, the figure shows that the muons from b-partons have a larger transverse momentum with respect to the remaining meson than the muons from the lighter c-meson. The larger the $\mathrm{P_T^{Rel}}$ of the muon, the higher the probability that the muon will escape the remaining jet and will be isolated. This will be of importance in the next sections where reconstructed high-$\mathrm{p_T}$ *isolated* muons are investigated.

4.3 Classification of 'extra' muons

As outlined in Section 4.1 the strategy is to look for reconstructed muons in the $t\bar{t}(e)$ channel that pass all muon selection criteria as discussed in Section 3.2 i.e. that are isolated high-$\mathrm{p_T}$ muons. In this section the muons are classified and the muon rates per jet will be discussed.

Classification

The selected muons can be divided in two classes and then classified according to their origin: *fake* and *non-prompt*.

- *Non-prompt* muons are reconstructed muons that can be matched to a muon in the truth list of the generator with a dR < 0.05 cut[1]. Once a muon is classified as being non-prompt there is a handle to the true muon and its origin. By going back in the particle list of the generator one can classify these non-prompt muons as coming from two sources: b-quarks and light quarks, where gluons are grouped with the light quarks.

- *Fake* muons are reconstructed muons that cannot be matched to a muon in the truth list of the generator. These are most likely reconstruction artifacts (detector hits caused by other particles that are by coincidence identified as a muon track) or badly reconstructed muons.

Since the inclusive branching ratio from B-mesons to high-$\mathrm{p_T}$ muons is much larger than from D-mesons (or even lighter mesons), most of the non-prompt muons in the $t\bar{t}$ (e) channel will be originating from the b-partons in the event. In 129,867 $t\bar{t}(e)$ events 630 muons (reconstructed by the `Staco` algorithm, see Section 3.2.2) have been found. The breakdown of their origin is presented in Table 4.1 and in the case with isolation requirement, $\mathrm{E_T^{dR=0.20}} < 6$ GeV[2], the most dominant source of extra muons (more than 90%) is semi-leptonic b-decay. Only a small fraction originates from the lighter c-quark. The influence of the isolation requirement will be studied later in this section since it is one of the most important variables to separate prompt muons from extra muons. Note that when removing the isolation requirement the number of muons found increases by an order of magnitude. The numbers without isolation requirement are also presented in Table 4.1.

	`Staco` isolated		`Staco` non-isolated		`MuId`	
origin	non-prompt	fake	non-prompt	fake	non-prompt	fake
b-quark	583		5358		561	
c-quark	25		372		23	
light q+g	15		105		10	
unknown		7		253		3
total	623 (99%)	7 (1%)	5835 (96%)	253 (4%)	594 (99%)	3 (1%)

Table 4.1: *Number and origin of extra (`Staco`) muons in $t\bar{t}(e)$ events with and without muon isolation requirement. The right column shows the origin of isolated `MuId` muons.*

As has been discussed in the precious section, both the b-and the c-quark form heavy mesons that can decay weakly into a muon and a neutrino accompanied by a jet. Due to

---

[1] $\mathrm{dR} = \sqrt{(\Delta\phi)^2 + (\Delta\eta)^2}$.

[2] $\mathrm{E_T^{dR=0.20}}$ is the transverse energy in a cone of dR = 0.20 around the muon. Note that this is slightly different from the selection criteria in Section 3.2.2.

the classification definition used, only quarks or gluons are given as origin for the muons. Although some muons will be produced by pion decay or kaon decay (respectively 2 and 7 out of 623 non-prompt muons), they will still be listed under the quark or gluon that produced the pion (kaon) since that allows to compute the inclusive probability that a parton produces (either direct or through cascades) a muon. This inclusive probability will be used to make predictions in Section 4.4. Note that the fake rate is almost negligible.

The difference between the `Staco` and the `MuId` muon reconstruction algorithms is small at this stage, as discussed in Section 3.2. For comparison the breakdown of the overall numbers for `MuId` is also quoted in Table 4.1 in the right column, which shows that `MuId` has a slightly lower non-prompt and fake rate.

Muon rates per jet

As we observe jets in the detector and not partons a more useful classification is the non-prompt muon rate per originating jet rather than per quark or gluon. We will use this in the rest of this section. It is more useful since it provides a way to estimate the number of non-prompt muons given the number of jets in a sample which is something that can be extracted from data. This means considering all muons that come from b-quarks per b-jet (likewise, all muons from light quarks/gluons per light jet) where a b-jet is defined as a reconstructed jet that passes the jet requirements as in Section 3.2.3[3] and is matched to a b-parton in the truth list of the generator with a dR < 0.4 cut. Light jets are jets that pass the same jet requirements but are not matched to a b-parton. The results from this classification are shown in Table 4.2 for isolated muons and for non-isolated muons.

origin	with isolation $\cdot 10^{-5}$	without isolation $\cdot 10^{-5}$
b quark	277 ± 11	2542 ± 34
light quark:	12 ± 1.9	141 ± 6.5

Table 4.2: *Non-prompt muon rate per originating jet with and without isolation requirement.*

As the branching ratio for b-quarks to muons is much higher than for light quarks and gluons and as muons from b-decay more easily escape the jet, the rate from b-quark per b-jet is much higher than the light rate per light jet. Since muons from b-decay are more likely to be isolated due to their larger $\mathrm{P_T^{Rel}}$, see Section 4.2, the effect of the isolation requirement is less dramatic for muons from b-quarks.
By studying the origin of extra muons, it is clear that the dominant contribution to extra muons comes from the leptonic decay of b-quarks. The rate per b-jet is around $270 \cdot 10^{-5}$ and an order of magnitude higher without an isolation requirement on the muon.

---

[3] For the study in this and the next chapter `Cone4H1Tower` jets have been used with the same selection criteria, i.e. $\mathrm{p_T} > 20$ GeV and $|\eta| < 2.5$ see Section 3.2.3.

4.3.1 Characteristics of the extra muons in $t\bar{t}(e)$

After having classified the extra muons, one can study their characteristics. In this section their $\mathrm{p_T}$, η and distance to jets distribution will be shown, mainly as reference for the next sections. In Figure 4.4 the $\mathrm{p_T}$ of non-prompt (light) and fake muons (dark) is shown on the left and the η of non-prompt (light) and fake muons (dark) on the right.

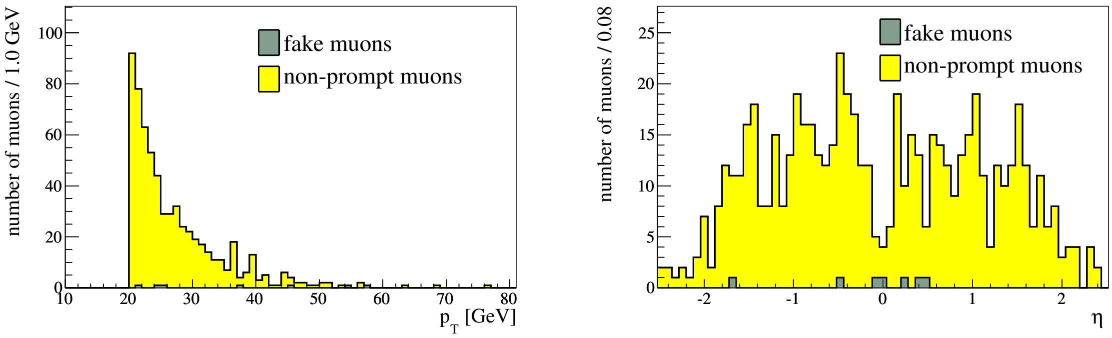

Figure 4.4: *Left: p_T of non-prompt (light) and fake muons (dark). Right: η of non-prompt (light) and fake muons (dark).*

Naturally the $\mathrm{p_T}$ spectrum of the extra muons starts at 20 GeV, since this is one of the muon selection cuts. Also it can be noted that the extra muons are mainly low-$\mathrm{p_T}$ muons. In the η plot there are no distinctive features. Another feature that characterizes the extra muons is their distance to jets. One would expect that prompt and non-prompt muons differ greatly in their minimal distance to jets. In Figure 4.5 (left) one can see the distance to the nearest jet that passes all jet criteria, see Section 3.2, for prompt (dark) and extra muons (light). The right plot of Figure 4.5 shows the same distribution, but both normalized to unity.

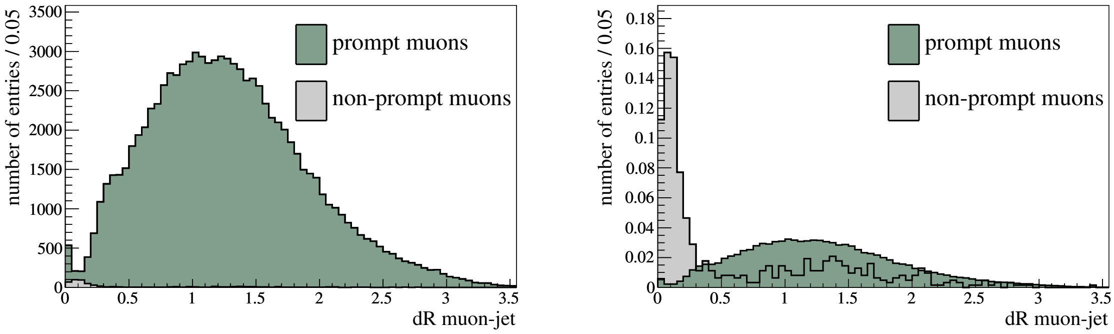

Figure 4.5: *Left: Distance between selected jets and isolated high-p_T muons for prompt muons (dark) and non-prompt muons (light). Right: same, but normalized to unity.*

It can be noted that there are a lot of extra muons that are not close to a reconstructed jet (more than 35% with dR > 0.4). This is mainly due to the fact that the jets the muon originated from do not pass the $\mathrm{p_T} > 20$ GeV cut.

4.3.2 Dependence of non-prompt muon rate on the $\mathrm{p_T}$ of the originating parton

To make predictions about non-prompt muons it is important to understand the dependence of the production of non-prompt muons on the $\mathrm{p_T}$ of their originating parton. That there is a dependence on the $\mathrm{p_T}$ of the originating parton has been shown in Figure 4.2 (right) where the probability was plotted for a b-parton to produce a muon with $\mathrm{p_T} > 20$ GeV. Different physics processes might have different parton spectra (and thus jet spectra) and this needs to be taken into account.

Probability for a b-parton to produce an isolated high-$\mathrm{p_T}$ muon

In this section the probability to produce a reconstructed isolated high-$\mathrm{p_T}$ muon from b-partons will be studied. This will give us information about how b-partons (and eventually b-jets) produce muons that pass all our muon selection cuts. The probability for light partons is computed in the same way and the results are shown in the next section. In Figure 4.6 (left) the $\mathrm{p_T}$ of all b-partons in $t\bar{t}(e)$ is shown together with the b-partons that decayed semi-leptonically producing an isolated muon (both normalized to unity). It can be seen that only b-partons of at least 30 GeV will produce an isolated high-$\mathrm{p_T}$ muon, which is expected due to the 20 GeV cut on the muon $\mathrm{p_T}$. Now the probability for a b-parton to produce an isolated muon as a function of $\mathrm{p_T}$ can be computed. By dividing the (non-normalized) light graph in Figure 4.6 (left) by the dark one, a probability distribution as is shown in Figure 4.6 (right) is obtained.

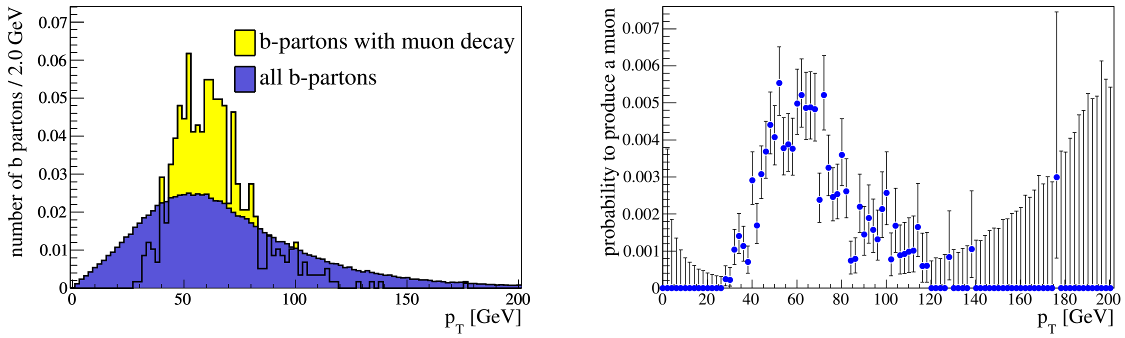

Figure 4.6: *Left: normalized p_T spectrum of all (dark) and muon producing (light) b-partons. Right: probability of a b-parton to produce an isolated muon as a function of b-parton p_T.*

The probability to produce an isolated high-$\mathrm{p_T}$ muon from a b-parton starts around

30 GeV due to the 20 GeV requirement on the muon-p_T. This is the same turn-on as be seen in the probability plot to produce a true muon with $p_T > 20$ GeV, Figure 4.2 (right). The maximum probability (~0.5%) is reached around 60 GeV. The decrease after about 70 GeV can be explained by the absolute isolation cut used in the isolation requirement. Two effects play a role here: the higher the p_T of the *b*-parton, the more collinear the muon and the *b*-jet will be. As a consequence the muon will less likely escape the jet and will less likely be isolated. The other effect is the absolute cut on isolation energy. Even if only a fraction of a jet is close to the reconstructed muon this fraction exceeds the 6 GeV isolation cut more easily when the jet is more energetic.

Effect from the isolation requirement

In Figure 4.7 the probability to produce an isolated high-p_T muon as a function of *b*-parton p_T is plotted similar to Figure 4.6 (right), but varying the isolation cut from 6 GeV (default) up to 100 GeV (non-isolated).

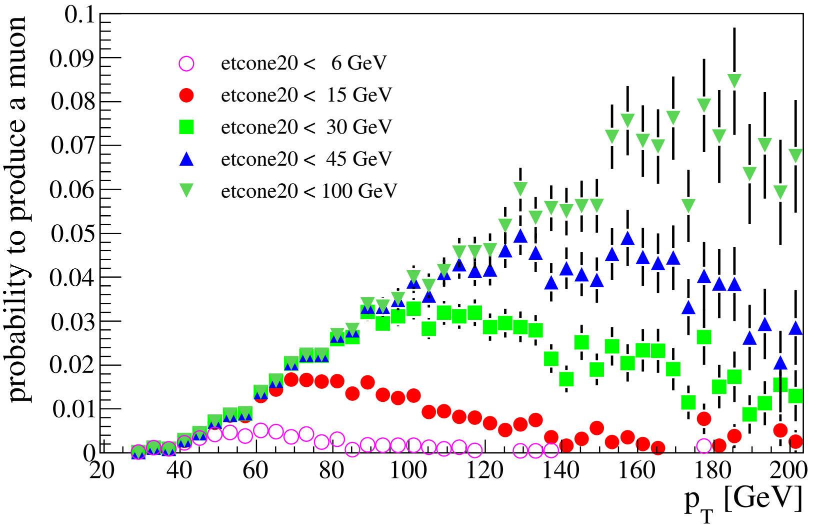

Figure 4.7: *Probability of a b-parton to produce an isolated muon as a function of b-parton p_T for different isolation cuts.*

The probability for the non-isolated case keeps rising with rising p_T which means that a more energetic *b*-parton is more likely to produce a high-p_T muon. This is exactly what one would expect from Figure 4.2 (right), where the same probability was plotted for a true muons with $p_T > 20$ GeV. The only difference between the two plots is the reconstruction efficiency.

Fit of the probability distribution

We use a smooth parametrization of the probability plots to make predictions to other topologies. It turns out that a Landau fits the distribution for b-partons well, see Figure 4.8 (left).

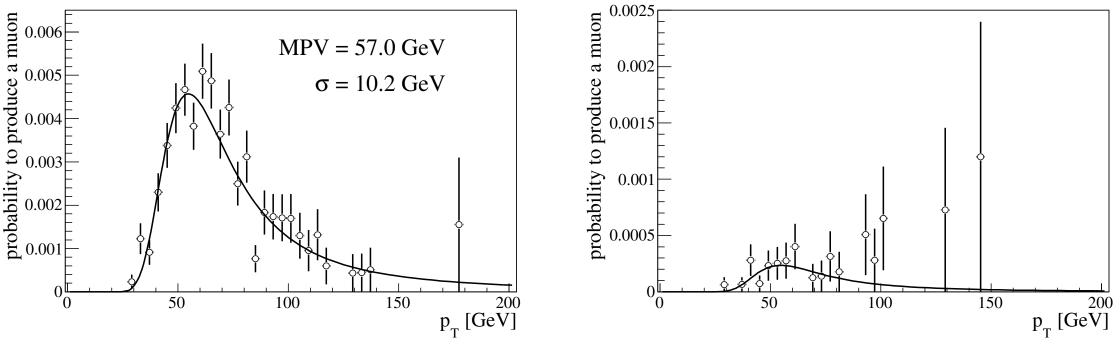

Figure 4.8: *Probability of a parton to produce an isolated muon with $p_T > 20$ GeV as a function of parton p_T fitted with a Landau: for b-partons (left) and for light partons (right).*

A Landau fit is described by a MPV (most probable value), a σ (the spread of the function) and a normalization factor. The fit yields the results for the b-parton probability (with isolation requirement on the muon) determined from $t\bar{t}(e)$ as quoted in Table 4.3. Since the statistics for muons from light partons or gluons is very small, see Figure 4.8 (right), we use the fit results from the b-parton probability and only vary the normalization. The underlying physical assumption is that the processes for heavy and light partons have roughly the same dependence on $\mathrm{p_T}$. We checked the validity of this by looking for muons that pass the same cuts as before, but lowering the requirement on the $\mathrm{p_T}$ from 20 to 10 GeV, as that increases the statistics in the light parton sample. In Figure 4.9 the probability of a parton to produce an isolated muon with $\mathrm{p_T} > 10$ GeV as a function of parton $\mathrm{p_T}$ is fitted with a Landau for b-partons (left) and for light partons (right). Note that the MPV has shifted from 57.0 GeV to 42.6 GeV by lowering the muon-$\mathrm{p_T}$ cut as partons with a lower $\mathrm{p_T}$ can produce a muon that passes the $\mathrm{p_T}$ cut.

On the right side of this figure the probability for light partons is shown with a fit that was obtained by varying just the normalization (dark line). For comparison also the direct fit of the graph is shown (light line). We thus establish that the light-quark probability can be fitted by using the MPV and σ result from the b-parton fit. This is now applied to the original probability distribution to produce muons with $\mathrm{p_T} >$ 20 GeV. Using the fixed MPV and σ from the b-partons the light parton fit yields: normalization factor $= 1.3\times10^{-3}$, see Figure 4.8 (right). These fit results will be used for the extrapolations to different topologies, by applying the probability function for a parton to produce an isolated high-$\mathrm{p_T}$ muon to a given parton spectrum.

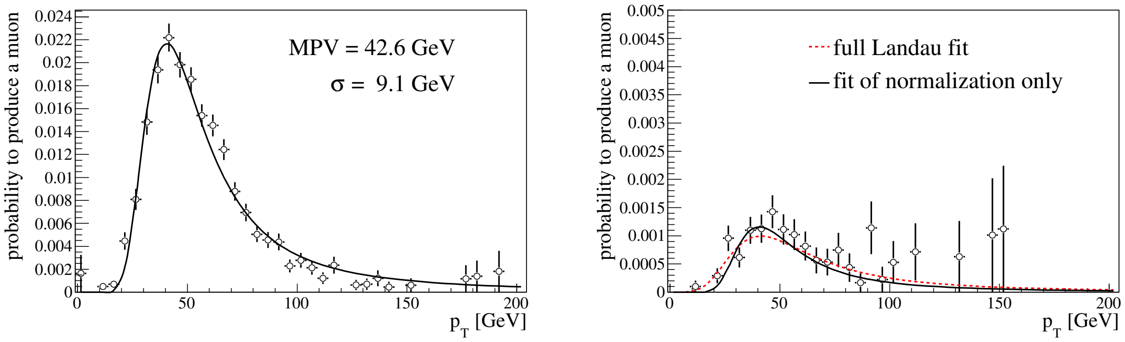

Figure 4.9: *Probability for a parton to produce an isolated muon with $p_T > 10$ GeV as a function of parton p_T fitted with a Landau. Left: for b-partons. Right: for light partons. The dark line is the fit with the fixed MPV and σ from the b-parton fit. Light line is a direct fit.*

	MPV	σ	normalization
b-parton	57.0 ± 1.0	10.2 ± 0.7	$(2.5 \pm 0.2) \times 10^{-2}$
light parton	fixed	fixed	$(1.3 \pm 0.3) \times 10^{-3}$

Table 4.3: *Landau fit results for the probability of a parton to produce an isolated high-p_T muon.*

4.3.3 Dependence of non-prompt muons on the originating parton η

Since the detector coverage in η is not fully uniform for muons, see Section 2.2.4, there might be a strong η dependence in the probability to reconstruct extra isolated high-p_T muons. Especially in the region around $|\eta| = 1.5$, the crack region, the calorimeter coverage is limited, see Section 2.2.3, and at that position it is harder to measure the energy deposition around the muon. The η distribution for the non-prompt and fake muons was shown in Figure 4.4 (right). More insightful and useful, as was done for the p_T spectrum, is the probability plot Figure 4.10 of b-partons to produce an isolated high-p_T muon versus η of the originating b-parton.
The probability distribution can effectively be modeled by a flat distribution.

4.3.4 Dependence of the extra muon rate on jet multiplicity

The probability to reconstruct an isolated high-p_T muon might also depend on the number of reconstructed jets in the event, i.e. the jet multiplicity. One might expect a priori that in events with more jets it will be less likely that the muon is isolated because there will simply be less phase space not occupied by other objects for the muon in the detector. Another reason to study jet-multiplicity dependence is that $t\bar{t}$ events and

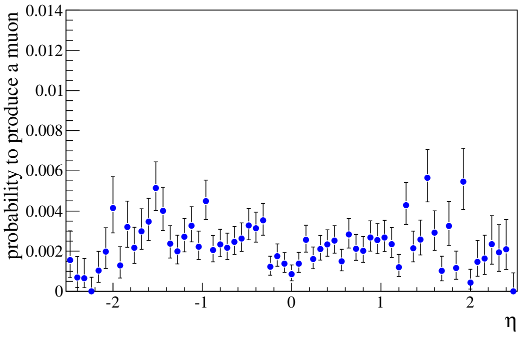

Figure 4.10: *Probability of a b-parton to produce an isolated muon as a function of b-parton η.*

QCD events will differ in their jet topology. Since top-quark pair events feature a large range of jet multiplicities, see Section 3.3, one can study this dependence in detail on $t\bar{t}$ samples.
For this specific study the sample has been divided according to the number of jets per event that pass all jet selection criteria as described in Section 3.2. In Table 4.4 the non-prompt muon rate **per event** as a function jet multiplicity in the $t\bar{t}(e)$ channel with and without isolation requirement is shown.

	non-prompt rate per event $\cdot 10^{-5}$	
	with isolation requirement	without isolation requirement
3 jets	528 ± 43	3985 ± 117
4 jets	487 ± 34	4606 ± 104
5 jets	416 ± 37	4853 ± 124
6 jets	353 ± 50	4981 ± 185
7 jets	442 ± 96	5324 ± 326

Table 4.4: *Non-prompt muon rate per event as a function of jet multiplicity in the $t\bar{t}(e)$ channel with and without isolation requirement.*

Table 4.4 seems to suggest that the isolated non-prompt rate per event drops when going to higher jet multiplicities. A straight line fit ($y = p_1 \cdot x + p_0$) to a set of 10,000 MC pseudo-experiments that assume a constant dependence with the jet multiplicity and errors equal to those in Table 4.4 result in a p_1 greater or equal to that in our fit in only 3% of the cases. Our straight line fit gives a linear coeficient of $(-47.5 \pm 17.8) \cdot 10^{-5}$ and has a χ^2 of 1.81 for 3 degrees of freedom (61% χ^2 probability). In the following we will assume a linearly decreasing rate with increasing jet multiplicity [123]. In addition to reduced available space in the detector there are more effects that contribute to this behaviour. The different effects are studied in detail in this section.

Check: non-prompt muons from *b*-partons

To disentangle the effects that contribute to the rate of non-prompt muons, the rate originating from b-partons per event and eventually from b-partons per b-jet is extracted. As there are always exactly two hard b-quarks in a $t\bar{t}$ event, one would a priori expect that the rate of non-isolated non-prompt muons per event from b-partons is independent of the number of jets reconstructed. This is however not the case as is clear from Table 4.5 where the non-prompt muon rate from b-parton per event as a function jet multiplicity in the $t\bar{t}(e)$ channel with and without isolation requirement is shown.

	non-prompt rate per event **from b** $\cdot 10^{-5}$	
	with isolation requirement	without isolation requirement
3 jets	492 ± 42	3664 ± 112
4 jets	446 ± 33	4300 ± 100
5 jets	389 ± 36	4421 ± 119
6 jets	338 ± 49	4499 ± 176
7 jets	421 ± 94	4861 ± 312

Table 4.5: *Non-prompt muon rate from b-parton per event as a function jet multiplicity in the* $t\bar{t}(e)$ *channel with and without isolation requirement.*

The increase can be explained by the fact that the higher the jet multiplicity the higher the number (on average) of reconstructed high-p_T b-jets (and thus high-p_T b-partons). The average number of reconstructed b-jets per jet multiplicity is shown in Figure 4.11 (left). We therefore expect that the rate of muons per reconstructed b-jet is independent on the jet multiplicity. In Figure 4.11 (right) the number of non-prompt muons without isolation cut from b-partons per b-jet is shown as a function of jet multiplicity. Here the first bin is normalized to 1 and the prompt, matched muon rate from $t\bar{t}(\mu)$ is also plotted per event as reference. The non-prompt muon rate without isolation requirement from b-partons per b-jet is indeed constant.

It has been shown that the non-prompt rate without isolation requirement from b-partons per reconstructed b-jet is constant versus jet multiplicity, as expected. This means that once the b-jet spectrum of a certain sample is know, the spectrum of extra high-p_T muons can be derived. In the next paragraph the decrease in the isolated non-prompt rate from b-partons will be investigated.

Effect of reduced phase space: prompt versus non-prompt muons

After having checked that the non-isolated muon rate from b-partons per b-jet is constant, this section concentrates on the understanding of the isolated case. As mentioned in the introduction to this section, it is clear that with increasing jet multiplicity the detector occupancy increases. This is however not the main cause of the decrease of extra muon rate when requiring isolation. This is clear when the prompt and non-prompt rates are compared as a function of the jet multiplicity. If the busier environment in the

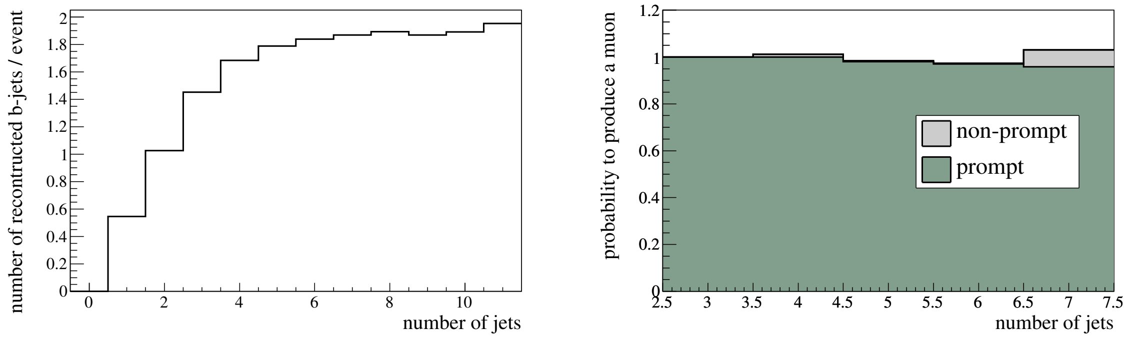

Figure 4.11: *Left: number of b-jets per event per jet multiplicity. Right: non-prompt rate without isolation cut from b-partons per b-jet (light) and the prompt matched rate per event (dark) as a function of jet multiplicity.*

detector would be the main cause of the decreasing non-prompt rates, the same decrease should be observed in the prompt rates. In Table 4.6 the rates are shown for both muon types relative to that in 3 jet events (the rate in 3 jet events has been normalized to 100%).

	rate in percent per event	
	prompt	non-prompt
3 jets	100	100
4 jets	99.9 ± 0.46	90.6 ± 10.2
5 jets	98.4 ± 0.52	79.1 ± 9.9
6 jets	97.4 ± 0.70	68.8 ± 11.6
7 jets	95.9 ± 1.2	85.6 ± 20.4

Table 4.6: *Prompt matched muon rate per event in the $t\bar{t}(\mu)$ channel and non-prompt muon rate from b-partons in the $t\bar{t}(e)$ channel as a function of jet multiplicity relative to that in 3 jet events. The 3 jet bin is normalized to 100%.*

The muon rates as function of the jet multiplicity drop much less for prompt muons than for the extra muons. The reason for the enhanced decrease in the non-prompt rates in events with more jets is related to the way in which they are produced and will be explained in the following section.

Difference in extra energy around the non-prompt muon

There is an extra effect that causes non-prompt muons to be less isolated in multi-jet events than prompt muons: there is more often another jet close-by. Non-prompt muons (from *b*-partons) are produced inside jets, i.e. they are generally close to jets. This fact does however not explain the enhanced decrease with more jets in the event compared to prompt muons. For this one more ingredient is needed: when going to higher jet multiplicities the extra jets originate from QCD radiation and are preferentially close to the parton they radiated from [29]. These extra jets are then also close to the non-prompt muon and will cause the muon to be non-isolated. The minimum distance of the muon to the second closest jet, a measure for the energy around the jet-cone, is shown in 4.12 (left) for events with four selected jets for prompt and non-prompt (from b-parton) muons. It can be seen that the non-prompt muons are on average closer to a second jet than the prompt muons. The faster decrease is best illustrated by Figure 4.12 (right) where the relative number of events surviving a certain dR cut (here 0.9) to the second closest jet is shown of prompt muons and non-prompt muons for different number of jets in the event. In the plot fractions are normalized such that the prompt fraction is always one.

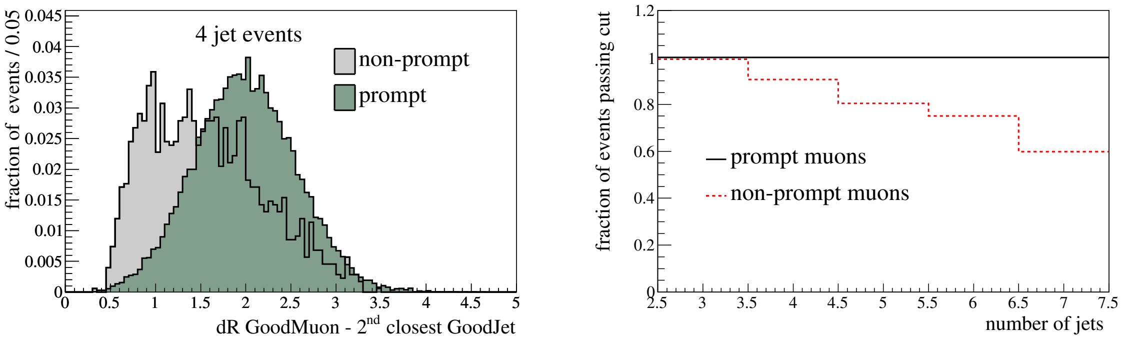

Figure 4.12: *Left: minimal distance to second closest jet for prompt high-p_T muons (dark) and non-prompt high-p_T muons (light) in events with four selected jets. Right: fraction of events after cutting on dR=0.9 to second closest jet for prompt muons (dark) and non-prompt muons (light). The fractions are normalized so that they are equal to one for the prompt muons.*

In Figure 4.12 (right) it can clearly be seen that the non-prompt fraction decreases faster when more jets are reconstructed in the event. This is the reason why the non-prompt rate for higher number of jets per events decreases more rapidly than the rate for prompt muons.

The jet multiplicity is of importance in the production of non-prompt muons. It has been shown that more jets in the event decrease the probability to find an isolated high-$\mathrm{p_T}$ muon from b-partons. This is not only due to the higher detector occupancy, but mainly caused by the production of these muons inside jets.

4.3.5 Trigger

Since the selection of events used for the $t\bar{t}(\mu)$ analysis relies on the single muon trigger, see Section 3.3, it is important to understand how many of the extra muons pass the event filter (EF) trigger requirement. For the study in this chapter the `EFmu15` trigger was investigated, which triggers on muons with $\mathrm{p_T}$ over 15 GeV. In Table 4.7 the number of extra muons in the $t\bar{t}(e)$ channel before and after EF trigger is shown.

	before EF	after EF
all extra muons	630	438
non-prompt muons	623	437
fake muons	7	1

Table 4.7: *Number of extra muons in 129,867 $t\bar{t}(e)$ events before and after event filter (EF) trigger selection.*

There are almost no fake muons left and also the non-prompt are decreased by about 30%. This decrease is caused by two main effects: the trigger efficiency is not 100% even for prompt muons, see Section 3.1 and the trigger has an implicit isolation cut which rejects muons that have some energy around them. The isolation cut of the trigger is in a sense complementary with the (absolute) isolation cut used in the offline selection.

4.4 Extrapolation to different topologies

As discussed in Section 4.1 it is important to see if the understanding of the dependence of the production rate of non-prompt muons on $\mathrm{p_T}$, η or jet multiplicity can be used to predict the extra muon rates in topologies different from semi-leptonic $t\bar{t}$. In this section the reach of the prediction possibilities will be tested by predicting the extra muon rate in a different event type close in topology to semi-leptonic $t\bar{t}$ (fully hadronic $t\bar{t}$) and by studying the characteristics of the extra muons in an event type far away in topology (QCD). The first step is to predict the number and spectrum of non-prompt muons in the fully hadronic $t\bar{t}$ channel. In Section 4.4.2 a large QCD sample is studied.

4.4.1 Fully hadronic $t\bar{t}$

The event type that closely resembles semi-leptonic $t\bar{t}$ events is fully hadronic $t\bar{t}$. The main difference between the two is that the high-$\mathrm{p_T}$ prompt lepton and neutrino are replaced by two light partons, see Figure 1.7. On average one more good light jet is reconstructed in the event, since the reconstruction efficiency is not 100% and not all the light partons from the W-boson pass the 20 GeV jet cut. In Figure 4.13 the transverse momentum distribution for light jets (light) and b-jets (dark) in fully hadronic $t\bar{t}$ are shown.

Predicting the extra muon rate

The idea of the method is to use the understanding of the $\mathrm{p_T}$ dependence on the production of muons to predict the non-prompt muon spectrum from a given jet spectrum. The reason to only use the $\mathrm{p_T}$ dependence is that the η dependence is flat, as has been

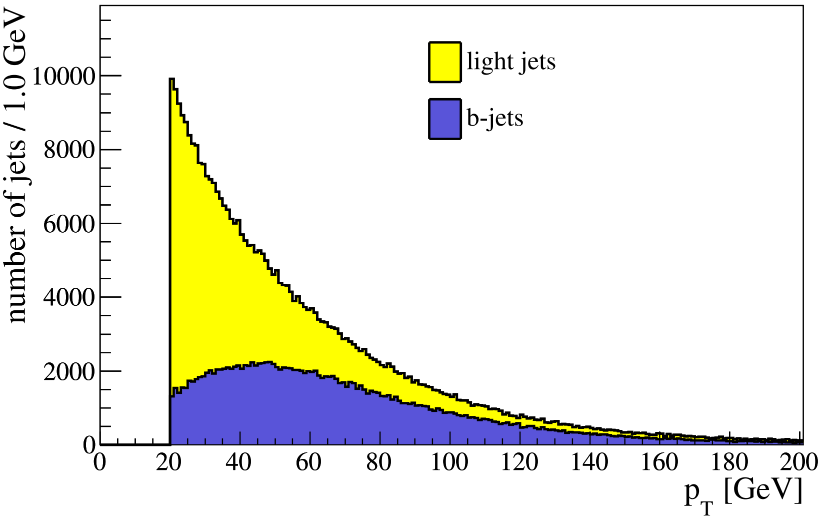

Figure 4.13: *Transverse momentum distribution for light jets (light) and b-jets (dark) in fully hadronic $t\bar{t}$.*

shown in Section 4.3.3, and the jet multiplicity is an understood effect, but hard to parametrize. From the results obtained in this section, just using $\mathrm{p_T}$ is a good first order approximation. The following steps have to be taken to arrive at a prediction for the rate and $\mathrm{p_T}$ spectrum of non-prompt muons. They will be explained in more detail below:

- Step 1: obtain the (b) jet $\mathrm{p_T}$ spectrum in the fully hadronic $t\bar{t}$ channel, see Figure 4.13.
- Step 2: translate the (b) jet $\mathrm{p_T}$ spectrum into a parton $\mathrm{p_T}$ spectrum by the transfer function, as obtained from semi-leptonic $t\bar{t}$.
- Step 3: use the Landau fitted probability functions from the previous section, see Figure 4.8, to get the spectrum of (b) partons that produce an isolated high-$\mathrm{p_T}$ muon.
- Step 4: use a 2-dimensional distribution of the muon-$\mathrm{p_T}$ versus the (b) parton-$\mathrm{p_T}$ obtained from semi-leptonic $t\bar{t}$ to arrive at a $\mathrm{p_T}$ distribution for non-prompt muons.

With these steps we are able to predict the $\mathrm{p_T}$ spectrum of muons in other topologies.

Prediction for muons from b jets

From the previous section one can predict the muon spectrum from a given parton spectrum in $\mathrm{p_T}$ making use of the fitted probability functions, Figure 4.8. Predicting the non-prompt muons spectrum from a given jet spectrum can not be directly done, since the muons are generally not close to their originating jet as was shown in Figure 4.5. The missing link is a transfer function from a given jet spectrum to a parton spectrum: **Step 2**. Using the semi-leptonic $t\bar{t}(e)$ events as baseline, one can divide the b-parton spectrum by the b-jet spectrum, see Figure 4.14 (left) and obtain exactly that correction function see Figure 4.14 (right). The shape and height of this function is due to two effects: a shift in $\mathrm{p_T}$ (reconstructed jets have often lower $\mathrm{p_T}$ than the parton they originated from) and the fact that some jets are simply not reconstructed.

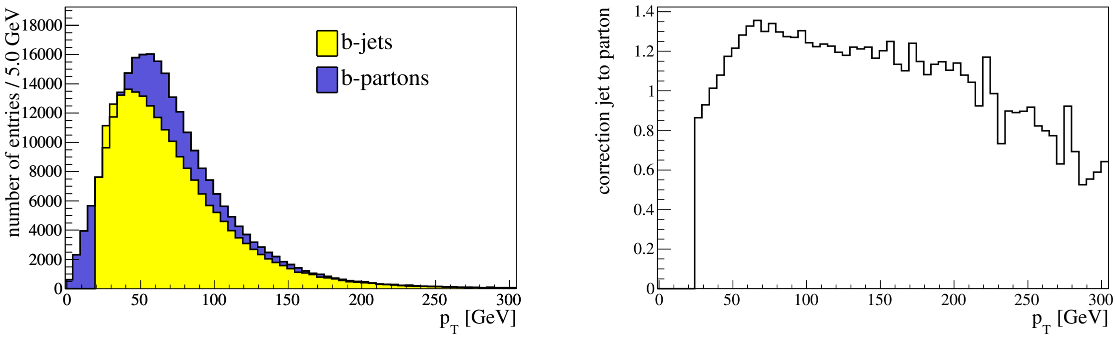

Figure 4.14: *Left: p_T of b-partons (dark) and b-jets (light). Right: transfer function in p_T to go from jets to partons.*

As a proof of principle one can use the b-jet distribution from the fully hadronic sample and the correction function given above to predict the spectrum of the b-partons in this sample. The predicted spectrum of transverse momentum for b-partons is shown in Figure 4.15 (left).

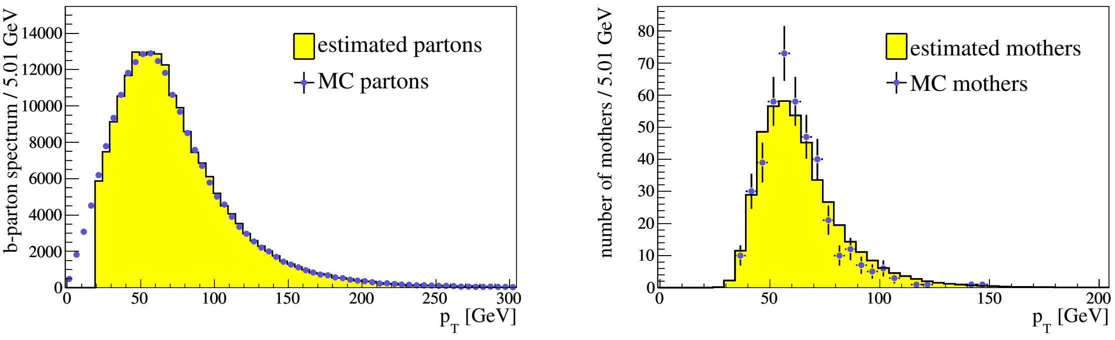

Figure 4.15: *Left: p_T of b-partons (dark) and estimated spectrum (light). Right: p_T of b-partons that produce a muon (dark) and estimated spectrum (light).*

The measured and estimated spectra in Figure 4.15 (left) are in good agreement. That there is no prediction for partons below 20 GeV is clear: the jet selection only passes jets with $\mathrm{p_T}$ above that value. **Step 3**: from b-partons to b-partons that produce a muon. The next step is to use the predicted b-parton spectrum and the fitted probability curves shown in Section 4.3.2 to compute the $\mathrm{p_T}$ spectrum of the b-partons that will produce an isolated high-$\mathrm{p_T}$ muon, called muon-mothers. The result is shown in Figure 4.15 (right) where it is compared to the true spectrum from $t\bar{t}$ fully hadronic events.

Step 4: the last step needed to predict a muon spectrum in $\mathrm{p_T}$ from b-jets is to translate from the $\mathrm{p_T}$ spectrum of the mothers to that of the actual muon. This is done by using a 2-dimensional distribution of muon $\mathrm{p_T}$ versus b-parton $\mathrm{p_T}$, shown in Figure 4.16 (left). Since what is needed from this plot is only kinematics of how muons are produced in b-quark decay, no isolation cut on the muons was applied. This was done to increase the statistics of the plot. Knowing what the $\mathrm{p_T}$ distribution is of a muon produced by a b-parton with a given $\mathrm{p_T}$, one can construct the final muon $\mathrm{p_T}$ spectrum. In Figure 4.16 (right) the $\mathrm{p_T}$ of non-prompt muons from b-partons (dark) and the estimated spectrum (light) is shown. It can be seen that the prediction is a bit higher than the actual measured muons. The integral of this distribution gives the number of non-prompt muons. The predicted number of events is compared to the true number in Table 4.8. The comparison is split in muons from b-jets and muons from light jets (see following subsection). The quoted errors are deduced from the fit errors, see Table 4.3, by varying the MPV, σ and normalization factor within their error to find the highest and lowest value of predicted muons. This is a conservative estimate and can be seen as the statistical error. The systematic error is not computed at this point.

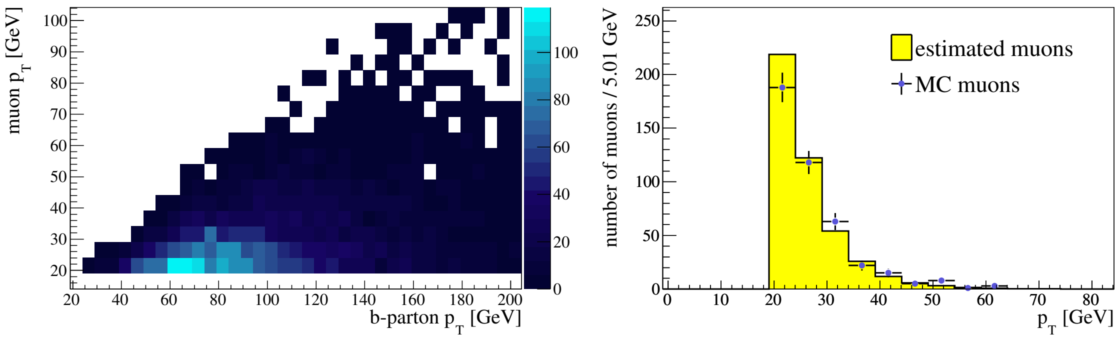

Figure 4.16: *Left: p_T of b-parton versus the p_T of the resulting muon above 20 GeV without isolation requirement. Right: p_T of non-prompt muons from b (dark) and estimated spectrum (light).*

Prediction for muons from light jets

Although the extra muon rate is dominated by semi-leptonic b-decay, there is also a contribution from light jets. One can apply the same procedure to the muons from light partons and gluons. First the light jets spectrum is obtained from the fully hadronic $t\bar{t}$ sample, Figure 4.13. On this spectrum a transfer function similar to the one used

	from b	from light	total
predicted	445^{+61}_{-59}	45^{+15}_{-13}	490^{+63}_{-60}
fully hadronic MC	423	50	473

Table 4.8: *Predicted and MC number of non-prompt muons from b-partons and light partons in the fully hadronic sample.*

for b-jets, Figure 4.14 (right), is used to obtain the predicted light parton spectrum. By multiplying the predicted light parton spectrum with the probability function for a light parton to produce a high-$\mathrm{p_T}$ isolated muon, one obtains a prediction for the light partons that will produce an isolated high-$\mathrm{p_T}$ muon. In Figure 4.17 (left) one can see the predicted and MC spectrum of the partons that will produce a high-$\mathrm{p_T}$ isolated muon. The last step is again, as in the b-jet section, the application of a 2-dimensional plot that correlates parton-$\mathrm{p_T}$ to muon-$\mathrm{p_T}$ to arrive at a predicted $\mathrm{p_T}$ spectrum of muons from light jets. In Figure 4.17 (right) the predicted and MC spectrum of those muons is shown. Prediction and MC are in good agreement.

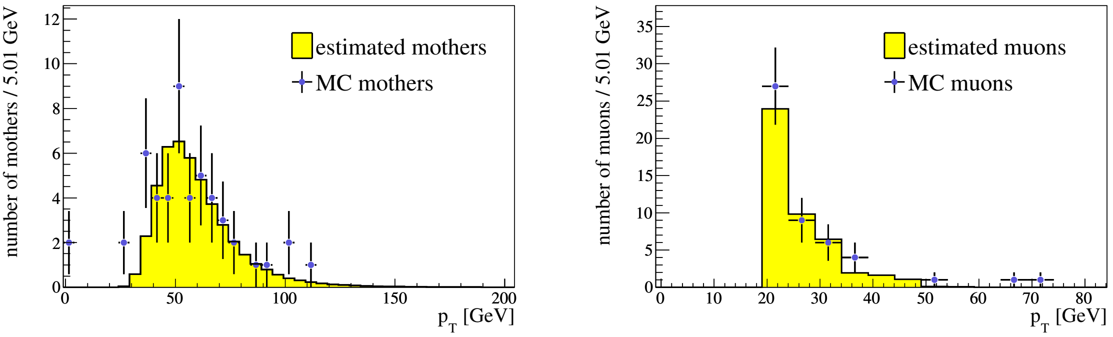

Figure 4.17: *Left: p_T of light partons that produce a muon (dark) and estimated spectrum (light). Right: p_T of non-prompt muons from light (dark) and estimated spectrum (light).*

Summary

The $\mathrm{p_T}$ spectrum of non-prompt muons from b and light partons has been predicted using the (b-) jet spectrum of the fully hadronic $t\bar{t}$ channel as input. Prediction and MC are in good agreement. This is remarkable since one would expect an overestimation due to the higher number of jets in the event. On average a fully hadronic event has one more good jet than a semi-leptonic one. As has been shown in Section 4.3.4 the more jets there are in the event, the less muons will be found.

We have shown that results from the $t\bar{t}(e)$ channel (like the transfer function to translate from jets to partons, probability function in $\mathrm{p_T}$ for a (b) parton to produce an isolated high-$\mathrm{p_T}$ muon and the 2-dimensional plot of (b) parton $\mathrm{p_T}$ versus resulting muon $\mathrm{p_T}$) can be used to make a prediction about non-prompt muons in the fully hadronic $t\bar{t}$ channel. This is done using the (b) jet spectra of the fully hadronic $t\bar{t}$ sample. Since the main goal of this chapter is to understand and estimate the QCD background, the next section will describe the extrapolation to a QCD topology. The QCD event topology is notably different from $t\bar{t}$ topology due to generally lower jet $\mathrm{p_T}$, fewer (hard) b-partons and lower jet multiplicity.

4.4.2 Extra muons in the QCD sample

Even though they have large cross section, most QCD processes will hardly produce any events with more than two hard jets or a high-$\mathrm{p_T}$ lepton. In order to have a manageable sample of events that pass the $t\bar{t}$ jet selection or the high-$\mathrm{p_T}$ isolated muon selection, the events in the QCD sample, see Section 1.4.3, have been pre-selected to contain high-$\mathrm{p_T}$ jets or a high-$\mathrm{p_T}$ muon. This selection efficiency can be as low as $\sim 10^{-3}$. In the following section we will have a look at the extra muons that are reconstructed in this sample and their characteristics.

Breakdown of extra muons

The events in the QCD sample are weighted to compensate for the difference in available statistics between different event types, as explained in Section 1.4.3. These weights are either 2, 1 or 0.3. The whole sample consists of events that fired at least one of the muon triggers. The Monte Carlo statistics in the muon stream is 1,367,739 unweighted events, which translates into 1,121,731 weighted events. The number and origin of extra muons in the QCD sample normalized to represent 10 pb^{-1} is shown in Table 4.9.

	Extra muons	
origin	non-prompt	fake
b-quark	24996	
c-quark	10950	
light q/ g	2836	
unknown		133
total	38782 (99.7%)	133 (0.3%)

Table 4.9: *Number and origin of extra muons in QCD, normalized to represent 10 pb^{-1}.*

The composition of the non-prompt muons is not surprising: most of the muons come from a b-quark. That there is relatively quite a large number that originates from a light quark is due to the relative small fraction of b-jets in QCD. Even in this preselected sample there are more than five times more light jets than b-jets.

Characteristics of extra muons

In this section the main characteristics of the extra muons will be studied. Figure 4.18 shows the $\mathrm{p_T}$ (left) and η (right) distributions of non-prompt (light) and fake muons (dark) in the QCD sample. Both plots are normalized to represent an integrated luminosity of 10 pb^{-1}.

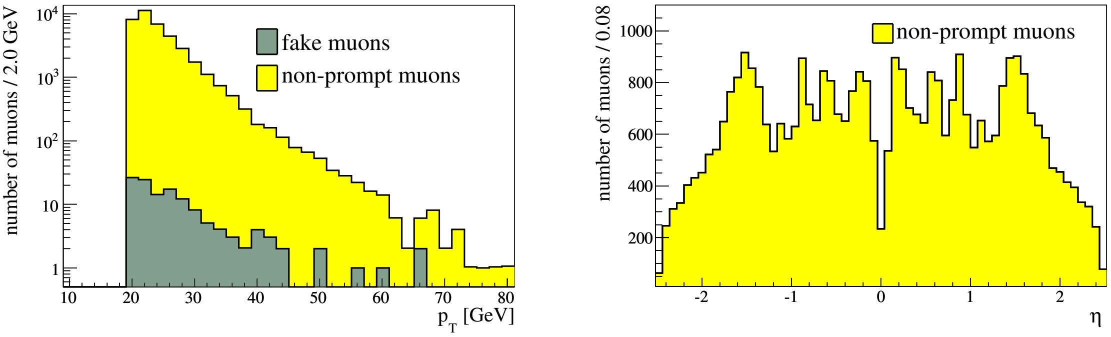

Figure 4.18: *Left: p_T of non-prompt (light) and fake muons (dark) in the QCD sample. Right: η of non-prompt (light) and fake muons (dark) in QCD sample. Both plots are normalized to represent 10 pb^{-1}.*

Both the η and $\mathrm{p_T}$ distribution have the same main features as the ones shown in the beginning of this chapter for muons in $t\bar{t}(e)$, see Figure 4.4: a steeply falling function in $\mathrm{p_T}$ and a distribution without remarkable features in η. As has been mentioned in the previous sections, there are two main distributions that separate prompt muons from extra muons: their distance to jets and their isolation energy. In Figure 4.19 (left) the normalized distribution of the minimal distance to the nearest jet (dR) for prompt muons in $t\bar{t}(\mu)$ (dark) and extra muons in QCD (light) is shown normalized. Note that there is a small peak near dR = 0.1 for the prompt muons. These are events in which the muon actually fakes an accompanying jet.

The reason that there are so many extra muons (~66%) *not* close to a jet (dR > 0.2) is simply because these are only the jets that pass all jet selection criteria. Often, when a heavy meson produces a high-$\mathrm{p_T}$ muon, the remaining meson cannot form a jet with $\mathrm{p_T} > 20$ GeV and will not make it into the plot. This also explains the peak around 3 for the extra muons: most of the QCD events are di-jet events and when the jet the muon originates from is lost, the next closest will be almost back to back with the muon. We expect non-prompt muons to be less likely isolated than prompt muons. The isolation energy ($\mathrm{E_T^{dR=0.20}}$) is shown in Figure 4.19 (right) after all other muon cuts for prompt muons in $t\bar{t}(\mu)$ (dark) and extra muons in QCD (light), normalized.

Comparing the rate of muons

It is hard to compare the rates of extra muons between the semi-leptonic $t\bar{t}$ sample, the fully hadronic $t\bar{t}$ sample and the QCD sample. The difficulty is caused by the pre-

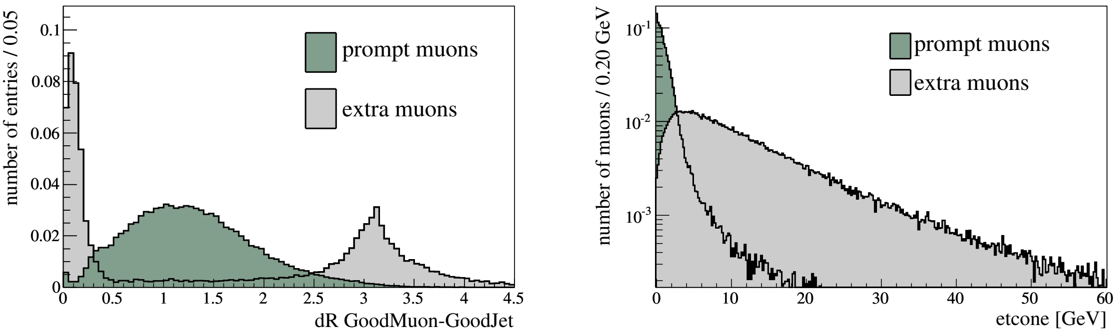

Figure 4.19: *Left: minimal distance to nearest jet (dR) for prompt muons in* $t\bar{t}(\mu)$ *(dark) and extra muons in QCD (light) normalized. Right: the* $E_T^{dR=0.20}$ *distribution after all other muon cuts for prompt muons in* $t\bar{t}(\mu)$ *(dark) and extra muons in QCD (light), normalized.*

selection of the QCD sample. The definition of muon rates per originating jet is not feasible after pre-selection since the events have been preselected to contain a true muon with $p_T > 10$ GeV and will thus also contain most likely a high-p_T b-jet. Due to this high-p_T b-jet biased feature it is not possible to scale the jet spectrum back to the true QCD cross sections.

4.5 Summary

This chapter was intended as a background study on the extra muons that can be found in QCD (multi-jet) events. We have studied the extra muons in $t\bar{t}(e)$ first to get a feeling for how muons are produced in events that contain multiple jets. It has been shown that the majority of the extra muons are non-prompt muons originating from semi-leptonic b-quark decay. We have studied their characteristics and shown that we understand them well enough to predict their p_T-spectrum from the jet spectrum in the fully hadronic $t\bar{t}$ sample. Also the origin of extra muons in a large $\sqrt{s} = 10$ TeV QCD multi-jet sample (9.6 pb^{-1}) has been investigated. As expected, also these muons are dominated by non-prompt muons originating from b-quark decays. In the next chapter we will test two existing data-driven methods to estimate the amount of QCD background after selecting top-quark events.

CHAPTER 5

DATA-DRIVEN QCD BACKGROUND DETERMINATION METHODS

In the previous chapter we mainly focused on the understanding of extra muons in $t\bar{t}$ like topologies. We have seen that most of these muons are non-prompt muons originating from semi-leptonic b-decay. The study was done on Monte Carlo, using truth information. In this chapter we will focus on data-driven methods to estimate the amount of QCD events that pass the $t\bar{t}$ cuts and especially the isolated muon cut, see Chapter 3. We explore two different methods from literature to achieve this goal [126]. This study has been performed on the $\sqrt{s} = 10$ TeV MC samples and serves as background to the method we will develop in Chapter 7 for the $\sqrt{s} = 7$ TeV data taken in 2010.

In Section 5.1 we present the strategy to do a data-driven estimation. Hereafter, in Section 5.2, we will show the input distributions that we use. Sections 5.3 and 5.4 will explain in detail the two methods. The results will be summarized in Section 5.5.

5.1 Strategy

We present two data-driven methods to estimate the QCD content after all the $t\bar{t}$ selection cuts [126]. Note that we will use selections close to the base selection presented in Section 3.3.1 and not the two extra requirements presented there (Sections 3.3.2 and 3.3.3), nor will we use the overlap removal of muons that are close to jets. The reason for this is that we want to make use of distributions of non-isolated muons originating from QCD to extrapolate into the isolated signal region. The overlap removal of muons to jets works like an isolation cut and leaves us with too little statistics in the non-isolated region. The first method is called the *ABCD method* and makes use of two uncorrelated observables in four regions of their two-dimensional phase space. We construct the regions such that only one of the regions is dominated by signal and the information of the other three is used to estimate the background contribution in the signal region. The second method, the *fit method*, is based on the observation that the isolation of muon tracks is very different for signal muons compared to QCD muons. This information is used to fit the isolation distribution in a QCD dominated region and extrapolate into the signal region. Both methods rely on the fact that there is an observable that behaves differently for signal and background and that one can find a region for that observable that is dominated by background.

5.2 Input distributions

In order to separate signal and QCD-background we need observables that differ between the two. In Chapter 4 we have seen and studied the distributions of some of these observables. The main differences were seen in the isolation of the muons and their distance to the closest jets. However, in order to use the ABCD method in its simplest form (described further in Section 5.3) the distributions used have to be uncorrelated. This is not the case for the isolation of a muon and its distance to the closest jet. Instead we exploit another variable which represents our knowledge that the extra muons mainly come from semi-leptonic *b*-decays: the impact parameter significance. We investigate both the muon isolation and the muon impact parameter significance in more detail.

5.2.1 Absolute isolation and relative isolation

Until now we have used the absolute isolation of a muon. The two methods to estimate the QCD contribution in a data-driven way that we will explore in this chapter, have however been developed using a relative isolation: $\mathrm{E_T^{dR=0.20}/p_T}$ [1]. In Figure 5.1 the relative isolations is shown for prompt muons in $t\bar{t}(\mu)$ and for the muons in the QCD sample.

We note that the distribution resembles the one that was shown in the previous chapter, Figure 4.19 (right). To compare the two, the fraction of muons that passes a given cut is shown in Table 5.1. By placing the cut at 0.14 the efficiency for prompt muons is the same as it was for the absolute isolation cut, but with higher rejection for QCD muons. The cut for the relative isolation variable has been put at 0.10. It can be seen that cutting at 0.10 on the relative isolation yields a little lower signal efficiency, but also a much higher background rejection.

	rejection of muons	
	prompt muons	extra muons
$\mathrm{E_T^{dR=0.20}} < 6$ GeV	4%	67%
$\mathrm{E_T^{dR=0.20}/p_T} < 0.14$	4%	83%
$\mathrm{E_T^{dR=0.20}/p_T} < 0.1$	6%	90%

Table 5.1: *Percentage of prompt ($t\bar{t}(\mu)$) and extra (QCD) muons that does not pass a given isolation cut.*

---

[1] $\mathrm{E_T^{dR=0.20}}$ is the transverse energy in a cone of dR = 0.20 around the muon.

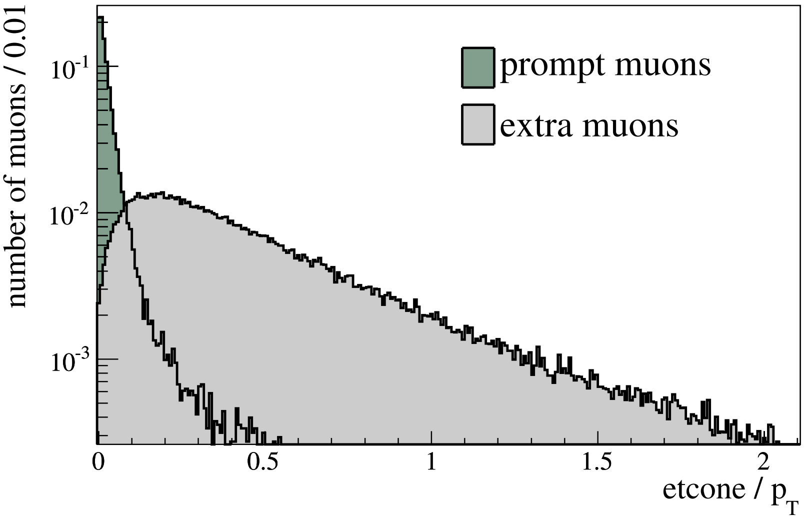

Figure 5.1: *The* $E_T^{dR=0.20}/p_T$ *distribution after all other muon cuts for prompt muons in* $t\bar{t}(\mu)$ *(dark) and extra muons in QCD (light), normalized.*

The isolation variable is clearly a good variable to distinguish signal and background. The reason behind this is the difference in production mechanism for prompt and extra muons, as explained in Chapter 4.

5.2.2 Impact parameter significance

We have shown in the previous chapter that most of the extra muons originate from semi-leptonic b-decay. There is one feature of this type of decay that hasn't been exploited yet: B-mesons live relatively long. The average lifetime of bottom-mesons is of the order of 10^{-12} s, which means they travel on average a few mm before they decay (for a b-jet p_T typical for the $t\bar{t}$ topology of around 60 GeV). This feature is represented in the d0 variable, which is the distance of closest approach in the transverse plane between a track or object and the interaction point, see Figure 5.2 (left). The distance in the transverse plane is used since the boost in the z-direction can be large due to large differences between x_1 and x_2 see Section 1.2. However, due to beam-spot width and displacement most interactions will not be located at the center of the ATLAS coordinate system, but at a primary vertex, that may be displaced from it. The d0 variable that is quoted the rest of this chapter is calculated with respect to this primary vertex (and is sometimes referred to as the corrected d0). In Figure 5.2 (right) the d0 of prompt ($t\bar{t}(\mu)$) and extra (QCD) muons is shown. The distributions are normalized to unity and we note that the QCD muons give rise to a broader distribution.

The error on the d0 of a muon can be quite large and therefore a more powerful discrimination between signal and background can be achieved by using the significance of the d0 parameter, which is defined by: d0 significance = d0/σ(d0). The uncertainty

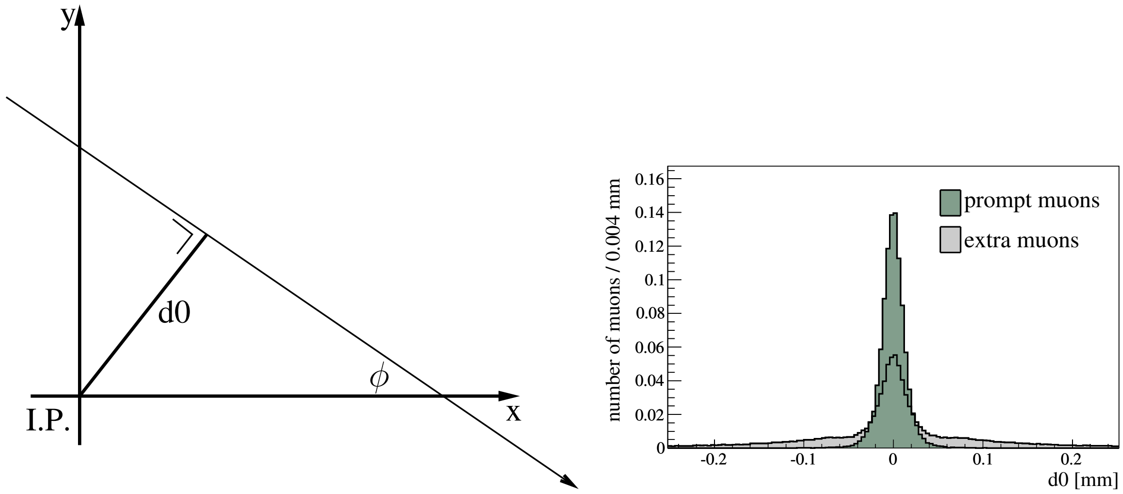

Figure 5.2: *Left: when a track traverses the detector, d0 is defined as the transversal distance to the interaction point (I.P.). Right: the d0 distribution for prompt muons in* $t\bar{t}(\mu)$ *(dark) and QCD muons (light), normalized to unity.*

on the d0 significance ($\sigma(d0)$) is given by the uncertainty that comes directly from the measurement of the d0, but also has to contain the uncertainty on the primary vertex which was used in the calculation of the corrected d0. The full $\sigma(d0)$ definition that we use is given by:

$$\sigma(d0) = \sqrt{\sigma_{d0}^2(\mu) + \sin^2(\phi)\sigma_x^2 + \cos^2(\phi)\sigma_y^2 - 2\sin(\phi)\cos(\phi)\sigma_x\sigma_y}, \tag{5.1}$$

where ϕ is the angle in the transverse plane of the muon track, $\sigma_{d0}(\mu)$ is the uncertainty on the d0 of the muons and σ_x (σ_y) the uncertainty on the x (y) parameter of the primary vertex. The $\sigma_{d0}(\mu)$ and the σ_x/σ_y are of the same order of magnitude, but due to the angle ϕ terms in Equation 5.1, the uncertainty on the d0 of the muon is the dominant source of the uncertainty of the $\sigma(d0)$ parameter. In Figure 5.3 the d0 significance of both prompt muons in $t\bar{t}(\mu)$ (dark) and QCD muons (light) is shown. We observe that prompt muons have a steeper peak at low values.

Both the impact parameter significance and the relative isolation are variables to distinguish between signal and QCD background. Note that the background that we consider here is only QCD. Muons from W+jets or other top channels will in these distributions end up in the signal region since the muons are in principle prompt muons (from a W) and cannot be distinguished from the muons in $t\bar{t}(\mu)$. Those backgrounds have to be determined with other methods, as was discussed in Section 3.3.

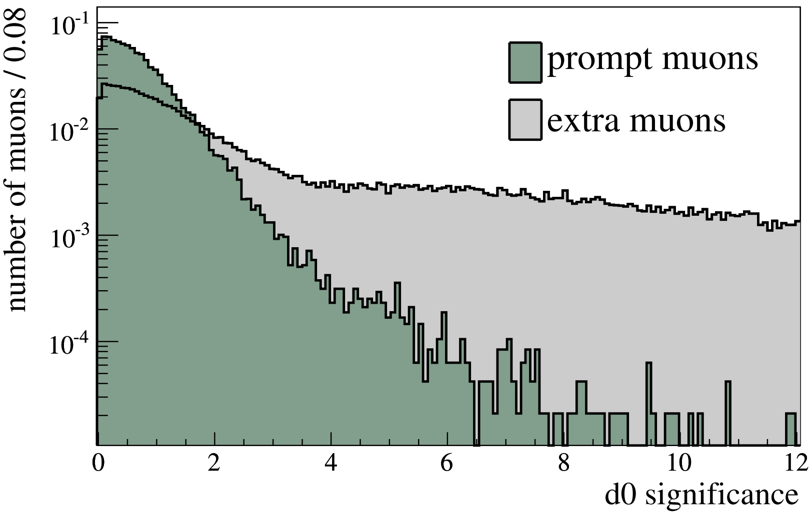

Figure 5.3: *Impact parameter significance (d0 significance) for prompt muons in* $t\bar{t}(\mu)$ *(dark) and QCD muons (light), normalized to unity.*

5.3 ABCD method

The ABCD method relies on the fact that one has two independent distributions to distinguish between signal and background. We have shown in the previous section that the impact parameter significance (d0 significance) and the relative isolation are powerful variables to distinguish between prompt and non-prompt muons. In Figure 5.4 the d0 significance versus relative isolation (after all other muon cuts and shown for events with 2 jets) is shown, where we divided the distribution in four boxes. The boundaries of these boxes are chosen such that C is the signal region or put differently: all other regions should be signal free. This is ensured also by not letting the boxes connect. The choice of the boundaries for the relative isolation is on the one side the normal cut-value of 0.1 and on the other side a larger value where no prompt muons should be found: 0.15, see Figure 5.1. For the d0 significance boundaries the same arguments hold: a lower one at 3 since almost all signal will be contained within, see Figure 5.3 and a higher one to have a signal-free region. Thus the four boxes are defined as:

$$
\begin{array}{llll}
\mathrm{A:} & \text{d0 significance} < 3 & \text{relative isolation} & > \; 0.15 \\
\mathrm{B:} & \text{d0 significance} > 5 & \text{relative isolation} & > \; 0.15 \\
\mathrm{C:} & \text{d0 significance} < 3 & \text{relative isolation} & < \; 0.10 \\
\mathrm{D:} & \text{d0 significance} > 5 & \text{relative isolation} & < \; 0.10
\end{array}
$$

If the two assumptions mentioned here hold (the distributions are independent and regions A,B and D are signal muon free) then the ratio of the content of A and C should be equal to B and D (also A/B and C/D should be equal, the system is over constrained).

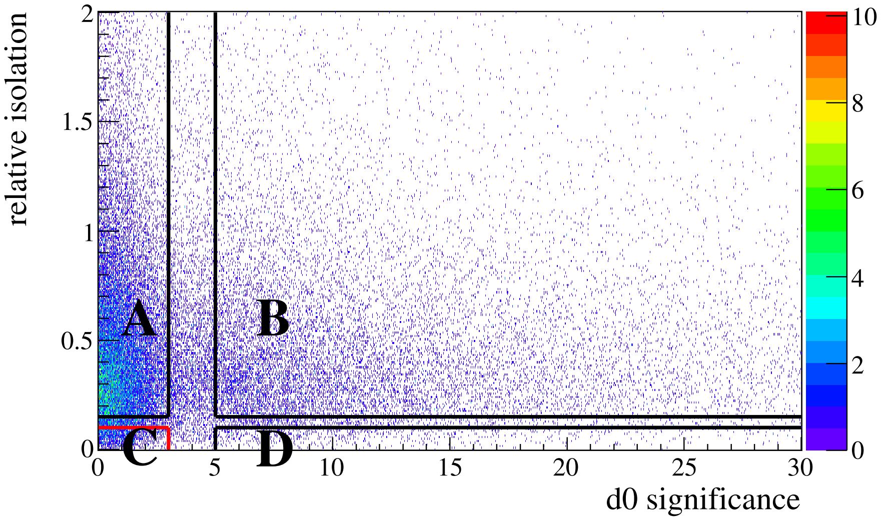

Figure 5.4: *The d0 significance versus the relative isolation distribution after all other muon cuts for muons from* $t\bar{t}$ *, QCD, W+jets and single top in 2 jets events.*

The above explanation leads to the simple expression:

$$\mathrm{C} = \mathrm{A} \cdot \frac{\mathrm{D}}{\mathrm{B}}, \tag{5.2}$$

where C is the number of QCD events in the region where we expect $t\bar{t}$ to end up. We can thus calculate the number of QCD events that will pass all our $t\bar{t}$ selections and will be mistaken for signal.

5.3.1 Independent distributions

We can check that these distributions are indeed independent by looking at the correlation coefficient that is shown for different jet multiplicities in Table 5.2. The correlation coefficient (ρ) of two variables x and y is defined as[2]: $\rho = \frac{<xy> - <x><y>}{\sigma_x \sigma_y}$.
The correlation coefficient lies in the interval [-1,1], where 1 (-1) means that the variables are fully (anti-)correlated. A ρ of zero means that x and y are uncorrelated. As can be seen in the table, the relative isolation and d0 significance are hardly correlated except in two jet events. This means that the assumption of independent variables only holds truly for higher jet multiplicities. Note that the correlation coefficient can be calculated from data and the assumption can thus be tested. The independence of the variables

---

[2] The error on ρ when N is large is given by: $\sigma_\rho = \frac{(1-\rho^2)}{\sqrt{N-1}}$

number jets	ρ
all	0.103 ± 0.003
2	0.139 ± 0.004
3	0.084 ± 0.005
4	-0.002 ± 0.005

Table 5.2: *Correlation coefficient of the relative isolation and d0 significance variable of muons in the QCD sample for events with 2,3 and 4 jets.*

means that the distribution of relative isolation looks the same at any given value of d0 significance (the same is true the other way round). That this is the case can be visualized by plotting the relative isolation in slices of the d0 significance and by looking at d0 significance in slices of relative isolation, see Figure 5.5. The total number of events per slice differs and the plots are normalized to show that they have indeed the same shape.

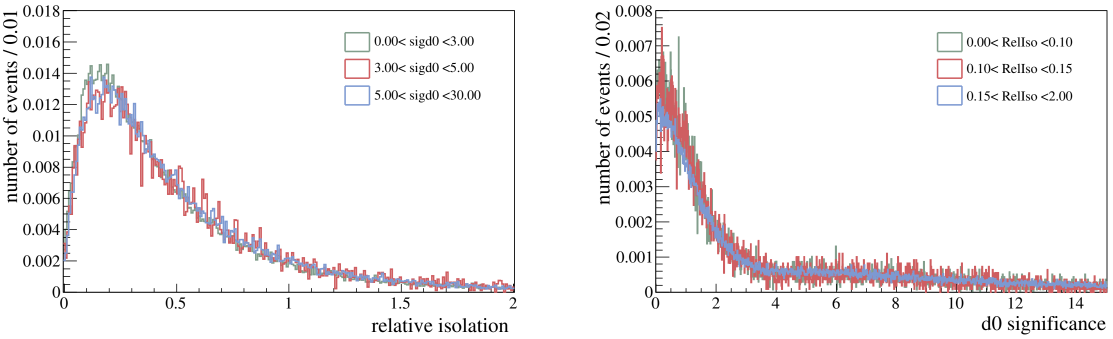

Figure 5.5: *Left: relative isolation of QCD muons after all other cuts in slices of d0 significance normalized to unity. Right: d0 significance of QCD muons after all other cuts in slices of relative isolation normalized to unity.*

This feature is the reasoning behind the method, since if the distribution of one variable is the same for different slices of the other variable then the ratios that we mentioned above should indeed be equal.

5.3.2 Application of the method

If we now count the events from QCD, the other major background samples and the signal samples, we get the results presented in Table 5.3. Here we show the number of events in each region for QCD, signal ($t\bar{t}$ (μ)), W+jets together with single top and total number of events. In the left table this is presented in the case of two jet events, hence the contribution of non-QCD events is low. In the right table the numbers are presented for events that pass all top cuts and we see that region C is now dominated by prompt muons. Note here that the regions A and B are virtually signal free. The region D however contains almost as many signal-like muons (i.e. from $t\bar{t}$, W+jets or single top) as QCD muons. Most of these muons can be traced back to τ decays in $t\bar{t}(\tau)$ or $W(\tau)$ events. This obviously violates the second assumption.

2 jet events					4 jet events + all other top cuts				
	QCD	$t\bar{t}$ (μ)	W+jets, single top	total		QCD	$t\bar{t}$ (μ)	W+jets, single top	total
A	22263.9	1.3	49.7	22318.0	A	1345.7	12.9	8.7	1392.3
B	16497.1	0.7	4.4	16504.1	B	1375.5	6.3	3.2	1416.7
C	1531.3	31.0	2909.5	4504.2	C	12.7	153.9	119.5	311.6
D	982.2	0.1	38.8	1021.7	D	6.5	0.7	2.4	11.9

Table 5.3: *Number of events from different samples per region for 9.6 pb^{-1}. Left: in events with 2 jets. Right: in events that pass all top event selection cuts. Note that $t\bar{t}(\mu)$ is shown separately, but the total includes all other $t\bar{t}$ events.*

If we use the expression for C to predict the number of QCD events in the signal region we get the results show in Table 5.4, where we show the results for various jet multiplicities and on the last row for events after all top cuts.

Jets	QCD predicted	QCD MC
2	1381.6 ± 44.7	1531.3 ± 44.4
3	437.2 ± 23.2	501 ± 22.4
≥4	199.6 ± 15.2	217.4 ± 14.7
all top cuts	11.7 ± 2.6	12.7 ± 3.6

Table 5.4: *Predicted and MC number of QCD events in region C for 9.6 pb^{-1}. First three rows without $\not\!\!E_T$ constraint, last row with all top cuts.*

From Table 5.4 it is clear that the predictions, although too low for the 2 jet case, are very good for the higher jet multiplicity events. The quoted error is only the statistical error and clearly does not reflect the full uncertainty on the prediction. Note that the statistical error here is not $\sqrt{N}$, with N the number of events. This is due to the fact that all samples are scaled down to represent 9.6 pb^{-1} (as the QCD sample) and also the negative weights of `MC@NLO` are taken into account. In order to find the systematic uncertainty that is associated with this method we varied the boundaries of the method. By shifting either the upper bound of the d0 significance or the upper bound of the relative isolation we left the signal region C untouched. By varying these boundaries we evaluated the change in the predicted number of events compared to the baseline prediction. The results are shown in Figure 5.6 where we show the shifted prediction divided by the baseline value. This by construction gives value 1 for the d0 significance at 5 and for the relative isolation at 0.15.

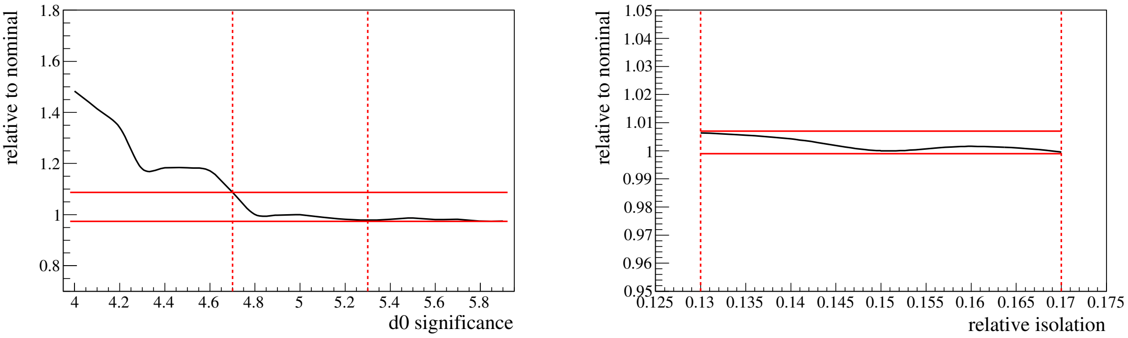

Figure 5.6: *Relative change of the predicted number of QCD events in region C due to change of boundaries. Left: changing d0 significance. The red lines denote what has been taken as systematic uncertainty. Right: changing relative isolation.*

The first thing that has to be noted are the apparent jumps in the plot (left) of the d0 significance. This has been investigated and traced back to single QCD events with high weight migrating from one region into another. This effect is thus due to limited statistics of the sample. The rise however that can be seen is caused by the isolated muons (from signal or other non-QCD background) entering region D. When moving to lower values of the upper d0 significance boundary this is likely to happen more frequently. The nominal value of 5 is on a plateau and thus a good choice. We assigned a systematic uncertainty of +9% and -3% to this systematic corresponding to the change in the prediction when varying the value of d0 significance ±0.3. On the right side, the relative isolation, we note that the prediction is stable with respect to changing the boundary. The change is smaller than 1%. The overall result of this method is then:

$$\mathrm{C} = 11.7 \pm 2.6\ (\mathrm{stat})\ {}^{+1.1}_{-0.4}\ (\mathrm{syst}) \tag{5.3}$$

5.3.3 Conclusion

The ABCD method in its most simple form relies on the use of two independent distributions that can distinguish between prompt and non-prompt muons. We have shown that we can predict the number of QCD events in the signal region with the method. One of the regions however is not prompt muon free (as we assume) and this should ideally be taken into account. Since the system is over constrained one option would be to introduce an efficiency for prompt and non-prompt muons to enter D. This system is then still solvable and accounts for the contamination. One apparent problem of the method at this stage is that we end up calculating the amount of QCD in a region that is not exactly the same as the nominal $t\bar{t}$ selection region. We introduced a new cut: the d0 significance cut. There are good reasons however to use this cut anyway. First of all it removes almost no signal (154 compared to 157 events after all cuts in 9.6 pb^{-1}). Secondly it not only removes QCD muon, it also protects the analysis from cosmic muons since they do not originate from the interaction point. By studying the systematic error associated with varying the boundaries it became clear that shifting towards lower values of the d0 significance parameter the estimation blows up. Since this however can be measured from data and one can put the higher bound at a value where the distribution levels off, see Figure 5.6, this should not be a problem. We will see in Chapter 6 however that the statistics in the early data is too low to use this method, but we will develop a method that is closely related to the ABCD method.

5.4 Fit method: extrapolation of the isolation variable

The second method that we will use to predict the number of QCD events that pass the top event selection uses the shape of relative isolation for muons in QCD events. By measuring the distribution of relative isolation of muons after all other muon cuts and fitting it in a region that contains no signal-like muons (no isolated muons from $t\bar{t}$ or W+jets), we can extrapolate the distribution into the signal region. The integral of this extrapolation below the cut value then estimates the number of QCD events in the top selection. In Figure 5.7 the distribution of relative isolation is shown of all muons that pass all cuts except the isolation cut in two jet events (left) and events that pass all top event selection cuts (right). The samples used here are the QCD samples, W+jets, single top and the full $t\bar{t}$ sample. The fit is performed from 0.1 to 2 and then extrapolated down to the signal region (dark line). For comparison we also show the actual QCD spectrum.

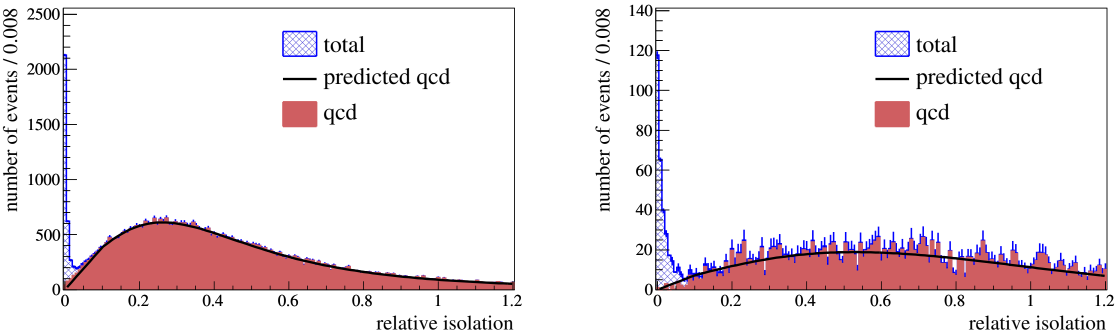

Figure 5.7: *Relative isolation of muons after all other muon cuts for $t\bar{t}$, W+jets, single top and QCD (hashed) normalized to 9.6 pb^{-1}. The black line is the prediction (plus the fit) and the light filled graph the QCD spectrum. Left: in two jet events. Right: events that pass all top-cuts.*

The fit that we use is a Landau-function multiplied by a third order polynomial and the extrapolation uses a straight line from (0,0) to the end-point of the fit. This linear extrapolation was chosen in order to not be too dependent on the exact shape of the isolation distribution in the signal region. We noticed that the shape in Monte Carlo changed when going to higher jet multiplicities between being convex and concave and thus the straight line is a simple and stable average. We can see that indeed above 0.1 there is hardly any signal ($t\bar{t}(\mu)$) or other signal-like isolated muons (the difference between QCD and the total above 0.1 is negligible). The extrapolation yields the numbers as given in Table 5.5, where we show the integral (I) of the extrapolated fit (relative isolation < 0.1) compared to the MC number of QCD events in the region.

Jets	QCD predicted	QCD MC
2	2403.4 ± 203.3	3112.6 ± 55.8
3	852.5 ± 77.5	1057.5 ± 32.9
≥4	468.8 ± 72.1	485.3 ± 22.9
all top cuts	45.3 ± 6.1	34.6 ± 6.2

Table 5.5: *Predicted and MC number of QCD events in signal region (relative isolation < 0.1) for 9.6 pb^{-1} in different jet multiplicity bins.*

The error that is quoted in Table 5.5 can be seen as the statistical error that comes from the fit. By varying the parameters within their uncertainty we get the plot that is shown in Figure 5.8, where we can see what each parameter variation does to the total fit. Since we are only interested in the error on the y-value of the endpoint for the extrapolation, we used the following formula for the error matrix of a function given the error matrix of the different variables [127]: $V(x) = GV(f)G^{-1}$, with G the vector with elements $\frac{\partial y}{\partial p_i}$ and $V(x)$ the covariance matrix. In this notation y is the function that determines the endpoint of the fit and p_i are the different parameters. More precise for this case the vector G is filled with the change of the value y of the endpoint due to a change of a given parameter within its error divided by that error: $\frac{\partial y}{\partial p_i} = \frac{\Delta(y(p_0)-y(p_i+\sigma_{p_i}))}{\sigma_{p_i}}$. We then used the error on the endpoint to calculate the error of the extrapolation.

The systematic error has been calculated for this method in the same manner as for the ABCD method: by varying the boundary. In this case we have varied the starting point of the fit (nominal at 0.1) and we found that the fit is stable around the nominal starting value (in a range of 0.7 - 1.3) and we have assigned a systematical error of ±10%. This summarizes the fit result as follows:

$$\mathrm{I} = 45.3 \pm 6.1\ (\mathrm{stat}) \pm 4.5\ (\mathrm{syst}) \tag{5.4}$$

5.4.1 Conclusion

The fit method relies on the fact that the distribution of the relative isolation of muons after all other muon cuts above 0.1 is dominated by QCD muons. This distribution can then be fitted and extrapolated into the signal region. We have shown that with a linear extrapolation we can predict the number of QCD events in the signal region with reasonable errors. The method is based on the idea that we can measure this relative isolation distribution in data and that we can also clearly see the kink that marks the

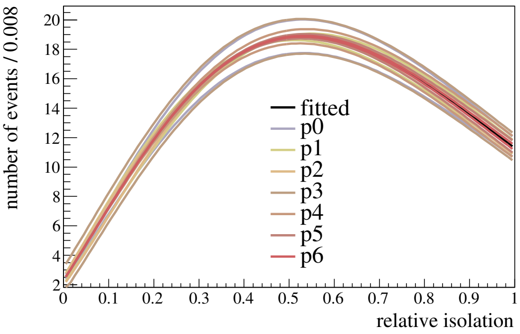

Figure 5.8: *Variation of the fit when varying the parameters within their uncertainty, of importance for us is the value at 0.1 (the endpoint).*

transition between prompt and non-prompt (mainly QCD) muons. If this kink is not there then one has to be careful with the assumption that there are no prompt muons above 0.1. A way to check this could be to try to find regions that are enriched with QCD (like 2 jet events) or regions that are QCD free by only investigating muons after overlap removal to jets which should be very isolated.

5.5 Summary

In this chapter we have investigated two methods to determine the QCD content after applying the base selection cuts. Both the ABCD method and the fit method give good results with total errors (statistical and systematical) under 20% with only 9.6 pb^{-1}. The dominating errors are statistical. The main problem with the ABCD method as it is now is that it predicts the number of QCD events after one extra cut: the d0 significance. This is also the reason that both methods cannot be compared directly. In order to do so one would either have to cut on d0 significance also for the fit method or find a way of returning not only the number of events in region C, but also the QCD content of D and the region in between. On the other hand however, the d0 significance cut has more advantages, like rejecting cosmic muon, and might be worthwhile considering as standard cut.

This study was performed using the $\sqrt{s} = 10$ TeV samples. We know however that the first collisions will occur at a center of mass energy of 7 TeV. We will see that with the lower statistics in the data sample and with the tighter cuts that will be used for the first top-quark pair production cross section measurement (including the overlap removal of muons close to jets) that the two methods presented here will not be adequate, see next chapter. In Chapter 7 we will develop a new method that is related to the here presented ABCD method using the knowledge that was gained in the last two chapters.

CHAPTER 6

DISTRIBUTIONS IN DATA

On the 30th of March 2010 the `LHC` collided protons at a center of mass energy ($\sqrt{s}$) of 7 TeV for the first time. Until Monday the 30th of August `ATLAS` had recorded over 3 pb^{-1} of data at this energy. The era of complex physics analyses at the `LHC` energy scale and therefore also top-quark analysis had started. In this chapter we will study the data and the distributions of objects important to the top-quark pair production cross section measurement will be shown. Note that not only is the energy less than the $\sqrt{s} = 10$ TeV that was planned for, also the amount of accumulated data is lower than was anticipated. Nonetheless, in the next chapters we will show that data-driven QCD estimates and ultimately the measurement of the top-quark pair production cross section are possible with this small data-set.

After a more detailed account of the available data in Section 6.1 we will start the data analysis by looking at basic distributions to assess whether the data behaves as expected in Section 6.2. The last part of this chapter, Section 6.3 will be dedicated to the test of our methods of the previous chapter. In the next chapter we will perform the QCD estimation in the selected sample of $t\bar{t}$ candidates in detail.

6.1 The full dataset

In the first 5 months of operation the `ATLAS` detector recorded more than 700 million collision events [128]. Not all of these collisions passed our quality cuts. For a run to be accepted for physics analysis all sub-detectors have to flag the data quality of a run as *good* [129] according to the status of all their systems. All data quality decisions are then used to create so called ‘good run lists’ (GRL’s) which differ for different physics analyses. For complex analyses all detector subsystems have to be working nominally and the GRL for such an analysis will only contain a sub-sample of the total data. After requiring the runs to pass the GRL for top physics, the total of recorded data added up to 2.89 pb^{-1} [130], which is about 80% of the recorded integrated luminosity.

The runs are divided in different periods, where each period is defined as a time of data-taking with consistent detector and trigger settings [131]. A significant change to the configuration defines the start of a new period. In Table 6.1 the periods are listed with their integrated luminosity after the required top GRL.

	time period	integrated luminosity nb^{-1}
A+B	Mar 30 - May 17	8.43
C	May 18 - Jun 05	8.44
D	Jun 24 - Jul 19	$2.78 \cdot 10^2$
E	Jul 29 - Aug 18	$1.00 \cdot 10^3$
F1+F2	Aug 19 - Aug 30	$1.59 \cdot 10^3$
total	Mar 30 - Aug 30	$2.89 \cdot 10^3$

Table 6.1: *Integrated luminosity as recorded by* `ATLAS` *per run period after requiring the top GRL.*

Since period A and B were reprocessed together in order to have a consistent set of `ATLAS` software over the entire data-taking period, they are always grouped together and we quote them as such. We can note that there is almost an exponential growth in integrated luminosity over time due to higher luminosities delivered by the `LHC`. This increase in instantaneous luminosity is caused by decreasing the size of the interaction region through focusing of the beams (‘squeezing’) and later by increasing the number of colliding bunches and the number of protons per bunch, see Section 2.1. In Figure 6.1 we show the integrated luminosity as it is delivered by `LHC` and recorded by `ATLAS`.

6.2 Data validation

Since this is the first time that the data is investigated, some basic distributions will have to be shown to spot possible detector problems and gain better understanding of the objects that are important for our analysis. All sub-detector systems have performed extensive validation of their system and no major problems have been identified. In this section distributions will be shown of a subset of the data that is interesting for the $t\bar{t}(\mu)$ searches. Events are selected with the following cuts to ensure that the topology of the investigated events is already close to the top environment and to avoid non-collision backgrounds (like cosmic muons) and events where we have known problems:

- passed muon trigger with $\mathrm{p_T} > 10$ GeV
- at least one muon that passes all the top-muon-cuts except isolation cuts
- at least one jet with $\mathrm{p_T} > 20$ GeV
- a primary vertex with at least 4 tracks
- no jets marked as *bad* in the event,

where *bad* is a way of marking jets that are most likely to originate from noise or detector problems [116].

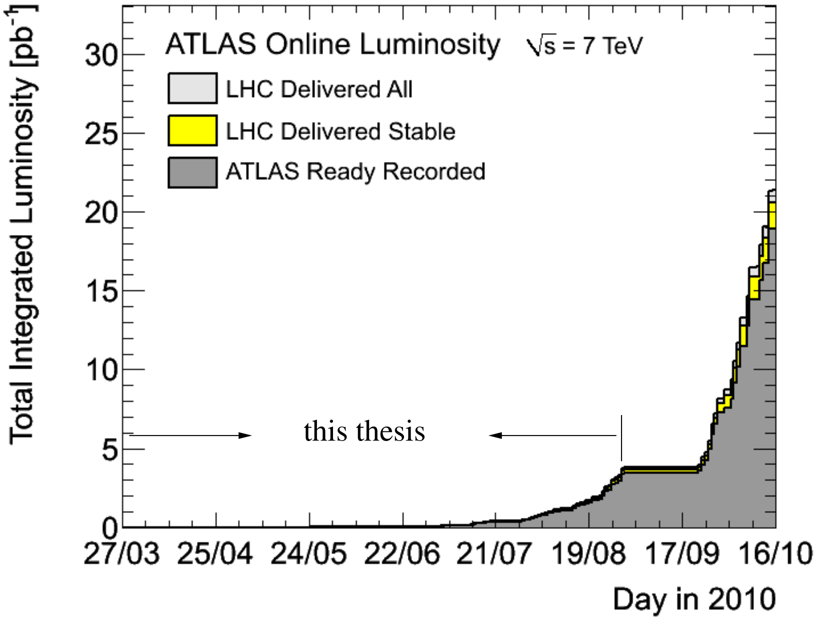

Figure 6.1: *The integrated luminosity as it is delivered by the* `LHC` *machine and recorded by* `ATLAS` *in* pb^{-1}.

6.2.1 Primary vertex

We know from the previous chapter that the location of the primary vertex plays a role in the computation of the d0 significance of the muon. It is also an interesting starting point for the data distributions since the primary vertex marks the spot of the interaction that we will study. In Figure 6.2 (left) we show the location of the primary vertex in the plane transverse to the beam direction and the uncertainty of the x-coordinate of the primary vertex is shown in Figure 6.2 (right).

We note that the interactions seem to occur mostly almost centered around zero in x and shifted up slightly in y with respect to the (0,0) of the `ATLAS` detector. This has no consequence for physics analyses since all quantities will be computed with respect to the primary vertex. The less pronounced second accumulation of primary vertices which can be seen in lower left side of the plot are the primary vertices from the early runs with different `LHC` settings. The spread in the z coordinate, along the beam axis, is much larger: of the order of 100 mm. The uncertainty on the location of the primary vertex is small (the distribution for the y-coordinate looks similar) since we select events on having at least four tracks in the primary vertex [132]. The mean of the uncertainty on x (y) is found to be $< \sigma_x > = 18\ \mu m$ ($< \sigma_y > = 18\ \mu m$).

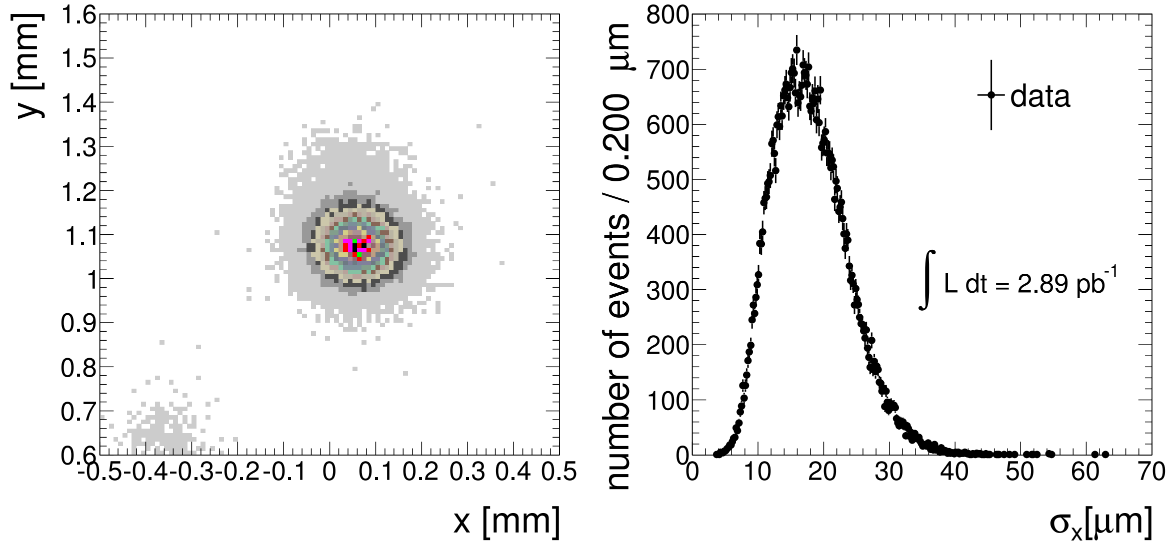

Figure 6.2: *Left: the location of the primary vertex in x and y in mm. Right: uncertainty of the vertex position in x in μm.*

6.2.2 Trigger efficiency

In trying to isolate $t\bar{t}(\mu)$ candidates from all interactions, the presence of an isolated muon is vital. It is therefore important to study the muon-trigger efficiency since it will enter directly the cross section calculation in Chapter 8. The muon trigger used for the first analysis was the `mu10` trigger meaning that it triggers on muons with p_T above 10 GeV. The offline selection of muons with p_T above 20 GeV ensures that efficiency is at the plateau of the turn-on curve of the trigger, see Section 3.1. The efficiency in data is obtained using a *tag-and-probe* method in a sample of $Z \to \mu^+\mu^-$ events [106]. The *tag* is a muon that passes all our selection criteria and is matched to a trigger object and the *probe* is any muon that satisfies all muon criteria and the requirement that the muons have opposite charge and have an invariant mass within 12 GeV of the Z-mass. The trigger efficiency is then defined as:

$$\epsilon_{\text{trigger}} = \frac{N_{(\text{probe, matched})}}{N_{(\text{probe, all})}}, \tag{6.1}$$

where $N_{(\text{probe, matched})}$ is the number of trigger objects matched to the *probe* offline lepton. From this efficiency differences between Monte Carlo and data can be identified and treated with scale factors (SF). The SF for the muon trigger is given by:

$$\text{SF}_{\text{trigger}} = \frac{\epsilon_{\text{trigger}}(\text{data})}{\epsilon_{\text{trigger}}(\text{MC})}, \tag{6.2}$$

where the efficiencies are as defined above. If this $\text{SF}_{\text{trigger}}$ is not equal to one, we need to include it in all our data-MC comparison plots by normalizing the MC to $\text{SF}_{\text{trigger}}$. It turns out that the trigger efficiency of the data taken in the period A-F is not the same as the one for the Monte Carlo. $\mathrm{SF}_{\mathrm{trigger}}$ depends on the pseudorapidity of the muon (η) and is given by [106]:

$$\begin{aligned} |\eta_{\mathrm{muon}}| \leq \;& 1.05 \quad : \mathrm{SF}_{\mathrm{trigger}} = 0.919\ ^{+0.022}_{-0.020}\ (\mathrm{stat}+\mathrm{syst}), \\ |\eta_{\mathrm{muon}}| > \;& 1.05 \quad : \mathrm{SF}_{\mathrm{trigger}} = 0.967\ ^{+0.014}_{-0.018}\ (\mathrm{stat}+\mathrm{syst}). \end{aligned} \tag{6.3}$$

We will show all comparisons between data and Monte Carlo with this scale factor applied to the MC distributions from here-on.

6.2.3 Muons

Isolated muons play a key role in selecting $t\bar{t}(\mu)$ candidates from background events. In this section the muon distributions will be presented that are important for the top-quark pair production cross section analysis in the muon channel and the data driven background estimation of QCD. All plots shown in the rest of this chapter will contain QCD multi-jet Monte Carlo and *signal* MC, where *signal* refers to samples that contain prompt muons. The signal MC is a mix of $t\bar{t}$ simulated events and the prompt backgrounds (W+jets also containing W+bb+jets, W+cc+jets and W+c+jets, Z+jets, single top and di-boson) as mentioned in Section 1.4.3.

Isolation

As was stressed before, the muon isolation is probably the single most important variable to distinguish prompt from non-prompt muons. One does not expect the isolation to look exactly the same in data as in MC, since it is a complicated variable to model. The isolation involves understanding the precise energy deposit in cells in the calorimeter, subtracting the expected loss term of the muon itself and correcting for dead material like cables according to the direction of the muon. We do expect to see long tails associated with QCD and a sharp peak at low values that indicates the prompt component. The isolation distribution will also be a clear indicator if data and Monte Carlo are in agreement since it has some separating power to see whether any discrepancy comes from signal samples or from QCD multi-jet events. In Figure 6.3 (left) the $\mathrm{E}_{\mathrm{T}}^{\mathrm{dR}=0.30}$ is presented[1] for events with the cuts given at the beginning of Section 6.2. Also shown are the signal Monte Carlo samples and the QCD Monte Carlo.
Although at low values of the isolation the data and MC distributions are in reasonable agreement, there is a large discrepancy at high E_{T}. The shape of the distribution at higher values however seems to be simulated correctly and follows the shape of the QCD distribution. This hints at an underestimation of the QCD background. In Figure 6.3 (right) we show the same distribution, but with the QCD Monte Carlo scaled up by a factor three compared to its nominal predicted yield. The agreement between data and simulation is good after the scaling. Although the scale factor is by no means a

---

[1] $\mathrm{E}_{\mathrm{T}}^{\mathrm{dR}=0.30}$ is the transverse energy in a cone of $\mathrm{dR} = \sqrt{(\Delta\phi)^2 + (\Delta\eta)^2} = 0.30$ around the muon.

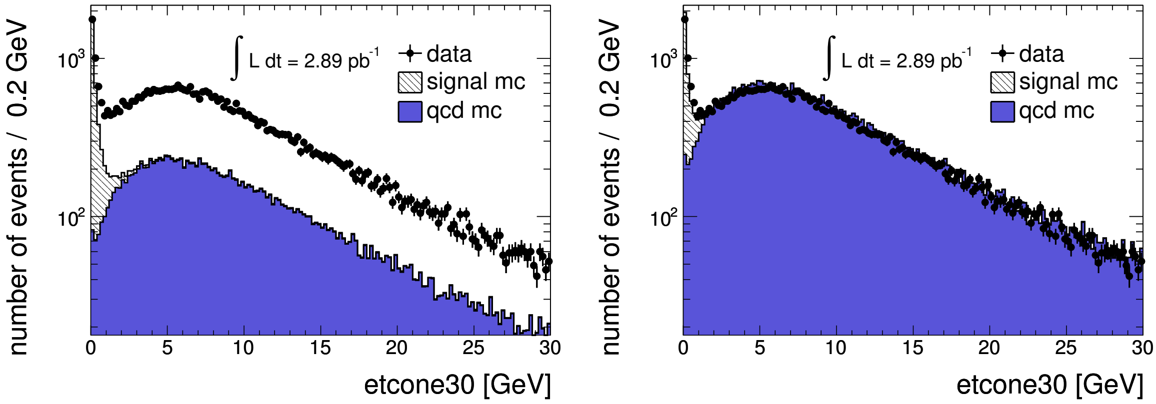

Figure 6.3: *$E_T^{dR=0.30}$ after requiring at least one good jet. Left: QCD and signal Monte Carlo. Right: QCD scaled up by a factor 3.*

precise measure, we will use it throughout this chapter to compare data and Monte Carlo shapes. We can conclude already that understanding QCD in more detail will be of great importance for the cross section measurement, since simulation underestimates this background. There are two more variables that characterize the isolation of the muon: the sum of the transverse momentum of all tracks in a cone around the muon track and the distance of the muon to the closest jet [118]. In Figure 6.4 the $\mathrm{p_T^{dR=0.30}}$ is shown[2] for data and MC in the left plot and the distance of the muon to the closest good jet ($\mathrm{p_T} > 20$ GeV) is presented in the right plot.

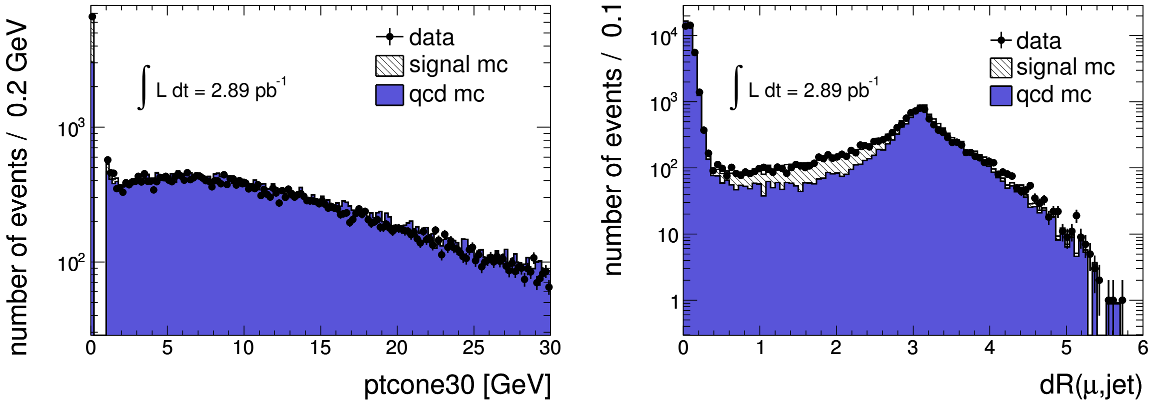

Figure 6.4: *Left: $p_T^{dR=0.30}$ after requiring at least one jet. Right: distance of muon to the closest good jet ($p_T > 20$ GeV) after requiring at least one jet. QCD is scaled up by a factor 3.*

Both figures show that data behaves as expected from MC. The distribution of the $\mathrm{p_T}$ of

---

[2] $\mathrm{p_T^{dR=0.30}}$ is the transverse momentum of all tracks in a cone of dR = 0.30 around the muon.

all tracks around the muon has an empty bin near zero since it uses only tracks with a minimum p_T of 1 GeV. In Figure 6.5 same distributions are shown after requiring the muon to have an $E_T^{dR=0.30}$ less then 4 GeV.

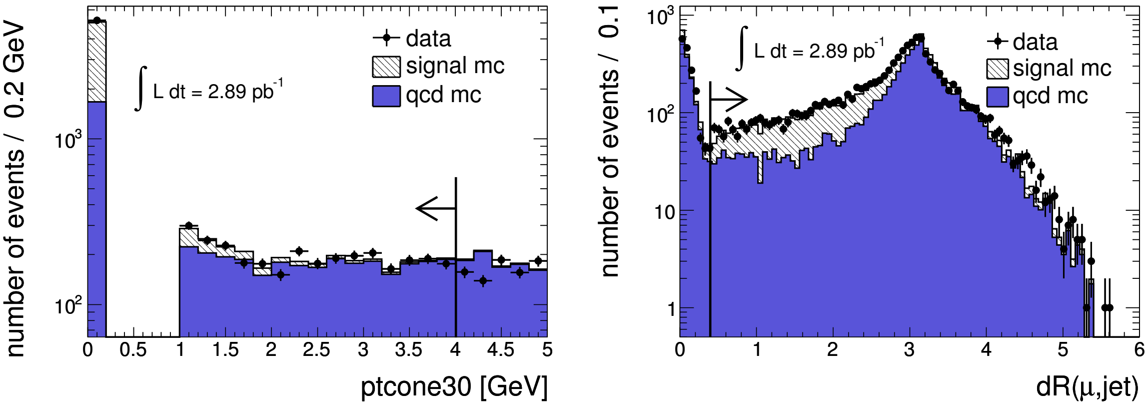

Figure 6.5: *Muons with $E_T^{dR=0.30} < 4$ GeV. Left: $p_T^{dR=0.30}$ after requiring at least one jet. Right: distance of muon to the closest good jet ($p_T > 20$ GeV) after requiring at least one jet. QCD is scaled up by a factor 3.*

The plots show good agreement between data and MC. Since the isolation of the muon behaves as expected from simulation, we will require in the following comparisons the muon to be isolated using the following selection criteria, see Section 3.2.2:

- $E_T^{dR=0.30} < 4$ GeV
- $p_T^{dR=0.30} < 4$ GeV
- no jet with $p_T > 20$ GeV closer than dR = 0.40 to the muon.

We refer to muons that pass these requirements as ‘analysis muons’. The $E_T^{dR=0.30} < 4$ GeV requirement is justified by Figure 6.3 (right) and the second and third requirement are justified by Figure 6.5 where the requirements are indicated by arrows. Note that the isolation cuts above are somewhat different from the ones in the previous chapter as has been mentioned before.

Pseudo rapidity and transverse momentum

When requiring at least one selected jet (which is a jet with $|\eta| > 2.5$ and p_T above 20 GeV) and an analysis muon, we are entering the kinematic region of the top-quark. It is informative to show first the pseudo rapidity and the transverse momentum of the analysis muon. In Figure 6.6 $|\eta|$ and p_T of the muon are shown after requiring at least one selected jet.

Note that after the analysis muon requirement the MC is underestimating the data even after scaling the QCD up by a factor three. This underestimation might originate

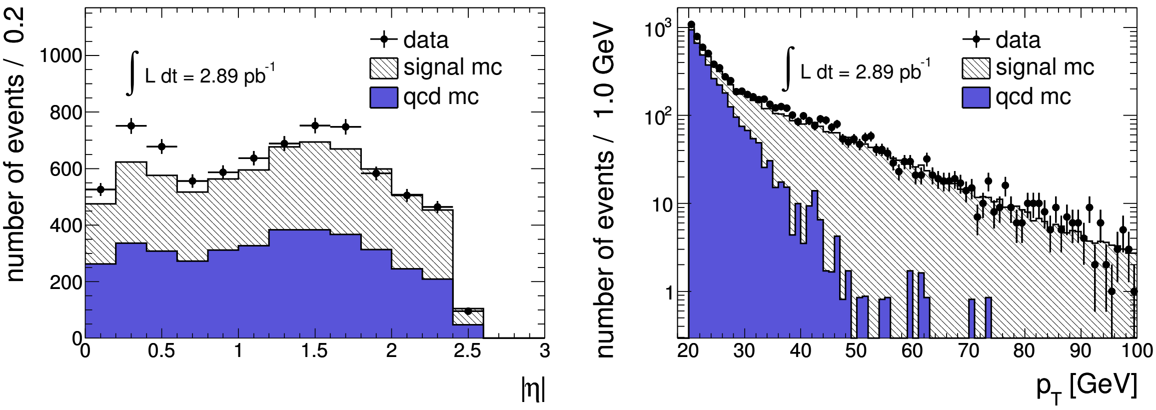

Figure 6.6: *Muon distribution after requiring an analysis muon and at least one selected jet. The QCD is scaled up by a factor 3. Left: muon-$|\eta|$. Right: muon-p_T.*

not only from the QCD contribution, but also signal processes like W+jets might be underestimated. We will look into this in more detail in the next chapter. The plot of the $|\eta|$ of the muon has a seemingly large discrepancy around $|\eta| = 0.2$. We think that this is caused by low statistics of the QCD sample (scaled up by a factor 3), an upward fluctuation of the data in that region and the overall underestimation mentioned above. No problems with the η distribution have been reported by the `ATLAS` muon performance group.

Impact parameter significance

The impact parameter and the impact parameter significance are both useful variables to distinguish prompt from non-prompt muons. In the ABCD method of Section 5.3 we used this separation power. In Figure 6.7 the impact parameter (left) and the impact parameter significance (right) are shown for analysis muons requiring at least one selected jet.

Both the impact parameter and the impact parameter significance distributions are not in perfect agreement when comparing data and MC. The peak at very low values seems to agree with the signal MC and the tail at high value seems well simulated by the QCD MC. There is however a discrepancy at intermediate values. It has been suggested that the prompt peak is indeed slightly wider than expected. Fortunately this does not influence the methodology used in our data-driven studies since our cut-value used for the ABCD method in the previous chapter of d0 significance equal to 3 seems to reside inside the QCD tail[3]. The mean of the uncertainty on the d0 of the muon is $<\sigma_{d0}(\mu)> = 16\ \mu m$ which is of the same order of magnitude as the uncertainty on the transverse coordinates of the primary vertex, see Figure 6.2 (right). From Equation 5.1 it can be seen that both uncertainties are taken into account when calculating the d0 significance.

---

[3] In Chapter 8 we will even change to 5 for the 'matrix method'.

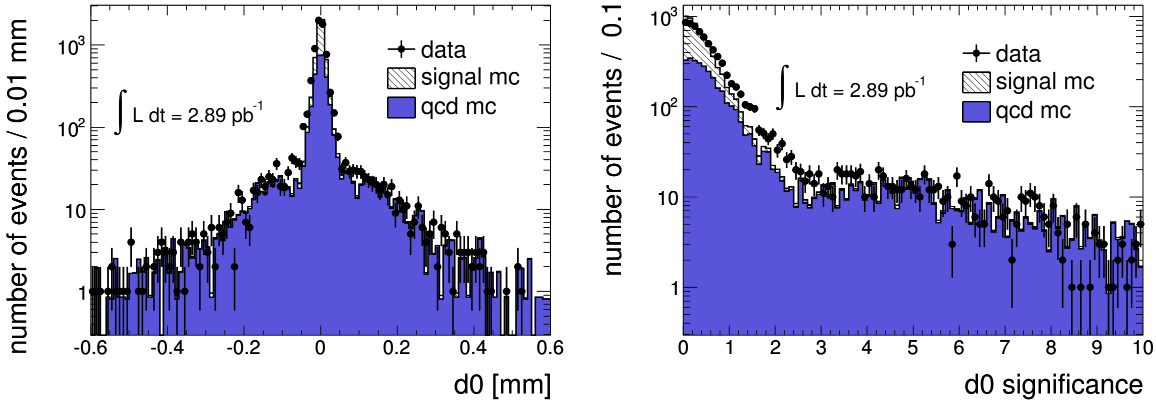

Figure 6.7: *Left: the impact parameter of analysis muons. Right: the impact parameter significance of analysis muons. Events have at least one selected jet and the QCD is scaled with a factor 3.*

Due to the ϕ terms needed to correct the uncertainty on the primary vertex coordinates however, the dominant uncertainty for the calculation of the d0 significance is $\sigma_{d0}(\mu)$.

6.2.4 Missing transverse energy

The missing transverse energy ($\not{E}_T$) is an important variable to distinguish top signal from QCD background due to the undetectable neutrino in $t\bar{t}(\mu)$ decays. In principle QCD events are expected to have low $\not{E}_T$, so any measured $\not{E}_T$ is due to reconstruction issues like noise and missed jets (or neutrinos from heavy quark decays). In Figure 6.8 the $\not{E}_T$ distribution is shown for events with at least one selected jet and an analysis muon.

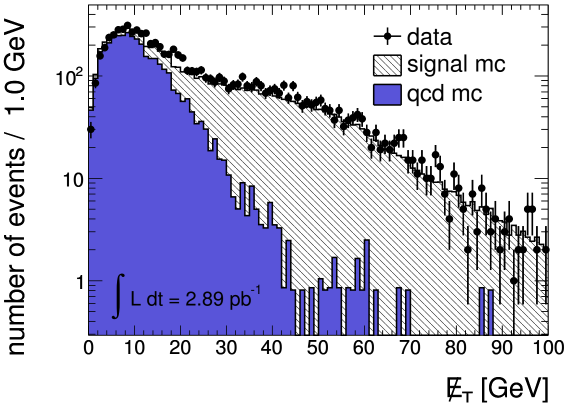

Figure 6.8: *The $\not{E}_T$ distribution after requiring an analysis muon and at least one selected jet. The QCD is scaled with a factor 3.*

After scaling-up the QCD Monte Carlo, we note that the shape of the data distribution is well simulated by MC. This is non trivial since the $\not{E}_T$ is a difficult variable to simulate due to the interplay of all aspects of the detector like muon energy loss terms and the jet reconstruction. The small difference in the signal tail hints towards a possible underestimation of the signal component. Note that the uncertainty on the $t\bar{t}$ and W+jets production cross section is not negligible. The plot however does give us confidence that the $\not{E}_T$ cut we obtained from MC studies is indeed behaving as expected. Note also that we will cut quite hard on QCD when we require $\not{E}_T$ above 20 GeV (the QCD efficiency for this cut is $\sim 10\%$ see Section 1.4.3).

6.2.5 Jets

Jets are essential for understanding the top-quark pair decay since the semi-leptonic decay channel of $t\bar{t}$ involves in principle four jets, see Figure 1.7. Since we select events on the number of high-p_T jets they contain, it is important to see if data looks similar to what we expect in the distribution of the number of jets. We show in Figure 6.9 (left) the jet multiplicity (i.e. the number of selected jets with $p_T > 20$ GeV) after the cuts described at the beginning of Section 6.2 with the additional isolation requirement on the muon as in Section 6.2.3 (i.e. requiring an analysis muon).

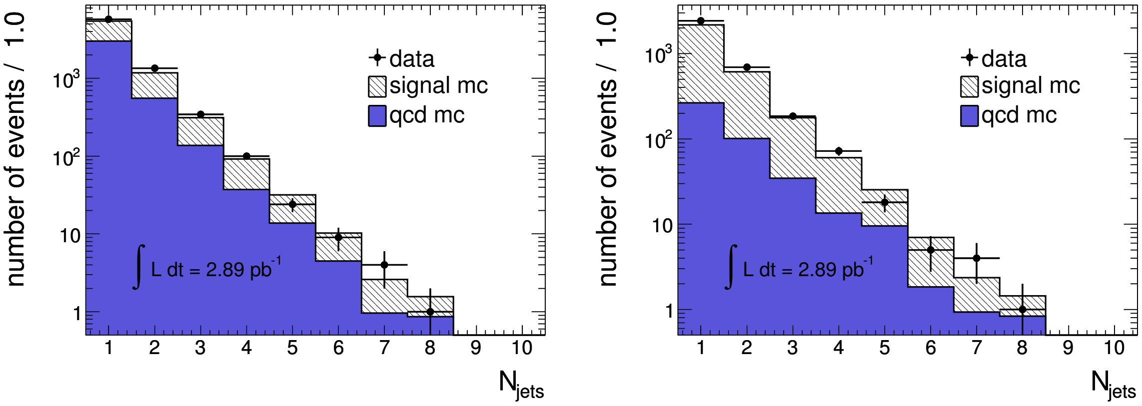

Figure 6.9: *Left: the number of selected jets with $p_T > 20$ GeV after requiring an analysis muon. Right: with additional $\not{E}_T > 20$ GeV cut. The QCD is scaled with a factor 3.*

We can conclude that with the QCD scaled up, the MC simulates the data well in shape. The normalization seems also here (see the previous sections) not perfect: the first four jet bins are slightly underestimated. One reason for this effect could be a difference in the jet energy scale between data and Monte Carlo, causing more jets to be selected in data. Since the shape of the jet multiplicity distribution is the same however, this does not change the selection efficiency and inspires confidence that we can use the jet selection as was discussed in Chapter 3. The same distribution but with additional $\not{E}_T$ cut, shown in Figure 6.9 (right), exhibits the same behaviour with ten times less QCD and suggests that it is the signal MC that is slightly underestimated. As a last check before moving on to the actual estimation of QCD background, we show the p_T distribution of the selected jet with highest p_T , the *leading* jet, (left) and of the selected jet with the 4th highest p_T (right) in Figure 6.10 after requiring an analysis muon.

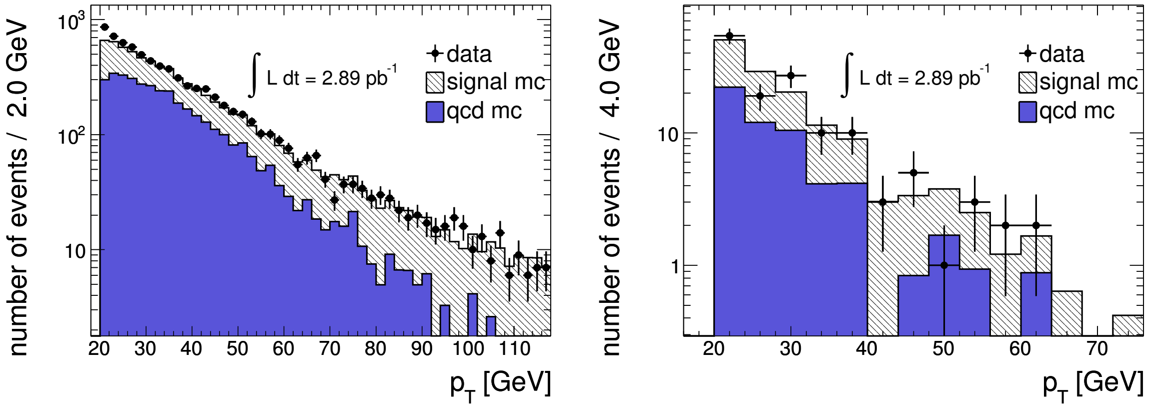

Figure 6.10: *Distribution of the jet p_T after requiring an analysis muon and at least one selected jet. Left: the leading jet. Right: the fourth jet. QCD is scaled with factor 3.*

It can be seen that for the leading jet p_T the agreement between data and MC is not perfect. In the low p_T region the discrepancy is large. It is not a priori clear whether this comes from an underestimation of the signal MC or the QCD simulation. Since the uncertainties of the production rates of both are large (dominated by the W+jets uncertainty for the signal MC), data-driven techniques will be used to estimate the background contributions to the top-quark pair production cross section measurement.

6.3 First test of methods to estimate QCD

In the previous section we established that the data behaves as expected in most basic variables used in selecting $t\bar{t}$ candidates. This section will focus on checks of the QCD estimation methods discussed in the previous chapter. Note that the center of mass energy that was anticipated in Chapter 5 was unfortunately not reached. Data at an energy of 7 TeV was delivered, where an energy of 10 TeV was used to develop the methods. This lowers the cross section of top-quark pair production substantially, but also the QCD production rate [73,81]. The consequence of the low integrated luminosity is that statistics will be the limiting factor for the data-driven methods. Since we also tightened the good muon cuts to deal with the higher-than-expected QCD rates, this might render the methods not feasible.

6.3.1 ABCD method

The first method to estimate the QCD background, discussed in Section 5.3, is the ABCD method. The ABCD method is uses two uncorrelated variables: the d0 significance and the relative isolation. By dividing a two dimensional plot into four regions, the QCD content in the signal region was computed by using the simple Equation 5.2: $\mathrm{C} = \frac{\mathrm{A}\cdot\mathrm{D}}{\mathrm{B}}$. To check whether the method can be used to obtain a solid estimate of the QCD background in the small data-set, we will test the method in the signal region as was defined in the previous chapter. In Figure 6.11 (left) the d0 significance versus the relative isolation after all other muon cuts in events with at least 4 selected jets after $\not{E}_\mathrm{T}$ cut is presented. The table in Figure 6.11 (right) shows the number of selected events per region.

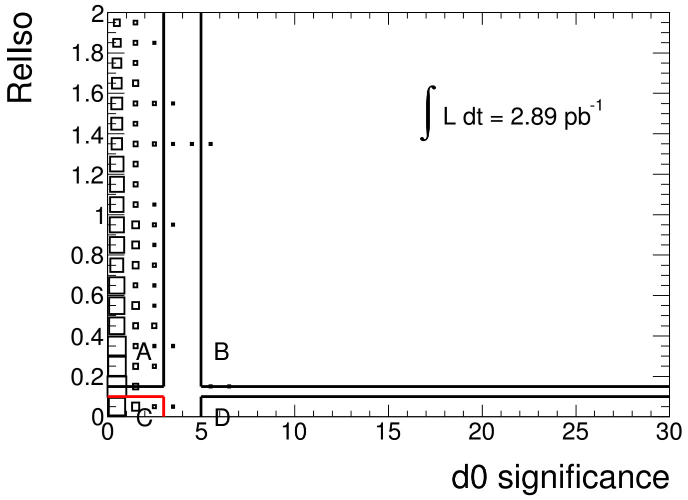

	number of events
A	1825
B	4
C	73
D	0

Figure 6.11: *Left: the d0 significance versus the relative isolation after all other muon cuts for events with at least 4 selected jets after $\not{E}_T$ cut. Right: number of events in each region of the ABCD plot for events with at least four selected jets and after $\not{E}_T$ cut.*

Due to the empty region D and the low statistics in B, there is unfortunately only one possible conclusion: the ABCD method is not suitable with only 2.89 pb^{-1} of data at $\sqrt{s} = 7$ TeV. Possible fixes include choosing the regions differently or using an extension of the ABCD method. These fixes are implemented in the so-called *matrix method*. The matrix method allows for signal events to enter the control region by assigning an efficiency to events to enter different regions. In the limit of no signal events outside of the signal region the ABCD method is mathematically equivalent to the matrix method. We will explore this method in the next chapter.

6.3.2 Fit method

For the fit method, discussed in detail in Section 5.4, the tail of the isolation distribution was used to fit for the QCD distribution and then extrapolate this fit into the signal region. As was done for the ABCD method in the previous section, we will check the fit method here before going into the data-driven QCD estimation in detail in Chapter 7. In Chapter 5 the relative isolation was used to perform the fit. In Figure 6.12 (left) the relative isolation for muons after all other muon cuts and $\not{E}_T$ requirement for events with 4 or more jets is shown.

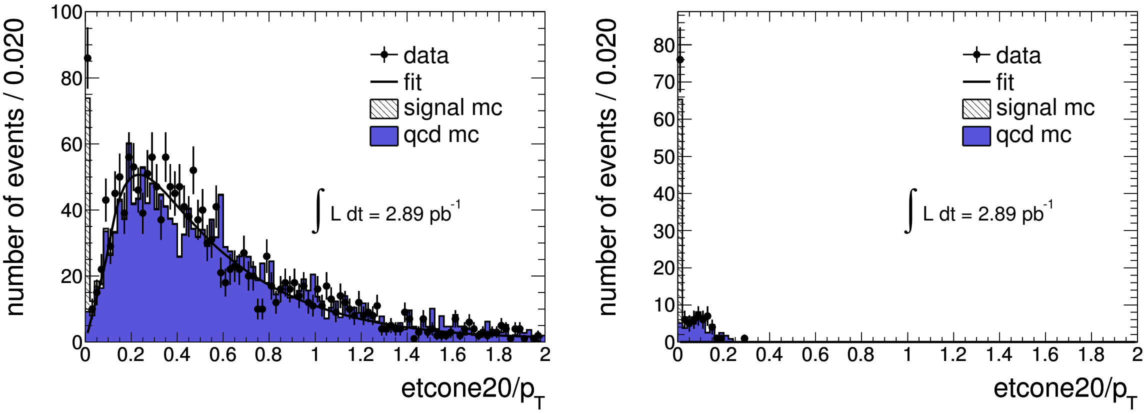

Figure 6.12: *The relative isolation for the muon after all other muon cuts and $\not{E}_T$ requirement for events with at least 4 selected jets. Left: without overlap removal. Right: with overlap removal*

The fit that was used is a combination of a Landau with a third order polynomial (same as in Section 5.4). The prediction of the number of QCD events below relative isolation of 0.1 given by extrapolating the fit in Figure 6.12 (left) is:

$$\mathrm{I} = 68.6 \pm 11.8\ (\mathrm{stat}), \tag{6.4}$$

events in the signal region where the error is the statistical error as explained and computed in Section 5.4. Note that the relative isolation cut was optimized for 10 TeV collisions and Figure 6.12 (left) seems to suggest that the cut value would need to be re-optimized. A shift from 0.1 to 0.05 seems reasonable and would yield an estimate for the number of QCD events under the new cut value (using the same fit) of $\mathrm{I}_{0.05} = 17 \pm 3$. However in the previous section it was already shown that the QCD contribution is larger than expected and this lead us to the use of even tighter muon cuts, i.e. additional muon cuts. Especially the overlap removal of muons to jets removes a large amount of QCD background. In Figure 6.12 (right) the relative isolation for the muon after all other muon cuts and $\not{E}_T$ requirement events with 4 or more selected jets is presented after overlap removal. Unfortunately the conclusion also for this method is simple: the fit method does not work with the proposed cuts with only 2.89 pb^{-1} of data at $\sqrt{s} = 7$ TeV since there is no statistics left above the cut value (even with a re-optimized value) to perform the fit.

Solutions to this could be loosening the cuts, especially the overlap removal. From both the relative isolation in Figure 6.12 (left) and the absolute isolation in Figure 6.3 (right) one might conclude that the isolation cuts could be tightened, deeming the overlap removal unnecessary. There is however a strong argument to use the overlap removal: one knows that the muons close to a jet are non-prompt muons from heavy flavour decay and hence should not be taken for top-quark analysis. It has been decided by the `ATLAS` collaboration to use the overlap removal cut as a default muon cut in the top-quark analysis. This decision has lead us to investigate the *matrix method* to estimate the QCD background. This method will be discussed and used on data in the next chapter.

6.4 Summary

In this chapter input distributions for the estimation of the QCD background and eventually for the top-quark pair production cross section determination have been presented. A first comparison between data and Monte Carlo suggests that the QCD background is roughly a factor three higher than expected. By scaling the QCD Monte Carlo with this factor the combined simulated signal samples ($t\bar{t}$, W+jets, Z+jets, single top and di-boson) and the QCD Monte Carlo describe the data well. The small discrepancy in normalization can be explained by the crude scaling of the QCD Monte Carlo but also by the large uncertainties of production cross section of the W+jets samples. Therefore a data-driven QCD estimation is needed, which will be presented in the next chapter. In Chapter 8 also a data-driven technique for the W+jets estimation will be shown.

The QCD estimation methods of Chapter 5 have been tested. The small data-set at lower than anticipated energy caused the ABCD method to become unsuited for a solid estimation of the QCD background due to lack of statistics. The second method presented in the previous chapter, the fit method, performs well with the cuts it was optimized for. Due to a decision of the `ATLAS` collaboration to adopt the overlap removal requirement of muons to jets, the distribution needed to perform the fit at high values of the relative isolation lacks statistics. The overlap removal cut made also this method not suitable for the small data-set available.

In Chapter 7 we will present an alternative method to estimate the QCD background for the $t\bar{t}$ cross section measurement. The method will utilize many of the key aspects of prompt and non-prompt muons that have been discussed in this chapter.

CHAPTER 7

MATRIX METHOD USING THE IMPACT PARAMETER SIGNIFICANCE

Due to the relative small data sample and scrutinizing requirements on the muons both the ABCD and the fit method had to be abandoned as methods to estimate the QCD background in the selected sample of $t\bar{t}$ candidates. Fortunately there is an extension of the ABCD method that can cope with the lower statistics: the 'matrix method'. In the following chapter we will work out this method in detail, shows its performance in Monte Carlo and make an estimation of the QCD contribution in data. In the next chapter the estimate of QCD background will be used in the first top-quark pair production cross section measurement in `ATLAS`. Note that QCD data-driven estimates are not only important for the $t\bar{t}$ production cross section measurement directly but are also used as input for other physics studies. For the data-driven measurement of the W+jets background in events with four jets for example the QCD prediction in events with two jets is of importance [133, 134].
First we will explain the matrix method in Section 7.1 and show how the method can be used for the estimation of QCD background in Section 7.2. The most important ingredient for the matrix method will be estimating the fake efficiency which will be explained in Section 7.3 together with its performance on Monte Carlo. We will have a look at the dominant systematics for the method in Section 7.3.2. The rest of the chapter will be devoted to QCD estimation in data. The final results after the base selection are presented in 7.4. The effect of the two extra cuts that lower the background presented in Chapter 1.4.3 will be investigated in Section 7.5 and we will conclude with overall results in Section 7.6.

7.1 Matrix method

The matrix method, which was already used at the `D0` experiment in 2007 [45], is based on the difference of real and fake events in their probability to pass a number of requirements. These requirements then define two groups of events: loose and tight, where tight events are a subset of loose events that also pass the additional requirements. This principle is illustrated in Figure 7.1.

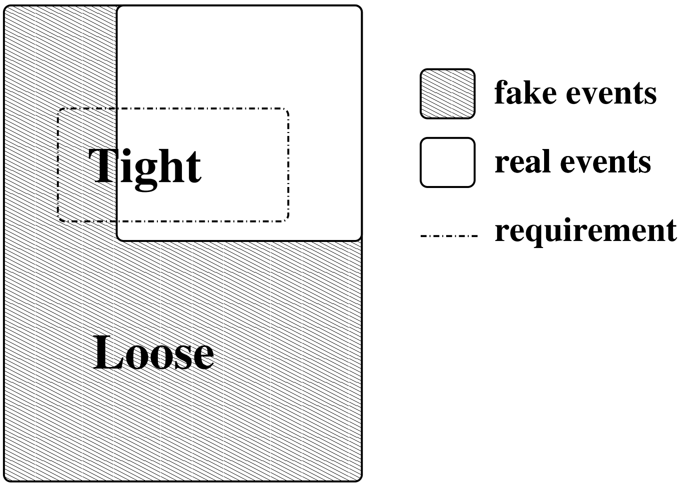

Figure 7.1: *Illustration of real and fake events that are grouped in the loose or in the tight selection (which is a subset of the loose selection).*

Since the tight selection is chosen to be a subset of the loose selection, the number of N^{loose} and N^{tight} is given by

$$\begin{aligned} N^{\text{loose}} &= N^{\text{loose}}_{\text{real}} + N^{\text{loose}}_{\text{fake}}, \\ N^{\text{tight}} &= \epsilon_{\text{real}} N^{\text{loose}}_{\text{real}} + \epsilon_{\text{fake}} N^{\text{loose}}_{\text{fake}}, \end{aligned} \tag{7.1}$$

where ϵ_{real} (ϵ_{fake}) represents the probability for a real (fake) event that satisfies the loose criteria, to also satisfy the tight ones. Therefore, these efficiencies are defined as:

$$\epsilon_{\text{real}} = \frac{N^{\text{tight}}_{\text{real}}}{N^{\text{loose}}_{\text{real}}}, \tag{7.2}$$

$$\epsilon_{\text{fake}} = \frac{N^{\text{tight}}_{\text{fake}}}{N^{\text{loose}}_{\text{fake}}}. \tag{7.3}$$

The system of equations in Equation 7.1 can be solved to yield the number of fake events, $N^{\text{tight}}_{\text{fake}}$, in the tight sample as:

$$N^{\text{tight}}_{\text{fake}} = \frac{\epsilon_{\text{fake}}}{\epsilon_{\text{real}} - \epsilon_{\text{fake}}} (N^{\text{loose}} \epsilon_{\text{real}} - N^{\text{tight}}). \tag{7.4}$$

We have now derived a formula that expresses the number of fake events that passes the tight selection in terms of the number of loose events, N^{loose}, the number of tight events, N^{tight}, and two efficiencies, ϵ_{fake} and ϵ_{real}. This is the basic matrix method formula.

7.1.1 Statistical uncertainty

Before we study how we can use the matrix method to estimate the QCD background after $t\bar{t}$ selection cuts, we will investigate the uncertainties that are involved. The formula takes four terms as input (N^{loose}, N^{tight}, ϵ_{fake} and ϵ_{real}), but it can be argued that the purely statistical uncertainty on the $N^{\text{tight}}_{\text{fake}}$ prediction comes from the uncertainty on N^{loose} and N^{tight} only. This is to certain extent a matter of taste, but the reasoning is that although the efficiencies have statistical uncertainties themselves only the uncertainty on the numbers of events entering the formula will be treated as statistics. We will follow this reasoning throughout the rest of this thesis. The uncertainty on the efficiencies that comes into the prediction by the propagation of errors then becomes a systematic uncertainty. Since N^{loose} and N^{tight} are correlated (N^{tight} is a subset of N^{loose}) we first need to separate the terms of Formula 7.1 into fully uncorrelated terms. Define N^{Δ}:

$$N^{\Delta} = N^{\text{loose}} - N^{\text{tight}}. \tag{7.5}$$

Now that N^{Δ} and N^{tight} are fully uncorrelated, one can rewrite the matrix method formula from Equation 7.4:

$$N^{\text{tight}}_{\text{fake}} = \frac{\epsilon_{\text{fake}}}{\epsilon_{\text{real}} - \epsilon_{\text{fake}}}((\epsilon_{\text{real}} - 1)N^{\text{tight}} + \epsilon_{\text{real}}N^{\Delta}). \tag{7.6}$$

In order to propagate the errors from all the inputs parameters we write out the partial derivative of the rewritten matrix formula (Equation 7.6) to all its components and then write out the purely statistical component of the uncertainty. See Appendix A for details. If we then compute the relative uncertainty, we get:

$$\frac{\sigma(N^{\text{tight}}_{\text{fake}})}{N^{\text{tight}}_{\text{fake}}} \sim \frac{1}{\sqrt{N^{\Delta}}}. \tag{7.7}$$

From Equation 7.7 it can be concluded that one needs to choose the requirements to define the loose and tight samples such that N^{Δ} is large to keep the statistical uncertainty low. This means choosing the loose definition as loose as possible, since the tight definition is dictated by the analysis. The loose selection should however already reflect the basic event selections to avoid completely kinematically different regions of phase space which may introduce large systematic uncertainties.

7.1.2 Systematic uncertainty

As discussed in the previous section the uncertainty due to $\sigma(\epsilon_{\text{real}})$ and $\sigma(\epsilon_{\text{fake}})$ will be classified as systematic uncertainty. By error propagation, see Appendix A, and assuming that $N^{\text{tight}}_{\text{fake}}$ is dominated by the error on ϵ_{fake}, we can write the relative uncertainty as:

$$\frac{\sigma(N^{\text{tight}}_{\text{fake}})}{N^{\text{tight}}_{\text{fake}}} \sim \frac{\epsilon_{\text{fake}}\epsilon_{\text{real}}}{\epsilon_{\text{real}} - \epsilon_{\text{fake}}}\sigma(\epsilon_{\text{fake}}). \tag{7.8}$$

From Equation 7.8 we can conclude that in order to keep the systematic uncertainty from the efficiencies low, we need to choose the selection (and thus the loose definition) such that ϵ_{fake} and ϵ_{real} are as different as possible.

7.2 Implementation of the matrix method

We want to use the matrix method to estimate the QCD content in our signal region. This means that we identify fake events with QCD events and the number of QCD events after all cuts with $N^{\mathrm{tight}}_{\mathrm{fake}}$. An event will be classified as real or fake according to the source of the muon in the event since top-quarks, W+jets and Z+jets produce prompt (i.e real) muons and QCD produces non-prompt (i.e fake) muons. The tight selection corresponds to our top-quark pair selection.

We can compute the number of QCD events in the tight sample by measuring N^{loose} and N^{tight} assuming that we can estimate the two efficiencies ϵ_{real} and ϵ_{fake} in suitable control regions. The measurement of ϵ_{real} is usually done with a tag-and-probe method using $Z \to \mu^+\mu^-$ events. Since for the first data the statistics is however low and small variations in ϵ_{real} have only a small impact on the final prediction of $N^{\mathrm{tight}}_{\mathrm{fake}}$, we will use the ϵ_{real} as obtained from Monte Carlo. Measuring N^{loose} and N^{tight} is straightforward and estimating ϵ_{fake} is the most difficult part of the matrix method and will be the subject of the next section. First we will concentrate on the definition of the loose selection.

In the previous section is was shown that the uncertainty from the matrix method is lowest when N^{loose} and $\epsilon_{\mathrm{real}} - \epsilon_{\mathrm{fake}}$ are large. In principle one is free to choose the loose selection as loose as one wants. Since we are interested however in the difference between real and fake muons (corresponding to prompt and non-prompt muons) it makes sense to use the same selection as the tight muon selection (the selections that define an analysis muon), but omitting the quality requirements on the muon. Tight refers to the muon selection used for the top-quark pair production cross section measurement as defined in Section 6.2.3. As was presented in the previous chapters the main difference between prompt and non-prompt muons is their isolation. By choosing the requirements such that loose and tight selection only differ in the isolation criteria one is also guarantied not to select events with completely different kinematic properties from top-quark events. We have investigated two different definitions of loose events:

- *class1*: same as tight events, but no cut on the $\mathrm{E_T}$ or $\mathrm{p_T}$ in a cone around the muon and no overlap removal of muons to jets.
- *class2*: same as *class1*, but with overlap removal of muons to jets.

Since the *class1* definition is the looser of the two, the efficiency associated with it will be smaller making the difference between ϵ_{fake} and ϵ_{real} larger and thus minimizing the uncertainty. It turns out however that the *class1* definition has a few problems.

Problems with the *class1* definition

An important issue for the *class1* selection is that the ϵ_{real} associated to it is not the same for top-quark pairs as for Z-events. Without the overlap removal to jets the effect that was shown in Section 4.3.4 will become important: due to the busier topology of $t\bar{t}$ events compared to Z events the probability will be lower to find an isolated muon. The consequence of this difference in ϵ_{real} for the different prompt samples is that the efficiency needed for the matrix method (which will be a weighted average of all prompt samples in this case) cannot be obtained from a tag-and-probe $Z \to \mu^+\mu^-$ analysis [106]. The difference can be as large as 30%. In Figure 7.2 the efficiency loose → tight, given simply by $\epsilon_{MM} = N^{\text{tight}}/N^{\text{loose}}$, is shown for three different prompt samples (top, Z and W) for both *class1* (ϵ_1, left) and *class2* (ϵ_2, right).

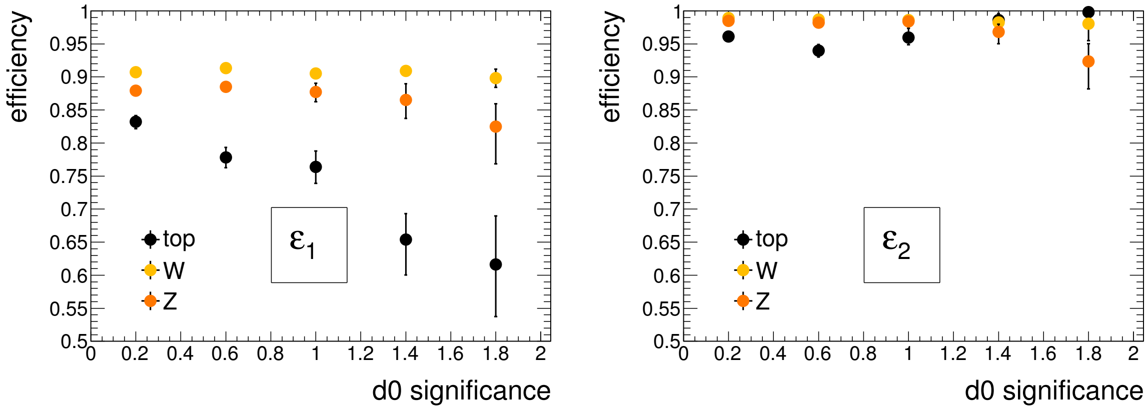

Figure 7.2: *Efficiency, ϵ_{MM}, in the 1 jet inclusive bin for different prompt samples. Left:* class1. *Right:* class2.

Note that ϵ_2 is much higher than ϵ_1, which is expected. It has also been observed that ϵ_{fake} is not flat as a function of the number of jets in the event for the *class1* definition, due to the same arguments as given above. This is on itself not bad, but it means that this has to be understood and that extrapolation from lower to higher jet-multiplicities is not straightforward. These arguments have lead to the decision to use *class2* as default loose definition throughout the rest of this chapter.

7.3 Measuring the fake efficiency

The measurement of ϵ_{fake} has to fulfill two requirements to ensure that the measured efficiency is indeed the QCD efficiency in the signal region. First of all, a control region has to be found that is dominated by QCD such that the measurement is not biased by prompt events leaking in. In addition we have to show that the efficiency measured in the control region can be extrapolated to the signal region. The efficiency has to be constant with respect to this extrapolation.

Most incarnations of the matrix method obtain their ϵ_{fake} in a control region that has low $\not{E}_{\mathrm{T}}$. We have seen before that indeed that region is dominated by QCD. However, $\not{E}_{\mathrm{T}}$ is not the most optimal choice. If ϵ_{fake} is measured in a region with low $\not{E}_{\mathrm{T}}$ it has to be extrapolated to use it in the high-$\not{E}_{\mathrm{T}}$ region, our signal region. Since $\not{E}_{\mathrm{T}}$ and isolation might be correlated, ϵ_{fake} might not be flat as a function of $\not{E}_{\mathrm{T}}$ and one might need to make corrections in order to be able to make this extrapolation. We have seen in the previous chapters that the impact parameter significance is a powerful and uncorrelated parameter to distinguish between prompt and non-prompt muons. We will exploit this feature to get an estimate for ϵ_{fake}.

From the previous chapters we know that the isolation and the impact parameter significance are uncorrelated for muons from QCD. This implies that the efficiency for fake muons as a function of d0 significance is expected to be flat since the efficiency ϵ_{MM} is only given by the isolation cuts. In Figure 7.3 the efficiency ϵ_{MM} is shown for the QCD Monte Carlo sample as a function of d0 significance. Since the QCD muons are fake only, we effectively plot ϵ_{fake}, which is indeed constant as a function of d0 significance. If we plot the efficiency of a combined sample of $t\bar{t}$, W+jets, Z+jets and single top (all produce real leptons) plus QCD as a function of d0 significance we expect to see the high efficiency of ϵ_{real} in the low d0 significance part and the low efficiency of the ϵ_{fake} in the higher d0 significance region. In Figure 7.3 we show this combined efficiency together with the true ϵ_{fake} of the pure QCD sample.

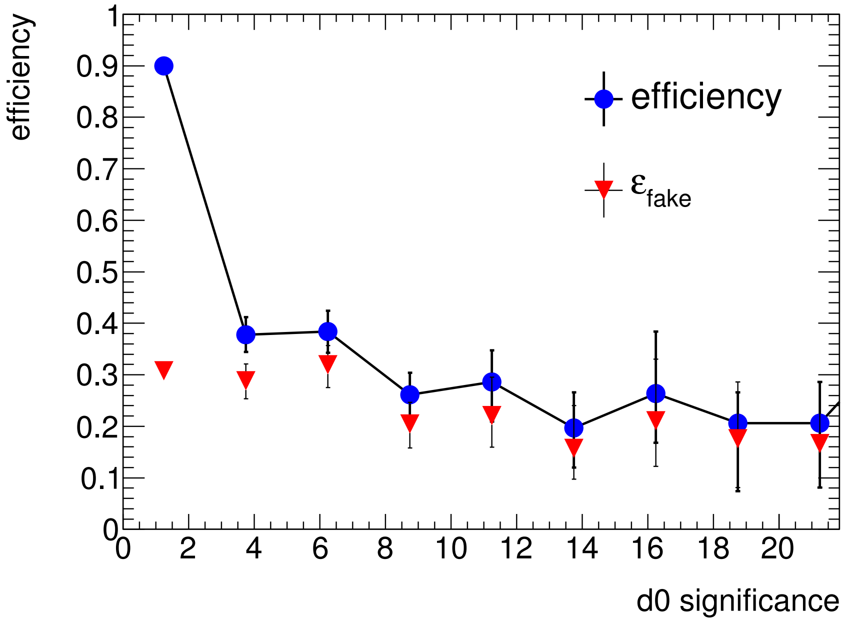

Figure 7.3: *The combined efficiency ϵ_{MM} (connected dots), and the ϵ_{fake} of QCD (triangles) for events with at least 1 jet.*

As expected we can can conclude that ϵ_{fake} is approximately flat with respect to d0 significance. We can also see that the combined efficiency behaves much like ϵ_{fake} in the high d0 significance region. This means that when we measure the combined efficiency above d0 significance = 5, we effectively measure ϵ_{fake}, which is exactly what we are trying to achieve. The ϵ_{fake} is then given by

$$\epsilon_{\text{fake}} = \frac{N^{\text{tight}}_{\text{d0 significance>5}}}{N^{\text{loose}}_{\text{d0 significance>5}}} \text{ (1 jet inclusive bin).} \tag{7.9}$$

In MC we find an efficiency for the 1 jet inclusive bin of (0.302 ± 0.024)% with this method. The measured ϵ_{fake} could in principle depend on the number of selected jets in the event. In Table 7.1 we show the efficiency of the 1 jet inclusive bin and also the efficiencies for the exclusive jet bins.

	ϵ_{fake}
1 jet	0.324 ± 0.034
2 jets	0.299 ± 0.041
3 jets	0.231 ± 0.076
≥4 jets	0.245 ± 0.087
≥1 jet	0.302 ± 0.024

Table 7.1: *Fake-efficiency (ϵ_{fake}) as measured in various jet bins in percent.*

From Table 7.1 we can conclude that the efficiencies measured per jet bin agree within their error with the ϵ_{fake} measured in the 1 jet inclusive bin. This means that we can use the ϵ_{fake} from the 1 jet inclusive bin for all other jet bins and thereby decrease the uncertainty substantially. Comparing the ≥4 jets bin with the 1 jet inclusive measurement we can see an improvement from 36% uncertainty down to 8%. From here-on we will use ϵ_{fake} from the 1 jet inclusive bin and we will also show in Section 7.5 that the same ϵ_{fake} can be used even after extra cuts.

7.3.1 Performance on simulated events

In this section the method is tested on MC first before being applied to data, as we will do in Section 7.4. The performance is measured by testing how well the estimation matches the true number of QCD events in MC. As value for ϵ_{real} the efficiency is used obtained from prompt Monte Carlo in the jet bin where the QCD estimation is performed. The values vary from 99% in the 1 jet bin to 97% in the 4 jet bin and have almost no influence on the final value of $N^{\text{tight}}_{\text{fake}}$. With more data one would get this efficiency from tag-and-probe $Z \to \mu^+\mu^-$ events [106], but it has been shown that simulation and data are in good agreement [3] and we will assign an extra uncertainty to this in Section 7.3.2. In Figure 7.4 we show the estimated and true number of QCD events in various jet bins (left) and the ratio of prediction and true number of events (right). The numbers are listed in Table 7.2.

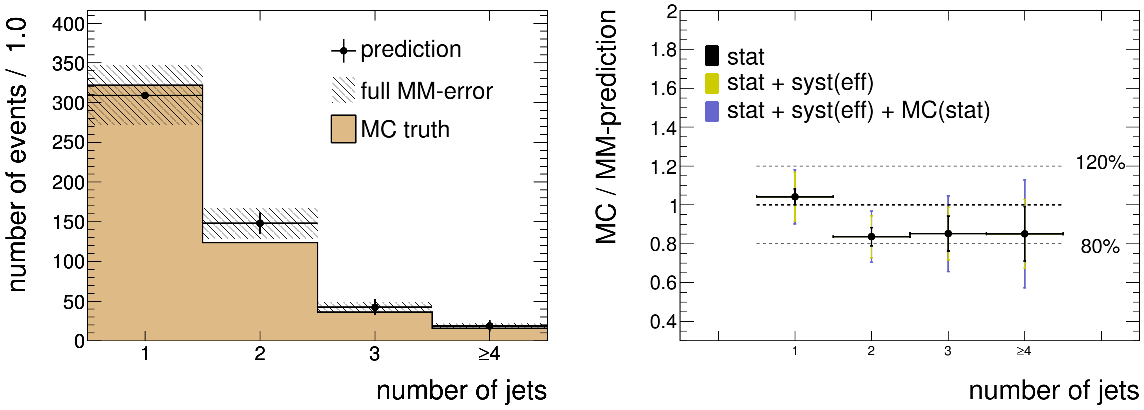

Figure 7.4: *Left: comparison between estimated and true number of QCD events in various jet bins. Right: the ratio between matrix method prediction and Monte Carlo truth. The plots are normalized to 10* pb^{-1}.

In Figure 7.4 (left) we only show both the purely statistical error and also the combined statistical and systematic error as defined by Sections 7.1.1 and 7.1.2. The agreement between prediction and truth is good, except in the 2 jet bin as can be more clearly seen in Figure 7.4 (right) where we present the ratio between matrix method prediction and Monte Carlo truth. The maximum difference is about 16%, which will be quoted as systematic in the next section.

jets	1	2	3	≥4
prediction	309.1 ± 12.1	148.1 ± 8.3	42.6 ± 4.5	18.8 ± 3.1
MC truth	322.0 ± 17.9	123.8 ± 11.1	36.3 ± 6.0	16.0 ± 4.0

Table 7.2: *Number of predicted and Monte Carlo true QCD events with a given number of jets after* $\not{E}_T$ *cut. The errors are statistical only and the numbers are normalized to 10* pb^{-1}.

7.3.2 Systematic uncertainties on QCD estimate

After the performance test of the method in MC in the previous section we will investigate in more detail the uncertainties that are involved. The uncertainties that are directly associated to the matrix method formula (Formula 7.1) have already been discussed in Section 7.1.1 and 7.1.2 and involved the statistical uncertainty from N^{loose} and N^{tight} and the systematic uncertainty from the efficiencies. Various other sources of systematic uncertainties have been investigated and the following list shows the ones that are dominant:

A Control region: the main assumption of this method is that events with d0 significance > 5 are outside the tail of prompt muons and thus only QCD events. We assign a systematic to this assumption by varying the value of the d0 significance cut and calculating the QCD prediction with the newly obtained ϵ_{fake}. We have varied between 4.5 and 6.5 and the change in estimation can be seen in Figure 7.5 where we show the estimated number of QCD events for various values of the d0 significance cut for events with at least 4 selected jets after $\not\!\!E_{\text{T}}$ cut.

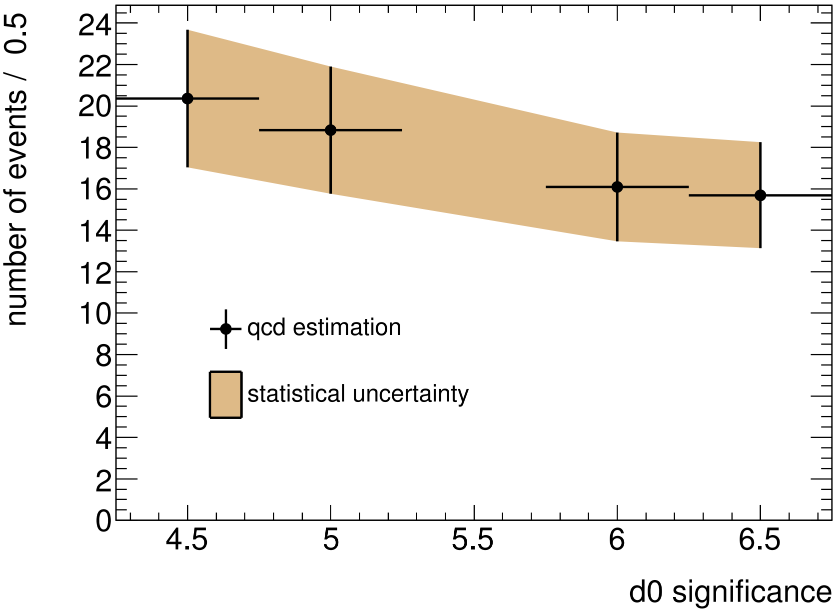

Figure 7.5: *Number of estimated QCD events for various values of the d0 significance cut for events with at least 4 selected jets after $\not\!\!E_T$ cut. The errors are statistical only.*

We will repeat this on data and quote the following systematic uncertainty, σ_A:

$$\sigma_A = \frac{\Delta(N_{\text{fake}}^{\text{tight}}) - N_{\text{fake}}^{\text{tight}}}{N_{\text{fake}}^{\text{tight}}}, \tag{7.10}$$

where $\Delta(N_{\text{fake}}^{\text{tight}})$ is the maximum deviation for the estimated value (obtained with a different d0 significance cut) from the nominal value of $N_{\text{fake}}^{\text{tight}}$ (with d0 significance cut at 5). In the example in Figure 7.5 this would be the value obtained at d0 significance 6.5.

B Contamination: it can be concluded from Figure 7.3 that the control region is (slightly) contaminated by prompt events. We already have seen that also muons from τ decays in $t\bar{t}(\tau)$ or $W(\tau)$ can end up in this region. To test how much the predictions change when changing the prompt content of the control region we scaled the W/Z/top-quark pair contribution up/down within their theoretical uncertainties and we assign as systematic σ_B the largest deviation from nominal.

The uncertainty on the prompt production cross section depends on the jet bin. Since we obtain ϵ_{fake} in the 1 jet bin we can use the uncertainty from that bin, which is 8.5% for top-quark pairs and 20% for W and Z [28, 135, 136]. Also this uncertainty will be computed on data by adding/subtracting W/Z/top Monte Carlo to the data according to the given uncertainties.

C Performance: to account for small biases in the method. On a simulated sample the method should, if all the assumptions were correct, provide a perfect agreement between prediction and MC-truth. We have seen in Section 7.3.1 that the largest difference occurs in the 2 jet bin and is 16%. We will quote this number as systematic uncertainty σ_C.

D Prompt efficiency: since we take ϵ_{real} from Monte Carlo, we assign an additional 2% uncertainty. This is conservative since the first measurements of ϵ_{real} on data suggest that the numbers agree within 1% [3].

These four sources are the main systematic uncertainties that we will quote on top of the systematic uncertainty associated with the errors on ϵ_{real} and ϵ_{fake}. We will evaluate the full systematics on data in Section 7.4.1. The performance systematic (σ_C) will be the largest source of uncertainty.

7.4 QCD estimate from data

In this section the QCD prediction in the signal region will be extracted after the default $t\bar{t}$ selection. As was discussed in Section 3.3 for the first top-quark pair production cross section measurement jets with $\mathrm{p_T}$ larger than 25 GeV are used to reduce some of the backgrounds and to gain significance. This is not the same as was used in the MC studies in the previous sections where the jets were selected with $\mathrm{p_T}$ larger than 20 GeV, but this does not change the topology of the selected events. This has been verified by checking the performance on simulated events with four or more jets with $\mathrm{p_T}$ larger than 25 GeV. The deviation from the MC-true number of QCD events was found to be 13%, compared to 15% in the same bin with jets of $\mathrm{p_T}$ larger than 20 GeV, see Table 7.2.

7.4.1 Prediction and full systematics

In this section the matrix method will be applied to the first 2.89 pb^{-1} recorded by `ATLAS` to estimate the QCD background in the selected sample of top-quark candidates. We selected the events according to the selection shown in Section 3.3 with base cuts (all requirements up to and including the missing energy cut) and divided them into exclusive jet bins. In Table 7.3 we show the number of loose and tight events per jet bin.

The efficiency ϵ_{MM} is presented for the 1 jet inclusive bin in Figure 7.6. This plot is to be compared with the MC plot of Figure 7.3.

The plot shows all features discussed in the previous sections: high efficiency in the low d0 significance region (dominated by prompt muon events) and lower efficiency at high

jets	1	2	3	≥4
N^{loose}	2676	662	170	72
N^{tight}	1939	455	114	61

Table 7.3: *Number of loose and tight events with a given number of jets with $p_T > 25$ GeV after $\not{E}_T$ cut.*

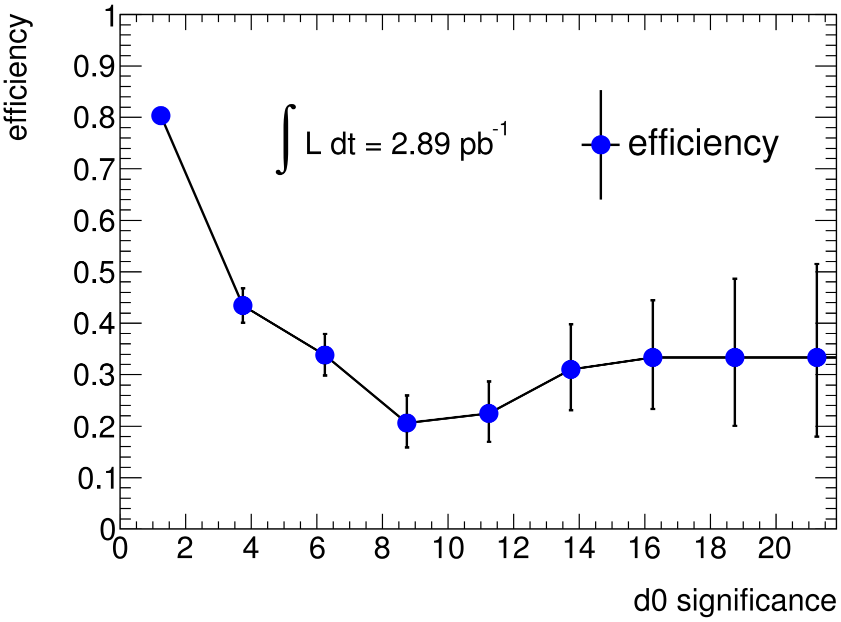

Figure 7.6: *The efficiency for events to go from the loose to the tight sample for 1 jet inclusive events.*

d0 significance (dominated by QCD). We note here that the efficiency in the low d0 significance looks lower than in Monte Carlo. This feature hints towards a higher QCD content in data than simulated in Monte Carlo, as we have also seen in the previous chapter. The efficiency we derive from all events with d0 significance > 5 is:

$$\frac{N^{\text{tight}}_{\text{d0 significance}>5}}{N^{\text{loose}}_{\text{d0 significance}>5}} = \epsilon_{\text{fake}} = 0.295 \pm 0.025 \text{ (stat)}, \tag{7.11}$$

which agrees well with the Monte Carlo value of $\epsilon^{MC}_{\text{fake}} = 0.302 \pm 0.024$ (stat). Using this ϵ_{fake} obtained from data, the N^{loose} and N^{tight} as quoted above and the ϵ_{real} from Monte Carlo we can estimate the number of QCD events per jet bin using Equation 7.4. The estimation results are listed in Table 7.4 where we also quote the Monte Carlo numbers, scaled to 2.89 pb^{-1} and corrected with the appropriate trigger efficiency scale factors (SF) as discussed in Section 6.2.2, and the number of data events.

We also plotted these numbers in Figure 7.7 in the form of a stacked plot where the QCD

jets ($p_T > 25$ GeV)	1	2	3	≥4
QCD	300.7 ± 11.4	84.2 ± 6.1	22.7 ± 3.2	3.9 ± 1.4
top MC	1.6	6.4	13.0	19.0
rest MC	1486.8	358.7	80.1	24.0
total estimate	1789.1	449.4	115.8	46.9
data	1939	455	114	61

Table 7.4: *Number of estimated QCD events plus statistical uncertainty and the number of Monte Carlo events scaled to 2.89 pb^{-1} after $\not{E}_T$ cut for a given number of selected jets. Also the number of data events is shown.*

is our data-driven estimate. The labels *j25* refer to the selection of jets with $\mathrm{p_T}$ larger than 25 GeV. The last bin includes all events with at least 4 jets with $\mathrm{p_T}$ larger than 25 GeV.

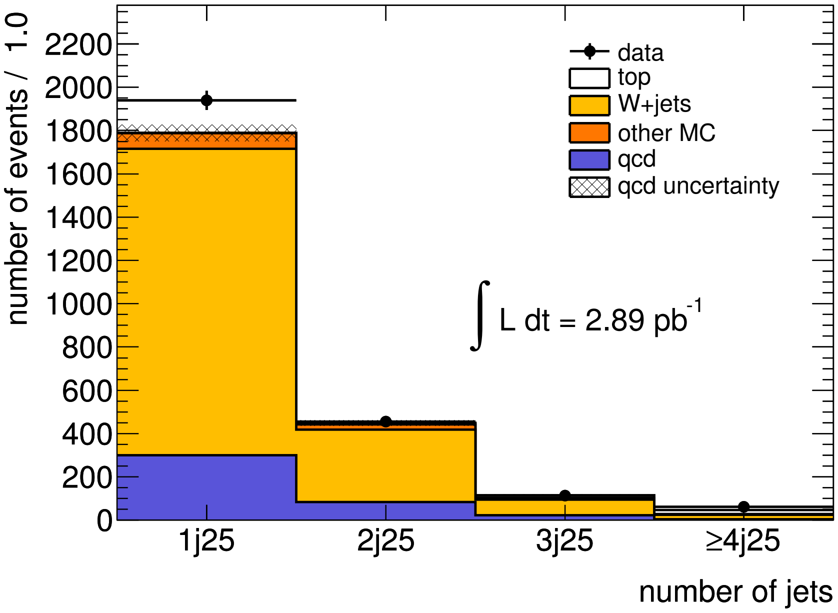

Figure 7.7: *Monte Carlo of various samples scaled to 2.89 pb^{-1} added to the data-driven QCD estimate per jet bin after $\not{E}_T$ cut. The data points are also shown. The uncertainty is statistical plus systematic uncertainty from the matrix method formula.*

It can be seen from the plot (and also from the table) that the agreement between the total estimate (QCD data-driven plus Monte Carlo samples) is good except for the 1 jet bin. The difference is about 8% and most likely due to an underestimation of both the QCD content and W+jets Monte Carlo. This will become clear in the next section where we show control plots that clearly separate prompt samples and non-prompt muon samples.

Before we will show the full systematics of the estimated numbers we compare the QCD data-driven numbers with the Monte Carlo. To do so, we revert to the jet selection of jets with $\mathrm{p_T} > 20$ GeV and we obtain Table 7.5:

jets ($p_T > 20$ GeV)	1	2	3	$\geq$4
QCD	287.7 ± 11.1	121.4 ± 7.3	42.9 ± 4.3	13.3 ± 2.5
top MC	0.8	4.2	10.2	24.7
rest MC	1905.9	506.8	133.4	46.4
total estimate	2194.4	632.4	186.5	84.5
data	2419	691	185	100

Table 7.5: *Number of estimated QCD events plus statistical uncertainty and the number of Monte Carlo events scaled to 2.89 pb^{-1} after $\not{E}_T$ cut for a given number of selected jets with $p_T > 20$ GeV. Also the number of data events is shown.*

The table can now directly be compared to Table 7.2. The estimated QCD is almost the same as the Monte Carlo prediction of Table 7.2, but for only a third of the integrated luminosity: 2.89 compared to 10 pb^{-1}. This confirms our preliminary conclusion in the previous chapter that the number of QCD events is larger in data than expected from Monte Carlo. The difference is about a factor 3, which was used for the rough scaling in Chapter 6. Comparing Table 7.4 (jets with $\mathrm{p_T} > 25$ GeV) and Table 7.5 (jets with $\mathrm{p_T} > 20$ GeV) also immediately justifies the higher $\mathrm{p_T}$ cut for jets: the top-quark contribution in the $\geq$4 jet bin decreases by 23% whereas the QCD content in the same bin decreases by 70%.

Systematics

We will now present the full overview of the systematic uncertainties for the given results. As explained in Section 7.3.2 we will obtain the systematic uncertainties σ_A (control region) and σ_B (contamination) from data and use the value of $\sigma_C = 16\%$ for the performance test as indicated earlier. We also now quote here the uncertainty related to the efficiencies (E) as in equation (A.5). All relative uncertainties are listed in Table 7.6.

The first thing to note is that the largest single source of systematic uncertainty is the performance test (C). The other large sources of systematic uncertainties like A and E are actually statistics limited and will decrease when applied to larger data samples. The second thing to note is the large statistical uncertainty in the $\geq$4 jet bin due to the limited number of events in this bin ($N^{\mathrm{loose}} = 72$ and $N^{\mathrm{tight}} = 61$). Here one can clearly see the problem with our definition of the loose selection. Due to the small difference between N^{loose} and N^{tight}, the statistical uncertainty is going to be the largest source of uncertainty especially when applying even tighter cuts. It has been shown however that there are other problems with choosing a looser definition in Section 7.2.

jets	1	2	3	$\geq$4
A: control region	10.9 %	10.9 %	11.0 %	11.0 %
B: contamination	1.8 %	1.8 %	1.8 %	1.8 %
C: performance	16.0 %	16.0 %	16.0 %	16.0 %
D: $\epsilon_{\text{real}}^{MC}$	2.0 %	2.0 %	2.0 %	2.0 %
E: $\epsilon_{\text{real}}/\epsilon_{\text{fake}}$	11.9 %	12.0 %	12.1 %	14.9 %
total systematic uncertainty	22.9 %	23.0 %	23.0 %	24.6 %
statistical uncertainty	3.8 %	7.2 %	13.9 %	35.6 %

Table 7.6: *Relative systematic uncertainties for different jet multiplicities. Also shown is the statistical uncertainty.*

For completeness we present the full estimation in the different jet bins with their systematic and statistical errors in absolute values:

jets	1	2	3	$\geq$4
QCD	300.7 ± 11.4 ± 69.0	84.2 ± 6.1 ± 19.3	22.7 ± 3.2 ± 5.2	3.9 ± 1.4 ± 1.0

Table 7.7: *Number of estimated QCD events with statistical error (first) and systematic error (second) after $\not{E}_T$ cut for 2.89 pb^{-1} for a given number of selected jets with p_T above 25 GeV.*

7.4.2 Data driven QCD distributions

To be confident that the matrix method prediction is indeed QCD background and not something else, more is needed than just the overall numbers. The plot in Figure 7.7 and the numbers in Table 7.4 give already a good hint that the prediction is of the right order of magnitude since data and total estimation are in agreement. In this section three distributions will be studied that separate QCD background from events with prompt muons to understand the predicted background in more detail.

The matrix method can be used not only to estimate the number of QCD background events, but also to predict the shape of distributions of this background. The only difference to the method described above is that one uses N^{loose} and N^{tight} per bin in the variable one wants to predict in stead of for an entire sample. One has to assume that the efficiencies do not depend on the plotted variable, since only then one can use the earlier derived values for ϵ_{fake} and ϵ_{real}. In principle the efficiencies could be derived as a function of any variable, but the limited dataset available makes this impossible. To extract ϵ_{fake} as a function of any variable one needs in each bin events with d0 significance larger than 5. The statistics will then be severely limited. For now the assumption will be made that the ϵ_{fake} is flat as a function of the variable that is presented.

Missing transverse energy

Since QCD has low $\not{E}_T$ compared to the other background sources, $\not{E}_T$ is an interesting variable to investigate. In Figure 7.8 we show the $\not{E}_T$ in data with also the scaled Monte Carlo samples and the data-driven QCD shape after $\not{E}_T$ cut for 1 jet (left) and 2 jets (right). The errors are the full errors on the QCD estimate (systematic plus statistical uncertainty).

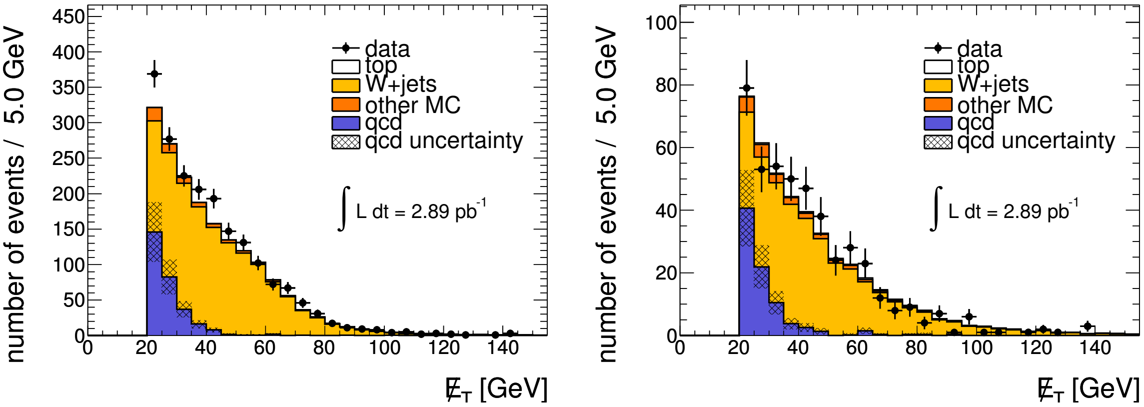

Figure 7.8: *The $\not{E}_T$ distribution with the Monte Carlo samples and the data-driven QCD shape after $\not{E}_T$ cut. Left: in the 1 jet bin. Right: in the 2 jet bin.*

As expected, we can see the bulk of the QCD at low values of $\not{E}_T$. Together (Monte Carlo and data-driven QCD) describe the data well within errors.

Transverse W-mass

Another useful variable to separate QCD and other backgrounds is the transverse W-mass. The transverse W-mass is given by:

$$\mathrm{M}_W^{\mathrm{trans}} = \sqrt{(\mathrm{p_T} + \not{E}_\mathrm{T})^2 - (\mathrm{p_x} + \not{E}_\mathrm{x})^2 - (\mathrm{p_y} + \not{E}_\mathrm{y})^2}, \qquad (7.12)$$

where the $\mathrm{p_T}$, $\mathrm{p_x}$ and $\mathrm{p_y}$ are muon quantities. There are two reasons that this is a very useful plot to distinguish QCD and other background. The first one is that we know that the biggest background to top-quark physics is W+jets and that this background will produce a Jacobian peak around 80 GeV in this distribution [29]. The other reason is that QCD will mainly have low $\mathrm{M}_W^{\mathrm{trans}}$. To see this we rewrite the equation as follows:

$$\mathrm{M}_W^{\mathrm{trans}} = \sqrt{2\mathrm{p_T}\not{E}_\mathrm{T}(1 - \cos\Delta_\phi)}, \qquad (7.13)$$

where Δ_ϕ is the difference in the ϕ angle between the lepton and the direction of $\not{E}_T$ in the transverse plane. We know that if QCD passes the $\not{E}_T$ requirement it is usually due to the missed b-jet and hence the Δ_ϕ will be peaked around 0. This will result in generally very low $\mathrm{M}_W^{\mathrm{trans}}$ for QCD events.

In Figure 7.9 we show the Δ_ϕ as mentioned above between the muon and the $\not{E}_{\mathrm{T}}$ for the data and for the Monte Carlo plus data driven QCD estimate.

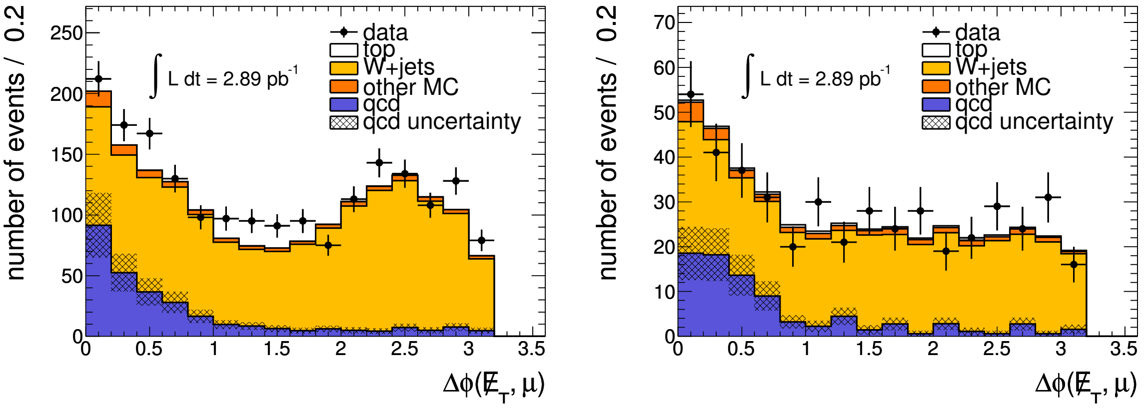

Figure 7.9: *The Δ_ϕ of muon and $\not{E}_T$ with the Monte Carlo samples and the data-driven QCD shape after $\not{E}_T$ cut. Left: in the 1 jet bin. Right: in the 2 jet bin.*

Note that QCD is indeed located at low Δ_ϕ and that the data could not be described by the prompt Monte Carlo samples alone. The measurement of the $Z \to \mu^+\mu^-$ production cross section [137] has revealed that the width of the Z mass distribution is larger in data than in Monte Carlo. This effect is due to the momentum resolution which is not as good as described by simulation, most likely due to more material than was accounted for. To better compare MC and data, a prescription has been given that involves smearing the muon $\mathrm{p_T}$ [106], which will be used when plotting the transverse mass.

In Figure 7.10 we show the transverse mass in data with also the scaled Monte Carlo samples and the data-driven QCD shape after $\not{E}_{\mathrm{T}}$ cut for 1 jet (upper left), 2 jets (upper right), 3 jets (bottom left) and 4 jets (bottom right). The errors are the full errors (systematic plus statistical uncertainty).

One can immediately note the W peak the we mentioned above, which is nicely described by the W+jets Monte Carlo (as expected). On the low $\mathrm{M}_W^{\mathrm{trans}}$ we see a large excess of data events that are not described by the prompt Monte Carlo samples. However, we see that this region is well described by the QCD matrix method estimate, except in the 1 jet bin. In this bin there is an underestimation in both the QCD region and the W+jets region. This underestimation was already noted in Figure 7.7. Since both the data-driven QCD and the W+jets simulation have large uncertainties, the data is well described within the errors. To check how well data is described by the data-driven QCD and the Monte Carlo the Kolmogorov-Smirnov (KS) test has been performed [138]. The KS test is non-parametric test of the equality of one-dimensional distributions and returns a value between one and zero, where one is a perfect match. It takes into account the shapes, but also the normalization. The KS test returns a value of 0.43 for the one jet bin and confirms that the agreement is poor. It seems that in this bin the QCD

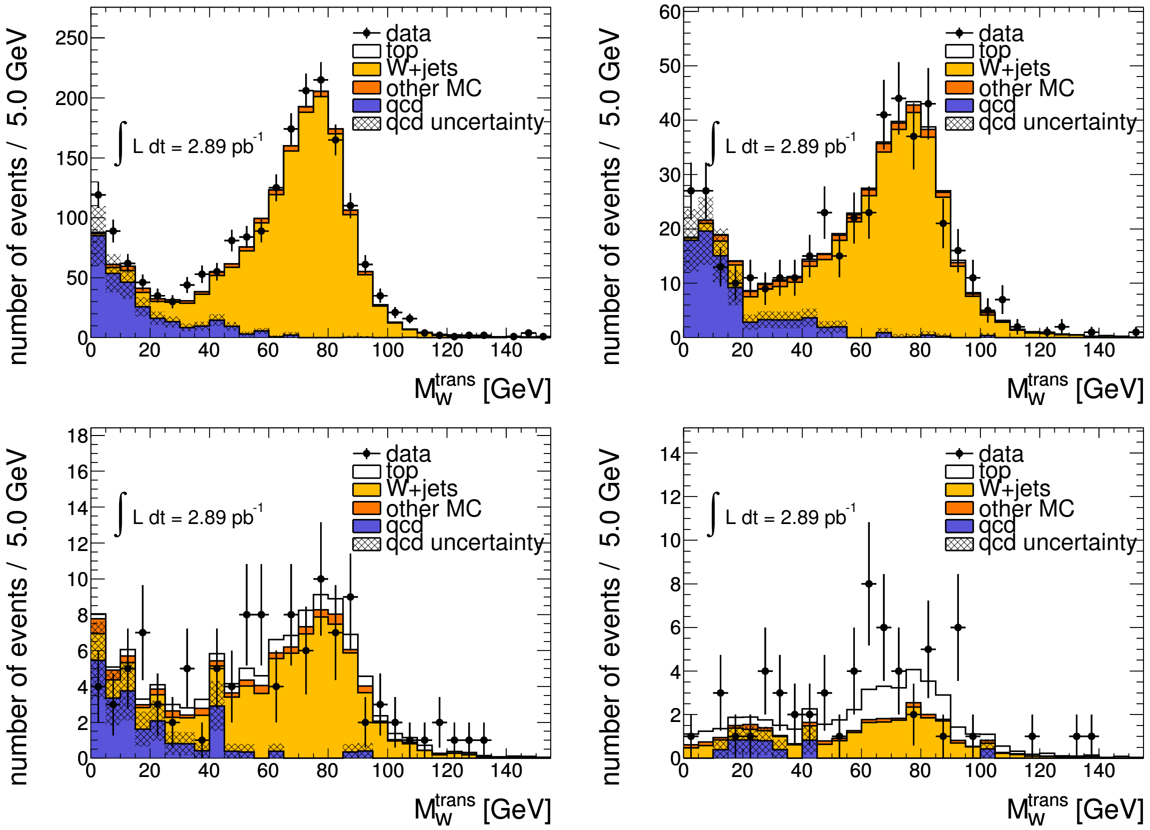

Figure 7.10: *The transverse W-mass with the Monte Carlo samples and the data-driven QCD shape after $\not{E}_T$ cut. Upper left: in the 1 jet bin. Upper right: in the 2 jet bin. Bottom left: in the 3 jet bin. Bottom right: in the 4 jet inclusive bin.*

underestimation is causing the low KS value. This has been checked by scaling the QCD up with only 10% to yield a KS value of 0.89. In the 2 jet bin however the KS test returns a value of 1.00. Values of 0.91 and 0.97 have been found for the 3 and 4 jet bin respectively. This now is convincing evidence that the method predicts QCD well in a region where we expect almost pure QCD.

7.5 Additional cuts to reduce the QCD background

In the previous chapter it was already concluded that the QCD content is larger than expected from Monte Carlo, which was confirmed by the results in the previous sections. In Section 3.3 it was mentioned that there are two cuts that lower the background from QCD drastically: b-tagging and the triangular cut (which is given by ($\not{E}_T$ + M_W^{trans}) > 60 GeV). Note that b-tagging also cuts away most other backgrounds, notably W+jets and is an important tool to purify the selected sample of $t\bar{t}$ candidates. Since both cuts are efficient in rejecting QCD we have to adapt our method slightly to be able to deal with the small number of events after these additional cuts. In Section 7.5.1 the effect of requiring a b-tag will be discussed, Section 7.5.2 will cover the triangular cut and finally in Section 7.5.3 the combination of both cuts will be investigated.

7.5.1 Additional requirement 1: at least one *b*-tagged jet

In Section 3.3.2 we have seen that requiring at least one b-tagged jet is an efficient way to reduce the main backgrounds, W+jets and QCD. The requirement greatly improves the purity for $t\bar{t}$ analysis. The number of N^{loose} and N^{tight} events after requiring at least one jet with a b-tag (SV0 weight > 5.72 see Section 3.3.2) is presented in table 7.8.

jets	1	2	3	≥4
N^{loose}	114	76	34	24
N^{tight}	49	38	20	21

Table 7.8: *Number of loose and tight events with a given number of jets with $p_T > 25$ GeV after $\not{E}_T$ cut and b-tagging.*

The table can be compared to Table 7.3 where we showed the numbers without b-tag requirement. It is directly clear how powerful the b-tag cut is, not only for QCD, but for all backgrounds when comparing the tables and noting that the efficiency to tag at least one b-jet in a $t\bar{t}$ event is about 75%, see Table 3.1. Due to the small number of events it is hard to directly apply the method since there are simply almost no events with d0 significance > 5 to obtain ϵ_{fake}. We cannot just use the ϵ_{fake} as was obtained pretag (i.e. before requiring at least one b-tagged jet) since a priori we cannot be sure that it is the same as after b-tag requirement. The ϵ_{fake} obtained in the 1 jet inclusive bin after b-tag is:

$$\epsilon_{\text{fake}} = 0.276 \pm 0.083 \text{ (stat)}. \tag{7.14}$$

We can see by comparing (7.11) and (7.14) that the uncertainty on ϵ_{fake} increases by more than a factor three. The efficiency agrees with the pretag efficiency within their errors. Having checked that the pretagged efficiency can be used for the b-tagged QCD estimation still leaves the problem of the small number of events of N^{loose} and N^{tight} after b-tagging which will generate a large statistical uncertainty. The solution that we have adopted for this problem is to extrapolate the pretagged QCD estimates to the tagged numbers by using the b-tag efficiency per jet multiplicity from Monte Carlo. The arguments to support our choice to do so are the following:

- The b-tagging efficiency is well modeled for heavy flavour (HF) jets. The uncertainty on the b-tagging efficiency is less than 20% for b-jets [120] and due to limited statistics higher for c-jets (estimated to be twice the b-tag uncertainty). We will quote 30% to be conservative.

- We believe that all our muons originate from HF decay. Apart from our Monte Carlo studies of Chapter 4 and 5 there are also data studies that show that almost all high-$\mathrm{p_T}$ muons originate from semi-leptonic HF decay [139]. The HF fraction is measured to be above 70% for muons with $\mathrm{p_T}$ between 10 and 20 GeV. This fraction is expected to be even larger for our selections that include the $\mathrm{p_T}$ of the muon above 20 GeV, at least 1 jet with $\mathrm{p_T}$ over 25 GeV and missing energy.

- By looking in a QCD enhanced control region in both Monte Carlo and data we compared the b-tag efficiency. As we have seen in Figure 7.10, the lower $\mathrm{M}_W^{\mathrm{trans}}$ region is dominated by QCD and as control region one can look at events with $\mathrm{M}_W^{\mathrm{trans}} < 10$ GeV. Table 7.9 shows the number of tagged/pretagged events in Monte Carlo and data. We can conclude that the agreement between the b-tag efficiencies is reasonable.

	data	Monte Carlo
pretagged	199	292
b-tagged	5	12
$\epsilon_{b-\mathrm{tag}}$	(2.5 ± 1.1) %	(4.0 ± 1.2) %

Table 7.9: *Number of b-tagged and pretagged events and the b-tag efficiency (ϵ_{b-tag}) in data (2.89 pb^{-1}) and QCD Monte Carlo (10 pb^{-1}) with 1 jet with $p_T > 25$ GeV after $\not{E}_T$ cut and with $M_W^{trans} < 10$ GeV.*

- As a cross check we computed the number of QCD events using the method by obtaining the ϵ_{fake}, N^{loose} and N^{tight} after b-tag and performing the estimation directly and also by using the pretagged QCD numbers and applying the b-tagging efficiency in the 1 jet bin. With the direct estimation we found 24.63 ± 3.09 events and by extrapolating we estimated 21.03 ± 0.80 events. The QCD estimates are in reasonable agreement with each other.

We have shown that we can use the Monte Carlo b-tag efficiency per jet bin to extrapolate from the pretagged to the b-tagged results. Table 7.10 shows the efficiency to tag at least one jet per jet bin (jets with $\mathrm{p_T} > 25$ GeV).

jets	1	2	3	≥4
$\epsilon_{b-\mathrm{tag}}$	(7.0 ± 1.5) %	(12.9 ± 4.2) %	(15.6 ± 9.9) %	(59.3 ± 16.8) %

Table 7.10: *Efficiency in percent to find at least one b-tagged jet in the event per jet bin from Monte Carlo after $\not{E}_T$ requirement.*

The b-tag efficiency increases from only 7% in the 1 jet bin to about 60% in bin with 4 or more jets. The increase can be understood by the large probability of the HF parton that produced a high-$\mathrm{p_T}$ muon not to produce a high-$\mathrm{p_T}$ reconstructed jet (as was already mentioned in Section 4.3.1). This leads to events that are biased towards less reconstructed b-jets, especially at lower jet multiplicities.

Results

Using the $\epsilon_{b-\mathrm{tag}}$ from Table 7.10 we extrapolate the results as obtained after $\not{E}_{\mathrm{T}}$ cut to obtain the QCD estimate after b-tag. In Table 7.11 we present the estimated number together with the Monte Carlo and the number of data events. The uncertainty listed in the table is the statistical and the full systematic error. Note that the systematic error now contains a b-tag term coming from the statistical uncertainty of the $\epsilon_{b-\mathrm{tag}}$, see Table 7.10, and an extra 30% from the b/c-tagging uncertainty as explained above. Also shown in Table 7.11 are the results after triangular cut and the combination of b-tag requirement and triangular cut that will be derived in the next sections (the results after base selection were presented in Table 7.4).

b-tag

jets	1	2	3	≥4
QCD	21.0 ± 0.8 ± 9.1	10.9 ± 0.8 ± 5.4	3.5 ± 0.5 ± 2.6	2.3 ± 0.8 ± 1.1
top MC	0.7	4.0	9.4	14.2
rest MC	22.0	12.9	5.8	2.6
total	43.7	27.8	18.7	19.1
data	49	38	20	21

triangular cut

jets	1	2	3	≥4
QCD	50.6 ± 4.9 ± 11.7	14.5 ± 2.7 ± 3.4	4.7 ± 1.5 ± 1.1	1.5 ± 0.9 ± 0.5
top MC	1.5	5.7	11.2	16.8
rest MC	1399.1	334.9	73.4	21.9
total	1451.2	355.1	89.3	40.1
data	1556	367	97	55

b-tag + triangular cut

jets	1	2	3	≥4
QCD	3.5 ± 0.3 ± 1.5	1.9 ± 0.3 ± 0.9	0.7 ± 0.2 ± 0.5	0.9 ± 0.6 ± 0.5
top MC	0.6	3.6	8.1	12.8
rest MC	20.2	12.2	5.2	2.3
total	24.4	17.7	14.1	16.0
data	30	30	18	19

Table 7.11: *Number of estimated QCD events and the number of Monte Carlo events scaled to 2.89 pb^{-1} after the $\not{E}_T$ cut for a given number of selected jets. Also the number of data events is shown. The first error is the statistical error, the second is the full systematic error. Upper: after b-tag requirement. Middle: after triangular cut. Bottom: after both b-tag requirement and triangular cut. The results after base selection were presented in Table 7.4.*

The same numbers are shown in a stacked plot where the uncertainty is given by the statistical plus systematic uncertainty from the matrix method formula, see Figure 7.11.

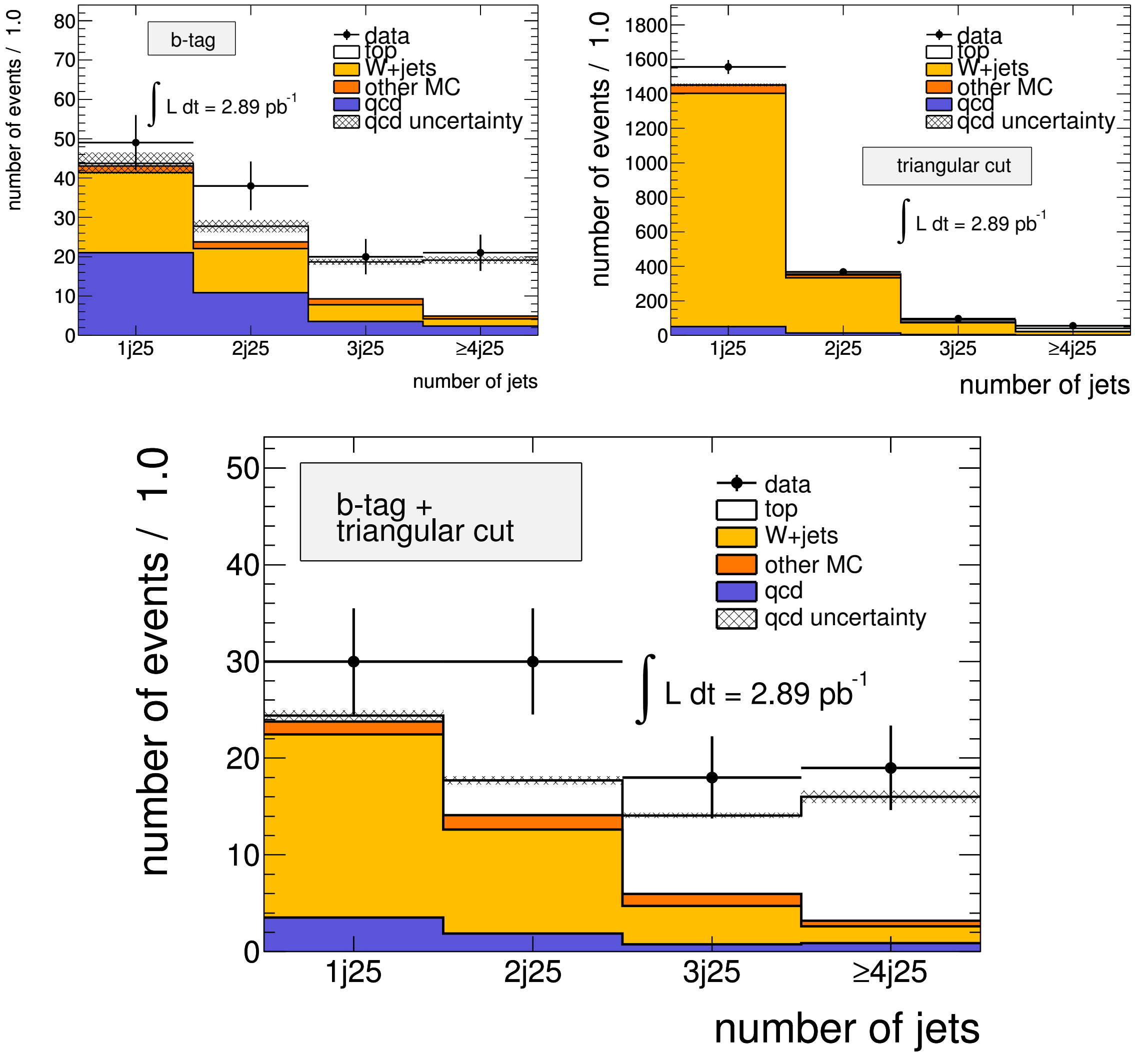

Figure 7.11: *Jet multiplicity distribution of various Monte Carlo samples scaled to 2.89 pb^{-1} added to the data-driven QCD estimate per jet bin after $\not\!\!E_T$ cut. The data points are also shown. The uncertainty is given by the statistical plus systematic uncertainty from the matrix method formula. Upper left: after b-tag requirement. Upper right: after triangular cut. Bottom: after both b-tag requirement and triangular cut.*

There is good agreement between the number of data events and the total of QCD prediction and prompt Monte Carlo events. In Figure 7.11 (top left) we can clearly see the large top-quark pair contribution in the 4 jet bin as is expected after *b*-tagging. The number of observed events in the 2 jet bin after the *b*-tag requirement is larger than predicted from simulation and data-driven QCD. As in the previous section, the origin of this can be checked by plotting the transverse mass and its QCD prediction.

In Figure 7.12 we show the transverse mass in data with also the scaled Monte Carlo samples and the data-driven QCD shape after $\not{E}_T$ cut and with at least one b-tagged jet for 1 jet (top left) and 2 jets (top right). The errors are the full errors (statistical plus systematic uncertainty).

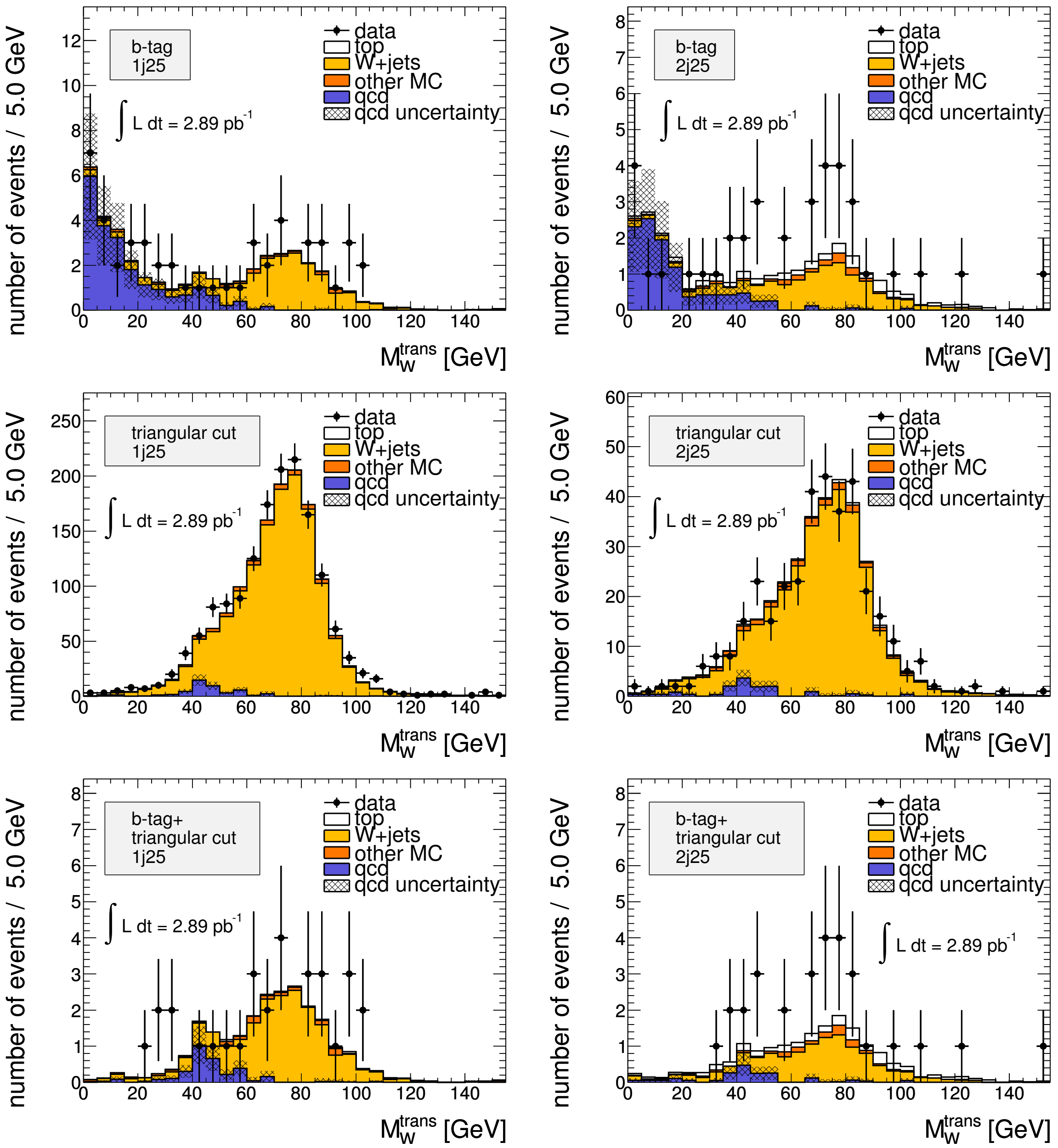

Figure 7.12: *The transverse mass with the Monte Carlo samples and the data-driven QCD shape after $\not{E}_T$ cut in the 1 and 2 jet bin. Upper: after b-tag requirement. Middle: after triangular cut. Bottom: after both b-tag requirement and triangular cut.*

The agreement between data and QCD plus Monte Carlo is in both figures good within their error, but the 2 jet bin (right) suggests a deficit in the number of simulated W+jet events. This will be confirmed in the next chapter where a data-driven W+jets estimate will be given in Section 8.2.1. We have thus confidence that the discrepancy in the 2 jet bin between data and the full estimate does not originate from underestimation of the QCD prediction.

7.5.2 Additional requirement 2: triangular cut

Probably the most powerful cut apart from lepton isolation to reduce QCD background is the triangular cut, as we have shown in Chapter 3, see Figure 3.6. By requiring $(\not{E}_{\mathrm{T}} + \mathrm{M}_W^{\mathrm{trans}}) > 60$ GeV we essentially cut away the entire low $\mathrm{M}_W^{\mathrm{trans}}$ region, which is dominated by QCD as we have seen before, for example in Figure 7.12 (top). Due to the effectiveness of the cut we have the same problem as in the previous section: low statistics. Since we do not expect the probability of a loose muon to become tight to change after the cut, our solution to the problem will be to use the ϵ_{fake} as obtained before the triangular cut. The assumption that ϵ_{fake} does not change has been tested on MC with a performance test as described in Section 7.3.1 and the biggest difference that was found was 24%. Note that this difference was observed in the 4 or more jet bin where the statistics is low and the predicted and true number of QCD events agreed well within the errors. No extra systematic uncertainty will be assigned to this assumption. Using the ϵ_{fake} as before on the N^{loose} and N^{tight} after triangular cut we obtain the estimated QCD numbers as shown in Table 7.11 (middle), where we again also show the prompt Monte Carlo numbers and the number of data events. In Figure 7.11 (top right) the same numbers are shown graphically.

As in the pretagged case, we see a small deficit in the 1 jet bin when we compare data to Monte Carlo plus QCD. Again we will have to look at the transverse mass plot to identify the origin of this. In Figure 7.12 (middle) we show the transverse mass in data with also the Monte Carlo samples and the data-driven QCD shape after $\not{E}_{\mathrm{T}}$ cut and triangular cut for 1 jet (left) and 2 jets (right). The errors are the full errors (statistical plus systematic uncertainty).

From Figure 7.12 (middle) we can conclude that data and Monte Carlo plus QCD agree well. The Kolmogorov-Smirnov (KS) test has been performed [138] and the KS values that were found are 0.90 and 0.98 for the 1 and the 2 jet bin respectively. Also note that when the QCD estimate is not taken into account when performing the KS test, these values decrease to 0.17 and 0.91 respectively.

7.5.3 Combined requirements 1 and 2

In this section we will use both the triangular cut and b-tagging to obtain an estimate of QCD in a very pure top-quark pair sample. This is the selection that will be used in Chapter 8 for the top-quark pair production cross section measurement. For this estimate the numbers of the previous section, i.e. after triangular cut, are used and the b-tag efficiency is applied as mentioned in Table 7.10. We show the estimated QCD prediction and the Monte Carlo numbers in Table 7.11 (bottom). In Figure 7.11

(bottom) the same numbers are presented graphically. Note that 19 events have passed all requirements and are considered $t\bar{t}$ candidate events.
Figure 7.11 (bottom) shows good agreement between data and Monte Carlo plus QCD prediction. The only bin that seems underestimated is the 2 jet bin again, as in Section 7.5.1. We have already seen that this is most likely due to an underestimation of W+jets which can be seen by plotting the transverse mass. In Figure 7.12 (bottom) we show the transverse mass in data with also the scaled Monte Carlo samples and the data-driven QCD shape after $\not{E}_{\mathrm{T}}$ cut with at least one b-tagged jet and triangular cut for 1 jet (left) and 2 jets (right). The errors are the full errors (statistical plus systematic uncertainty). The agreement between data and Monte Carlo plus QCD is good (within statistics) which is reflected in the KS test values of 0.88 and 1.00 for the 1 jet and 2 jet bin respectively. The transverse mass distribution shows that the deficit in the 2 jet bin stems from both the region where the QCD is present, but also from the almost pure W+jets region.

7.6 Results

In this chapter we have shown that the matrix method is a powerful tool to obtain an estimate of the QCD background in the top-quark pair signal region, but also in regions with less jets. The results of the QCD prediction will be used for the top-quark pair production cross section measurement in the next chapter and by others for data-driven estimation of the W+jets contribution in various jet bins for example. The results after base selection show good agreement between data and MC plus data-driven QCD in important control distributions like $\not{E}_{\mathrm{T}}$ and $\mathrm{M}_{\mathrm{W}}^{\mathrm{trans}}$. Note that the QCD background is three times larger than predicted by existing simulation. In Section 7.5.1 we investigated the usability of the method after b-tagging, since b-tagging jets is a useful tool to reduce all backgrounds like W+jets and QCD. The results show good agreement again between data and MC plus data-driven QCD, albeit with large uncertainties. The QCD estimate has also been shown after the triangular cut. In the last section both cuts have been applied and the QCD estimate is presented that can be directly used for the cross section calculation in the next chapter. In the signal region after all cuts with four or more jets we arrived at an estimate of the QCD background of 0.9 ± 0.6 (stat) ± 0.5 (syst) events. In that same bin the MC top-quark pair expectation is 12.8 events and 2.3 events are expected from other backgrounds, see Table 7.11 (bottom).

CHAPTER 8

TOP-QUARK PAIR PRODUCTION CROSS SECTION MEASUREMENT

In this chapter the observation of $t\bar{t}$ production at the `LHC` at $\sqrt{s} = 7$ TeV will be presented. With the `ATLAS` detector 19 candidate events have have been observed that survived all selection criteria in the muon channel (see Table 7.11, bottom). In Figure 8.1 we show a typical selected $t\bar{t}$ candidate event. The number of selected events together with the number of estimated background events can be translated into a $t\bar{t}$ production cross section measurement. Like the previous chapter, this study was performed in the context of the first top-quark pair production cross section publication [3] ("Measurement of the top quark-pair production cross section with `ATLAS` in pp collisions at $\sqrt{s} =$ 7 TeV.") and we will follow the paper closely in estimation of other backgrounds apart from QCD. Method and systematic uncertainty studies from the paper will be used, but the number of estimated QCD background events are taken from this thesis[1].

The 'cut and count' method, which will be used to extract the cross section, is presented in Section 8.1. The main backgrounds to the analysis, apart from QCD, are discussed in Section 8.2, where we focus in particular on W+jets background. In Section 8.3 the top-quark pair production cross section is extracted and an overview of all involved systematic uncertainties is given. The chapter closes with a summary in Section 8.4 and an outlook in Section 8.5.

8.1 The 'cut and count' method

The 'cut and count' method is the most straightforward method to extract the $t\bar{t}$ production cross section. Due to the low statistics and the early analysis, it is this simple and therefore robust method that has been chosen as the default method for the first top-quark pair production cross section publication of `ATLAS`. The method is based on an

---

[1] The estimated number of QCD events derived in the previous chapter served as input for the paper.

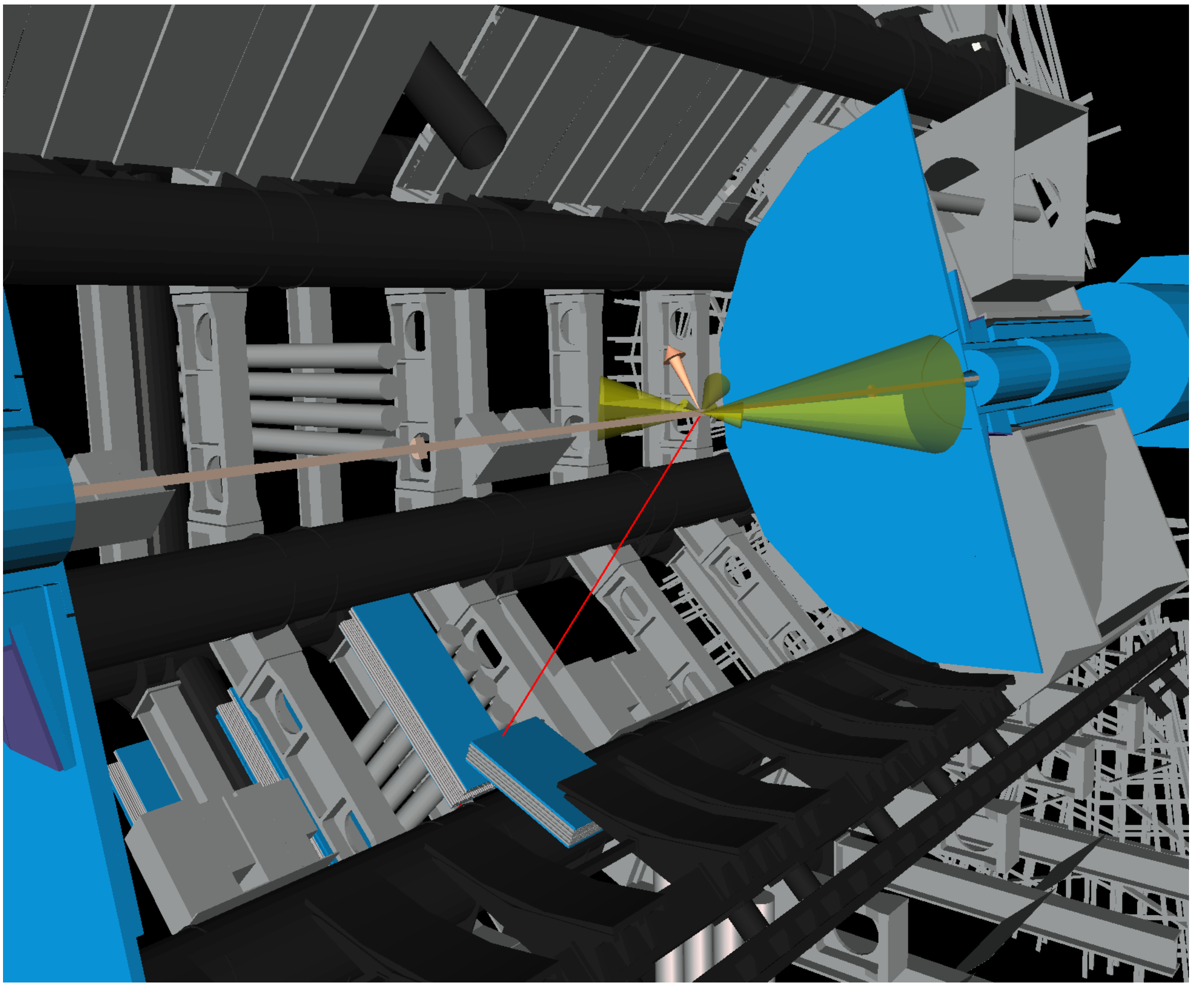

Figure 8.1: *A $t\bar{t}$ candidate event recorded on the 20th of August 2010 (run-number 162347, event-number 34820367) selected with the base selection plus extra requirements. The jets are depicted as cones, the $\not{E}_T$ is the arrow-cone and the muon track is drawn as the red line. The display is made with* `VP1` *[140].*

estimated number of signal events (N_{sig}) in the b-tagged sample with four or more jets, which is computed by subtracting the estimated background (N_{bkg}) from the observed event yield (N_{obs}). The $t\bar{t}$ cross section is then extracted using the formula:

$$\sigma(t\bar{t}) = \frac{N_{sig}}{\mathcal{L} \times \epsilon} = \frac{N_{obs} - N_{bkg}}{\mathcal{L} \times \epsilon}, \tag{8.1}$$

where $\mathcal{L}$ is the integrated luminosity and ϵ the efficiency for $t\bar{t}$ events to pass the selection criteria. The latter is estimated from simulation and can be directly derived from the $t\bar{t}$ numbers of Table 3.1 corrected with the scale factor of Equation 6.3 to be: $\epsilon = \frac{12.81}{250.79} = 0.051 \pm 0.014$ (stat). Since the MC signal sample used in this thesis does not include fully hadronic $t\bar{t}$ events[2], the efficiency has to be corrected with the theoretical branching ratio of semi-leptonic and dileptonic $t\bar{t}$: $\frac{1.00}{0.54}$, see Section 1.3.2. With the measured $\mathcal{L}$, the observed number of events and the estimated number of background events $\sigma(t\bar{t})$ can be computed.

8.2 Background estimations

The cross section determination will be performed after having applied all the requirements discussed in the previous chapter ensuring a pure selection of top-quark candidates. These requirements include the triangular cut ($\not{E}_{\mathrm{T}} + \mathrm{M}_W^{\mathrm{trans}} > 60$ GeV), at least four jets with $\mathrm{p_T} > 25$ GeV and at least one jet which is tagged as a b-jet (tagged jet). In the previous chapter the QCD background has been estimated as function of the number of selected jets with and without b-tagging. The W+jets background, which is the major background to top-quark analysis, can also be estimated in a data-driven way. All remaining backgrounds will be estimated with MC simulation only.

8.2.1 Data-driven W+jets background

The theoretical uncertainties on the amount of W+jets events in the signal region (as described in the previous section, with b-tag and at least four jets) is large due to variations of the renormalization scale in `ALPGEN` [141]. Fortunately this background can be obtained with a data-driven approach. In general we can write:

$$W_{\mathrm{tagged}}^{\geq 4\mathrm{jets}} = W_{\mathrm{pretagged}}^{\geq 4\mathrm{jets}} \cdot f_{\mathrm{tagged}}^{\geq 4-\mathrm{jet}}, \tag{8.2}$$

where $W_{\mathrm{pretagged}}^{\geq 4\mathrm{jets}}$ is an estimate of the number of events in the pretagged (without the b-tag requirement) selection and f_{tagged} is given by the fraction of events with more than three jets that have at least one b-tag. The fraction can be obtained from data in the following way:

$$f_{\mathrm{tagged}}^{\geq 4-\mathrm{jet}} = f_{\mathrm{tagged}}^{2-\mathrm{jet}} \cdot C_{2\to\geq 4}^{\mathrm{corr}}, \tag{8.3}$$

with $f_{\mathrm{tagged}}^{2-\mathrm{jet}}$ the fraction of tagged W+jets events in the two jet bin and $C_{2\to\geq 4}^{\mathrm{corr}}$ a correction function that takes into account the difference in tagging probability in the different jet bins and different flavour compositions. The correction function can be compared to the tagging efficiency presented in Table 7.10 where the efficiency was given for QCD events that produce an isolated muon. The measurement of the various terms will be discussed in detail in the following sections.

Estimate of the W+jets background before flavour tagging

It has been shown by Berends et al. [134] that the ratio of W+n+1 jet events to W+n jet events is expected to be approximately constant. Writing this ratio as α, the number of W+jets events in the three jet bin (N_3) and in the four jet bin (N_4) are given by:

---

[2] The $t\bar{t}$ events where both W-bosons decay hadronically, see Section 1.3.2.

$$\begin{aligned} N_3 &= \alpha N_2, \\ N_4 &= \alpha N_3 = \alpha^2 N_2, \end{aligned}$$

where N_2 is the number of W+jets events in the two jet bin. By induction it can be seen that for all events with four or more jets ($N_{\geq 4}$) the number of events can be written as:

$$N_{\geq 4} = N_2 \cdot \sum_{i=2}^{\infty} \alpha^i.$$

This feature can be used to extract the first term of Equation 8.2 with the following expression:

$$W^{\geq 4\text{jets}}_{\text{pretagged}} = W^{2\text{jets}}_{\text{pretagged}} \cdot \sum_{i=2}^{\infty} (W^{2\text{jets}}_{\text{pretagged}} / W^{1\text{jet}}_{\text{pretagged}})^i, \tag{8.4}$$

where all measurements are performed after the triangular cut, but without the requirement of a b-tag. The data-driven technique gives an estimate of the $W \to \mu\nu$ ($W \to e\nu$) background in the μ (e) channel. Although $W \to \tau\nu$, where the τ decays leptonically, is a significant background, the jet multiplicity of these events is different after selection from $W \to \mu\nu$ ($W \to e\nu$). This background is estimated separately using the data-driven $W \to \mu\nu$ ($W \to e\nu$) estimate and the rate of $W \to \tau\nu / W \to l\nu$ ($l = \mu, e$) background from MC.

Equation 8.4 shows that an estimate of the W+jets contribution in events with four or more jets can be obtained by measuring the number of W+jets events in the one and two jet bin which are almost free of $t\bar{t}$ events. The single largest non-W background in those jet bins is QCD, which has been estimated in the previous chapter. The purity of the W+jets selection can be seen in Figure 7.12 (middle) and the estimated number of $W \to \mu\nu$ is then given by subtracting the number of data-driven QCD events and the number of other backgrounds from the number of data events (W candidates). In Table 8.1 the number of W+jets candidates is shown for the one and two jet bin as well as the estimated data-driven QCD background and all other non-W backgrounds from simulation where the decay $W \to \tau\nu$ is included in the 'other background' category.
Note that about half of the 'other background' in the Table 8.1 is $W \to \tau\nu$. The estimated and MC simulated number of pretagged events agree within their error. With $W^{1\text{jet}}_{\text{pretagged}} = 1409 \pm 44$ and $W^{2\text{jet}}_{\text{pretagged}} = 314 \pm 21$, the ratio between the 2 jet and the 1 jet rate is 0.22 ± 0.02. This then leads to the following estimate according to Equation 8.4:

$$\begin{aligned} W^{\geq 4\text{jets}}_{\text{pretagged}}(\text{from } W \to \mu\nu) &= W^{2\text{jets}}_{\text{pretagged}} \cdot \sum_{i=2}^{\infty} (W^{2\text{jets}}_{\text{pretagged}} / W^{1\text{jet}}_{\text{pretagged}})^i \\ &= 314 \cdot 0.064 \\ &= 20.1 \pm 4.6 \text{ (stat)}, \end{aligned}$$

jets	1	2	2 with b-tag
data (W candidates)	1556	367	30
data driven QCD	50.6 ± 12.7	14.5 ± 4.3	1.9 ± 1.0
other backgrounds	96 ± 15	39 ± 7.0	5.8 ± 1.7
estimated $W \to \mu\nu$	1409 ± 44	314 ± 21	22.3 ± 5.8
MC $W \to \mu\nu$	1304 ± 309	302 ± 100	10.0 ± 7.0

Table 8.1: *Number of selected events in the 1 and 2 jet bin without b-tag requirement and in the 2 jet bin with b-tag.*

where the statistical uncertainty is given by the uncertainty on the number of estimated W+jets events in the 1 and 2 jet bin. The following list of systematic uncertainties has been identified when calculating the W+jets background without b-tag [133]:

- The purity of the W+jet sample is dominated by the QCD normalization uncertainty. Correlations of uncertainties between the jet bins are taken into account and the total uncertainty due to the purity is computed to be 11%.
- The assumption that the ratio W+n jets to W+n+1 jets is constant has been checked for predictions with different MC generators and generator settings at parton level. The average observed discrepancy was 24%.
- The only significant contribution to the experimental uncertainty on the assumption that the ratio $W + n$ jets to $W + n + 1$ jets is constant has been found to be the jet energy scale. This is computed to be 7%.

The $W \to \tau\nu$ contribution has been estimated using the ratio of $W \to \tau\nu/W \to l\nu$ from MC. We found 1.2 events in events with four or more jets. The total number of W-boson events decaying into muons including intermediate τ production is then:

$$W^{\geq 4\text{jets}}_{\text{pretagged}} = 21.3 \pm 7.6 \ (\text{stat} + \text{syst}), \tag{8.5}$$

which can be compared to the MC prediction of $W^{\geq 4\text{jets MC}}_{\text{pretagged}} = 19.6 \pm 13.1$. The estimated and the MC simulated number of $W \to \mu\nu$ events agree well within their error. The MC uncertainties include theoretical production uncertainties, but also jet energy scale effects and selection efficiencies and are scaled from the top-quark pair production cross section publication [3].

Estimate of the W+jets background in the tagged selection

In the previous section the number of W-boson events in the pretagged selection for events with four or more jets has been estimated. In this section we will extrapolate this estimate to the tagged selection using Equation 8.2 and 8.3. For the second term of Equation 8.2, the tagging fraction for events with four or more jets, $f^{\geq 4-\text{jet}}_{\text{tagged}}$, can be computed according to Equation 8.3. To extract $f^{2-\text{jet}}_{\text{tagged}}$ the number of $W^{2\text{jets}}_{\text{tagged}}$ events and

$W^{\mathrm{2jets}}_{\mathrm{pretagged}}$ events is needed. By computing the ratio, the fraction of tagged events in the two jet bin is computed. The numbers are given by subtracting the non-W background from the tagged and pretagged events in the 2 jet bin. For both the untagged and the tagged case the numbers were already presented in Table 8.1.
There is a difference in the estimated and MC simulated number of events after b-tag, which was also already observed and mentioned in Figure 7.11 (bottom). The ratio of tagged to pretagged events that was computed is:

$$f^{\mathrm{2-jet}}_{\mathrm{tagged}} = 0.068 \pm 0.014. \tag{8.6}$$

The last ingredient of Equation 8.3 is the correction factor for the tagging ratio between the two and four jet bin, $C^{\mathrm{corr}}_{2\to\geq 4} = f^{\geq 4-\mathrm{jet}}_{\mathrm{tagged}} / f^{\mathrm{2-jet}}_{\mathrm{tagged}}$. This factor has been derived from simulation studies and determined to be:

$$C^{\mathrm{corr}}_{2\to\geq 4} = 2.8 \pm 0.8\ (\mathrm{syst}). \tag{8.7}$$

The correction factor is different from what can be derived for QCD events from Table 7.10. Since the QCD events that were considered for that table are required to have produced an isolated high-$\mathrm{p_T}$ muon, the probability for the remainder of the b-jet to become a high-$\mathrm{p_T}$ jet is low. This leads to a lower tagging probability in events with less jets than for W+jets events. The assumptions that were made for the derivation of the correction factor and the associated uncertainties are the following [133]:

- An uncertainty on the MC prediction in the 2 jet bin of 300 % on the W+bb+jets and W+cc+jets fractions and 100% on the W+c+jets fraction is assumed.
- The difference between MC and data b-tag efficiency for b, c and light jets introduces an additional uncertainty of 20% for the heavy flavour and 100% for the light jet component.
- Variation of MC generator settings are considered that give rise to uncertainties on the ratios of fractions in the 2 jet and 4 jet bin for W+bb+jets, W+cc+jets and W+c+jets. The uncertainties derived are increased by a factor two to be conservative and add up to 40%-60%.

The dominant uncertainty for the correction factor comes from this last point. The reason that the systematic uncertainties, while large by themselves, translate into a small error on the correction factor is because of effective cancellations in the ratio of $f^{\geq 4-\mathrm{jet}}_{\mathrm{tagged}} / f^{\mathrm{2-jet}}_{\mathrm{tagged}}$.
Finally we conclude that using Equation 8.2 the estimated W+jets background in events with four or more jets with b-tagging is:

$$W^{\geq \mathrm{4jets}}_{\mathrm{tagged}} = 4.0 \pm 2.0\ (\mathrm{stat} + \mathrm{syst}), \tag{8.8}$$

which is more than twice the number expected from MC (1.7 events).

8.2.2 Summary of all backgrounds

The main backgrounds, W+jets and QCD, have been estimated in a data-driven way in Chapter 7 and Section 8.2.1 respectively. The other backgrounds will be extracted from MC simulation. They are expected to be smaller than W+jets and less uncertain than QCD. In Table 8.2 the full breakdown of all backgrounds in the four or more jet sample with b-tag is shown together with the observed number of $t\bar{t}$ candidate events, the MC numbers are taken from Table 3.1 (corrected with the scale factor of Equation 6.3).

	events
data-driven W+jets	4.0 ± 2.0
data-driven QCD	0.9 ± 0.7
MC Z+jets	0.1 ± 0.1
MC di-boson	0.1 ± 0.1
MC single top	0.5 ± 0.1
total background	5.6 ± 2.1
$t\bar{t}$ candidates (data)	19

Table 8.2: *Estimated number of background events in events with four or more jets with b-tag and the observed number of $t\bar{t}$ candidate events in data.*

The table shows the excess of events with respect to the estimated background, which will be identified with $t\bar{t}$ events and will be used in the next section to extract the $t\bar{t}$ cross section. The number of $t\bar{t}$ candidate events is then 13.4 which can be compared to the expected number of events from Monte Carlo of 12.8, see Table 7.11 (bottom).

8.3 Extracting the top-quark pair production cross section

The number of background events that passes the full selection has been estimated in the previous section and together with the number of selected $t\bar{t}$ candidates can now be used to quantify the significance of the observation of $t\bar{t}$ signal. After testing that the candidate events also fulfill the $t\bar{t}$ hypothesis by plotting their three jet invariant mass, we will finally extract the $t\bar{t}$ cross section.

Significance

A significance of $\sigma = 3.2$ has been computed for the observation of $t\bar{t}$ production in `Atlas` using the numbers in Table 8.2. With the use of pseudo-experiments it was found that in only a fraction of $5.9 \cdot 10^{-4}$ of the experiments 19 or more events were predicted. This translates into a 3.2σ excess. Given this excess we can claim to have observed $t\bar{t}$ production at the `LHC`.

Three jet invariant mass

For top-quark candidates it is expected that three of the reconstructed jets originate from the hadronically decaying top-quark, see Figure 1.7. The hadronic top-quark -candidate has been defined as the three jet combination with the highest vector summed $\mathrm{p_T}$ and the invariant mass of this candidate is presented in Figure 8.2 (left) for events without b-tag requirement for more statistics and in Figure 8.2 (right) after b-tag, with the data-driven QCD shape and the W+jets normalized to the data-driven estimate.

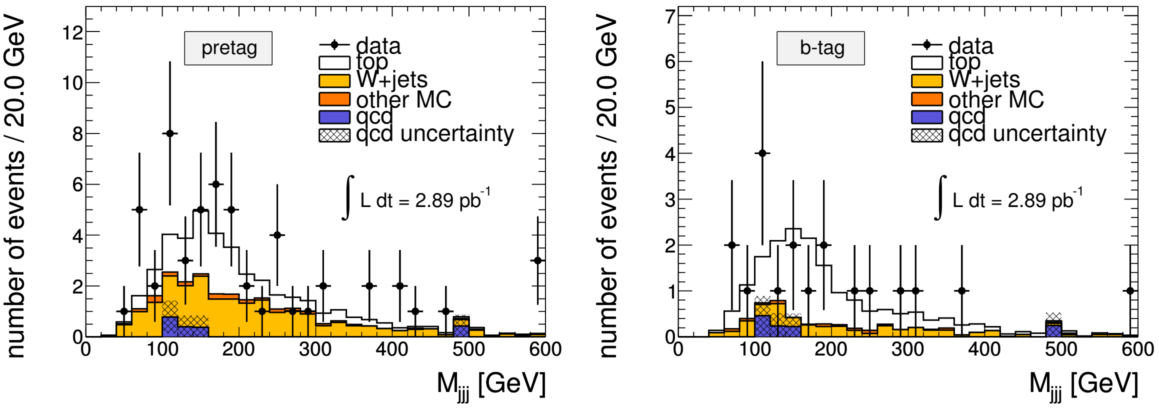

Figure 8.2: *The invariant mass of the three jet combination with the highest p_T for events that pass all selection with four or more jets with p_T > 25 GeV. Left: pretag. Right: with b-tag requirement.*

The mass distribution shows the expected top-quark mass peak. Since this choice of defining the hadronic top-quark candidate does not make use of the b-tagging information, the correct jets are selected in only 25% of the cases, which explains the large tails even for the MC signal sample.

Cross section extraction

Since the observation of $t\bar{t}$ has been established and it has been shown that the kinematical properties fulfill the $t\bar{t}$ hypothesis, the production cross section can be computed. From Equation 8.1 with $N_{obs} = 19$, $N_{bkg} = 5.6$, $\epsilon = 0.051 \times \frac{1.00}{0.54}$, $\mathcal{L} = 2.89$ we obtain for the $t\bar{t}$ cross section[3]:

$$\sigma(t\bar{t}) = 168 \pm 55 \text{ (stat) } {}^{+43}_{-40} \text{ (syst) } {}^{+21}_{-17} \text{ (lumi)}, \tag{8.9}$$

which is in good agreement with the `NNLO` calculation for a top-quark mass of 172.5 GeV of $\sigma(t\bar{t}) = 164.57 \; {}^{+4.30}_{-9.27}$ (scale) ${}^{+7.15}_{-6.51}$ (PDF) see Section 1.3.1. It is interesting to note that the result also clearly shows the measurement of $t\bar{t}$ pairs produced through gluon fusion, since the cross section from only $q\bar{q} \rightarrow t\bar{t}$ would be of the order of 30 pb, see Section 1.3.1. The discussion of the systematic uncertainties is given below.

---

[3] The signal efficiency is multiplied with the leptonic branching ratio, see Section 8.1

Systematic uncertainties

Systematic uncertainties enter the cross section calculation through the luminosity uncertainty, the uncertainty on the extracted $t\bar{t}$ signal acceptance and the uncertainty on the numbers of signal and background events. The uncertainty on the integrated luminosity is estimated to be 11% [142]. Table 8.3 shows the individual contributions to the relative uncertainty on the cross section.

Statistical error (%)	33
Object selection	
Lepton	2.3
Jet energy scale	10.5
b-tagging	+13.7/-9.5
Background rate	
normalization	15.7
Signal simulation	
ISR/FSR	8.2
PDF	2.4
Parton shower	3.0
NLO generator	5.6
Sum systematics	+25.8/-23.8
Integrated Luminosity	+12.4/-9.9

Table 8.3: *Individual uncertainties contributing to the cross section determination expressed as percentage.*

The dominant sources are:

- The *b*-tagging uncertainty is the largest single uncertainty in the cross section measurement since this uncertainty directly changes the $t\bar{t}$ signal efficiency [120]. By varying the fraction of tagged events according to the tagging uncertainty (the scale uncertainty for *b*-tagging is $\sim$ 20%) the uncertainty on the cross section is found as presented in Table 8.3.
- W+jets is the dominant background and the uncertainty on the data-driven normalization is large ($\sim$ 50%). This uncertainty will be the dominant source for the error on N_{bkg} and hence N_{sig}.
- An uncertainty on the jet energy reconstruction translates into reconstructing more or less events with $\mathrm{p_T} > 25$ GeV and accounts for a large error on the signal acceptance. The jet energy scale uncertainty can be as high as 9% for jets in the end cap region and $\mathrm{p_T}$ lower than 100 GeV. This uncertainty is lower in the central region and for higher $\mathrm{p_T}$ jets. The uncertainty on the cross section is computed by performing pseudo-experiments and changing the jet energy scale (as well as the sum of all transverse energy and the missing energy) according to

a p_T dependent scale fixed per pseudo-experiment. The uncertainty on the cross section from the jet energy scale uncertainty is then the deviation from the mean of all pseudo-experiments [116].

- Tuning the MC generator parameters for more or less initial and final state radiation (ISR/FSR in the table) will also result in a change in jet multiplicity and thus change the signal acceptance [81]. The quoted systematic uncertainty is the maximum deviation from the nominal obtained value for the cross section when using samples with different settings for initial and final state radiation.

8.4 Summary

In a dataset with 2.89 pb^{-1} integrated luminosity, 19 top-quark candidate events have been selected. With data-driven techniques (for QCD and W+jets) and MC simulation (for Z+jets and smaller backgrounds) the standard model background in the muon channel has been estimated to be 5.6 ± 2.1 events. It has been shown that the $t\bar{t}$ cross section can be extracted using a cut and count method and that the computed value is in agreement with theory predictions. The kinematical properties of the selected events are consistent with the $t\bar{t}$ hypothesis which can be seen in Figure 8.2.
The measurement of the $t\bar{t}$ cross section at $\sqrt{s} = 7$ TeV can be considered as yet another test of the Standard Model in general and perturbative QCD specifically. In Figure 8.3 the results of the measurements of the top-quark pair production cross section of the `CDF` and `DØ` experiments are shown, see Section 1.3.1, as well as the obtained value of this thesis. The results are presented together with the theoretical prediction as a function of $\sqrt{s}$ [143].
The value for the $t\bar{t}$ cross section is, albeit with large error, in good agreement with the theoretical predictions.

8.5 Outlook

In this section we will give an overview of the other $t\bar{t}$ channels that have been or can be measured, of other techniques to determine the cross section and also have a look into the near future.

Decay channels

The cross section measurement in this thesis focused on muons. The same measurement has been performed in the electron channel. The two measurements have been combined in [3] to yield a cross section of $\sigma(t\bar{t}) = 142 \pm 34$ (stat) $^{+50}_{-31}$ (syst). The combined measurement (based on 37 $t\bar{t}$ candidate events) agrees well with the predicted theoretical value.
There is yet another channel hardly mentioned in this thesis: the dileptonic $t\bar{t}$ channel, where both W-bosons decay leptonically, see Section 1.3.2. This channel is difficult to measure since the branching ratio is only about 10% and the statistical combination of

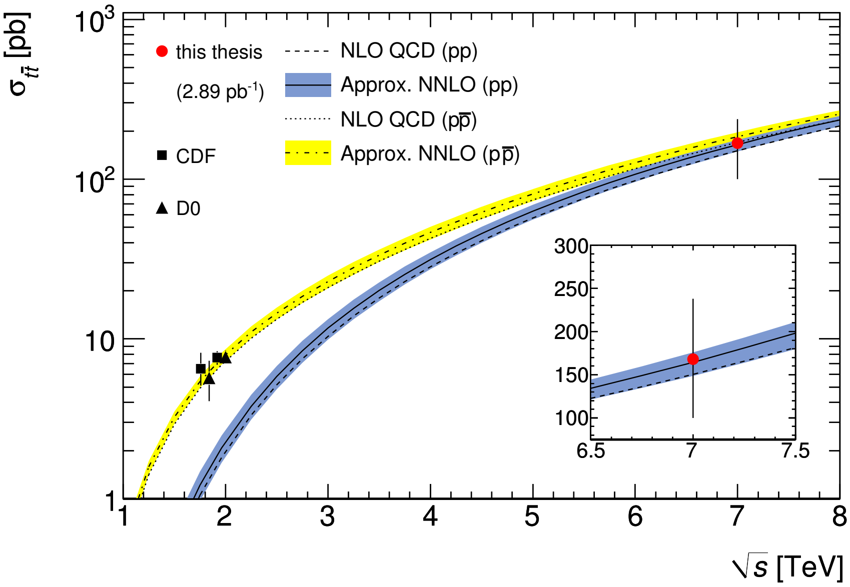

Figure 8.3: *The measured $t\bar{t}$ cross section from the `CDF` and `DØ` experiments at 1.8 (1.96) TeV and the result presented in this thesis at 7 TeV as a function of $\sqrt{s}$ compared to the theoretical prediction.*

e^+e^-, $e^{\pm}\mu^{\mp}$ and $\mu^+\mu^-$ channel is not straightforward. The statistical combination of both the single lepton and the dilepton cross section raised the significance to $\sigma = 4.8$ and yields a final cross section number of $\sigma(t\bar{t}) = 145 \pm 31$ (stat) $^{+42}_{-27}$ (syst) where the luminosity uncertainty is integrated in the systematic uncertainty.

Fit methods

There are many more ways to extract the $t\bar{t}$ cross section that all use different aspects of the decay kinematics. For the `ATLAS` top-quark pair production cross section publication [3] two more analyses have been investigated that use different physics assumptions and are considered useful cross checks. These methods fit templates of the three jet invariant mass for signal and background samples to the data. The fits are performed simultaneously in different selections to make use of the fact that there is useful information not only in the signal bin. One method uses the ratio of W+jet events between the three and four jet bin, the other makes use of the fraction of tagged and pretagged events. Both fitting methods provide similar results for the cross section and are expected to perform better than the cut and count method with more integrated luminosity.

More data

At the time of writing of this thesis, ATLAS has already recorded over 35 pb^{-1} of data that passes the top good run list selections. With a dataset that is more than an order of magnitude larger than the one discussed in this thesis, many more options are available. Obviously one of the first things to do is to check the existing methods with the larger dataset. As one of the key aspects of the matrix method, we not only expect ϵ_{fake} to be measured with higher accuracy with more data, but also to be able to measure the dependence of ϵ_{fake} on other variables directly. As discussed already in Section 7.3.2 many of the systematic uncertainties of the QCD estimation have a statistical origin and are expected to decrease with more data. The b-tagging efficiency per jet, now taken from MC and needed to predict the QCD contribution after b-tag in this small data-set, will be measured in data or will become obsolete as enough statistics after tagging is available. The uncertainty on the predicted number of QCD events will therefore rapidly decrease. For the cross section measurement the same arguments hold: many systematic uncertainties are caused by low statistics. The uncertainty on the QCD yield and therefore also the uncertainty on the W+jets contribution will decrease with more data. Together with the statistical uncertainty that will decrease with more luminosity the cross section measurement will become more precise. Ten times more luminosity leads to a statistical uncertainty of $\sim 10\%$ on the production cross section measurement.

Future measurements

With more data also other measurement than the production cross section will be performed. Measurements that will be performed in the near future consist of the top-quark mass, the W-boson helicity, the top-quark charge and spin. Also new physics searches come into reach. The invariant mass of the $t\bar{t}$ pair can be reconstructed. This variable is sensitive to many different kinds of new physics like extra dimensions, supersymmetric particles and little Higgs models [60]. The era of top-quark physics at the `LHC` has just begun...

APPENDIX A

ERROR PROPAGATION IN THE MATRIX METHOD FORMULA

The matrix method formula written such that the individual terms are not correlated:

$$N_{\text{fake}}^{\text{tight}} = \frac{\epsilon_{\text{fake}}}{\epsilon_{\text{real}} - \epsilon_{\text{fake}}}((\epsilon_{\text{real}} - 1)N^{\text{tight}} + \epsilon_{\text{real}}N^{\Delta}), \tag{A.1}$$

where N^{Δ} is given by:

$$N^{\Delta} = N^{\text{loose}} - N^{\text{tight}}. \tag{A.2}$$

In order to propagate the errors from all the input parameters we write out the partial derivative of the matrix method formula (A.1) to all its components:

$$\begin{aligned}
\frac{\partial N_{\text{fake}}^{\text{tight}}}{\partial N^{\text{tight}}} &= (\epsilon_{\text{real}} - 1)\frac{\epsilon_{\text{fake}}}{\epsilon_{\text{real}} - \epsilon_{\text{fake}}}, \\
\frac{\partial N_{\text{fake}}^{\text{tight}}}{\partial N^{\Delta}} &= \epsilon_{\text{real}}\frac{\epsilon_{\text{fake}}}{\epsilon_{\text{real}} - \epsilon_{\text{fake}}}, \\
\frac{\partial N_{\text{fake}}^{\text{tight}}}{\partial \epsilon_{\text{real}}} &= \epsilon_{\text{fake}}\frac{N^{\text{tight}} - \epsilon_{\text{fake}}N^{\text{loose}}}{\left(\epsilon_{\text{real}} - \epsilon_{\text{fake}}\right)^2}, \\
\frac{\partial N_{\text{fake}}^{\text{tight}}}{\partial \epsilon_{\text{fake}}} &= \epsilon_{\text{real}}\frac{\epsilon_{\text{real}}N^{\text{loose}} - N^{\text{tight}}}{\left(\epsilon_{\text{real}} - \epsilon_{\text{fake}}\right)^2}.
\end{aligned} \tag{A.3}$$

The purely statistical component of the uncertainty is then given by:

$$\sigma(N_{\text{fake}}^{\text{tight}}) = \sqrt{(\frac{\partial N_{\text{fake}}^{\text{tight}}}{\partial N^{\Delta}})^2(\sigma(N^{\Delta}))^2 + (\frac{\partial N_{\text{fake}}^{\text{tight}}}{\partial N^{\text{tight}}})^2(\sigma(N^{\text{tight}}))^2}, \tag{A.4}$$

where $\sigma(N^{\Delta}) = \sqrt{N^{\Delta}}$ and $\sigma(N^{\mathrm{tight}}) = \sqrt{N^{\mathrm{tight}}}$. The systematic uncertainty associated with the uncertainty of ϵ_{real} and ϵ_{fake} is then derived as:

$$\sigma(N^{\mathrm{tight}}_{\mathrm{fake}}) = \sqrt{(\frac{\partial N^{\mathrm{tight}}_{\mathrm{fake}}}{\partial \epsilon_{\mathrm{real}}})^2(\sigma(\epsilon_{\mathrm{real}}))^2 + (\frac{\partial N^{\mathrm{tight}}_{\mathrm{fake}}}{\partial \epsilon_{\mathrm{fake}}})^2(\sigma(\epsilon_{\mathrm{fake}}))^2}, \tag{A.5}$$

where $\sigma(\epsilon_{\mathrm{real}})$ and $\sigma(\epsilon_{\mathrm{fake}})$ are given by the binomial error.

APPENDIX B

MONTE CARLO SAMPLES

In this appendix all the samples are listed that were used for the analysis. In Section B.1 the $\sqrt{s} = 7$ TeV samples for the main analysis are presented. The $\sqrt{s} = 10$ TeV samples are shown in Section B.2.

B.1 The $\sqrt{s} = 7$ TeV samples

This is the detailed list of all $\sqrt{s} = 7$ TeV samples used for the analysis in Chapters 3, 6, 7 and 8 [81, 86]. Table B.1 shows the $t\bar{t}$ sample, the W+jets sample, the Z+jets samples and the other prompt background samples.

$t\bar{t}$	cross section [pb]
mc09_7TeV.105861.TTbar_PowHeg_Pythia_e521_s765_s767_r1302_r1306	79.118
W+jets	
mc09_7TeV.107680.AlpgenJimmyWenuNp0_pt20_e511_s765_s767_r1302_r1306	6913.3
mc09_7TeV.107681.AlpgenJimmyWenuNp1_pt20_e511_s765_s767_r1302_r1306	1293.0
mc09_7TeV.107682.AlpgenJimmyWenuNp2_pt20_e511_s765_s767_r1302_r1306	377.1
mc09_7TeV.107683.AlpgenJimmyWenuNp3_pt20_e511_s765_s767_r1302_r1306	100.9
mc09_7TeV.107684.AlpgenJimmyWenuNp4_pt20_e511_s765_s767_r1302_r1306	25.3
mc09_7TeV.107685.AlpgenJimmyWenuNp5_pt20_e511_s765_s767_r1302_r1306	6.9
mc09_7TeV.107690.AlpgenJimmyWmunuNp0_pt20_e511_s765_s767_r1302_r1306	6935.4
mc09_7TeV.107691.AlpgenJimmyWmunuNp1_pt20_e511_s765_s767_r1302_r1306	1281.2
mc09_7TeV.107692.AlpgenJimmyWmunuNp2_pt20_e511_s765_s767_r1302_r1306	375.3
mc09_7TeV.107693.AlpgenJimmyWmunuNp3_pt20_e511_s765_s767_r1302_r1306	101.1
mc09_7TeV.107694.AlpgenJimmyWmunuNp4_pt20_e511_s765_s767_r1302_r1306	25.7
mc09_7TeV.107695.AlpgenJimmyWmunuNp5_pt20_e511_s765_s767_r1302_r1306	7.0
mc09_7TeV.107700.AlpgenJimmyWtaunuNp0_pt20_e511_s765_s767_r1302_r1306	6835.8
mc09_7TeV.107701.AlpgenJimmyWtaunuNp1_pt20_e511_s765_s767_r1302_r1306	1276.8
mc09_7TeV.107702.AlpgenJimmyWtaunuNp2_pt20_e511_s765_s767_r1302_r1306	376.6
mc09_7TeV.107703.AlpgenJimmyWtaunuNp3_pt20_e511_s765_s767_r1302_r1306	100.8

`mc09_7TeV.107704.AlpgenJimmyWtaunuNp4_pt20_e511_s765_s767_r1302_r1306`	25.7
`mc09_7TeV.107705.AlpgenJimmyWtaunuNp5_pt20_e511_s765_s767_r1302_r1306`	7.0
Z+jets	
`mc09_7TeV.107650.AlpgenJimmyZeeNp0_pt20_e529_s765_s767_r1302_r1306`	661.9
`mc09_7TeV.107651.AlpgenJimmyZeeNp1_pt20_e529_s765_s767_r1302_r1306`	133.3
`mc09_7TeV.107652.AlpgenJimmyZeeNp2_pt20_e529_s765_s767_r1302_r1306`	40.3
`mc09_7TeV.107653.AlpgenJimmyZeeNp3_pt20_e529_s765_s767_r1302_r1306`	11.2
`mc09_7TeV.107654.AlpgenJimmyZeeNp4_pt20_e529_s765_s767_r1302_r1306`	2.7
`mc09_7TeV.107655.AlpgenJimmyZeeNp5_pt20_e529_s765_s767_r1302_r1306`	0.8
`mc09_7TeV.107660.AlpgenJimmyZmumuNp0_pt20_e529_s765_s767_r1302_r1306`	657.7
`mc09_7TeV.107661.AlpgenJimmyZmumuNp1_pt20_e529_s765_s767_r1302_r1306`	132.8
`mc09_7TeV.107662.AlpgenJimmyZmumuNp2_pt20_e529_s765_s767_r1302_r1306`	39.6
`mc09_7TeV.107663.AlpgenJimmyZmumuNp3_pt20_e529_s765_s767_r1302_r1306`	11.1
`mc09_7TeV.107664.AlpgenJimmyZmumuNp4_pt20_e529_s765_s767_r1302_r1306`	2.8
`mc09_7TeV.107665.AlpgenJimmyZmumuNp5_pt20_e529_s765_s767_r1302_r1306`	0.8
`mc09_7TeV.107670.AlpgenJimmyZtautauNp0_pt20_e529_s765_s767_r1302_r1306`	657.4
`mc09_7TeV.107671.AlpgenJimmyZtautauNp1_pt20_e529_s765_s767_r1302_r1306`	133.0
`mc09_7TeV.107672.AlpgenJimmyZtautauNp2_pt20_e529_s765_s767_r1302_r1306`	40.4
`mc09_7TeV.107673.AlpgenJimmyZtautauNp3_pt20_e529_s765_s767_r1302_r1306`	11.0
`mc09_7TeV.107674.AlpgenJimmyZtautauNp4_pt20_e529_s765_s767_r1302_r1306`	2.9
`mc09_7TeV.107675.AlpgenJimmyZtautauNp5_pt20_e529_s765_s767_r1302_r1306`	0.7
W+$b\bar{b}$+jets	
`mc09_7TeV.106280.AlpgenJimmyWbbNp0_pt20_e524_s765_s767_r1302_r1306`	3.2
`mc09_7TeV.106281.AlpgenJimmyWbbNp1_pt20_e524_s765_s767_r1302_r1306`	2.6
`mc09_7TeV.106282.AlpgenJimmyWbbNp2_pt20_e524_s765_s767_r1302_r1306`	1.4
`mc09_7TeV.106283.AlpgenJimmyWbbNp3_pt20_e524_s765_s767_r1302_r1306`	0.6
single top	
`mc09_7TeV.108340.st_tchan_enu_McAtNlo_Jimmy_e508_s765_s767_r1302_r1306`	7.152
`mc09_7TeV.108341.st_tchan_munu_McAtNlo_Jimmy_e508_s765_s767_r1302_r1306`	7.176
`mc09_7TeV.108342.st_tchan_taunu_McAtNlo_Jimmy_e508_s765_s767_r1302_r1306`	7.128
`mc09_7TeV.108343.st_schan_enu_McAtNlo_Jimmy_e508_s765_s767_r1302_r1306`	0.4685
`mc09_7TeV.108344.st_schan_munu_McAtNlo_Jimmy_e508_s765_s767_r1302_r1306`	0.4684
`mc09_7TeV.108345.st_schan_taunu_McAtNlo_Jimmy_e508_s765_s767_r1302_r1306`	0.4700
`mc09_7TeV.108346.st_Wt_McAtNlo_Jimmy_e508_s765_s767_r1302_r1306`	14.581
di-boson	
`mc09_7TeV.105985.WW_Herwig_e521_s765_s767_r1302_r1306`	1.52
`mc09_7TeV.105987.WZ_Herwig_e521_s765_s767_r1302_r1306`	1.58
`mc09_7TeV.105986.ZZ_Herwig_e521_s765_s767_r1302_r1306`	1.20

Table B.1: *The $\sqrt{s} = 7$ TeV prompt samples used in this thesis.*

In the following table the QCD MC samples are presented. Table B.2 shows the light jet samples, the light jet samples with muon filter, the $b\bar{b}$+jet samples and the $b\bar{b}$+jet samples with muon filter.

light jets	cross section [pb]
mc09_7TeV.108362.AlpgenQcdJ4Np2_pt20_e522_s765_s767_r1302_r1306	12064
mc09_7TeV.108363.AlpgenQcdJ4Np3_pt20_e522_s765_s767_r1302_r1306	24138
mc09_7TeV.108364.AlpgenQcdJ4Np4_pt20_e522_s765_s767_r1302_r1306	17319
mc09_7TeV.108365.AlpgenQcdJ4Np5_pt20_e522_s765_s767_r1302_r1306	7777
mc09_7TeV.108366.AlpgenQcdJ4Np6_pt20_e522_s765_s767_r1302_r1306	3088
mc09_7TeV.108367.AlpgenQcdJ5PlusNp2_pt20_e522_s765_s767_r1302_r1306	269
mc09_7TeV.108368.AlpgenQcdJ5PlusNp3_pt20_e522_s765_s767_r1302_r1306	640
mc09_7TeV.108369.AlpgenQcdJ5PlusNp4_pt20_e522_s765_s767_r1302_r1306	625
mc09_7TeV.108370.AlpgenQcdJ5PlusNp5_pt20_e522_s765_s767_r1302_r1306	383
mc09_7TeV.108371.AlpgenQcdJ5PlusNp6_pt20_e522_s765_s767_r1302_r1306	217
light jets with muon filter	
mc09_7TeV.107912.AlpgenQcdJ1Np2_TOPfiltmu_pt20_e561_s765_s767_r1302_r1306	28343
mc09_7TeV.107913.AlpgenQcdJ1Np3_TOPfiltmu_pt20_e561_s765_s767_r1302_r1306	1008
mc09_7TeV.108818.AlpgenQcdJ2Np2_TOPfiltmu_pt20_e540_s765_s767_r1302_r1306	27927.0
mc09_7TeV.108819.AlpgenQcdJ2Np3_TOPfiltmu_pt20_e540_s765_s767_r1302_r1306	10660.9
mc09_7TeV.108820.AlpgenQcdJ2Np4_TOPfiltmu_pt20_e540_s765_s767_r1302_r1306	1248.9
mc09_7TeV.108821.AlpgenQcdJ2Np5_TOPfiltmu_pt20_e540_s765_s767_r1302_r1306	148.4
mc09_7TeV.108822.AlpgenQcdJ2Np6_TOPfiltmu_pt20_e540_s765_s767_r1302_r1306	42.4
mc09_7TeV.108823.AlpgenQcdJ3Np2_TOPfiltmu_pt20_e540_s765_s767_r1302_r1306	3004.2
mc09_7TeV.108824.AlpgenQcdJ3Np3_TOPfiltmu_pt20_e540_s765_s767_r1302_r1306	3709.0
mc09_7TeV.108825.AlpgenQcdJ3Np4_TOPfiltmu_pt20_e540_s765_s767_r1302_r1306	1224.9
mc09_7TeV.108826.AlpgenQcdJ3Np5_TOPfiltmu_pt20_e540_s765_s767_r1302_r1306	359.1
mc09_7TeV.108827.AlpgenQcdJ3Np6_TOPfiltmu_pt20_e540_s765_s767_r1302_r1306	73.1
$b\bar{b}$+jets	
mc09_7TeV.107310.AlpgenQcdbbJ4Np0_pt20_e541_s765_s767_r1302_r1306	66.4
mc09_7TeV.107311.AlpgenQcdbbJ4Np1_pt20_e541_s765_s767_r1302_r1306	443.1
mc09_7TeV.107312.AlpgenQcdbbJ4Np2_pt20_e541_s765_s767_r1302_r1306	553.6
mc09_7TeV.107313.AlpgenQcdbbJ4Np3_pt20_e541_s765_s767_r1302_r1306	370.9
mc09_7TeV.107314.AlpgenQcdbbJ4Np4_pt20_e541_s765_s767_r1302_r1306	228.6
mc09_7TeV.107315.AlpgenQcdbbJ5PlusNp0_pt20.merge_e541_s765_s767_r1302_r1306	1.3
mc09_7TeV.107316.AlpgenQcdbbJ5PlusNp1_pt20.merge_e541_s765_s767_r1302_r1306	8.5
mc09_7TeV.107317.AlpgenQcdbbJ5PlusNp2_pt20.merge_e541_s765_s767_r1302_r1306	15.0
mc09_7TeV.107318.AlpgenQcdbbJ5PlusNp3_pt20.merge_e541_s765_s767_r1302_r1306	14.1
mc09_7TeV.107319.AlpgenQcdbbJ5PlusNp4_pt20.merge_e541_s765_s767_r1302_r1306	13.7
$b\bar{b}$+jets with muon filter	
mc09_7TeV.107335.AlpgenQcdbbJ1Np0_TOPfiltmu_pt20_e561_s765_s767_r1302_r1306	13741
mc09_7TeV.107336.AlpgenQcdbbJ1Np1_TOPfiltmu_pt20_e561_s765_s767_r1302_r1306	859.7
mc09_7TeV.107340.AlpgenQcdbbJ2Np0_TOPfiltmu_pt20_e541_s765_s767_r1302_r1306	5071
mc09_7TeV.107341.AlpgenQcdbbJ2Np1_TOPfiltmu_pt20_e541_s765_s767_r1302_r1306	4009.5
mc09_7TeV.107342.AlpgenQcdbbJ2Np2_TOPfiltmu_pt20_e541_s765_s767_r1302_r1306	1105.9

mc09_7TeV.107343.AlpgenQcdbbJ2Np3_TOPfiltmu_pt20_e541_s765_s767_r1302_r1306	230.6
mc09_7TeV.107344.AlpgenQcdbbJ2Np4_TOPfiltmu_pt20_e541_s765_s767_r1302_r1306	43.4
mc09_7TeV.107345.AlpgenQcdbbJ3Np0_TOPfiltmu_pt20_e541_s765_s767_r1302_r1306	384.5
mc09_7TeV.107346.AlpgenQcdbbJ3Np1_TOPfiltmu_pt20_e541_s765_s767_r1302_r1306	1162.3
mc09_7TeV.107347.AlpgenQcdbbJ3Np2_TOPfiltmu_pt20_e541_s765_s767_r1302_r1306	658.2
mc09_7TeV.107348.AlpgenQcdbbJ3Np3_TOPfiltmu_pt20_e541_s765_s767_r1302_r1306	231.1
mc09_7TeV.107349.AlpgenQcdbbJ3Np4_TOPfiltmu_pt20_e541_s765_s767_r1302_r1306	86.6

Table B.2: *The QCD samples used in this thesis.*

B.2 The $\sqrt{s} = 10$ TeV samples

This is the detailed list of all $\sqrt{s} = 10$ TeV samples used for the analysis in Chapters 4 and 5 [73, 82]. The signal samples and all background samples except for the QCD background sample are presented in Table B.3.

$t\bar{t}$	cross section [pb]
mc08.105200.T1_McAtNlo_Jimmy.recon.AOD.e357_s462_r541	202.86
mc08.105204.TTbar_FullHad_McAtNlo_Jimmy.recon.AOD.e363_s462_r563	170.74
W+jets	
mc08.107680.AlpgenJimmyWenuNp0_pt20.recon.AOD.e368_s462_s520_r808	12479.8
mc08.107681.AlpgenJimmyWenuNp1_pt20.recon.AOD.e368_s462_s520_r808	5080.5
mc08.107682.AlpgenJimmyWenuNp2_pt20.recon.AOD.e368_s462_s520_r808	2499.0
mc08.107683.AlpgenJimmyWenuNp3_pt20.recon.AOD.e368_s462_s520_r808	1099.4
mc08.107684.AlpgenJimmyWenuNp4_pt20.recon.AOD.e368_s462_s520_r808	431.3
mc08.107685.AlpgenJimmyWenuNp5_pt20.recon.AOD.e368_s462_s520_r808	141.5
mc08.107690.AlpgenJimmyWmunuNp0_pt20.recon.AOD.e368_s462_s520_r808	12476.7
mc08.107691.AlpgenJimmyWmunuNp1_pt20.recon.AOD.e368_s462_s520_r808	5080.8
mc08.107692.AlpgenJimmyWmunuNp2_pt20.recon.AOD.e368_s462_s520_r808	2498.6
mc08.107693.AlpgenJimmyWmunuNp3_pt20.recon.AOD.e368_s462_s520_r808	1099.7
mc08.107694.AlpgenJimmyWmunuNp4_pt20.recon.AOD.e368_s462_s520_r808	431.5
mc08.107695.AlpgenJimmyWmunuNp5_pt20.recon.AOD.e368_s462_s520_r808	141.5
mc08.107700.AlpgenJimmyWtaunuNp0_pt20.recon.AOD.e368_s462_s520_r808	12479.2
mc08.107701.AlpgenJimmyWtaunuNp1_pt20.recon.AOD.e368_s462_s520_r808	5079.2
mc08.107702.AlpgenJimmyWtaunuNp2_pt20.recon.AOD.e368_s462_s520_r808	2498.9
mc08.107703.AlpgenJimmyWtaunuNp3_pt20.recon.AOD.e368_s462_s520_r808	1098.3
mc08.107704.AlpgenJimmyWtaunuNp4_pt20.recon.AOD.e368_s462_s520_r808	432.0
mc08.107705.AlpgenJimmyWtaunuNp5_pt20.recon.AOD.e368_s462_s520_r808	141.2

single top	
`mc08.105500.AcerMC_Wt.merge.AOD.e352_s462_s520_r808_r838`	14.41
`mc08.105502.AcerMC_tchan.merge.AOD.e352_s462_s520_r808_r838`	41.12

Table B.3: *The $\sqrt{s} = 10$ TeV prompt samples used in this thesis in Chapters 4 and 5.*

The QCD Monte Carlo sample that was used in Chapters 4 and 5 consists of the same subsamples as presented in the previous section, but for $\sqrt{s} = 10$ TeV. We list here only the mixed sample: `user.RichardHawkings.0108176.topmix_Muon.AOD.v5` [73, 86].

REFERENCES

[1] B. Ryden, *Introduction to cosmology*, Addison Wesley, 2003.

[2] W. N. Cottingham and D. A. Greenwood, *An Introduction to the Standard Model of Particle Physics*, Cambridge University Press, 1999.

[3] G. Aad, B. Abbott, J. Abdallah, A. A. Abdelalim, A. Abdesselam, O. Abdinov, B. Abi, M. Abolins, H. Abramowicz, H. Abreu, and et al., *Measurement of the top quark-pair production cross section with ATLAS in pp collisions at* $\sqrt{s}$*=7 TeV*, European Physical Journal C **71** (2011) 1577.

[4] M. E. Peskin and D. V. Schroeder, *An Introduction to Quantum Field Theory*, Westview Press, 1995.

[5] M. C. Gonzalez-Garcia and Y. Nir, *Neutrino masses and mixing: evidence and implications*, Reviews of Modern Physics **75** (2003) 345.

[6] B. Kayser, *Neutrino physics: Where do we stand, and where are we going? - The theoretical-phenomenological perspective*, Nuclear Physics B **118** (2003) 425.

[7] P.W. Higgs, *Broken Symmetries, Massless Particles and Gauge Fields*, Phys. Lett. **12** (1964) 132.

[8] P.W. Higgs, *Broken Symmetries and the Masses of Gauge Bosons*, Phys. Rev. Lett. **13** (1964) 508.

[9] P.W. Higgs, *Spontaneous Symmetry Breakdown without Massless Bosons*, Phys. Lett. **145** (1966) 1156.

[10] F. Englert and R. Brout, *Broken Symmetry and the Mass of Gauge Vector Mesons*, Phys. Rev. Lett. **13** (1964) 321.

[11] I. J. Aitchison, *Supersymmetry and the MSSM: An Elementary Introduction*, arXiv:hep-ph/0505105, 2005.

[12] Cern Press Release (2008) , `http://press.web.cern.ch/press/PressReleases/Releases2008/PR17.08E.html`.

[13] `http://lhc-commissioning.web.cern.ch/lhc-commissioning/`.

[14] `http://www.fnal.gov/pub/now/tevlum.html`.

[15] `http://projects.hepforge.org/mstwpdf/plots/plots.html`.

[16] A. D. Martin, W. J. Stirling, R. S. Thorne, and G. Watt, *Parton distributions for the LHC*, European Physical Journal C **63** (2009) 189.

[17] `http://projects.hepforge.org/mstwpdf/`.

[18] D. Green, *High Pt Physics at Hadron Colliders*, Cambridge University Press, 2005.

[19] CDF Collaboration, F. Abe *et al.*, *Observation of top quark production in $\bar{p}p$ collisions*, Phys. Rev. Lett. **74** (1995) 2626.

[20] D0 Collaboration, S. Abachi *et al.*, *Observation of the top quark*, Phys. Rev. Lett. **74** (1995) 2632.

[21] S. W. Herb, D. C. Hom, L. M. Lederman, J. C. Sens, H. D. Snyder, J. K. Yoh, J. A. Appel, B. C. Brown, C. N. Brown, W. R. Innes, K. Ueno, T. Yamanouchi, A. S. Ito, H. Jöstlein, D. M. Kaplan, and R. D. Kephart, *Observation of a Dimuon Resonance at 9.5 GeV in 400 GeV Proton-Nucleus Collisions*, Phys. Rev. Lett. **39**(5) (1977) 252.

[22] `http://www.fnal.gov/pub/inquiring/physics/discoveries/bottom_quark_pr.html`.

[23] M. Kobayashi and T. Maskawa, *CP-Violation in the Renormalizable Theory of Weak Interaction*, Progress of Theoretical Physics **49** (1973) 652.

[24] W. Bernreuther, *Top quark physics at the LHC*, arXiv:0805.1333, 2008.

[25] K. Nakamura and Particle Data Group, *Review of Particle Physics*, Journal of Physics G Nuclear Physics **37**(7) (2010) 075021.

[26] Tevatron Electroweak Working Group, CDF, and D0 Collaborations, *Combination of CDF and D0 Results on the Mass of the Top Quark*, arXiv:1007.3178, 2010.

[27] Martin C. Smith and Scott S. Willenbrock, *Top-quark pole mass*, Phys. Rev. Lett. **79**(20) (1997) 3825.

[28] U. Langenfeld, S. Moch, and P. Uwer, *Measuring the running top-quark mass*, Phys. Rev. **D80** (2009) 054009.

[29] W.J. Sterling R.K. Ellis and B.R. Webber, *QCD and Collider physics*, Cambridge University Press, 1996.

[30] J. C. Collins, D. E. Soper, and G. Sterman, *Factorization of Hard Processes in QCD*, arXiv:hep-ph/0409313, 2004.

[31] J. R. Incandela, A. Quadt, W. Wagner, and D. Wicke, *Status and prospects of top-quark physics*, Progress in Particle and Nuclear Physics **63** (2009) 239.

[32] Martijn Gosselink, *Radiating Top Quarks*, PhD thesis, Nikhef, UvA (2010) .

[33] G. Altarelli and G. Parisi, *Asymptotic freedom in parton language*, Nuclear Physics B **126**(2) (1977) 298.

[34] V. N. Gribov and L. N. Lipatov, *Deep inelastic e p scattering in perturbation theory*, Sov. J. Nucl. Phys. **15** (1972) 438.

[35] L. N. Lipatov, *The parton model and perturbation theory*, Sov. J. Nucl. Phys. **20** (1975) 94.

[36] Yuri L. Dokshitzer, *Calculation of the Structure Functions for Deep Inelastic Scattering and e+ e- Annihilation by Perturbation Theory in Quantum Chromodynamics*, Sov. Phys. JETP **46** (1977) 641.

[37] J. C. Collins and D. E. Soper, *The theorems of perturbative qcd*, Annual Review of Nuclear and Particle Science **37** (1987) 383.

[38] `http://mcfm.fnal.gov/`.

[39] M. Cacciari, S. Frixione, M. L. Mangano, P. Nason, and G. Ridolfi, *Updated predictions for the total production cross sections of top and of heavier quark pairs at the Tevatron and at the LHC*, Journal of High Energy Physics **9** (2008) 127.

[40] S. Moch and P. Uwer, *Theoretical status and prospects for top-quark pair production at hadron colliders*, Phys. Rev. D. **78**(3) (2008) 034003.

[41] M. Aliev *et al.*, *– HATHOR – HAdronic Top and Heavy quarks crOss section calculatoR*, Comput. Phys. Commun. **182** (2011) 1034.

[42] P. M. Nadolsky, H.-L. Lai, Q.-H. Cao, J. Huston, J. Pumplin, D. Stump, W.-K. Tung, and C.-P. Yuan, *Implications of CTEQ global analysis for collider observables*, Phys. Rev. D **78**(1) (2008) 013004.

[43] T. Affolder, H. Akimoto, A. Akopian, M. G. Albrow, P. Amaral, S. R. Amendolia, D. Amidei, K. Anikeev, J. Antos, G. Apollinari, and et al., *Measurement of the $t\bar{t}$ production cross section in $p\bar{p}$ collisions at $\sqrt{s}$=1.8 TeV*, Phys. Rev. D. **64**(3) (2001) 032002.

[44] T. Affolder, H. Akimoto, A. Akopian, M. G. Albrow, P. Amaral, S. R. Amendolia, D. Amidei, K. Anikeev, J. Antos, G. Apollinari, and et al., *CDF Conf Note 9913.*

[45] D0 Collaboration, V. M. Abazov et al., *Measurement of the $t\bar{t}$ production cross section in $p\bar{p}$ collisions at $\sqrt{s} = 1.96\,TeV$ using kinematic characteristics of $lepton + jets$ events*, Phys. Rev. D **76**(9) (2007) 092007.

[46] V. M. Abazov et al., *D0 Conf Note 6037.*

[47] U. Baur and L. H. Orr, *Searching for $t\bar{t}$ resonances at the CERN Large Hadron Collider*, Phys. Rev. D **77**(11) (2008) 114001.

[48] The ATLAS collaboration, *A Search for $t\bar{t}$ Resonances in the Lepton Plus Jets Channel in 35 pb^{-1} of pp Collisions at $\sqrt{s} = 7$ TeV*, ATL-COM-PHYS-2011-070, 2011.

[49] CDF Collaboration Collaboration, A. Abulencia *et al.*, *Search for Charged Higgs Bosons from Top Quark Decays in $p\bar{p}$ Collisions at $\sqrt{s} = 1.96$ TeV*, Phys. Rev. Lett. **96**(4) (2006) 042003.

[50] Erik Eise van der Kraaij, *First top quark physics with ATLAS - a prospect*, PhD thesis, Nikhef, UvA (2009) .

[51] `http://www-d0.fnal.gov/Run2Physics/top/top_public_web_pages/top_feynman_diagrams.html`.

[52] A. Quadt, *Top quark physics at hadron colliders*, European Physical Journal C **48** (2006) 835.

[53] Vickey T, *Measurement of the W polarization in top quark decay*, FERMILAB-THESIS-2004-49.

[54] J. Z. Bai, *Measurements of the Cross Section for $e^+e^- \rightarrow$ Hadrons at Center-of-Mass Energies from 2 to 5 GeV*, Phys. Rev. Lett. **88**(10) (2002) 101802.

[55] Timo van Ritbergen and Robin G. Stuart, *Complete 2-loop quantum electrodynamic contributions to the muon lifetime in the fermi model*, Phys. Rev. Lett. **82**(3) (1999) 488.

[56] The ALEPH Collaboration, The DELPHI Collaboration, The L3 Collaboration, The OPAL Collaboration, The SLD Collaboration, The LEP Electroweak Working Group, and The SLD Electroweak Heavy Flavour Groups, *Precision electroweak measurements on the Z resonance*, Phys. Rep. **427** (2006) 257.

[57] A. Sirlin, *Radiative corrections in the $SU(2)_L \times U(1)$ theory: A simple renormalization framework*, Phys. Rev. D **22**(4) (1980) 971.

[58] `http://lepewwg.web.cern.ch/LEPEWWG/plots/summer2010/`.

[59] ALEPH Collaboration, DELPHI Collaboration, L3 Collaboration, OPAL Collaboration, and The LEP Working Group For Higgs Boson Searches, *Search for the Standard Model Higgs boson at LEP*, Physics Letters B **565** (2003) 61.

[60] R. Frederix and F. Maltoni, *Top pair invariant mass distribution: a window on new physics*, arXiv:0712.2355, 2007.

[61] M. Schmaltz and D. Tucker-Smith, *Little Higgs Theories*, Annual Review of Nuclear and Particle Science **55** (2005) 229.

[62] L. Randall and R. Sundrum, *Large Mass Hierarchy from a Small Extra Dimension*, Phys. Rev. Lett. **83** (1999) 3370.

[63] J.R. Lessard and M. Lefebvre, *Search for narrow resonances* ($pp \to X \to t\bar{t}$) *in the context of early ATLAS data*, ATL-COM-PHYS-2008-099, 2008.

[64] E. March, L. Ros and B. Salvachua, *Search for Kaluza-Klein excitations of the gluon in models with extra dimensions*, ATLAS-PHYS-PUB-2006-002, 2006.

[65] T. Gleisberg, S. Höche, F. Krauss, M. Schönherr, S. Schumann, F. Siegert, and J. Winter, *Event generation with SHERPA 1.1*, Journal of High Energy Physics **2** (2009) 7.

[66] G. Corcella, I. G. Knowles, G. Marchesini, S. Moretti, K. Odagiri, P. Richardson, M. H. Seymour, and B. R. Webber, *HERWIG 6: an event generator for hadron emission reactions with interfering gluons (including supersymmetric processes)*, Journal of High Energy Physics **1** (2001) 10.

[67] T. Sjöstrand, S. Mrenna, and P. Skands, *PYTHIA 6.4 physics and manual*, Journal of High Energy Physics **5** (2006) 26.

[68] M. L. Mangano, F. Piccinini, A. D. Polosa, M. Moretti, and R. Pittau, *ALPGEN, a generator for hard multiparton processes in hadronic collisions*, Journal of High Energy Physics **7** (2003) 1.

[69] S. Frixione and B.R. Webber, *Matching NLO QCD computations and parton shower simulation*, Journal of High Energy Physics **6** (2002) 29.

[70] P. Nason, *A New Method for Combining NLO QCD with Shower Monte Carlo Algorithms*, Journal of High Energy Physics **11** (2004) 40.

[71] J. C. Collins, *Sudakov Form Factors*, arXiv:hep-ph/0312336, 2003.

[72] S. Hoeche, F. Krauss, N. Lavesson, L. Lonnblad, M. Mangano, A. Schaelicke, and S. Schumann, *Matching Parton Showers and Matrix Elements*, arXiv:hep-ph/0602031, 2006.

[73] R. Hawkings M. Bosman and A. Shibata, *Understanding Monte Carlo Generators for Top Physics*, ATL-COM-PHYS-2009-334, 2009.

[74] `http://projects.hepforge.org/jimmy/`.

[75] J. M. Butterworth, Jeffrey R. Forshaw, and M. H. Seymour, *Multiparton interactions in photoproduction at HERA*, Z. Phys. **C72** (1996) 637.

[76] R. Field and R. Craig Group, *Pythia Tune A, Herwig, and Jimmy in Run 2 at CDF*, arXiv:hep-ph/0510198, 2005.

[77] The ATLAS Collaboration, *Charged-particle multiplicities in pp interactions measured with the ATLAS detector at the LHC*, arXiv:1012.5104, 2010.

[78] Geant4 Collaboration and S. Agostinelli, *Geant4-a simulation toolkit*, Nuclear Instruments and Methods in Physics Research A **506** (2003) 250.

[79] The ATLAS Collaboration, G. Aad, E. Abat, J. Abdallah, A. A. Abdelalim, A. Abdesselam, O. Abdinov, B. A. Abi, M. Abolins, H. Abramowicz, and et al., *The ATLAS Experiment at the CERN Large Hadron Collider*, Journal of Instrumentation **3** (2008) 8003.

[80] G. Aad, B. Abbott, J. Abdallah, A. A. Abdelalim, A. Abdesselam, O. Abdinov, B. Abi, M. Abolins, H. Abramowicz, H. Abreu, and et al., *The ATLAS Simulation Infrastructure*, European Physical Journal C **70** (2010) 823.

[81] The ATLAS collaboration, *Monte Carlo samples used for top physics: Top Working Group Note IX*, ATL-COM-PHYS-2010-836, 2010.

[82] B. Acharya, D. Bartsch, I. Besana, S. Bentvelsen, M. Bosman, I. C. Brock, M. Cobal, M. Cristinziani, M. De Sanctis, A. Doxiadis, V. Ferrara, P. Ferrari, L. Fiorini, U. Husemann, C. Lange, T. Lari, S. Melhlhase, L.M. Mir, I. Mussche, J. Nadal, M. Pinamonti, B. Radics, I. Riu, N. Ruckstuhl, G. Salamanna, K. Suruliz, C. Troncon, M. Tsiakiris, W. Verkerke, V. Vorwerk, and I. Van Vulpen, *Prospects for measuring the Top Quark Pair Production Cross-section in the Single Lepton Channel at ATLAS in 10 TeV p-p Collisions*, ATL-PHYS-INT-2009-071, 2009.

[83] UA1 Collaboration, G. Arnison *et al.*, *Experimental observation of isolated large transverse energy electrons with associated missing energy at* $\sqrt{s} = 540\ GeV$, Phys. Lett. **B122** (1983) 103.

[84] UA2 Collaboration, P. Bagnaia *et al.*, *Evidence for* $Z^0 \to e^+e^-$ *at the CERN* $\bar{p}p$ *collider*, Phys. Lett. **B129** (1983) 130.

[85] S. Frixione, G. Ridolfi, and P. Nason, *A positive-weight next-to-leading-order Monte Carlo for heavy flavour hadroproduction*, Journal of High Energy Physics **9** (2007) 126.

[86] `https://twiki.cern.ch/twiki/bin/view/AtlasProtected/TopMixingExercise`.

[87] `http://cdsweb.cern.ch/record/1165534/files/CERN-Brochure-2009-003-Eng.pdf`, 2008.

[88] L. Evans and P. Bryant, *LHC Machine*, Journal of Instrumentation **3** (2008) 8001.

[89] `http://public.web.cern.ch/public/en/LHC/Facts-en.html`.

[90] The LHCb Collaboration, A. A. Alves, Jr., L. M. A. Filho, A. F. Barbosa, I. Bediaga, G. Cernicchiaro, G. Guerrer, H. P. Lima, Jr., A. A. Machado, J. Magnin, and et al., *The LHCb Detector at the LHC*, Journal of Instrumentation **3** (2008) 8005.

[91] The ALICE Collaboration, K. Aamodt, A. Abrahantes Quintana, R. Achenbach, S. Acounis, D. Adamová, C. Adler, M. Aggarwal, F. Agnese, G. Aglieri Rinella, and et al., *The ALICE experiment at the CERN LHC*, Journal of Instrumentation **3** (2008) 8002.

[92] The CMS Collaboration, S. Chatrchyan, G. Hmayakyan, V. Khachatryan, A. M. Sirunyan, W. Adam, T. Bauer, T. Bergauer, H. Bergauer, M. Dragicevic, and et al., *The CMS experiment at the CERN LHC*, Journal of Instrumentation **3** (2008) 8004.

[93] *ATLAS detector and physics performance: Technical Design Report, 1*, Technical Design Report ATLAS. CERN, Geneva, 1999.

[94] *ATLAS detector and physics performance: Technical Design Report, 2*, Technical Design Report ATLAS. CERN, Geneva, 1999.

[95] F Bergsma, *Calibration of Hall sensors in three dimensions*, Proceedings of 13th International Magnetic Measurement Workshop (2003) 34.

[96] *ATLAS muon spectrometer: Technical Design Report*, Technical Design Report ATLAS. CERN, Geneva, 1997.

[97] `http://nikpc09/bsensor`.

[98] The ATLAS collaboration, *In-situ pseudo-rapidity inter-calibration to evaluate jet energy scale uncertainty and calorimeter performance in the forward region*, ATLAS-CONF-2010-055, 2010.

[99] The ATLAS collaboration, *Jet energy scale and its systematic uncertainty for jets produced in proton-proton collisions at sqrt(s) = 7 TeV and measured with the ATLAS detector*, ATLAS-CONF-2010-056, 2010.

[100] The ATLAS collaboration, *Performance of the Missing Transverse Energy Reconstruction and Calibration in Proton-Proton Collisions at a Center-of-Mass Energy of 7 TeV with the ATLAS Detector*, ATLAS-CONF-2010-057, 2010.

[101] Zdenko van Kesteren, *Identification of muons in ATLAS*, PhD thesis, Nikhef, UvA (2010) .

[102] F. Cerutti, C. Gatti, P. Kluit, O. Kortner, W. Liebig, J. Liu, G. Salamanna, A. Salvucci, E. van der Poel, and J. Zhu, *Muon Momentum Resolution in First Pass Reconstruction of pp Collision Data Recorded by ATLAS in 2010*, ATLAS-COM-CONF-2011-003, 2011.

[103] `https://twiki.cern.ch/twiki/bin/viewauth/Atlas/TriggerPhysicsMenu`.

[104] Christoph Eck, J. Knobloch, Leslie Robertson, I. Bird, K. Bos, N. Brook, D. Duellmann, I. Fisk, D. Foster, B. Gibbard, C. Grandi, F. Grey, J. Harvey, A. Heiss, F. Hemmer, S. Jarp, R. Jones, D. Kelsey, M. Lamanna, H. Marten, P. Mato-Vila, F. Ould-Saada, B. Panzer-Steindel, L. Perini, Y. Schutz, U. Schwickerath, J. Shiers, and T. Wenaus, *LHC computing Grid: Technical Design Report. Version 1.06 (20 Jun 2005)*, Technical Design Report LCG. CERN, Geneva, 2005.

[105] The ATLAS collaboration, *Performance of the ATLAS Muon Trigger in p-p collisions at* $\sqrt{s} = 7$ *TeV*, ATLAS-CONF-2010-095, 2010.

[106] The ATLAS collaboration, *Lepton Trigger and Identification for the first Top quark observation*, ATL-COM-PHYS-2010-826, 2010.

[107] G. Aad, B. Abbott, J. Abdallah, A. A. Abdelalim, A. Abdesselam, O. Abdinov, B. Abi, M. Abolins, H. Abramowicz, H. Abreu, and et al., *Measurement of the* $W \to l\nu$ *and* $Z/\gamma* \to ll$ *production cross sections in proton-proton collisions at* $\sqrt{s} = 7$ *TeV with the ATLAS detector*, Journal of High Energy Physics **12** (2010) 60.

[108] The ATLAS collaboration, *Electron and photon reconstruction and identification in ATLAS: expected performance at high energy and results at 900 GeV*, ATLAS-CONF-2010-005, 2010.

[109] The ATLAS collaboration, *Expected Performance of the ATLAS Experiment*, CERN-OPEN-2008-020, 2008.

[110] The ATLAS collaboration, *Electron performance in the ATLAS experiment*, ATL-COM-PHYS-2010-208, 2010.

[111] Atlas TWiki, *MuonRecoPedia*, `https://twiki.cern.ch/twiki/bin/view/AtlasProtected/MuonRecoPedia`.

[112] The ATLAS collaboration, *Performance of Jet Algorithms in the ATLAS Detector*, ATL-PHYS-INT-2010-129, 2010.

[113] G. P. Salam and G. Soyez, *A practical seedless infrared-safe cone jet algorithm*, Journal of High Energy Physics **5** (2007) 86.

[114] M. Cacciari, G. P. Salam, and G. Soyez, *The anti-*$\mathrm{k_T}$ *jet clustering algorithm*, Journal of High Energy Physics **4** (2008) 63.

[115] M. H. Seymour, *Jet shapes in hadron collisions: higher orders, resummation and hadronization*, Nuclear Physics B **513** (1998) 269.

[116] The ATLAS collaboration, *Jet selection for top physics*, ATL-COM-PHYS-2010-835, 2010.

[117] The ATLAS collaboration, *A Simple* p_T*- and* η*-Dependent Monte Carlo-Based Jet Calibration*, ATL-COM-PHYS-2009-076, 2009.

[118] The ATLAS collaboration, *Study on reconstructed object definition and selection for top physics*, ATL-COM-PHYS-2009-633, 2009.

[119] The ATLAS collaboration, *Calibrating the b-Tag and Mistag Efficiencies of the SV0 b-Tagging Algorithm in 3* pb^{-1} *of Data with the ATLAS Detector*, ATLAS-CONF-2010-099, 2010.

[120] The ATLAS collaboration, *B-tagging for top physics analyses with early ATLAS data at* $\sqrt{s} = 7$ *TeV*, ATL-COM-PHYS-2010-846, 2010.

[121] The ATLAS collaboration, *Missing Transverse Energy for Top Physics analyses with early ATLAS data at* $\sqrt{s}=7$ *TeV*, ATL-COM-PHYS-2010-821, 2010.

[122] A. Doxiadis and M. Kayl, *Estimating the isolated lepton rate in multi-jet events*, ATL-PHYS-INT-2008-022, 2008.

[123] S. Bordoni, A. Doxiadis, M. Ridel, S. Trincaz-Duvoid, and I. Van Vulpen, *Monte Carlo study of isolated leptons in multi-jet events*, ATL-PHYS-INT-2010-011, 2010.

[124] Particle Data Group Collaboration, C. Amsler *et al.*, *Review of particle physics*, Phys. Lett. **B667** (2008) 1.

[125] Onne Peters, *Measurement of the b jet cross section at* $\sqrt{s} = 1.96$*-TeV*, FERMILAB-THESIS-2003-25.

[126] The CMS collaboration, *Prospects for the first Measurement of the ttbar Cross Section in the Muon plus Jets Channel at* $\sqrt{s}=10$ *TeV with the CMS Detector*, CMS-PAS-TOP-09-003, 2009.

[127] R. Barlow, *Statistics. A guide to the use of statistical methods in the physical sciences*, Wiley, 1989.

[128] Atlas TWiki, *Atlas Run Query*, `http://atlas-runquery.cern.ch/`.

[129] The ATLAS collaboration, *Data Quality Status Flags and Good Run Lists for Physics Analysis in ATLAS*, ATL-COM-GEN-2009-015, 2009.

[130] Atlas TWiki, *Atlas Luminosity Calculator*, `https://atlas-datasummary.cern.ch/lumicalc/`.

[131] Atlas TWiki, *DataPeriods*, `https://twiki.cern.ch/twiki/bin/view/AtlasProtected/DataPeriods`.

[132] *Performance of primary vertex reconstruction in proton-proton collisions at $\sqrt{s} = 7$ TeV in the ATLAS experiment*, ATLAS-CONF-2010-069, 2010.

[133] The ATLAS collaboration, *Estimation of the W+Jets Background for Top Quark Re-Discovery in the Single Lepton+Jets Channel*, ATL-COM-PHYS-2010-834, 2010.

[134] F. A. Berends, H. Kuijf, B. Tausk, and W. T. Giele, *On the production of a W and jets at hadron colliders*, Nuclear Physics B **357** (1991) 32.

[135] The ATLAS collaboration, *Measurement of the $W \to l\nu$ production cross-section and observation of $ZW \to ll$ production in proton-proton collisions at $\sqrt{s}$=7 TeV with the ATLAS detector*, ATLAS-CONF-2010-051, 2010.

[136] The ATLAS collaboration, *Measurement of the Z to ll production cross section in proton-proton collisions at $\sqrt{s}$=7 TeV with the ATLAS detector*, ATLAS-CONF-2010-076, 2010.

[137] The ATLAS collaboration, *$W \to \mu\nu$ and $Z \to \mu\mu$ measurments in proton-proton collisions at $\sqrt{s}$=7 TeV with the ATLAS detector*, ATL-COM-PHYS-2010-685, 2010.

[138] W. T. Eadie, D. Drijard, and F. E. James, *Statistical methods in experimental physics*, North-Holland Publishing Co., 1971.

[139] The ATLAS collaboration, *Extraction of the prompt muon component in inclusive muons produced at $\sqrt{s} = 7$ TeV*, ATLAS-CONF-2010-075, 2010.

[140] T. Kittelmann, V. Tsulaia, J. Boudreau, and E. Moyse, *The Virtual Point 1 event display for the ATLAS experiment*, Journal of Physics Conference Series **219**(3) (2010) 032012.

[141] J. Alwall, S. Höche, F. Krauss, N. Lavesson, L. Lönnblad, F. Maltoni, M. L. Mangano, M. Moretti, C. G. Papadopoulos, F. Piccinini, S. Schumann, M. Treccani, J. Winter, and M. Worek, *Comparative study of various algorithms for the merging of parton showers and matrix elements in hadronic collisions*, European Physical Journal C **53** (2008) 473.

[142] The ATLAS collaboration, *Luminosity Determination Using the ATLAS Detector*, ATLAS-CONF-2010-060, 2010.

[143] *plot and theoretical predictions provided by Ulrich Husemann.*

SUMMARY

By analyzing the collisions at the Large Hadron Collider (`LHC`) thousands of particle physicists are trying to verify, understand and expand the Standard Model of particle physics. The Standard Model is the model that describes all matter particles and their interactions and governs three out of the four fundamental forces of nature. In this thesis we focussed on the top-quark. The top-quark, which is by far the heaviest of all quarks, has been observed for the first time in 1995 at the `Tevatron` collider near Chicago, USA. Its production rate, that is how often a top-quark is produced per collision, is known theoretically with great precision (uncertainties of less than 10%). Nevertheless it is one of the most interesting measurements at the `LHC` that can be performed with early data with the `ATLAS` detector. The reason for this is threefold: 1. The complex decay of the top-quark makes it a challenging particle to observe experimentally. 2. The measurement of the production rate of the top-quark is a test of the Standard Model. 3. The top-quark plays a special role in many extensions of the Standard Model and observation might provide a first glimpse at beyond Standard Model processes.

Testing the detector

The measurement of the top-quark production rate is an ideal test for the performance of the `ATLAS` detector. The top-quark is produced in pairs of top and antitop-quarks ($t\bar{t}$) in proton-proton collisions at the `LHC`. The decay of a pair of top-quarks is characterized in our analysis by three main objects: a muon (the heavier cousin of the electron) with high momentum, four or more regions of high energy depositions in the detector (called jets) and a large amount of 'missing transverse energy'. The latter is found by balancing the measured energy in the detector in all directions and labeling the unbalanced energy 'missing transverse energy'. This missing transverse energy in top-quark pair decays is accounted for by the escaping neutrino, which leaves no trace in the detector. In order to measure the top-quark decay all detector components have to be well understood and calibrated. It is in fact quite amazing that the `ATLAS` detector has identified and measured the top-quark within the first year of data-taking.

Standard Model predictions

Apart from testing the detector performance, measuring the top-quark pair production rate is also a test of the Standard Model itself. With the `LHC` we entered a higher energy regime (colliding at a center of mass energy of 7 TeV) and although the top-quark production is well understood, the theory has still to be confirmed at this higher energy. In particle physics the production rate is usually given as a cross section. In Figure 1 we show the measured and predicted production cross section (σ) of top-quarks at different energies. The black points are the measurements performed at the `Tevatron` at lower energy and the lighter point is the measurement performed in this thesis at 7 TeV. We can see that the experimental data and the theoretical prediction are in great agreement, confirming our Standard Model expectations.

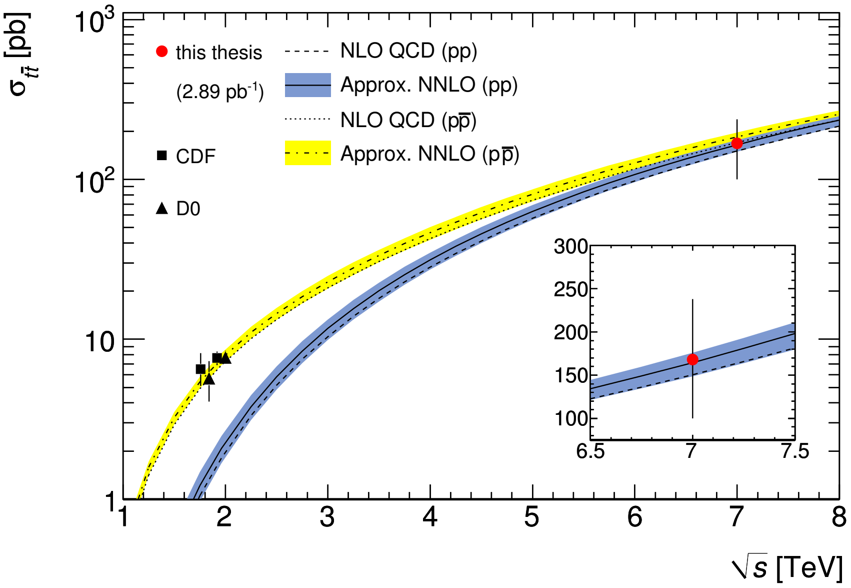

Figure 1: *The measured $t\bar{t}$ production cross section from the `CDF` and `DØ` experiments at 1.8 (1.96) TeV and the result presented in this thesis at 7 TeV as a function of the energy ($\sqrt{s}$) compared to the theoretical prediction.*

Extensions of the model

More importantly however and much more tantalizing is the possibility that there is more beyond the horizon than the Standard Model. Many models have been proposed over the years that all try to explain caveats in the existing model that would show up when reaching higher energies. The top-quark plays a special role in many of these models through its large mass and large coupling to the Higgs-field. Any new physics would reveal itself in the top-channel. A measurement of the top-quark production is essentially a model independent way of searching for new physics. At the moment there is unfortunately not enough data to draw any conclusions about new physics.

Selecting the right events

In order to perform measurement of the production rate, we need to understand the possible background events in the analysis. A background event is an event that is falsely selected as a top-quark event. We have shown that although many different event types are backgrounds to our analysis, there is one kind that is more troublesome than the others: multi-jet events. Most other event types are well understood, but these events can only be simulated with large uncertainties which means that we cannot trust the simulation to tell us how many of these events pass our selection and are thus wrongfully identified as top-quark events. These multi-jet events do not produce any muons directly. Since we select events with a high energetic muons, these events should a priori not pass our requirements. A large fraction of this thesis is therefore dedicated to the study of how these events produce extra muons indirectly and to the analysis of the muon properties. Since we cannot trust our simulation to model the amount of background from these events, we have developed a way of determining the normalization directly from data. We use the knowledge that was gained by studying the properties of these events and exploit finally that they predominantly come from the decay of bottom-quarks. The bottom-quark is the lighter sister of the top-quark and forms bound states (an intermediate clustering with other quarks) that travel on average a few millimeter before they decay. By measuring the distance from where a muon is produced to the primary point of interaction, the muons from top-quark decays (the signal) can be distinguished from the muons from bottom-quark decay (the background). This difference is then the basis to determine the number of multi-jet events that passed all our requirements.

Results

In the final analysis of the first data 19 top-quark pair event candidates have been identified. Of these 19 events we estimated 0.9 ± 0.7 to come from multi-jet background. Although the background seems extremely small, it is important to the measurement to have a solid estimate with well determined error. The $t\bar{t}$ production cross section (as a measure of the production rate) that we extracted from these numbers is $\sigma(t\bar{t}) = 168 \pm 55$ (stat) pb which is in beautiful agreement with the theoretical prediction, see again Figure 1. Note that the total cross section in proton-proton collisions at this center of mass energy is $\sim 10^{10}$ pb. Since the amount of events in the analysis is so low, we cannot rule out new physics models yet, but we can confirm the existence of the Standard Model top-quark. We have also shown that we can deduce the number of background events from data alone (albeit with large uncertainty). Fortunately more data is coming rapidly now and more data means a more precise measurement of the background and hence a more precise measurement of the top-quark production rate. With the full dataset recorded up to now the uncertainties are already of the same order as the theoretical error. This now means that the era of top-quark physics at the `LHC` has just begun...

SAMENVATTING

Door het analiseren van de botsingen bij de Large Hadron Collider (`LHC`), proberen duizenden deeltjes fysici het Standaard Model te bevestigen, begrijpen en uit te breiden. Het Standaard Model is het model dat alle materie deeltjes en hun onderlinge wisselwerkingen beschrijft and dat drie van de vier fundamentele natuurkrachten verenigt. In dit proefschrift concentreren wij ons op de top-quark. De top-quark, verreweg de zwaarste van alle quarks, is voor het eerst geobserveerd in 1995 bij de `Tevatron` versneller in de buurt van Chicago, VS. Zijn productie snelheid, dat wil zeggen hoe vaak hij wordt geproduceerd per botsing, is bekend in theorie met grote nauwkeurigheid (onzekerheden kleiner dan 10%). Desalniettemin is het een van de meest interessante metingen bij de `LHC` die kan worden gedaan met de `ATLAS` detector met de allereerste data. Hiervoor zijn drie redenen: 1. Het complexe verval van de top-quark maakt het een uitdagend deeltje om experimenteel waar te nemen. 2. Het meten van de productie snelheid van de top-quark is een test van het Standaard Model. 3. De top-quark speelt een speciale rol in veel uitbreidingen van het Standaard Model en de waarneming zou een eerste hint kunnen geven van processen die buiten het Standaard Model liggen.

Testen van de detector

De meting van de top-quark productie snelheid is een perfecte test voor de prestaties van de `ATLAS` detector. De top-quark wordt geproduceerd in paren van top en antitop-quarks ($t\bar{t}$) in proton-proton botsingen bij de `LHC`. Het verval van een top-quark paar wordt in onze analyse gekarakteriseerd door drie objecten: een muon (de zwaardere neef van het elektron) met hoge impuls, vier of meer regionen in de detector met hoge energie (genoemd jets) en veel ‘missende transversale energie’. Deze laatste term wordt gegeven door de energie balans op te maken uit de gemeten energie in de detector en de ongebalanceerde energie ‘missende transversale energie’ te noemen. Deze missende transversale energie in top-quark paar vervallen wordt gegeven door het ontsnappende neutrino, dat geen spoor achterlaat in de detector. Om het top-quark verval te meten moeten alle onderdelen van de detector goed begrepen en gekalibreerd zijn. Het is eigenlijk verbazingwekkend dat de `ATLAS` detector de top-quark heeft geïdentificeerd en gemeten in het eerste jaar van `LHC` activiteit.

Standaard Model voorspellingen

Los van het testen van de detector prestaties is het meten van de top-quark productie snelheid ook een test van het Standaard Model an sich. Met de `LHC` zijn we een hoger energie bereik binnen gedrongen (botsend op een energie van 7 TeV) en ook al is de top-quark productie goed begrepen, moet de theorie nog wel worden bevestigd bij deze hogere energie. In de deeltjesfysica wordt de productie snelheid meestal gegeven als een werkzame doorsnede. In Figuur 1 laten wij de gemeten en de voorspelde productie werkzame doorsnede (σ) van top-quarks zien bij verschillende energieën. De zwarte punten zijn de meting uitgevoerd bij de `Tevatron` bij lagere energieën en het lichtere punt is de meting uitgevoerd in dit proefschrift bij 7 TeV. We zien dat de experimentele data en de theoretische voorspellingen zeer goed overeenkomen en dus onze Standaard Model verwachtingen bevestigen.

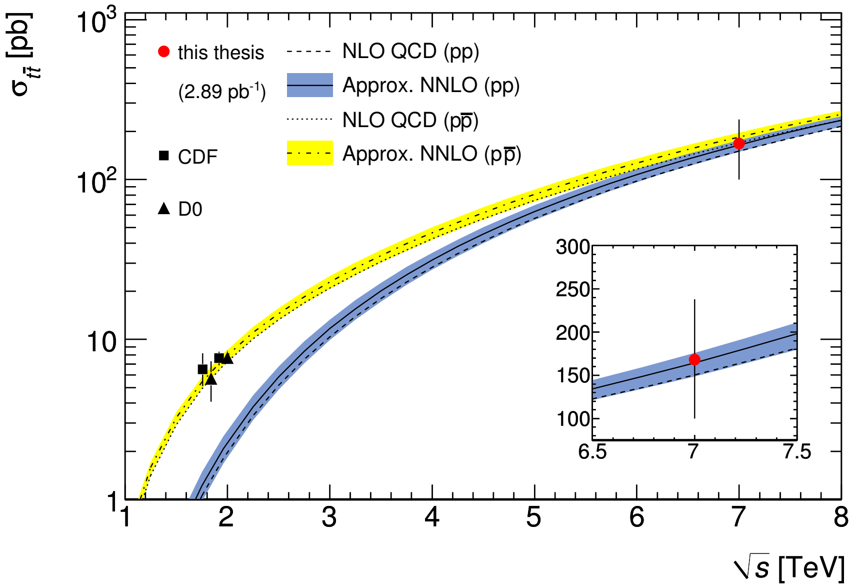

Figuur 1: *De $t\bar{t}$ productie werkzame doorsnede zoals gemeten door de `CDF` en `D0` experimenten bij een energie van 1.8 (1.96) TeV en het resultaat zoals het is gepresenteerd in dit proefschrift bij een energie van 7 TeV als een functie van de energie vergeleken met de theoretische voorspellingen.*

Uitbreidingen van het model

Misschien wel belangrijker en spannender is de mogelijkheid dat er meer is tussen hemel en aarde dan het Standaard Model. Veel modellen zijn gepresenteerd de afgelopen jaren die tekortkomingen van het bestaande model proberen op te lossen die zouden moeten ontstaan bij het bereiken van hogere energieën. De top-quark speelt in veel van deze modellen een belangrijke rol door zijn grote massa en koppeling aan het Higgs-veld. Elk nieuw fysica model zou zichzelf moeten prijsgeven in het top-kanaal. Een meting van de top-quark productie is in essentie een model onafhankelijke methode om nieuwe fysica te zoeken. Op het moment is er helaas nog niet genoeg data aanwezig om uitsluitsel te geven over nieuwe fysica.

Selectie van de juiste botsingen

Om de meting van de productie snelheid uit te kunnen voeren, moeten we de mogelijke achtergrond events (een event is een bepaald proces dat voortkomt uit een botsing) in onze analyse begrijpen. Een achtergrond event is een event dat foutief geselecteerd is als top-quark event. We hebben laten zien dat hoewel er veel verschillende types achtergrond events zijn voor onze analyse, er één type is die zorgelijker is dan de andere: de multi-jet events. De andere achtergrond events zijn goed begrepen, maar dit type kunnen wij alleen met grote onzekerheden simuleren, wat betekent dat we de simulatie niet kunnen vertrouwen om ons te laten zien hoeveel van deze events door onze selectie heen komen en dus valselijk als top-quark event worden aangezien. Deze multi-jet events produceren in principe geen muonen. Aangezien wij events selecteren op de aanwezigheid van een hoog energetisch muon, zouden deze events niet door onze selectie moeten heen komen. Een groot deel van dit proefschrift is gewijd aan de studie hoe deze events toch indirekt muonen produceren en het bestuderen van de eigenschappen van deze muonen. Omdat wij de simulatie niet kunnen vertrouwen om de grootte van deze achtergrond goed te modelleren, hebben wij een methode ontwikkeld om dit direkt uit de data te halen. We gebruiken de opgedane kennis uit de studie van deze events dat de muonen voornamelijk ontstaan bij het verval van bottom-quarks. De bottom-quark is het lichtere zusje van de top-quark en vormt gebonden toestanden (een tijdelijke clustering met andere quarks) die een paar millimeter kunnen reizen voordat ze vervallen. Door het meten van de afstand van waar het muon is geproduceerd tot het interactiepunt, kunnen de muonen van top-quark verval (het signaal) worden onderscheiden van de muonen van bottom-quark verval (de achtergrond). Dit verschil vormt de basis om het aantal multi-jet events af te schatten dat door onze selectie is heen gekomen.

Resultaten

In de uiteindelijke analyse van de eerste data zijn 19 top-quark paar kandidaten gevonden. Van deze 19 events hebben we geschat dat er 0.9 ± 0.7 komen van de multi-jet achtergrond. Hoewel de achtergrond zeer klein is, is het toch belangrijk voor de meting om een goede afschatting te hebben met goed bepaalde fout. De $t\bar{t}$ productie werkzame doorsnede (een maat voor de productie snelheid) die wij uit deze getallen hebben gehaald is $\sigma(t\bar{t}) = 168 \pm 55$ (stat) pb wat in mooie overeenstemming is met de theoretische voorspellingen, zie Figuur 1. We merken op dat de totale werkzame doorsnede in proton-proton botsingen bij deze energie $\sim 10^{10}$ pb is. Aangezien het aantal events in deze analyse zo laag is, kunnen wij geen nieuwe fysica modellen uitsluiten, maar wel het bestaan van de top-quark in het Standaard Model bevestigen. We hebben ook laten zien dat het aantal achtergrond events kan worden afgeschat puur uit de data zelf (zij het met grote onzekerheden). Gelukkig komt er nu snel meer data aan en meer data betekent een preciezere meting van de achtergrond en dus ook een preciezere meting van de top-quark productie snelheid. Met de volledige dataset die tot nu toe is gemeten zijn de onzekerheden als van dezelfde orde van grootte als de theoretische fouten. Dit betekent dat de tijd van de top-quark metingen bij de `LHC` pas is begonnen...

ACKNOWLEDGEMENTS

It feels almost surreal to be writing the acknowledgements to my thesis. It is the end of a long journey that was tough at times, but mainly very enjoyable and educational. I had planned to have this written weeks ago, but of course it had to be done last-minute. This is a shame since it is the one section of this book that almost everyone will read. It is however not just an obligatory part of the thesis: this work would have never been possible without the help of many. A disclaimer right from the start: lots of names will be missing here. I thank you nonetheless!

First of all I would like to thank my promotor Stan Bentvelsen who convinced me with his enthusiasm for this field of research and this detector to accept a position at the ATLAS group at Nikhef. Although he tricked me into believing that data would be coming soon, I was always grateful for his inspiration and devotion to science. As my co-promotor I was lucky to have Ivo van Vulpen, who hired me on his Vidi. Thank you for schooling me in the art that is high energy physics. Thanks also for sticking up for me in some political battles! In the last months of doing analysis my third and unofficial supervisor Jean-Francois Arguin was always there to help me out in many a skype session. Without you my results would not have been in the paper. Thanks also to my C3 supervisor Marcel Merk who made sure that we stuck to the plan.

Research in particle physics is a group effort and I would like to thank everyone at Nikhef who made this thesis possible. All my stupid computing questions where always answered, but maybe almost equally important were the Vrimibo's, three o'clock coffee breaks (koffie?) and other interesting social activities. Thanks to the cross section and AMA clan: Menelaos, Ido, Hegoi, Jörg, Guiseppe, Marcel, Pamela, Wouter and Max: without you, I would have not been able to analyze anything. In the last months of analysis, when there was finally data, I could not have coped without the help of Hurng and Daniel: thanks for fetching the data for me! Writing notes has been very helpful for the writing of this thesis and I would like to mention Manuel and Stefania here. Folkert, I am glad that we organized the pat together for a while.

Special thanks to Dr. Gossie who had to take care of me when I could not walk (cooking

for me every night!), but who also wrote a thesis that functioned as a great reference. Thanks to Unstoppable-Alex for accompanying me on some great trips, but also for many good (political) discussions. See you in the line-up, dude! Serena, bedankt voor altijd een mooie quote.
Going to Cern and living in Geneva was one of the great perks of this PhD. At cern I ran into a completely new group of people who once more proved that we are not just nerds. Gracias a Laurita y los boludos (Tincho, Basko, Gaston & Monti)! Especially for introducing me to Fernet-Branca, the new love of my life.

There are so many friends outside physics that helped me through the rough patches of this journey, but also showed interest when I was happy and wanted to talk about my research: thank you all. I could not have done it without you! I know it was not always easy... Thanks to the 'surfteam' for the trips to Lostmarc'h and to the night owls at the Engelbewaarder: it kept me sane. Thanks for reading my summary, Robert and Phil. Special thanks to Marc who put a wave on my cover and to Maarten for arranging the letters on short notice!

For those of you who know me a bit, it may come as no surprise that my family is very important to me. This journey would not have been the same without my sister Katherina. Dank je wel kleine! My parents however deserve the biggest thanks of all. It is basically there fault I ever went on this trip. At the same time they probably had to endure most of the stress that finishing this thesis produced. Danke für immer einen coolen Spruch und danke für immer ein offenes Ohr!

The bad news is we don’t have any control,
the good news is you can’t make any mistakes.
Chuck Palahniuk